

Probing the QCD phase diagram via net-proton number fluctuations at RHIC

By

ASHISH PANDAV

PHYS11201605002

**National Institute of Science Education and Research,
Bhubaneswar**

*A thesis submitted
to the Board of Studies in
School of Physical Sciences*

*In partial fulfillment of requirements
For the Degree of*

DOCTOR OF PHILOSOPHY

of

HOMI BHABHA NATIONAL INSTITUTE



January, 2023

Homi Bhabha National Institute

Recommendations of the Viva Voce Committee

As members of the Viva-Voce Committee, we certify that we have read the dissertation prepared by **Ashish Pandav** entitled "**Probing the QCD phase diagram via net- proton number fluctuations at RHIC**" and recommend that it may be accepted as fulfilling the thesis requirement for the award of Degree of Doctor of Philosophy.

Signature:

Sanjay Kumar Swain

Chairman - Prof. Sanjay Kumar Swain

24/04/23

Date:

Signature:

Bedangadas Mohanty

Guide / Convener - Prof. Bedangadas Mohanty

24/04/2023

Date:

Signature:

Victor Roy

Member 1 - Dr. Victor Roy

24.04.2023

Date:

Signature:

Amaresh Kumar Jaiswal

Member 2 - Dr. Amaresh Kumar Jaiswal

24.04.2023

Date:

Signature:

Md. Nosim

Member 3 - Dr. Md Nasim

24/04/2023

Date:

Signature:

Sadhana Dash

External examiner - Prof. Sadhana Dash

24.04.2023

Date:

Final approval and acceptance of this thesis is contingent upon the candidate's submission of the final copies of the thesis to HBNI.

I/We hereby certify that I/We have read this thesis prepared under my/our direction and recommend that it may be accepted as fulfilling the thesis requirement.

Date : April 24, 2023

Place : Bhubaneswar

Bedangadas Mohanty

(Guide)

STATEMENT BY THE AUTHOR

This dissertation has been submitted in partial fulfillment of requirements for an advanced degree at Homi Bhabha National Institute (HBNI) and is deposited in the library to be made available to borrowers under rules of the HBNI.

Brief quotations from this dissertation are allowable without special permission, provided that accurate acknowledgement of source is made. Requests for permission for extended quotation from or reproduction of this manuscript in whole or in part may be granted by the Competent Authority of HBNI when in his or her judgment the proposed use of the material is in the interests of scholarship. In all other instances, however, permission must be obtained from the author.

Date : April 24, 2023

Place : Bhubaneswar



(ASHISH PANDAV)

DECLARATION

I hereby declare that the investigation presented in the thesis has been carried out by me. The work is original and has not been submitted earlier as a whole or in part for a degree/diploma at this or any other Institution/University.

Date : April 24, 2023

Place : Bhubaneswar



(ASHISH PANDAV)

List of Publications related to thesis

Journal

Published

1. Nonmonotonic Energy Dependence of Net-Proton Number Fluctuations [STAR Collaboration], Primary contributors (Alphabetically): ShinIchi Esumi, Shu He, Xiaofeng Luo, Bedanga Mohanty, Toshihiro Nonaka, **Ashish Pandav**, Nu Xu, Zhenzhen Yang, Yu Zhang,
[Phys. Rev. Lett. 126, 092301 \(2021\)](#).
Journal link: <https://journals.aps.org/prl/abstract/10.1103/PhysRevLett.126.092301>
ArXiv link: <https://arxiv.org/abs/2001.02852>
2. Cumulants and Correlation Functions of Net-proton, Proton and Antiproton Multiplicity Distributions in Au+Au Collisions at energies available at the BNL Relativistic Heavy Ion Collider [STAR Collaboration], Primary contributors (Alphabetically): ShinIchi Esumi, Shu He, Xiaofeng Luo, Bedanga Mohanty, Toshihiro Nonaka, **Ashish Pandav**, Nu Xu, Zhenzhen Yang, Yu Zhang,
[Phys. Rev. C 104, 024902 \(2021\)](#).
Journal link: <https://journals.aps.org/prc/abstract/10.1103/PhysRevC.104.024902>
ArXiv link: <https://arxiv.org/abs/2101.12413>
3. Measurement of the Sixth-Order Cumulant of Net-Proton Multiplicity Distributions in Au+Au Collisions at $\sqrt{s_{NN}} = 27, 54.4, \text{ and } 200 \text{ GeV}$ at RHIC [STAR Collaboration], Primary contributors (Alphabetically): Roli Esha, ShinIchi Esumi, Shu He, Huan-Zhong Huang, Xiaofeng Luo, Bedangadas Mohanty, Toshihiro Nonaka, **Ashish Pandav**, Nu Xu, Yu Zhang,

- Phys. Rev. Lett.* 127, 262301 (2021).
 Journal link: <https://journals.aps.org/prl/abstract/10.1103/PhysRevLett.127.262301>
 ArXiv link: <https://arxiv.org/abs/2105.14698>
4. Beam Energy Dependence of Fifth and Sixth-Order Net-proton Number Fluctuations in Au+Au Collisions at RHIC [STAR Collaboration], Primary contributors (Alphabetically): ShinIchi Esumi, Xiaofeng Luo, Bedanga Mohanty, Toshihiro Nonaka, **Ashish Pandav**, Nu Xu, Yu Zhang,
Phys. Rev. Lett. 130, 082301 (2023).
 Journal link: <https://journals.aps.org/prl/abstract/10.1103/PhysRevLett.130.082301>
 ArXiv link: <https://arxiv.org/abs/2207.09837>
5. Effect of limited statistics on higher order cumulants measurement in heavy-ion collision experiments, **Ashish Pandav**, Debasish Mallick and Bedangadas Mohanty,
Nucl. Phys. A 991, 121608 (2019).
 Journal link: <https://www.sciencedirect.com/science/article/abs/pii/S0375947419301769>
 ArXiv link: <https://arxiv.org/abs/1809.08892>
6. Search for the QCD critical point in high energy nuclear collisions (Review article), **Ashish Pandav**, Debasish Mallick and Bedangadas Mohanty,
Prog. Part. Nucl. Phys. 125, 103960 (2022).
 Journal link: <https://www.sciencedirect.com/science/article/abs/pii/S0146641022000217>
 ArXiv link: <https://arxiv.org/abs/2203.07817>

Internal Analysis Note

1. Nonmonotonic Energy Dependence of Net-Proton Number Fluctuations, Primary contributors (Alphabetically): ShinIchi Esumi, Shu He, Xiaofeng Luo, Bedanga Mohanty, Toshihiro Nonaka, **Ashish Pandav**, Nu Xu, Zhenzhen Yang, Yu Zhang.
 Link: <https://drupal.star.bnl.gov/STAR/starnotes/private/psn0731>
2. Measurement of the Sixth-Order Cumulant of Net-Proton Multiplicity Distributions in Au+Au Collisions at $\sqrt{s_{NN}} = 27, 54.4, \text{ and } 200 \text{ GeV}$ at RHIC, Primary contributors (Alphabetically): Roli Esha, ShinIchi Esumi, Shu He, Huan-Zhong Huang, Xiaofeng

Luo, Bedangadas Mohanty, Toshihiro Nonaka, **Ashish Pandav**, Nu Xu, Yu Zhang.

Link: <https://drupal.star.bnl.gov/STAR/starnotes/private/psn0733>

3. Beam Energy Dependence of Fifth and Sixth-Order Net-proton Number Fluctuations in Au+Au Collisions at RHIC, Primary contributors (Alphabetically): ShinIchi Esumi, Xiaofeng Luo, Bedanga Mohanty, Toshihiro Nonaka, **Ashish Pandav**, Nu Xu, Yu Zhang.

Link: <https://drupal.star.bnl.gov/STAR/starnotes/private/psn0780>

Conference Proceedings

Related to thesis

1. Measurement of cumulants of conserved charge multiplicity distributions in Au+Au collisions from the STAR experiment,
[Nucl. Phys. A 1005 \(2021\), 121936](#)
Contribution to: Quark Matter 2019
Link: <https://doi.org/10.1016/j.nuclphysa.2020.121936>
2. Measurement of cumulants of net-proton distributions in Au+Au collisions at $\sqrt{s_{NN}} = 54.4$ GeV at RHIC,
[DAE Symp.Nucl.Phys. 64 \(2019\) 776-777](#)
Contribution to: DAE-NUC 2019
Link: <https://inspirehep.net/literature/1804018>
3. Measurement of Higher Moments of Net-Proton Distributions in Au+Au Collisions at $\sqrt{s_{NN}} = 54.4$ GeV at RHIC,
[Springer Proc. Phys. 250 \(2020\), 355-359](#)
Contribution to: Strangeness in Quark Matter 2019
Link: https://doi.org/10.1007/978-3-030-53448-6_56
4. Collision energy dependence of C_5 and C_6 of net-proton distributions at RHIC-STAR,
[PoS, CPOD2021, 029 \(2022\)](#)
Contribution to: CPOD 2021
Link: <https://doi.org/10.22323/1.400.0029>

Others

1. Cumulant measurement of net-kaon distributions in Au+Au collisions at $\sqrt{s_{NN}} = 27$ GeV from BES-II program at RHIC,
[Springer Proc. Phys.277 \(2022\), 333-337](#)
Contribution to: DAE-HEP 2020
Link: https://doi.org/10.1007/978-981-19-2354-8_60
2. Seventh and eighth order cumulants of net-proton number distributions in heavy-ion collisions at RHIC-STAR,
[EPJ Web Conf. 276, 01006 \(2023\)](#)
Contribution to: Strangeness in Quark Matter 2022
Link: <https://doi.org/10.1051/epjconf/202327601006>

Conference/Workshop Presentations

Related to thesis

1. Measurement of higher moments of net-proton distributions in Au+Au collisions at $\sqrt{s_{NN}} = 54.4$ GeV at RHIC (contributory talk),
Strangeness in Quark Matter 2019 (SQM 2019) - the 18th International Conference on Strangeness in Quark Matter, June 10 - 15, 2019, Bari, Italy.
2. Measurement of cumulants of conserved charge multiplicity distributions in Au+Au collisions from the STAR experiment (contributory talk),
Quark Matter 2019 - XXVIIIth International Conference on Ultra-relativistic Nucleus-Nucleus Collisions, November 4-9, 2019, Wuhan, China.
3. Measurement of cumulants of conserved charge multiplicity distributions in Au+Au collisions from the STAR experiment (contributory talk),
Workshop on the QCD phase structure at high baryon density, November 12 - 14, 2019, Wuhan, China.
4. Measurement of cumulants of net-proton distributions in Au+Au collisions at $\sqrt{s_{NN}} = 54.4$ GeV at RHIC (contributory poster),

DAE International Symposium on Nuclear Physics, December 23 - 27, 2019, Lucknow, India.

5. Collision energy dependence of C_5 and C_6 of net-proton distributions at RHIC-STAR (contributory talk),
CPOD 2021 - the International conference on Critical Point and Onset of Deconfinement, March 15 - 19, 2021, Online.
6. Probing the QCD Phase Diagram via Higher Order Net-particle Fluctuation Measurements from STAR-BES (invited talk),
2022 RHIC/AGS ANNUAL USERS MEETING, June 7 - 10, 2022, Online.
7. Experimental overview of critical fluctuations (invited talk),
CPOD 2022 - the International conference on Critical Point and Onset of Deconfinement, November 28 - December 2, 2022, Online.

Others

1. Measurement of Cumulants of Net-Charge Distributions in Au+Au Collisions at $\sqrt{s_{NN}} = 54.4$ GeV (contributory talk),
XXIII DAE-BRNS HIGH ENERGY PHYSICS SYMPOSIUM -2018, December 10 - 14, 2018, IIT Madras, Chennai, India.
2. Cumulant measurement of net-kaon distributions in Au+Au collisions at $\sqrt{s_{NN}} = 27$ GeV from BES-II program at RHIC (contributory talk),
XXIV DAE-BRNS HIGH ENERGY PHYSICS SYMPOSIUM -2020, December 14 - 18, 2020, NISER Bhubaneswar, India.
3. C_7 and C_8 of net-proton distributions in heavy-Ion Collisions at RHIC-STAR (contributory poster),
Quark Matter 2022 (QM 2022) - XXIXth International Conference on Ultra-relativistic Nucleus-Nucleus Collisions, April 4 - 10, 2022, Krakow, Poland.
4. Seventh and eighth order cumulants of net-proton number distributions in heavy-ion collisions at RHIC-STAR (contributory talk),
Strangeness in Quark Matter 2022 (SQM 2022) - the 20th International Conference on Strangeness in Quark Matter, June 13 - 17, 2022, Busan, Republic of Korea.

xii

Date : April 24, 2023

Place : Bhubaneswar

A handwritten signature in black ink, appearing to read 'Ashish Pandav', with a small flourish at the end.

(ASHISH PANDAV)

DEDICATED TO

*the supreme one, for being kind and blessing with the fortune of meeting so many
beautiful souls along the way.*

ACKNOWLEDGEMENTS

The completion of the thesis work required contributions from many kind persons. Above all, I would like to extend sincere thanks to my supervisor, Dr. Bedangadas Mohanty for providing immense support and guidance. I have greatly benefitted from his deep physics insights and many fruitful discussions with him. There were times when I lacked belief in myself and still he believed in me. His scientific temperament and technical knowledge, his systematic way of addressing a problem at hand, has impressed me a lot. Observing him for his unparalleled dedication and devotion to his duties has always amazed me. I am forever indebted to him for accepting me to his group and for whatever I could achieve in these years.

I am grateful to Dr. Nu Xu for his guidance while working on this topic. He has been a source of great support since my early days of starting this analysis. I have greatly benefitted from his meticulous approach and insightful comments during our analysis discussions.

My appreciation to director NISER, Dr. Sudhakar Panda for providing all support needed during my PhD. Many thanks to Dr. Ranbir Singh, Dr. Varchaswi kashyap and Dr. Ajay K. Dash for always being available to help, both academically and personally despite them being quite busy. Warm regards to Dr. Xin Dong for having me at the Berkeley lab as visiting fellow and helping with physics analysis with his in-depth knowledge. He was kind enough to support in several aspects of my stay there. Many thanks to Dr. Grazyna Odyniec for all the support received at the lab and providing nice suggestions.

I am grateful to doctoral committee members: Dr. Bedangadas Mohanty, Dr. Sanjay Kumar Swain, Dr. Victor Roy, Dr. Amaresh Jaiswal, Dr. Md Nasim and also to thesis reviewers: Dr. Sadhana dash, Dr. Raimond Snellings and Dr. Ankhi Roy for their constructive criticism and reviewing the thesis work, providing suggestions to improve

it. Thanks to Dr. Sorendu Gupta for useful discussions with him during his visits to NISER. I am grateful to STAR's physics working group conveners throughout these years, Dr. ShinIchi Esumi, Dr. Xiaofeng Luo, Dr. Jianguyong Jia, Dr. Hanna Zbroszczyk, Dr. Toshihiro Nonaka and analysis co-ordinators, Dr. Rongrong Ma, Dr. Takafumi Niida and Dr. Grigory Nigmatkulov for many discussions and sharing their suggestions and comments. Thanks to past and current STAR spokespersons: Dr. Zhangbu Xu, Dr. Helen Caines, Dr. Lijuan Ruan for their suggestions on analysis work and help for taking shifts at BNL. My regards to members of the STAR GPC committee for very diligently reviewing our paper manuscripts, especially, Dr. Declan Keane for important suggestions and quick responses. Thanks to Dr. Flemming Videbaek for hosting me at BNL during iTPC upgrade for STAR and Dr. Xiaofeng Luo for inviting us for analysis discussion at CCNU. Thanks to Dr. Tonko, Bob and Tim Camarda from BNL for helping with my tasks for the iTPC upgrade.

My regards to Dr. Debasish Mallick, for always willing to help with physics discussions. I learnt many things from him. Thanks to his jovial nature, discussions with him always felt effortless. The lab at NISER would have been a very different place for me, had it been not for my labmates and friends. Heartfelt thanks to Dr. Debasish Mallick, Dr. Dukhishyam Mallick, Dr. Sourav Kundu, Dr. Ashutosh Dash, Dr. Subhasis Samanta, Dr. Samir Banik, Dr. Vijay Iyer, Dr. Kishora Nayak, Dr. Yousuf Jamal, Dr. Vipul Bairathi and Dr. Debadeepti Mishra, Dr. Rihan Haque, Dr. Ananta Mishra, for being there to help always. My kind regards to Ms. Mouli Chowdhury, Mr. Prottay Das, Ms. Swati Saha, Mr. Sudipta Das, Mr. Danush S. and all students from our lab for being very supporting and accomodating throughout these years. My regards to Dr. Md Nasim, Dr. Subhash Singha, Dr. Chitrasen jena, Dr. Prithwish Tribedy, Dr. Lokesh Kumar for being considerate and happy to discuss physics anytime. My appreciation to Dr. Shuddha Shankar Dasgupta,

Dr. Ganesh Tambave, Dr. Raveendrababu Karnam, Mr. Lalatendu Mishra and Mr. Kirti Prasad Sharma for treating me like one of their friends. Thanks to Dr. Yu Zhang, Dr. Ho San Ko, Dr. Risa Nisitani, Dylan Neff for analysis related discussions.

Many thanks to all chairpersons for school of physical sciences (SPS) through my stay (Dr. Bedangadas Mohanty, Dr. Ashok Mohapatra and Dr. A.V Anil Kumar), convener SPS (Dr. Kartik Senapati, Dr. Ajay Nayak and Dr. Kush Saha) and Dean Academics (Dr. Pranay Swain) for helping with so many official requests and procedures. Thanks to Ms. Lipsa Das from Academic section and Mr. Gopal Rath from finance section for facilitating with processing of academic and finance related works. My regards to members of SPS Office: Mr. Dolananda Pradhan, Mr. Biplab Kanungo, Mr. Sabyasachi Subudhi, Mr. Badri and all others for quickly responding to any request from my side. Thanks to Mr. Subhas Rout for taking care of our lab and repairing devices when we run into issues. I appreciate the help received from Ms. Liz Mogavero during my stay at BNL, Ms. Ya Ma when visiting CCNU, and Ms. Lady Bonifacio during visiting experience at LBNL. I am grateful to DAE and DST Govt. of India, STAR-ALICE-India task force for providing assistance to traveling for shift work and to attend and present my work in conferences. Here I must note that ref computation grid at BNL and Garuda clusters at NISER were very much essential for carrying out analysis work.

I shall always be indebted to my teachers, especially P.C. Dasmohapatra Sir and Sashi Sir for imparting me their knowledge and mentoring me. I am grateful to my friends: Sunil Barik, Deepak Mahalik, Deba Mishra, Gyanada Mohanty for keeping in touch. Special thanks to Pump K.N. Leima, Manu Beniwal, Anmol Walia, Deepak Sharma, Abhinav Mahapatra, Jatin Kumar, Tanmay Kathel, Sonu Kumar, Sumit Kumar, Praveen Yadav and Siddharth Karmakar. Thanks to my batchmates, and other friends during PhD: Tanim Firdoshi, Rashmi Rekha Sahoo, Dipika Dash, Snigdha Pati, Soumya Mishra, Sourav

Bhakta, Sujith NS, Bimalesh Giri, Jagannath Santra, Subir Sen, Charanpreet Singh, Anupa Kumari, Geet Chaudhary and Sandeep Dudi, all others, for making the time memorable. My heartfelt gratitude to Akshaya Sahoo, Milan Patra, Rik Bhattacharria for many fond memories and always having my back at times of need.

Last of all, kindest regards to my family, specially, grandparents, parents, and siblings for their blessings and putting up with all my requests and understanding me when I needed. Their belief in me is what inspired me the most. I could not have asked for anything more.

ABSTRACT

Phase transitions are ubiquitous in nature and carry important implications in the understanding of matter around us. This thesis work is dedicated to the study of phase transition in the strongly interacting matter. The strong interaction is one of the four fundamental interactions of nature and is governed by Quantum Chromo Dynamics (QCD). Its phase diagram, demonstrating various phases of strongly interacting matter under varying external conditions, such as temperature (T) and baryonic chemical potential (μ_B), is called the QCD phase diagram. Unlike the phase diagram of water which has gathered quite a detailed understanding, the QCD phase diagram is largely speculated. There are at least two distinct phases of QCD matter: a hadronic phase where quarks and gluons are confined and a quark-gluon-plasma (QGP) phase where they are deconfined. First principle lattice QCD calculations predict the quark-hadron phase transition to be a crossover at vanishing μ_B . On the other hand, at large μ_B , QCD-based models suggest this to be a first-order phase transition terminating at a critical point (called the QCD critical point). Neither the nature of the QCD phase transition nor the existence of a possible critical point has been experimentally confirmed yet.

The QGP is believed to have existed in the primordial universe, which later transformed into hadrons as the universe expanded and cooled. To recreate the phase transition from hadronic matter to QGP in laboratory, heavy-ion collisions are performed at ultra-relativistic speed using the Relativistic Heavy-Ion Collider (RHIC) facility at Brookhaven National Lab. The study of this phase transition is facilitated by net-proton number fluctuations. Fluctuations are quantified via cumulants. Higher-order cumulants of event-by-event net-proton distributions are sensitive to the presence of QCD critical point as well as the nature of QCD phase transition. By event, we mean here collision of two heavy-ions. Before

embarking on the experimental measurement of net-proton cumulants, we performed a toy-model simulation study to obtain the minimum number of events needed for their proper estimation. Proton and antiproton numbers were assumed to follow independent; (a) Poisson distributions and (b) Binomial distributions in the simulation. For both cases, we found that events of the order of a million (billion) are needed for obtaining net-proton cumulants up to the fourth (sixth) order with a precision of better than 5%. The study also indicated that irrespective of the number of events, the cumulants of all orders generally agree with their true values within their respective $\pm 1\sigma$ statistical uncertainties.

In the experimental exploration of QCD phase structure, net-proton cumulants up to sixth-order were measured in Au+Au collisions at nine center-of-mass collision energies: $\sqrt{s_{NN}} = 7.7, 11.5, 14.5, 19.6, 27, 39, 54.4, 62.4$ and 200 GeV. Collisions at these energies were recorded by the Solenoidal Tracker at RHIC (STAR) detector in the first phase of the Beam Energy Scan (BES-I) program and provided an extensive μ_B coverage ($\mu_B \sim 20 - 420$ MeV) of the QCD phase diagram. Protons and antiprotons within transverse momentum (p_T) range, 0.4 to 2 GeV/c and rapidity (y) acceptance -0.5 to 0.5 were selected using the Time-Projection-Chamber (TPC) and Time-of-Flight (TOF) detectors. Collision centrality was determined using charged particle multiplicity that excluded (anti-) protons to avoid self-correlation effects. Corrections accounting for finite detector acceptance and finite centrality width were performed. Since higher-order cumulants are sensitive to the details of the distribution and can change appreciably with a minor change in the distribution's shape, careful estimation of uncertainties on cumulants was carried out. Three methods of statistical uncertainty estimation: the Delta theorem, Bootstrap, and Sub-group method, were studied and verified for their suitability. The Sub-group method was found to be inefficient in estimating statistical uncertainties on higher-order cumulants. The systematic uncertainties were estimated by considering variations of different sources,

which included track selection cuts, particle identification criteria, background estimates, and track reconstruction efficiency.

To compare the experimental measurements with various theoretical calculations, cumulant ratios up to the sixth order were constructed. First, we checked for observation of QCD thermodynamics in matter created from heavy-ion collisions. Within uncertainties, the net-proton (taken as proxy for net-baryon) cumulant ratios, in general, were found to be consistent with the ordering expected from QCD thermodynamics over the energy range 7.7 to 200 GeV. In regards to the QCD critical point search, a non-monotonic energy dependence of fourth-to-second order net-proton cumulant ratio (C_4/C_2) predicted by model calculations with a critical point was subjected to experimental verification. The measured net-proton C_4/C_2 was found to exhibit a non-monotonic variation as a function of collision energy for 0-5% centrality. The significance of this non-monotonic dependence was evaluated to be 3.1σ . Such a trend was not seen in peripheral 70-80% data and model calculations that do not include any criticality. The search for crossover was carried out using the sixth-to-second order net-proton (proxy for net-baryon) cumulant ratio (C_6/C_2). Within uncertainties, the C_6/C_2 measurements for 0-40% centrality showed progressively negative values with decreasing collision energy down to 7.7 GeV. The deviation of measurements from zero was found to be within 1.7σ . The observed negative sign and trend are consistent with lattice QCD calculations ($\mu_B \leq 110$ MeV) that include a crossover quark-hadron transition. In contrast, the peripheral 70-80% data and calculations from models that do not incorporate any phase transition effects were either positive or consistent with zero within uncertainties at all energies. Higher-order factorial cumulants (κ_n) of proton multiplicity distributions were presented as sensitive observables to probe a possible first-order phase transition. For energies above 7.7 GeV, the small values of κ_n and absence of sign-change with increasing order within uncertainties do not support the

two-component shape of proton multiplicity distributions that would be expected from a first-order phase transition.

Contents

List of Figures	xxvii
List of Tables	xli
1 Introduction	1
1.1 Phase transition	2
1.2 Quantum Chromodynamics (QCD) and its phase diagram	4
1.3 QCD phase structure	7
1.3.1 Quark Gluon Plasma (QGP)	7
1.3.2 Hadronic phase	13
1.3.3 Crossover	16
1.3.4 First-order phase transition	17
1.3.5 Critical Point	20
1.3.6 Transition temperature	22
1.4 Cumulants: probes of QCD phase structure	24
1.5 Relativistic heavy-ion collisions	28
1.5.1 Theoretical foundation and development	28
1.5.2 Kinematics of heavy-ion collisions	31
1.5.3 Natural unit	34
1.6 Motivation for the thesis	35
2 Statistics needed for cumulant estimation: a simulation study	47
2.1 Poissonian model	48
2.2 Binomial model	51
2.3 Limits on event statistics	54

2.4	Effect of detection efficiency	56
2.5	Summary	57
3	STAR experiment at RHIC	61
3.1	Introduction	61
3.2	The Relativistic Heavy-Ion Collider (RHIC) facility	62
3.3	The STAR detector	64
3.3.1	The Time Projection Chamber: TPC	66
3.3.2	The Time Of Flight Detector System	69
3.3.3	Particle identification (PID) using TPC and TOF	71
4	Experimental analysis details and techniques	77
4.1	Analysis details	77
4.1.1	Datasets	78
4.1.2	Event selection	79
4.1.3	Track Selection	84
4.1.4	Centrality determination	86
4.1.5	Proton acceptance and identification	90
4.2	Analysis techniques	94
4.2.1	Efficiency Correction	94
4.2.2	Centrality Bin Width Correction	98
4.3	Summary	100
5	Estimating uncertainties on cumulant measurements	105
5.1	Statistical uncertainty	105
5.1.1	Methods	106
	a) Delta theorem method	106
	b) Bootstrap method	109
	c) Subgroup method	111
5.1.2	Method comparisons and application in experiments	112
5.2	Systematic uncertainty	115
5.2.1	Sources	116
5.2.2	Barlow check	117
5.3	Summary	121

6	Experimental results on net-proton cumulants	125
6.1	Net-proton cumulant measurements	125
6.1.1	Event-by-event net-proton number distribution	126
6.1.2	Centrality dependence	128
6.1.3	Energy dependence	130
6.1.4	Hyper-order fluctuations	130
6.2	Baselines with no QCD criticality and phase transition	133
6.2.1	Models	134
	a) Statistical Baseline: Skellam	134
	b) Thermal model: HRG	135
	c) Transport model: UrQMD	136
6.2.2	Cumulant ratios and comparison with models	137
6.3	Test of QCD thermodynamics	139
6.3.1	Proposed theoretical prediction	139
6.3.2	Experimental results and model comparison	140
6.4	Probing the QCD critical point	141
6.4.1	Proposed theoretical prediction	141
6.4.2	Experimental results and model comparison	143
6.5	Probing the crossover	149
6.5.1	Proposed theoretical prediction	149
6.5.2	Experimental results and model comparison	151
6.6	Probing the first-order phase transition	154
6.6.1	Proposed theoretical prediction	154
6.6.2	Experimental results and model comparison	155
6.7	Summary	157
6.8	Appendices	161
6.8.1	Appendix A: Study on decay induced self-correlation	161
6.8.2	Appendix B: Acceptance dependence of cumulant ratios	163
6.8.3	Appendix C: Significance of energy dependence of C_2/C_1 and C_3/C_2	164
6.8.4	Appendix D: Cumulants and K-statistics	165
6.8.5	Appendix E: Statistics dependence of C_6/C_2	167
6.8.6	Appendix F: Two-component Model calculation	169

7 Conclusion	175
8 Future direction: Phase II of Beam Energy Scan	181
8.1 Prospects	181
8.2 Challenges	189

List of Figures

1.1	A simplified representation of different phases of water due to variation of pressure and temperature. The triple point, critical point corresponding to the liquid-gas phase transition, and melting and boiling point at 1 atm pressure are shown as filled circles. The blue lines represent lines of co-existence between different phases. The figure is taken from Ref. [2].	3
1.2	Momentum transfer dependence of α_s from QCD (shown as curves) along with various experimental measurements [7].	5
1.3	A conjectured phase diagram of QCD [9]. Crossover at the small μ_B region is indicated by a dashed line. This happens at a transition temperature T_c . A conjectured first-order phase transition line is shown as a black line terminating at the QCD critical point (shown as a filled square marker). The red-yellow dotted line corresponds to the chemical freeze-out (where the relative abundance of hadrons gets fixed) obtained from the fitting of particle yields. The ground state of nuclear matter ($T \approx 0$ and $\mu_B \approx 925$ MeV) [10] is also shown. The regions of the phase diagram accessed by ongoing (LHC, RHIC, SPS, and RHIC-FXT), past (AGS and SPS), and future (CBM-FAIR, NICA, CSR, and J-PARC) experimental facilities are presented on the top of the figure.	7
1.4	Normalized energy, pressure, and entropy density as a function of temperature obtained from LQCD calculations at vanishing baryonic chemical potential. The yellow band represents the transition temperature T_c [16].	8
1.5	Elliptic flow v_2 of identified hadrons π , K , p , Λ as a function of p_T in Au+Au collisions at $\sqrt{s_{NN}} = 200$ GeV from the STAR and PHENIX experiment. Expectations from ideal hydrodynamic calculations are shown as dashed and solid lines. Figure adapted from Ref. [24].	10

- 1.6 v_2/n_q of identified hadrons as a function of p_T/n_q in Au+Au collisions at $\sqrt{s_{NN}} = 200$ GeV from the STAR and PHENIX experiment. The figure is taken from Ref. [30]. 11
- 1.7 Ratio of yields of hadrons of various species from Au+Au collisions at $\sqrt{s_{NN}} = 200$ GeV [17]. The horizontal lines represent the fits to experimental data by a statistical thermal model with temperature $T = 163 \pm 4$ MeV, $\mu_B = 24 \pm 4$ MeV and strangeness suppression factor $\gamma_s = 0.99 \pm 0.07$ 12
- 1.8 Transverse momentum dependence of v_2 . The filled circles are measurements from the STAR experiment. The dashed lines represent viscous hydrodynamical calculations with different values of η/s . The figure is taken from Ref. [34]. 13
- 1.9 Ratio of yields, K^{*0}/K^- and ϕ/K^- measured from Pb+Pb collisions at $\sqrt{s_{NN}} = 2.76$ and 5.02 TeV, p+Pb collisions at $\sqrt{s_{NN}} = 5.02$ TeV and p+p collisions at $\sqrt{s} = 5.02$ TeV as a function of system size (collision centrality) using ALICE at the LHC [39]. 15
- 1.10 chiral susceptibility of light quarks for two values of temporal lattice spacing N_τ as a function of $6/g^2$, where g is the gauge coupling in QCD Lagrangian. The temperature T increases with $6/g^2$. Various markers represent different lattice volumes; the largest volume is eight times that of the smallest volume. Figure adapted from Ref. [41]. 16
- 1.11 Derivative of $\ln Z_c(T, N)$ vs. quark number density for various cases of T/T_c conditions. The figure is taken from Ref. [45]. 18
- 1.12 The slope of net-proton directed flow at midrapidity for mid-central Au+Au collisions at RHIC. Results are presented as a function of collision energy. The red dashed line is just to guide the eye. The figure is adapted from Ref. [46]. . . 19

- 1.13 Theory predictions on the location of QCD critical point. The labels are abbreviated for various theoretical models and publications (LQ: Lattice-QCD, SB: Statistical Bootstrap Model, DSE: Dyson-Schwinger equations, FRG: Functional Renormalization Group, LSM: Linear Sigma Model, RM: Random Matrix Model, CO: Composite Operator formalism, QCD-BHE: QCD from Black Hole Engineering, and CJT: Cornwall-Jackiw-Tomboulis effective potential). Predictions are taken from Ref. [48–63]. The orange-colored band represents crossover from lattice-QCD calculations. The open triangle markers are locations of chemical freeze-out obtained from fitting of yields measured in various experiments (SPS, AGS, STAR, and ALICE) using a statistical thermal model. The μ_B range covered by various experimental facilities and programs is also shown on the top. 20
- 1.14 Chiral susceptibility from lattice as a function of temperature for vanishing $\mu_{B,Q,S}$. Calculations with different numbers of temporal extension N_τ are presented. The figure is adapted from Ref. [66]. 22
- 1.15 (A) Net-proton (proxy for net-baryon) cumulant ratio C_4/C_3 (red filled markers) along with lattice QCD calculation (open markers) with different T_c shown as a function of collision energy. (B) Chi-square values from the comparison of experimental data and lattice calculation with different values of T_c . The figure is adapted from Ref. [67]. 23
- 1.16 A pictorial view of distributions with zero, positive and negative values for skewness (panel a) and kurtosis (panel b) is shown. Figures are taken from Ref. [73, 74]. 25
- 1.17 Chemical freeze-out parameters T and μ_B obtained by thermal model fits to experimental data on particle yields as a function of collision energies [81, 82]. Red lines represent parametrisations of T and μ_B on $\sqrt{s_{NN}}$ taken from Ref. [83]. 29

- 2.1 Cumulants of net-proton distribution up to sixth order presented as a function of event statistics [10]. The net-proton distribution is simulated as the difference of protons and antiprotons, which follow independent Poisson distributions. The experimental value of mean of proton ($\mu_1 = 5.66$) and antiproton ($\mu_2 = 4.11$) distributions in top 5% Au+Au collision at $\sqrt{s_{NN}} = 200$ GeV are taken as input parameters for the simulation. The orange band denotes the $\pm 1\sigma$ statistical uncertainties on cumulants. The solid red line is the true value of cumulants obtained analytically using the input parameters. The filled circle markers are the deviation of cumulants from their true value scaled by their statistical uncertainties. 49
- 2.2 Cumulants of net-proton distribution up to sixth order presented as a function of event statistics [10]. The net-proton distribution is simulated as the difference of protons and antiprotons, which follow independent Poisson distributions. The experimental value of mean of proton ($\mu_1 = 7.25$) and antiproton ($\mu_2 = 3.13$) distributions in top 5% Au+Au collision at $\sqrt{s_{NN}} = 62.4$ GeV are taken as input parameters for the simulation. The orange band denotes the $\pm 1\sigma$ statistical uncertainties on cumulants. The solid red line is the true value of cumulants obtained analytically using input parameters. The filled circle markers are the deviation of cumulants from their true value scaled by their statistical uncertainties. 50
- 2.3 Cumulants of net-proton distribution up to sixth order presented as a function of event statistics [10]. The net-proton distribution is simulated as the difference of protons and antiprotons, which follow independent Binomial distributions. The experimental value of mean and variance of proton ($\mu_1 = 5.66$ and $\sigma_{proton}^2 = 5.58$) and antiproton ($\mu_2 = 4.11$ and $\sigma_{anti-proton}^2 = 4.06$) distributions in top 5% Au+Au collision at $\sqrt{s_{NN}} = 200$ GeV are taken as input parameters for the simulation. The orange band denotes the $\pm 1\sigma$ statistical uncertainties on cumulants. The solid red line is the true value of cumulants obtained analytically using input parameters. The filled circle markers are the deviation of cumulants from their true value scaled by their statistical uncertainties. . . . 52

2.4	Cumulants of net-proton distribution up to sixth order presented as a function of event statistics [10]. The net-proton distribution is simulated as the difference of protons and antiprotons which follow independent Binomial distributions. The experimental value of mean and variance of proton ($\mu_{proton} = 7.26$ and $\sigma^2_{proton} = 7.06$) and antiproton ($\mu_{anti-proton} = 3.13$ and $\sigma^2_{anti-proton} = 3.07$) distributions in top 5% Au+Au collision at $\sqrt{s_{NN}} = 62.4$ GeV are taken as input parameters for the simulation. The orange band denotes the $\pm 1\sigma$ statistical uncertainties on cumulants. The solid red line is the true value of cumulants obtained analytically using input parameters. The filled circle markers are the deviation of cumulants from their true value scaled by their statistical uncertainties.	54
2.5	Minimum event statistics needed for estimation of net-proton cumulants from Poissonian model and Binomial model [10]. Net-proton distribution is simulated assuming both proton and antiprotons follow independent; (A): Poisson distributions and (B): Binomial distributions. There are two choices of input parameters considered for each of these models that are determined from experimental mean and/or variance of proton and antiproton distributions in top 5% Au+Au collisions at $\sqrt{s_{NN}} = 62.4$ GeV (open squares) and 200 GeV (filled circles).	55
2.6	Ratio of cumulants of net-proton distribution at the generated level to those obtained after binomial efficiency correction is applied to the cumulants at the measured level (we call this corrected level) [10]. The study is performed with the Poissonian model for protons and antiprotons with mean $\mu_1 = 7.25$ and $\mu_2 = 3.13$, respectively.	56
3.1	Aerial view of RHIC facility at Brookhaven National Laboratory. The figure is taken from Ref. [8].	62
3.2	A schematic diagram of injection of ions to RHIC. The figure is taken from Ref. [8].	63
3.3	Perspective view of the STAR detector system. Figure adapted from Ref. [13].	65
3.4	A schematic figure of the STAR TPC detector. Figure adapted from Ref. [14].	67
3.5	The layout of a TPC anode sector. The figure is taken from Ref. [14].	68
3.6	The internal layout of a TOF MRPC. Figure adapted from Ref. [18].	70

3.7	[Left panel (a)] $\langle(dE/dx)\rangle$ measured by TPC as a function of p/q in Au+Au collision at $\sqrt{s_{NN}} = 39$ GeV. The black lines are the Bichsel expectation for various charged particles. The figure is taken from Ref. [21]. [Right panel (b)] m^2 measured by TOF as a function of $p \times q$ for Au+Au collision at $\sqrt{s_{NN}} = 54.4$ GeV.	72
4.1	Analysis flow for net-proton fluctuation measurement.	78
4.2	Bad run removal using 3σ outliers method on various QA observables for Au+Au collisions at $\sqrt{s_{NN}} = 54.4$ GeV. To avoid lengthy nomenclature of runs in the figure, each run shown in the x-axis is assigned an index (Run Index).	80
4.3	Signed $\langle DCA_{xy} \rangle$ as a function of run time (shown in x-axis as event id) for a run with unstable signed $\langle DCA_{xy} \rangle$ in its early phase. The green and blue lines represent the global mean and 5σ standard deviation, respectively.	81
4.4	V_z distribution from Au+Au collisions at $\sqrt{s_{NN}} = 54.4$ GeV. Events enclosed by the red lines ($ V_z < 30$ cm) are selected for analysis and the rest rejected.	83
4.5	V_x vs. V_y from Au+Au collisions at $\sqrt{s_{NN}} = 54.4$ GeV. Events within the radius $\sqrt{V_x^2 + V_y^2} < 2$ cm shown by black circular line are selected for analysis.	83
4.6	$V_z - V_z(VPD)$ distribution from Au+Au collisions at $\sqrt{s_{NN}} = 54.4$ GeV. Events enclosed by the red lines ($ V_z - V_z(VPD) < 3$ cm) are selected for analysis.	83
4.7	Number of TPC tracks vs. the number of TPC tracks matched to TOF in Au+Au collisions at $\sqrt{s_{NN}} = 54.4$ GeV. Events below the red line are identified as pile-up events and discarded from the analysis.	84
4.8	A sketch of the geometry of relativistic heavy-ion collision.	87
4.9	Normalized Refmult3 distributions from Au+Au collisions at $\sqrt{s_{NN}} = 7.7 - 200$ GeV.	88
4.10	pp scattering cross section as a function of collision energy in the lab frame, E_{Lab} [9]. Red lines represent fit to data.	89
4.11	Refmult3 (black line) from Au+Au collisions at $\sqrt{s_{NN}} = 54.4$ GeV fitted with Glauber MC model (red line). Distributions are normalized. The blue dashed line represents the centrality cut for 0-5% collisions.	90
4.12	Proton phase-space acceptance shown in terms of transverse momentum (p_T) vs. rapidity (y) from Au+Au collisions at $\sqrt{s_{NN}} = 54.4$ GeV. The blue box is the region where protons and antiprotons are selected.	91

4.13 Ionization energy loss ($\langle dE/dx \rangle$) deposited by various charged particles in TPC for Au+Au collisions at $\sqrt{s_{NN}} = 54.4$ GeV vs. momentum.	92
4.14 Mass-squared ($mass^2$) of various charged particles measured by TOF for Au+Au collisions at $\sqrt{s_{NN}} = 54.4$ GeV as a function of momentum.	92
4.15 $n\sigma$ distribution for protons from TPC in the momentum range $0.4 < p_T < 0.8$ GeV/c (panel a) and $mass^2$ distribution for protons from TOF in the momentum range $0.8 < p_T < 2$ GeV/c (panel b) for Au+Au collisions at $\sqrt{s_{NN}} = 54.4$ GeV. The red dashed lines represent the cuts used for proton identification: $ n\sigma_{proton} < 2$ and $0.6 < mass^2 < 1.2 \text{ GeV}^2/c^4$. Other peaks in the distribution correspond to different particles.	93
4.16 TPC efficiency of protons and antiprotons in Au+Au collisions at $\sqrt{s_{NN}} = 7.7, 39$ and 200 GeV for 0-5%, 20-30% and 70-80% centrality. Errors are only statistical.	97
4.17 TOF matching efficiency of protons and antiprotons in Au+Au collisions at $\sqrt{s_{NN}} = 7.7, 39$ and 200 GeV for 0-5%, 20-30% and 70-80% centrality. Errors are only statistical.	98
4.18 Refmult3 dependence of efficiency corrected net-proton C_1 (mean) for Au+Au collisions at $\sqrt{s_{NN}} = 39$ GeV. The area enclosed by the red region corresponds to 0-5% central events.	99
5.1 An illustrative diagram of Bootstrap sample generation by random draw of elements from the parent sample ("Original data" in the diagram), with replacement allowed. The size of Bootstrap samples is same as the parent sample. The sketch is adapted from Ref. [8].	110

5.2	Verification of Gaussian nature of statistical uncertainties obtained with different methods for a Skellam sample of size 10^8 . The Skellam sample is characterized by its parameters $\mu_1 = 5.66$, $\mu_2 = 4.11$ (efficiency corrected mean of proton and antiproton measured at mid-rapidity for top 5% Au+Au collision at $\sqrt{s_{NN}} = 200$ GeV at STAR [9]). The distributions presented in each panel are values of fourth (C_4), sixth (C_6), and eighth-order (C_8) cumulants from 10000 samples generated from the parent Skellam sample using Bootstrap sampling. σ_G is the width of distributions obtained by fitting with a Gaussian function. The top, middle, and bottom rows correspond to Subgroup (σ_S), Delta theorem (σ_D), and Bootstrap method (σ_B), respectively. The number of random samples out of 10000 that have values of cumulants within $\pm 1\sigma$ statistical uncertainties estimated with various methods are also shown [4]. . .	113
5.3	Comparison of statistical uncertainty on net-proton cumulants up to fourth-order in Au+Au collisions at $\sqrt{s_{NN}} = 19.6$ GeV, estimated using Bootstrap and Delta theorem method [10]. The uncertainties are presented as a function of average number of participant nucleons ($\langle N_{part} \rangle$). The red and dashed blue lines represent uncertainties from the Delta theorem and Bootstrap methods, respectively.	114
5.4	$\Delta Y / \sigma_B$ obtained from DCA variations for net-proton cumulant ratio C_4 / C_2 in 0-5% central Au+Au collisions at $\sqrt{s_{NN}} = 54.4$ GeV.	119
5.5	Contribution from each source relative to total systematic uncertainties (in percentage) for net-proton cumulant ratio C_4 / C_2 in 0-5% central Au+Au collisions at $\sqrt{s_{NN}} = 54.4$ GeV.	119
5.6	Systematic uncertainties on net-proton cumulants up to fourth-order as a function of collision centrality (average number of participant nucleons, $\langle N_{part} \rangle$) in Au+Au collisions at $\sqrt{s_{NN}} = 54.4$ GeV. The systematic uncertainties are shown as $\pm \sigma_{sys}$ on the horizontal line at $y = 0$	120
6.1	Event-by-event net-proton number distributions in central (0-5%) Au+Au collisions from $\sqrt{s_{NN}} = 7.7$ to 200 GeV [3–5]. The distributions are not corrected for detector efficiency and finite centrality width. The dashed lines represent fit with the Skellam function. The lower panel shows the ratio of data to Skellam expectations at $\sqrt{s_{NN}} = 7.7$ and 200 GeV.	127

- 6.2 Event-by-event net-proton number distributions in peripheral (70-80%) peripheral Au+Au collisions from $\sqrt{s_{NN}} = 7.7$ to 200 GeV [3–5]. The distributions are not corrected for detector efficiency and finite centrality width. The dashed lines represent fit with the Skellam function. The lower panel shows the ratio of data to Skellam expectations for $\sqrt{s_{NN}} = 7.7$ and 200 GeV. 128
- 6.3 Cumulants of net-proton number distribution up to fourth-order in Au+Au collisions from $\sqrt{s_{NN}} = 7.7$ to 200 GeV presented as a function of centrality [3, 4]. Measurements are done with rapidity coverage of $|y| < 0.5$ and momentum coverage of $p_T = 0.4 - 2.0$ GeV/c. The bars and the shaded bands on the data points represent statistical and systematic uncertainties, respectively. 129
- 6.4 Cumulants of net-proton number distribution up to fourth-order for 0-5% (filled circles), 30-40% (filled squares) and 70-80% (open diamond) collision centrality in Au+Au collisions from $\sqrt{s_{NN}} = 7.7$ to 200 GeV [3, 4]. Measurements are done with rapidity coverage of $|y| < 0.5$ and momentum coverage of $p_T = 0.4 - 2.0$ GeV/c. The bars and the shaded bands on the data points represent statistical and systematic uncertainties, respectively. 131
- 6.5 Ratio of sixth-to-second order cumulant (C_6/C_2) of net-proton distributions as a function of centrality from Au+Au collisions at $\sqrt{s_{NN}} = 27$ (green crosses), 54.4 (blue squares) and 200 GeV (red circles) [6]. Results from eight centralities: (0-10%, 10-20%, 20-30%, 30-40%, 40-50%, 50-60%, 60-70%, and 70-80%) are presented. Measurements are done with rapidity coverage of $|y| < 0.5$ and momentum coverage of $p_T = 0.4 - 2.0$ GeV/c. The bars and the shaded bands on the data points represent statistical and systematic uncertainties, respectively. 132
- 6.6 Ratio of fifth-to-first order cumulant (C_5/C_1 , panel (a)) and sixth-to-second order cumulant (C_6/C_2 , panel (b)) of net-proton distributions in Au+Au collisions as a function of collision energy from $\sqrt{s_{NN}} = 7.7 - 200$ GeV [7]. Results are presented for 0-40% and 70-80% centrality. Measurements are done with rapidity coverage of $|y| < 0.5$ and momentum coverage of $p_T = 0.4 - 2.0$ GeV/c. The bars and the shaded bands on the data points represent statistical and systematic uncertainties, respectively. 133

- 6.7 Ratio of cumulants up to sixth-order of net-proton distributions in Au+Au collisions as a function of collision energy from $\sqrt{s_{NN}} = 7.7 - 200$ GeV. Results are presented for 0-5% (for cumulant ratio up to fourth-order), 0-40% (for hyper-order cumulant ratios), and 70-80% centrality. For hyper-order cumulant ratios, a wider 0-40% centrality range is considered to improve the statistical precision of measurement. The bars and the shaded bands on the data points represent statistical and systematic uncertainties, respectively. The expectation from the UrQMD model, ideal HRG (GCE) model, and Skellam baseline are also presented [3, 4, 6, 7]. 138
- 6.8 Cumulant ratios of net-proton distributions: C_3/C_1 (filled square), C_4/C_2 (open cross), C_5/C_1 (open diamond) and C_6/C_2 (filled circle), in 0-40% Au+Au collisions from 7.7 GeV to 200 GeV [7]. The bars and the shaded bands on the data points represent statistical and systematic uncertainties, respectively. The red, blue, and brown bands represent LQCD (39 – 200 GeV) [17], FRG (7.7–200 GeV) [18] and UrQMD calculations (0-40% centrality), respectively. The C_6/C_2 data at 7.7 and 11.5 GeV are scaled down by a factor of 10 for clarity of presentation. 140
- 6.9 Quartic cumulant κ_4 of the Ising model magnetization near the critical point (shown as red point) [20]. The y axis is the reduced temperature, and the x axis reflects the external ordering field. 142
- 6.10 A sketch depicting the behavior of net-proton kurtosis as a function of collision energy $\sqrt{s_{NN}}$ in the presence of QCD critical point from linear sigma model calculations [20]. 142
- 6.11 The ratio of fourth to second-order cumulant, C_4/C_2 (same as $\kappa\sigma^2$) of net-proton distributions in Au+Au collisions as a function of collision energies over the range $\sqrt{s_{NN}} = 7.7 - 200$ GeV [3–5]. The results are shown for 0-5% and 0-80% collision centrality. The bars and brackets on the data points represent the statistical and systematic uncertainties, respectively. Also presented are expectations from various variants of the HRG model and the UrQMD model [5]. The Skellam baseline for C_4/C_2 is at unity. 143

- 6.12 Difference of measured $\kappa\sigma^2$ of net-proton distribution in 0-5% Au+Au collisions from calculations from UrQMD, various variants of HRG, Skellam baseline, and measured 70-80% peripheral data [3–5]. The obtained differences are scaled with total uncertainties and presented as a function of collision energy over the range $\sqrt{s_{NN}} = 7.7 - 200$ GeV. The total uncertainties are evaluated by adding the statistical uncertainties and systematic uncertainties in quadrature (uncertainties in model calculations, if any, are also included in the evaluation of total uncertainties by adding in quadrature). 145
- 6.13 The ratio of measured net-proton $\kappa\sigma^2$ from 0-5% central Au+Au collisions with expectations from Skellam baseline, HRG model with canonical ensemble (HRG CE), and UrQMD over the collision energy range $\sqrt{s_{NN}} = 7.7 - 62.4$ GeV [3–5]. The bars on the ratios represent total uncertainties obtained by adding statistical and systematic uncertainties in quadrature (uncertainties in model calculations, if any, are also included in the evaluation of total uncertainties by adding in quadrature). The polynomial fits to the obtained ratios with respect to Skellam, HRG CE, and UrQMD calculations are shown as red, magenta, and blue lines, respectively. The chi-square values per degree of freedom from these fits are also mentioned. Derivatives of the polynomial fit functions from the three cases are shown in the lower panel for each energy. The bars on derivatives are the total uncertainties obtained by the quadrature sum of statistical and systematic uncertainties. 147
- 6.14 Panel (a): Ratio of fifth-to-first (R_{51}^B) and sixth-to-second (R_{62}^B) order net-baryon number susceptibility (equivalently cumulant ratios C_5/C_1 and C_6/C_2) as a function of collision energy from LQCD [17]. Panel (b): R_{62}^B from FRG model as a function of collision energy [18]. 150
- 6.15 Cumulant ratio C_5/C_1 of net-proton distribution in Au+Au collision as a function of collision energy from $\sqrt{s_{NN}} = 7.7$ to 200 GeV [7]. Measurements are presented for 0-40% (filled circles) and 70-80% centralities (open diamonds). The bars and the shaded bands on the data points represent statistical and systematic uncertainties, respectively. Calculations from LQCD [17] (red band), FRG [18] (grey band), HRG CE [15] (dashed brown line), Poisson baseline (dotted black line), and UrQMD (green band) models are also presented. . . . 151

- 6.16 Cumulant ratio C_6/C_2 of net-proton distribution in Au+Au collision as a function of collision energy from $\sqrt{s_{NN}} = 7.7$ to 200 GeV [7]. Measurements are presented for 0-40% (filled circles) and 70-80% centralities (open diamonds). The bars and the shaded bands on the data points represent statistical and systematic uncertainties, respectively. Calculations from LQCD [17] (red band), FRG [18] (grey band), HRG CE [15] (dashed brown line), Poisson baseline (dotted black line at unity), and UrQMD (green band) model are also presented. 153
- 6.17 A pictorial representation of a two-component/bimodal distribution with Poissonian and Binomial distribution as its constituents. Figure adapted from Ref. [26]. 155
- 6.18 Factorial cumulants κ_4 (a), κ_5 (b), κ_6 (c) of proton multiplicity distribution from Au+Au collisions at collision energies from $\sqrt{s_{NN}} = 7.7$ to 200 GeV. The measurements are presented for 0-40% (square markers) and 50-60% (diamond markers) centralities. The bars and the shaded bands on the data points represent statistical and systematic uncertainties, respectively. Also shown are the calculations from Two-Component Model (for 0-40%) and the UrQMD model (for 0-40% and 50-60%) as red, brown bands, and blue dashed lines, respectively. The Two-Component Model (with Binomial and Poisson distributions as constituent components) considers factorial cumulants up to the fourth order as inputs in its construction to predict κ_5 and κ_6 . Uncertainties on the model calculations are purely statistical. The Poisson baseline for κ_n presented is at zero. For clarity of presentation, the κ_5 and κ_6 measurements at 7.7 GeV for 0-40% centrality are scaled down by a factor of 4 [7]. 156
- 6.19 Collision centrality dependence of net-proton cumulant ratio C_4/C_2 in Au+Au collision at center-of-mass energy $\sqrt{s_{NN}} = 7.7$ (panel 1) and 200 GeV (panel 2) from HIJING model [5]. Results are obtained from different choices of centrality definitions labeled as (a) Centrality - default: the centrality definition as used in the experimental data, (b) Centrality - A: same as (a) except pions and kaons from weak decays are removed provided the daughter protons for such decay are considered in net-proton fluctuation measurement, (c) Centrality - B: same as (b) except we removed pions from Δ decays instead of weak decay, (d) Centrality - C: its a combination of (b) and (c), i.e., pions and kaons from weak decays as well as Δ decays are removed. 162

- 6.20 Net-proton C_4/C_2 from 0-5% central collisions as a function of rapidity coverage (a) and momentum coverage (b) in Au+Au collisions at $\sqrt{s_{NN}} = 54.4$ GeV [3, 4]. The bars and the shaded bands on the data points represent the statistical and systematic uncertainties, respectively. 163
- 6.21 Energy dependence of net-proton cumulant ratios C_2/C_1 (same as σ^2/M) (a), C_3/C_2 (same as $S\sigma$) (b) and C_4/C_2 (same as $\kappa\sigma^2$) (c) from 0-5% central Au+Au collisions over the range $\sqrt{s_{NN}} = 7.7 - 62.4$ GeV [3, 4]. The bars on the data points represent total uncertainties obtained by adding statistical and systematic uncertainties in quadrature. Polynomial fits to data points along with χ^2/ndf value are shown. The lower panels show the derivative of the fitted polynomials as a function of energy. 164
- 6.22 The cumulant ratio C_5/C_1 and C_6/C_2 of net-proton distribution in Au+Au collisions at $\sqrt{s_{NN}} = 7.7$ GeV and their corresponding K -statistics ratios. Results are presented for 0-40% (a) and 50-60% (b) collision centrality class. Only statistical uncertainties on data points are presented [7]. 167
- 6.23 Sample size dependence of C_6/C_2 (filled circles) and the corresponding K -statistics ratio (open circles). Samples of varying sizes are constructed by random draw of events from the recorded events in 0-40% central Au+Au collision by STAR at $\sqrt{s_{NN}} = 7.7$ GeV. Measurements are corrected for finite detection efficiency and finite centrality width (by applying CBWC). The observed STAR C_6/C_2 data for 0-40% centrality (filled square in magenta color) is also shown. Only statistical uncertainties are presented [7]. 168
- 8.1 A photo of testing of FEE cards (green colored circuit boards with a golden structure attached to it). The FEE cards are assembled with sink (the golden structure) and mounted on a single sector of TPC. The output from all FEE cards are fed to a RDO board (red colored circuit board). 185

8.2	Net-proton/proton C_4/C_2 in 0-5% Au+Au collisions from $\sqrt{s_{NN}} = 3.0$ to 200 GeV [5–8]. The 3 GeV results were measured with half rapidity coverage ($-0.5 < y < 0$). Also shown are results from HADES for 0-10% centrality [9]. The bars and shaded bands on the data points represent the statistical and systematic uncertainties, respectively. The brown marker(only at 3 GeV) and the band are UrQMD model calculations. The current projection of statistical uncertainty from BES-II at collider energies is shown as a green band. The double-headed arrow demarcates the energy range covered by the FXT program [1].	187
8.3	Net-proton/proton C_6/C_2 in 0-40% and 50-60% Au+Au collisions from $\sqrt{s_{NN}} = 3.0$ to 200 GeV [12]. The 3 GeV results were measured with half rapidity coverage ($-0.5 < y < 0$). The bars and the shaded bands on the data points represent statistical and systematic uncertainties, respectively. Calculations from LQCD (red band), FRG (blue band), HRG CE (green line), and UrQMD (brown band and dashed lines) models are also presented.	188
8.4	Proton phase space acceptance in terms of rapidity ($y-y_{cm}$ where y_{cm} is the rapidity in center-of-mass frame) vs. momentum (p_T) coverage from Au+Au collisions [8]. The top panel is for collision at $\sqrt{s_{NN}} = 3$ GeV collected in FXT mode, while the bottom panel is for collision at $\sqrt{s_{NN}} = 54.4$ GeV collected in collider mode.	189

- 8.5 A correlation plot of charged particle multiplicity from UrQMD model selected within same acceptance as used for centrality definition in $\sqrt{s_{NN}} = 3$ GeV at STAR vs. the number of participant nucleons (N_{part}) [15]. The red horizontal and vertical lines represent the centrality cuts obtained using charged particle multiplicity and N_{part} , respectively, for selecting 0-5% central Au+Au collision events. The figure taken from Ref. [15]. 191

List of Tables

- 1.1 Mass, length, and time in natural units. 34
- 4.1 Center-of-mass collision energy, year, production tag, trigger Id used and μ_B at chemical freezeout from Cleyman's parametrization [1]. 79
- 4.2 List of event cuts applied on primary vertex for each collision energy and the number of remaining good events. Note that at $\sqrt{s_{NN}} = 14.5$ GeV, $V_r < 1$ cm was applied since the beam pipe was narrower compared to other energies due to the installation of Heavy-Flavor tracker for that dataset [5]. 82
- 5.1 Percentage relative statistical uncertainties (σ_Y/Y , Y is an observable) for net-proton cumulant ratios C_4/C_2 (0-5% centrality) and C_6/C_2 (0-40% centrality) in Au+Au collisions at $\sqrt{s_{NN}} = 7.7, 39$, and 200 GeV. 0-40% centrality is chosen for C_6/C_2 to reduce the statistical uncertainties. 115
- 5.2 Table of selection cut variations from different sources considered for estimating systematic uncertainties on net-proton cumulants along with the default selection criteria. 116
- 5.3 Percentage relative systematic uncertainties (σ_Y/Y) for net-proton cumulant ratios C_4/C_2 (0-5% centrality) and C_6/C_2 (0-40% centrality) in Au+Au collisions at $\sqrt{s_{NN}} = 7.7, 39$, and 200 GeV. 120

6.1	The right tail p -value obtained from χ^2 test between experimentally measured net-proton C_4/C_2 in 0-5% centrality and expectations from UrQMD model and various variants of HRG models using Grand canonical ensemble: ideal HRG (HRG GCE), HRG with excluded volume (HRG GCE EV) and using canonical ensemble (HRG CE) calculated over the collision energy range of $\sqrt{s_{NN}} = 7.7 - 27$ GeV.	146
6.2	The parameters of the Two-Component Model calculations at all collision energies [7].	171
8.1	Event statistics collected for Au+Au collisions from BES-II at various center-of-mass energies from 7.7 GeV to 19.6 GeV in collider mode and their corresponding μ_B values [2].	182
8.2	Event statistics collected for Au+Au collisions from BES-II at various center-of-mass energies from 3 GeV to 7.7 GeV in fixed target mode and their corresponding μ_B values [2].	183

Chapter 1

Introduction

Phase transition is a ubiquitous phenomenon in nature. It is central to our understanding of matter around us and is one of the most widely studied subjects across various disciplines of science. A recent interesting study posits that the feeling of "love" in the human brain could also be a phase transition [1]. This thesis work is dedicated to the study of phase transition in strong interactions, one of the four fundamental interactions of nature. The strength of strong interaction is the highest among all and is responsible for holding nucleons together in nuclei and confining the fundamental constituents of visible matter; quarks and gluons inside hadrons.

This introductory chapter begins with a brief discussion of the phenomenon of phase transition. Then it explains in detail the phase structure of strongly interacting matter and its understanding at present. The remaining part of the chapter discusses how the phase structure can be experimentally studied by measurement of fluctuations of conserved quantities in heavy-ion collisions.

1.1 Phase transition

Phase transition of a thermodynamical system is the transformation of the system from one phase or physical state to another phase due to changes in external conditions. It is accompanied by a change in certain properties of a phase, often sharply. According to Ehrenfest's classification, phase transition can be categorized into three classes: first-order, second-order, and crossover. For a first-order phase transition, the first derivative of free energy is discontinuous with respect to some thermodynamic variable. Such transitions involve a latent heat and are accompanied by a mixed phase where both phases coexist. A second-order phase transition exhibits discontinuity at the second derivative of free energy while the lower derivative is continuous. A crossover has no discontinuity in free energy and its derivatives, and thus there is a smooth transition from one phase to another. A well-known example of phase transition that is encountered in everyday life is that of water. It is perhaps the most profoundly studied phase transition to date and has gathered a very detailed understanding. A phase diagram representing different phases of water is shown in Fig. 1.1. Vapourization of liquid water into gas, melting of ice, and formation of frost are common examples of phase transition of water. Different phases of water can exist together in equilibrium along the lines of co-existence in the phase diagram. The phase diagram consists of a triple point at $(0.01^\circ \text{C}, 0.006 \text{ atm})$ where all three phases coexist. Based on Ehrenfest's classification, the phase transition happening across the co-existence lines are of first-order in nature. They are characterized by the discontinuity in density, which is the inverse of the derivative of free energy with respect to pressure. An interesting feature of liquid-gas phase transition is the existence of a critical point at $(374^\circ \text{C}, 218 \text{ atm})$. The critical point marks the end of phase co-existence. At this point the liquid-gas transition is a second order phase transition. Beyond the critical point, the phase boundary vanishes

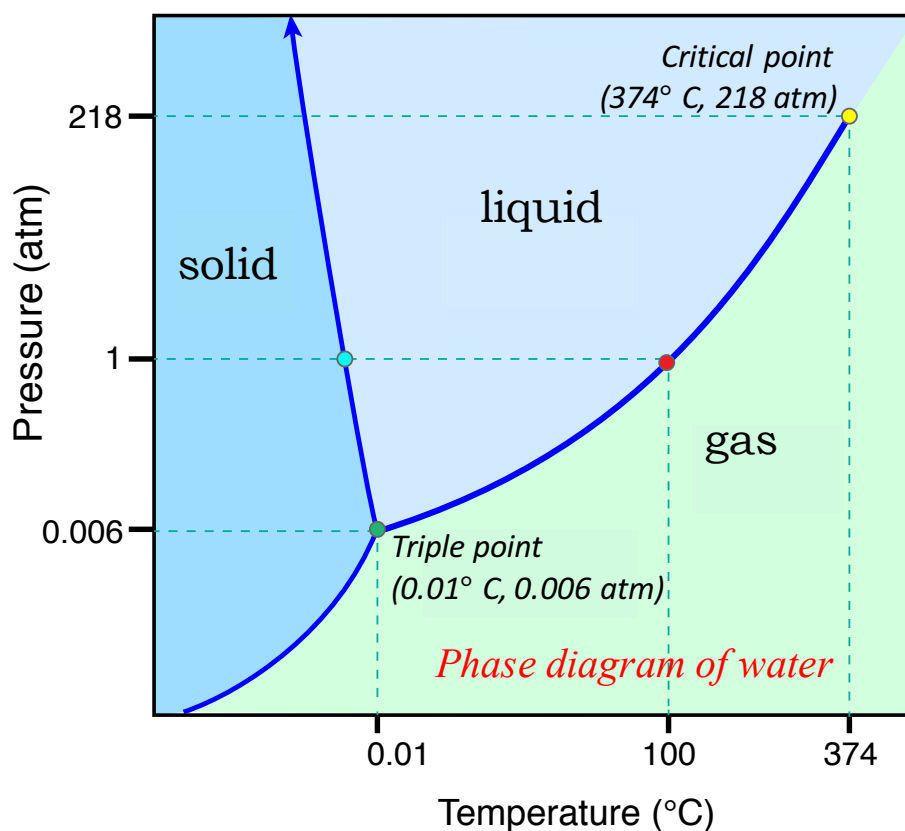


Figure 1.1: A simplified representation of different phases of water due to variation of pressure and temperature. The triple point, critical point corresponding to the liquid-gas phase transition, and melting and boiling point at 1 atm pressure are shown as filled circles. The blue lines represent lines of co-existence between different phases. The figure is taken from Ref. [2].

and there is no distinction between the two phases. The critical point is accompanied by divergence of correlation length. Large correlation length results in development of large and long-range density fluctuations and as a consequence divergence of susceptibility of the system. This has important implication such as the scaling behaviour (power law behaviour of correlations at criticality) and universality, i.e., the critical behaviour being independent of microscopic details of system and only relying on degrees of freedom and symmetries [3]. A well-known critical phenomenon is the critical opalescence in liquid-gas

transitions. Though both liquid and gas phases of compounds like CO_2 are transparent, upon approaching the critical point, they start appearing milky. This is because the divergence of correlation length leads to large density fluctuations. This results in fluctuation of the refractive index of the medium, which then behave like atomic scatterers. They scatter the incoming light making the medium appear milky white.

Other familiar examples of phase transitions include metal-insulator transition, ferromagnetic transition, superfluid transition, etc. In all these transitions, including that of water, the underlying interactions are electromagnetic in nature and governed by Quantum Electrodynamics – the theory of electromagnetic interactions. Analogously, the strongly interacting matter also undergoes phase transition. The theory governing strong interaction is called Quantum Chromodynamics (QCD). The work reported in this thesis is aimed at the study of the phase diagram of QCD.

1.2 Quantum Chromodynamics (QCD) and its phase diagram

Quantum Chromodynamics (QCD) is the theory of strongly interacting matter. It is an important part of the Standard Model of elementary particles. QCD is a gauge field theory that belongs to the non-Abelian group $SU(3)$. The theory came into existence after Gross, Wilczek, and Politzer discovered the concept of asymptotic freedom [4–6] in 1973. Like the theory of Quantum electrodynamics (QED) describes interactions of particles having electric charges, the QCD deals with color charges. In QCD, the quarks and gluons carry color charges. Analogous to photons coupling with electric charges with coupling constant α ($\alpha = 1/137$ for low energy) in QED, the gluons couple with color charges with coupling constant α_s in QCD. The running coupling constant α_s (the phrase "running" stands for the

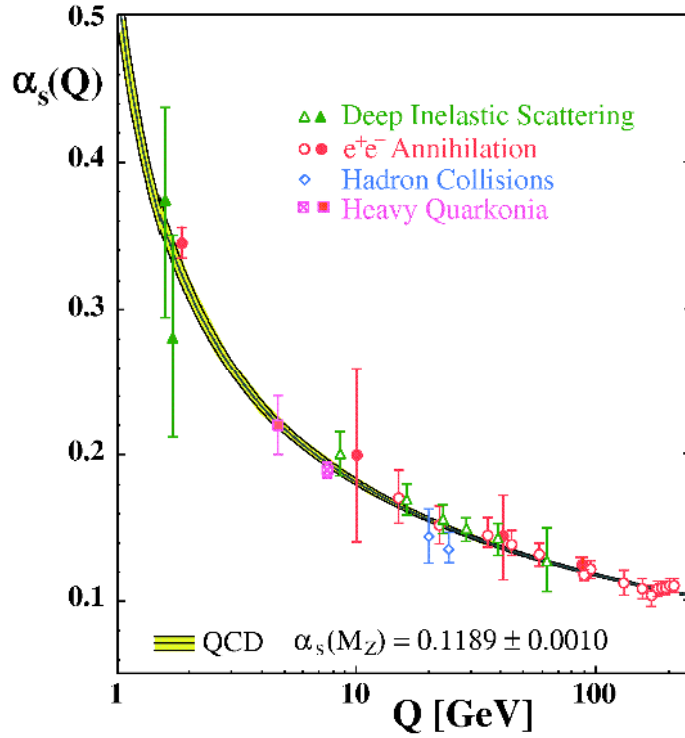


Figure 1.2: Momentum transfer dependence of α_s from QCD (shown as curves) along with various experimental measurements [7].

fact that the coupling constant depends on energy) is defined as follows,

$$\alpha_s(Q^2) \approx \frac{12\pi}{(11n_c - 2n_f) \ln(|Q^2|/\Lambda^2)}. \quad (1.1)$$

Here, Q^2 is the momentum transfer, n_c is the number of quark colors, n_f is the number of quark flavors, and Λ represents the scale factor. Figure 1.2 shows the dependence of α_s on momentum transfer. The energy (or Q^2) dependence of the α_s results in two significant consequences, *asymptotic freedom* and *confinement*. At large momentum transfer ($Q^2 \gg \Lambda$) or small distance, the α_s becomes very small, resulting in a free state of quarks and gluons. This property is called asymptotic freedom. At such a high energy scale, the degree of freedom is essentially quarks and gluons. Together, the quarks and gluons are called partons. At small Q^2 or large distance, we approach the strong coupling limit of

QCD as the α_s becomes large. Due to large α_s , the quarks and gluons are no longer free but bound together in the form of colorless hadrons. This property is known as confinement. The effective degree of freedom at such low energy scales is the hadrons. Hence, the basic QCD interactions give rise to the transition from confined degrees of freedom to deconfined degrees of freedom. The deconfined phase of quarks and gluon is called the Quark-Gluon-Plasma (QGP).

The earliest phase diagram depicting a confined state of quarks and a deconfined state of quarks was made by Cabibbo and Parisi in 1975 in their paper "Exponential Hadronic Spectrum and Quark Liberation" [8]. Over the years, with advancements in the theoretical and experimental study of the strong interaction, a much-improved understanding of the QCD phase diagram has been reached at present though many aspects still remain a conjecture. The QCD phase diagram is usually expressed as a function of temperature T vs. chemical potential (μ_q) associated with conserved quantities (q) in strong interactions like baryon number (B), electric charge (Q), and strangeness number (S). μ_q is essentially the energy needed to increase/decrease the conserved quantum number ($q = B, Q, S$) of a system. When exploring the QCD phase diagram by performing nuclear collisions in experiments, additional constraints apply to μ_q . The values of μ_Q and μ_S are specified as a consequence of: (a) colliding nuclei have a fixed ratio of electric charge to baryon number and (b) they are strangeness neutral, i.e., there is no net-strangeness. Hence, in its experimental realization, the QCD phase diagram essentially reduces to a plot of T vs. μ_B . A conjectured phase diagram of QCD from present times is shown as Fig. 1.3. Its rich phase structure comprises of: a QGP phase at high temperature, a hadronic phase at low temperature, a crossover in the small baryonic potential (μ_B), a first-order phase transition at large μ_B , a QCD critical point between the crossover and first-order phase transition line, and transition temperature. These are discussed in detail in the next section.

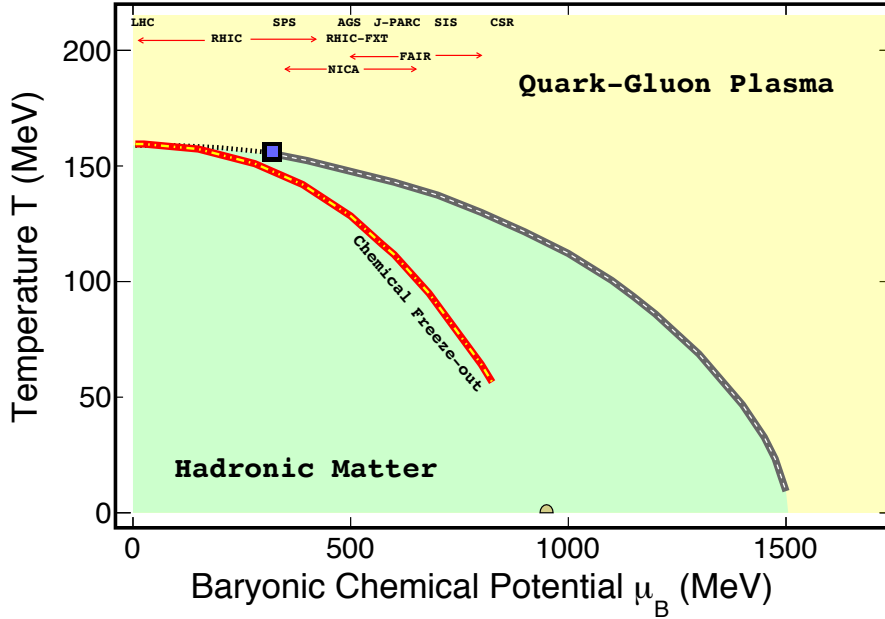


Figure 1.3: A conjectured phase diagram of QCD [9]. Crossover at the small μ_B region is indicated by a dashed line. This happens at a transition temperature T_c . A conjectured first-order phase transition line is shown as a black line terminating at the QCD critical point (shown as a filled square marker). The red-yellow dotted line corresponds to the chemical freeze-out (where the relative abundance of hadrons gets fixed) obtained from the fitting of particle yields. The ground state of nuclear matter ($T \approx 0$ and $\mu_B \approx 925$ MeV) [10] is also shown. The regions of the phase diagram accessed by ongoing (LHC, RHIC, SPS, and RHIC-FXT), past (AGS and SPS), and future (CBM-FAIR, NICA, CSR, and J-PARC) experimental facilities are presented on the top of the figure.

1.3 QCD phase structure

1.3.1 Quark Gluon Plasma (QGP)

QCD at sufficiently high energies (weak coupling constant α_s) can be handled in the same way as the QED by employing perturbation theory. But as the energy decreases and α_s increases, the perturbative approach fails. In addition, QCD being a non-Abelian field theory complexifies the calculation further. Unlike photons, which do not couple with each other, the gluons can couple with one another in addition to quarks. This makes analytical

QCD calculation for physical quantities extremely difficult, and hence one resorts to the numerical methods, *i.e.* the lattice-QCD (LQCD) simulations [11–14]. LQCD is a non-perturbative first-principle approach to solve QCD on a discrete space-time grid or lattice numerically. LQCD can calculate the bulk thermodynamic variables like pressure, entropy density, and energy density. It was seen in LQCD that the bulk thermodynamic variables at high temperature strongly depended on the number of quark flavours [15]. Calculations

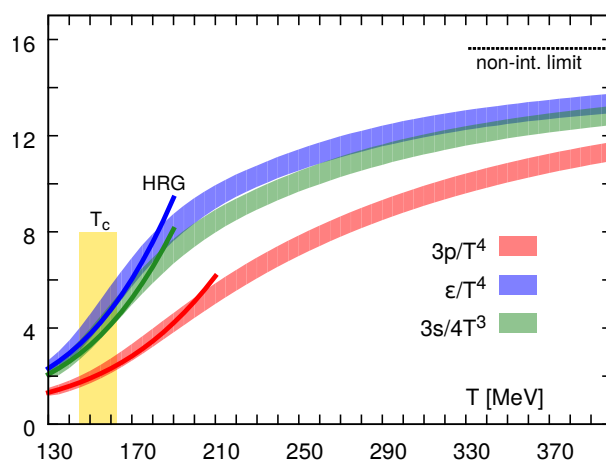


Figure 1.4: Normalized energy, pressure, and entropy density as a function of temperature obtained from LQCD calculations at vanishing baryonic chemical potential. The yellow band represents the transition temperature T_c [16].

on energy, pressure, and entropy densities from LQCD as a function of temperature, is shown in Fig. 1.4. At temperature greater than $T \sim 154 \pm 9 \text{ MeV}$, a rapid rise in energy density and the other thermodynamic variables is seen due to an increase in degrees of freedom marking the formation of QGP. This temperature $T = T_c$ is called the transition temperature. QGP is defined as a thermodynamically equilibrated deconfined phase of quarks and gluons [17]. Several theoretical works have been carried out to calculate the properties of QGP, especially shear viscosity (η) or its ratio relative to entropy density (η/s) [18–20]. Comparison with experimental data from heavy-ion collision reveals that

QGP is the most perfect fluid [21] known to date.

Experimental study:

There are several interesting observations made by heavy-ion collision experiments that suggest of formation of the QGP in heavy-ion collisions. One such important observation comes from azimuthal anisotropy measurements.

A medium can be characterized by its collective behavior, i.e., how the medium moves as a whole. The collectivity of the medium formed in the heavy-ion collision is studied by employing relativistic hydrodynamics. In non-central nuclear collisions, the anisotropic geometry of the overlap region gives rise to azimuthally-varying pressure gradients. The initial spatial anisotropy of the overlap region is translated into momentum anisotropy which subsequently results in anisotropy of produced particles along the azimuth. The azimuthal distribution of produced particles can be expressed in terms of a Fourier series [22, 23] as follows

$$\frac{dN}{d\phi} \propto 1 + 2v_1 \cos(\phi - \psi) + 2v_2 \cos(2(\phi - \psi)) + \dots, \quad (1.2)$$

where ϕ is the azimuthal angle (angle between the momentum vector of charged particle projected to the x-y plane and x-axis). ψ is the reaction plane angle, i.e., the angle subtended by the reaction plane (the plane made by impact parameter and z-axis) with the x-axis. These definitions are based on the convention that the z-axis is the beam axis, i.e., the axis along which the beams or heavy ions are made to collide. The first two coefficients v_1 and v_2 in the Fourier expansion are called the directed flow and elliptic flow, respectively. Both are sensitive observables in the study of the expansion of the medium produced. Of the two, here we will discuss the elliptic flow measurements. Figure 1.5 shows v_2 of various hadrons produced in Au+Au collisions at $\sqrt{s_{NN}} = 200$ GeV from the STAR and PHENIX experiment [25–28].

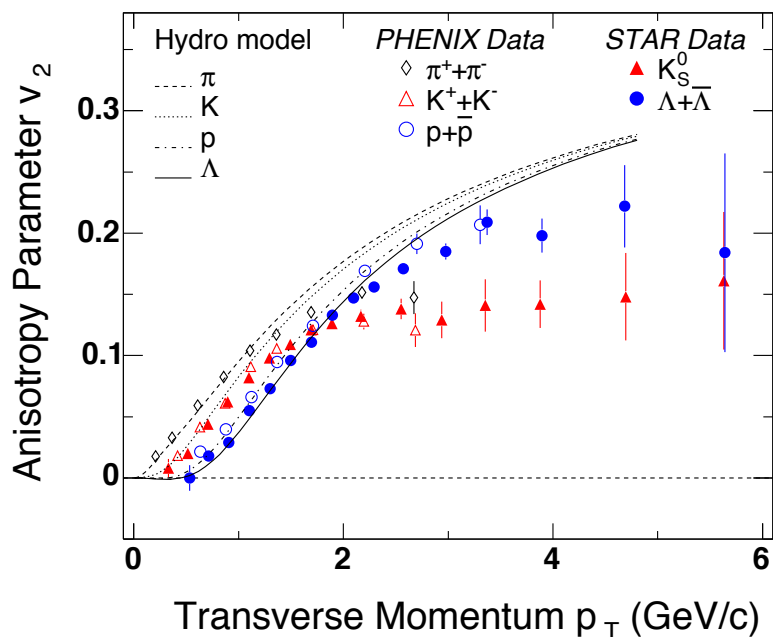


Figure 1.5: Elliptic flow v_2 of identified hadrons π , K , p , Λ as a function of p_T in Au+Au collisions at $\sqrt{s_{NN}} = 200$ GeV from the STAR and PHENIX experiment. Expectations from ideal hydrodynamic calculations are shown as dashed and solid lines. Figure adapted from Ref. [24].

For transverse momentum, $p_T < 2$ GeV/c, a mass ordering of v_2 is seen in the experimental measurements, i.e., the lighter the hadrons larger the v_2 . Such an ordering is consistent with ideal hydrodynamic calculations that include the equation of state for the QGP [29]. In the low momentum region $p_T < 1$ GeV/c good quantitative agreement can be observed between experimental data and ideal hydrodynamic predictions. At the higher p_T region ($p_T > 2$ GeV/c), the mass ordering is no longer observed, and the measurements get separated into two classes, mesons and baryons. But once the experimental data is scaled by the number of constituent quarks (n_q), within a few percent level, the v_2/n_q of all the particles seem to follow a universal curve as a function of p_T/n_q [30]. This behavior can be seen from Fig. 1.6 and is called the number of constituent quark (ncq) scaling. This suggests that at the time flow dynamics were developed in the medium due to the

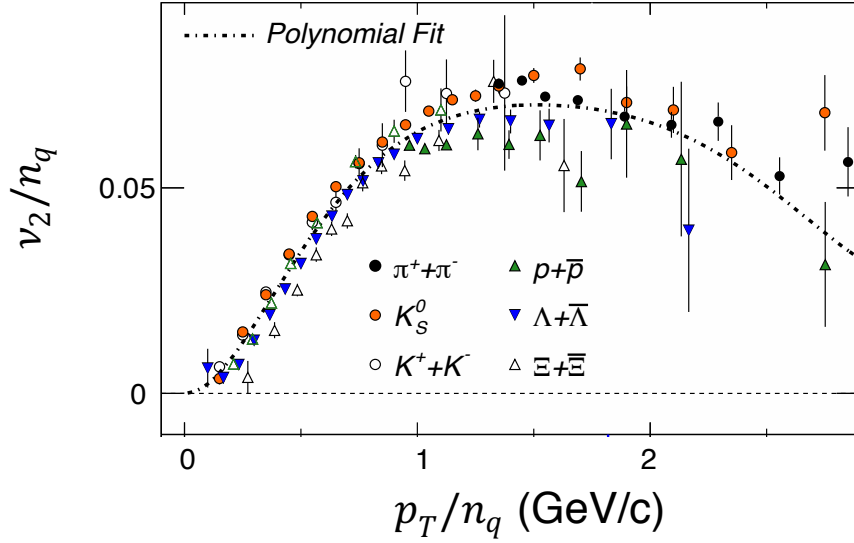


Figure 1.6: v_2/n_q of identified hadrons as a function of p_T/n_q in Au+Au collisions at $\sqrt{s_{NN}} = 200$ GeV from the STAR and PHENIX experiment. The figure is taken from Ref. [30].

pressure gradients, the relevant degrees of freedom were partonic, which is a necessary criterion for QGP formation. A strong collective flow that exhibits mass ordering and nq scaling is indicative of a strongly interacting medium of free quarks and gluons. Several other signatures of QGP formation have been also observed but not discussed here. These include – jet quenching [17], strangeness enhancement [31] and J/Ψ suppression [32] due to Debye screening.

It is important to study if the produced medium attains thermal equilibrium. Description of experimentally measured hadron yields and ratios using the statistical thermal model is used for such studies. Figure 1.7 shows the ratio of yields of various hadron species along with statistical thermal model fits. The excellent agreement of the measured ratios to the fits from a statistical thermal model with parameters (temperature $T = 163 \pm 4$ MeV, $\mu_B = 24 \pm 4$ MeV) is supportive of the conclusion that both thermal and chemical equilibrium is attained. While the results discussed above employed hadron yields (which

is same as the mean), higher order fluctuation measurements have also been considered by authors of Ref. [33], as a more robust test for thermal equilibrium. Requiring a simultaneous description of thirteen observables (which included up to third-order fluctuations of pions, kaons, protons, their anti-particles, net-proton, net-kaon and net-charge) by thermal model, their studies indicate that for Au+Au collisions, equilibrium is attained at collision energies above $\sqrt{s_{NN}} > 27$ GeV while that may not be the case for lower collision energies.

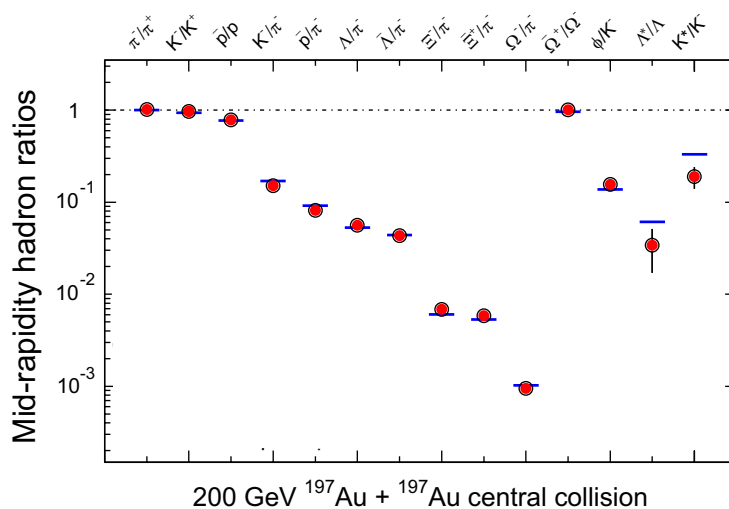


Figure 1.7: Ratio of yields of hadrons of various species from Au+Au collisions at $\sqrt{s_{NN}} = 200$ GeV [17]. The horizontal lines represent the fits to experimental data by a statistical thermal model with temperature $T = 163 \pm 4$ MeV, $\mu_B = 24 \pm 4$ MeV and strangeness suppression factor $\gamma_s = 0.99 \pm 0.07$.

Flow measurements are also used to study the shear viscosity to entropy density ratio (η/s) of the medium created in heavy-ion collisions. This requires a comparison of v_2 measurements with viscous hydrodynamical calculations. It is worth mentioning that based on anti-de Sitter/Conformal Field Theory (AdS/CFT), there is a lower bound to η/s in the strong coupling limit. This lower bound is called the KSS bound, and its value is $\eta/s = \frac{1}{4\pi} \simeq 0.08$ [35]. The majority of fluids have values much larger than KSS bound. Figure 1.8, shows v_2 measurements from STAR and viscous hydrodynamical calculations

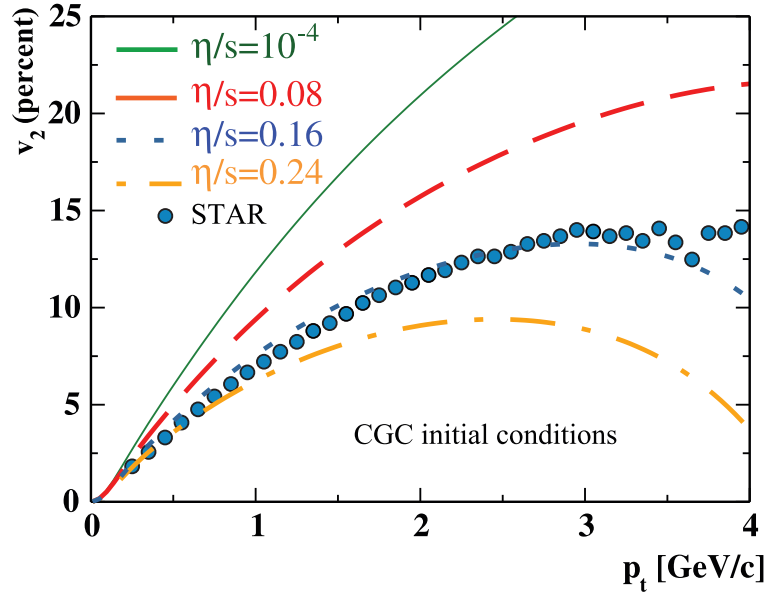


Figure 1.8: Transverse momentum dependence of v_2 . The filled circles are measurements from the STAR experiment. The dashed lines represent viscous hydrodynamical calculations with different values of η/s . The figure is taken from Ref. [34].

with different values of η/s , including the KSS bound. The experimental measurements are best described by hydrodynamical calculations with $\eta/s = 0.16$, which is just larger than KSS bound by a factor of two. The results are indicative of the almost perfect fluidity of the produced medium of deconfined partons.

1.3.2 Hadronic phase

The hadronic phase comprises of hadrons, which are confined states of partons with zero net color charge. In the collision of heavy-ion nuclei, a large amount of energy is deposited in a very small volume. This tiny volume is the subject of interest. If it has reached a temperature higher than the transition temperature T_c , a phase transition to de-confined state of quarks and gluons is expected. The system may not be in thermal equilibrium initially, but with the interactions among quarks and gluons, a local thermal equilibrium is expected

soon. This thermalized state of matter could be identified as the QGP. Subsequently, as the system starts to expand and cool, hadronization takes place, and a stage is reached where the inelastic interactions among the constituents cease [36]. This stage is called the chemical freeze-out and is characterized by temperature T_{ch} . The relative abundance of hadrons gets fixed at this stage, and only elastic interactions among hadrons are possible. With decreasing temperature due to further expansion of the system, there comes a stage called the kinetic freeze-out characterized by temperature T_{fo} where even the elastic interactions stop [37, 38]. At this point, the mean free path of hadrons is larger than the size of the system, and thus, the particles come out freely and fall on the detectors. The hadronic phase constitutes the time between the chemical freeze-out and the kinetic freeze-out.

Experimental study:

An experimental way to study the hadronic phase is via the measurement of resonance yields. Resonances are short-lived hadrons that decay via the strong interaction. If the lifetime of resonance is smaller than the hadronic phase, its decay daughters will be affected by rescattering from other hadrons. One such resonance is K^{*0} meson, which decays to charged kaon and pion. Rescattering could change the decay daughters' momentum, and thus, the invariant mass technique fails to reconstruct the mother resonance. A pion from K^{*0} decay can get scattered with other pion, $\pi^- \pi^+ \rightarrow \rho^0 \rightarrow \pi^- \pi^+$. As a consequence, the resonance yield will decrease compared to what it was at chemical freeze-out. There is also another possibility, called the regeneration effect, where pseudo-elastic scattering, such as $\pi^- K^+ \rightarrow K^{*0} \rightarrow \pi^- K^+$ increases the K^{*0} yield. Due to the pion-pion interaction cross section being significantly larger (by five times) than that of the pion-kaon [40], the rescattering effect is expected to dominate. Hence, the ratio of K^{*0} yield with respect to a stable hadron, K^- , from heavy-ion collisions will be suppressed compared to pp collisions.

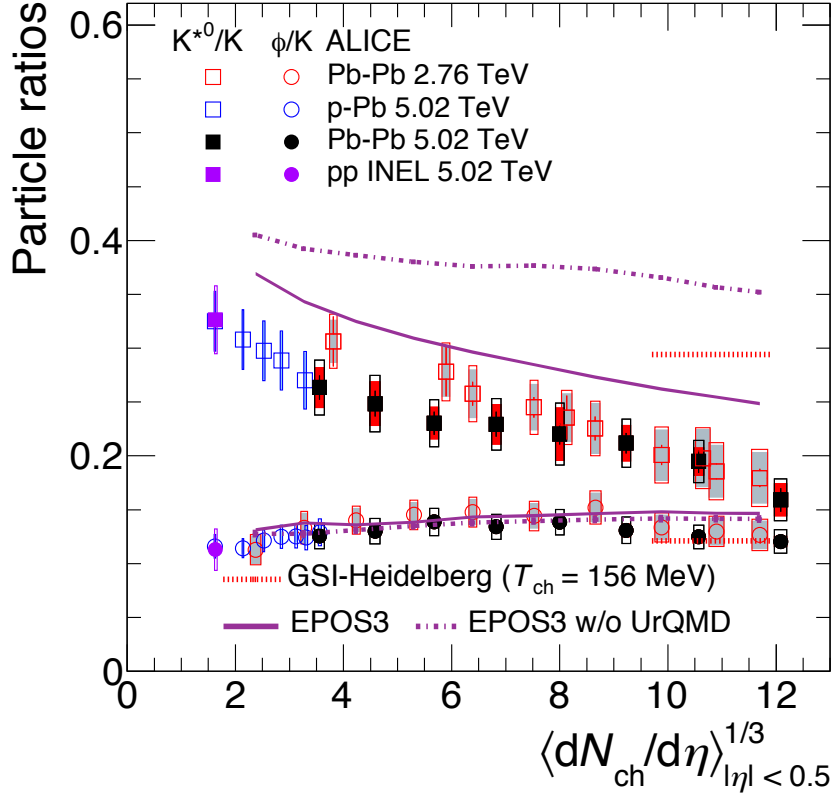


Figure 1.9: Ratio of yields, K^{*0}/K^- and ϕ/K^- measured from Pb+Pb collisions at $\sqrt{s_{NN}} = 2.76$ and 5.02 TeV, p+Pb collisions at $\sqrt{s_{NN}} = 5.02$ TeV and p+p collisions at $\sqrt{s} = 5.02$ TeV as a function of system size (collision centrality) using ALICE at the LHC [39].

The K^{*0}/K^- ratio is also expected to decrease with increasing centrality (due to the higher lifetime of the hadronic phase in central collisions). These trends are indeed observed in experimental measurements (shown in Fig 1.9). The ratio of K^{*0}/K^- yields in Pb+Pb is suppressed compared to that p+Pb and p+p collisions at the same center-of-mass energy. The ratio decreases with increasing collision centrality. In contrast, the yield ratio of ϕ/K^- shows no such trend. This is because the lifetime of ϕ meson is 10 times that of K^{*0} meson and it decays ($\phi \rightarrow K^-K^+$) outside of the hadronic phase. These studies are also used to determine the lifetime of the hadronic phase. A hadronic phase lifetime of 4 – 7 fm/c is obtained for Pb+Pb collisions at LHC [39].

1.3.3 Crossover

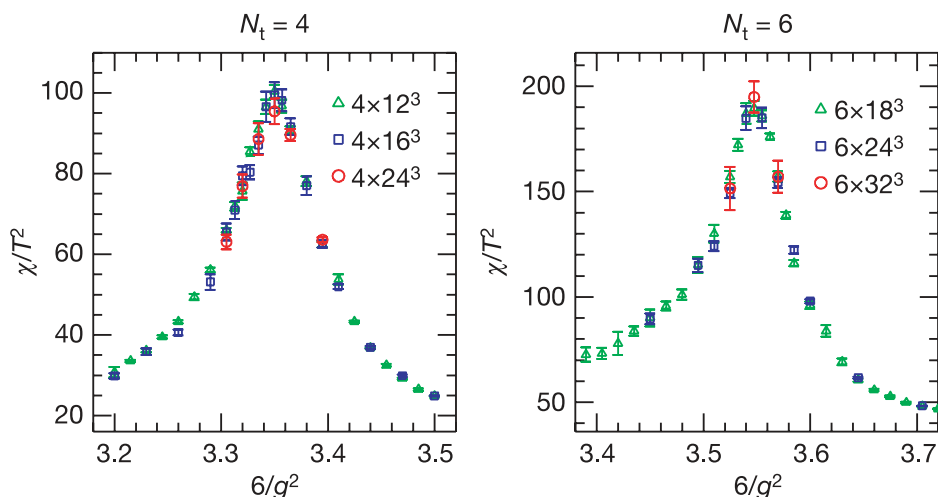


Figure 1.10: chiral susceptibility of light quarks for two values of temporal lattice spacing N_τ as a function of $6/g^2$, where g is the gauge coupling in QCD Lagrangian. The temperature T increases with $6/g^2$. Various markers represent different lattice volumes; the largest volume is eight times that of the smallest volume. Figure adapted from Ref. [41].

LQCD calculations at vanishing μ_B have shown that the nature of phase transition between the hadronic phase and QGP phase is a smooth crossover [41]. Every phase transition is associated with an order parameter – a quantity that is different in the two phases. In LQCD calculations, the chiral susceptibility serves as the order parameter distinguishing the phases. It is defined as $\chi(N_s, N_\tau) = (\partial^2 / \partial m_{ud}^2)(T/V) \log Z$, where m_{ud} is the mass of the light u, d quarks, Z is the partition function, N_τ and N_s are the euclidean time extension and spatial extension, respectively, and V the system volume in LQCD. The smooth crossover was established by demonstrating that the temperature dependence of the peak and the width of the chiral susceptibility are independent of the system volume. Figure 1.10 presents the light quark susceptibilities for $N_\tau = 4$ and 6. For both cases, by increasing the lattice volume by a factor of 8, no significant change in the susceptibility peak was observed. For a first-order phase transition, one would expect the height of the

susceptibility peak to vary proportionally to the volume and width inversely with volume. For a second-order transition, a singular behavior is expected with the volume of the system (V^α , α is some critical exponent).

1.3.4 First-order phase transition

LQCD calculations at finite μ_B suffer from the notorious issue of the sign problem. Typically, in lattice calculations, the expectation value of certain observable X , $\langle X(m_v) \rangle = \frac{\int DU \exp(-S_G) X(m_v) \text{Det } M(m_s)}{\int DU \exp(-S_G) \text{Det } M(m_s)}$ needs to be evaluated, where M represents the Dirac matrix in color, spin, flavor and co-ordinate space for sea quarks with mass m_s , S_G represents the gluonic action. The observable X could be a function of fermion propagators mass m_v . The calculation relies on $\text{Det } M$ being positive definite, but for finite μ that is not the case. Hence, the evaluation of the expectation values using numerical methods is difficult. This complication in the lattice calculation is known as the *sign problem*. However, considering effective potentials and several approximations in the calculations, exploring the QCD phase structure at finite μ_B is possible. Several lattice calculations and QCD-based models like Nambu-Jona-Lasinio (NJL) [42], Polyakov-loop-extended NJL (PNJL) model [43], Linear sigma field model [44], take this approach and indicate that at large μ_B and low temperature, the QGP-hadron phase transition is a first-order phase transition. One such calculation on lattice was carried out by Ejiri [45]. Evaluating the canonical partition function ($Z_c(T, N)$, where T is temperature) by fixing the number of quarks (N) and its number density (ρ) and minimizing the effective potential ($V_{eff}(N)$), the first order phase transition was demonstrated. Due to the existence of mixed phase in a first-order phase transition, the effective potential will have more than one minima at different values of N characterized by vanishing first-order derivative. With the introduced potential, $V_{eff}(N) = -\ln Z_c(T, N) - \frac{N\mu_q}{T}$ (μ_q is quark chemical potential) by Ejiri, the relation $\frac{\partial \ln Z_c(T, N)}{\partial N} = -\frac{\mu_q}{T}$ has to be satisfied

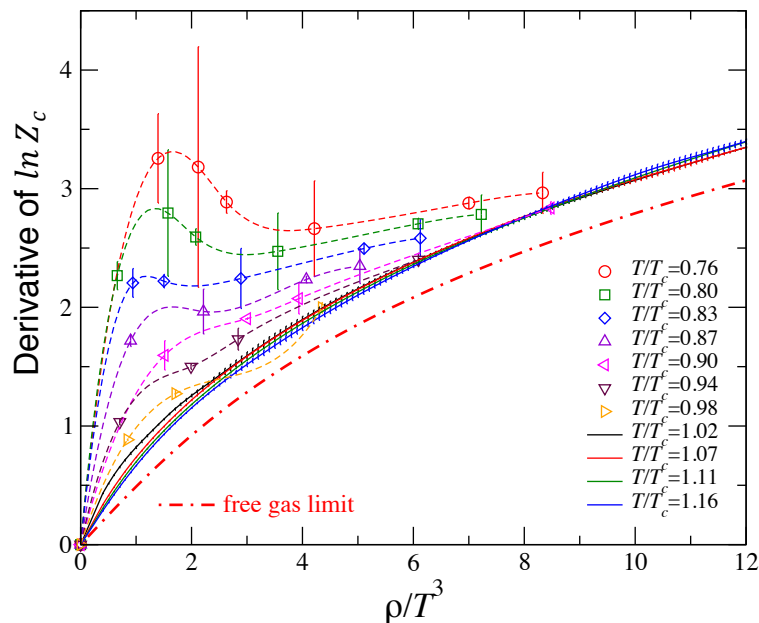


Figure 1.11: Derivative of $\ln Z_c(T, N)$ vs. quark number density for various cases of T/T_c conditions. The figure is taken from Ref. [45].

at minima. This meant that there should be different values of ρ (or N) corresponding to different minima where the derivative of $\ln Z_c(T, N)$ are exactly the same (equal to $-\frac{\mu_q}{T}$). Hence the derivative of $\ln Z_c(T, N)$ as a function of ρ would be non-monotonic. From Fig. 1.11, it can be seen that for low temperatures, below $T/T_c \leq 0.8$, the derivative of $\ln Z_c(T, N)$ shows an s-shape dependence on ρ/T^3 . There are more than one values of ρ/T^3 where the derivative of $\ln Z_c(T, N)$ are equal – a signature of first-order phase transition. On the other hand, as we start going higher on temperature $T/T_c > 0.8$, the derivative of $\ln Z_c(T, N)$ increases monotonically with ρ/T^3 .

Experimental study:

A system undergoing a first-order phase transition passes through a mixed phase where it is at its softest equation-of-state (EoS). The softest EoS is the one that exhibits a small change in pressure with respect to change in volume. This softening is caused due to

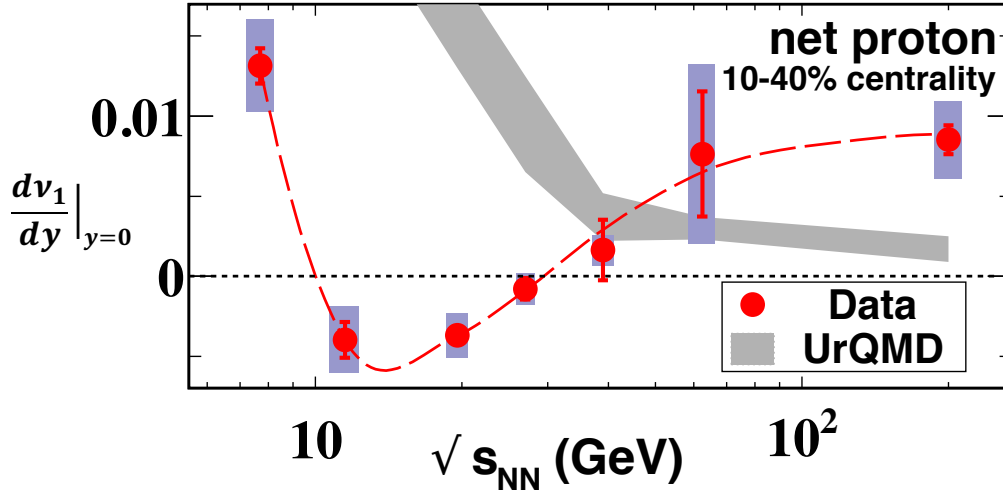


Figure 1.12: The slope of net-proton directed flow at midrapidity for mid-central Au+Au collisions at RHIC. Results are presented as a function of collision energy. The red dashed line is just to guide the eye. The figure is adapted from Ref. [46].

the latent heat involved in first-order phase transition. Directed flow measurements have been suggested as sensitive observables to the softening of EoS. The first coefficient in the Fourier expansion of the azimuthal distribution of produced particles, v_1 (see equation 1.2 for details), is called the directed flow. Hydrodynamical calculations with a first-order phase transition predict a non-monotonic collision energy dependence of slope of the directed flow of net-baryons at mid-rapidity [46, 47]. Experimental measurements on net-proton directed flow are carried out as a proxy of net-baryon directed flow [46]. The slope of net-proton directed flow at midrapidity for mid-central Au+Au collision is shown in Fig. 1.12. The measurements exhibit a non-monotonic collision energy dependence consistent with the hydrodynamic predictions suggesting the softening of EoS. Calculation from the hadronic transport model UrQMD that does not include a first-order phase transition fails to explain the measurements.

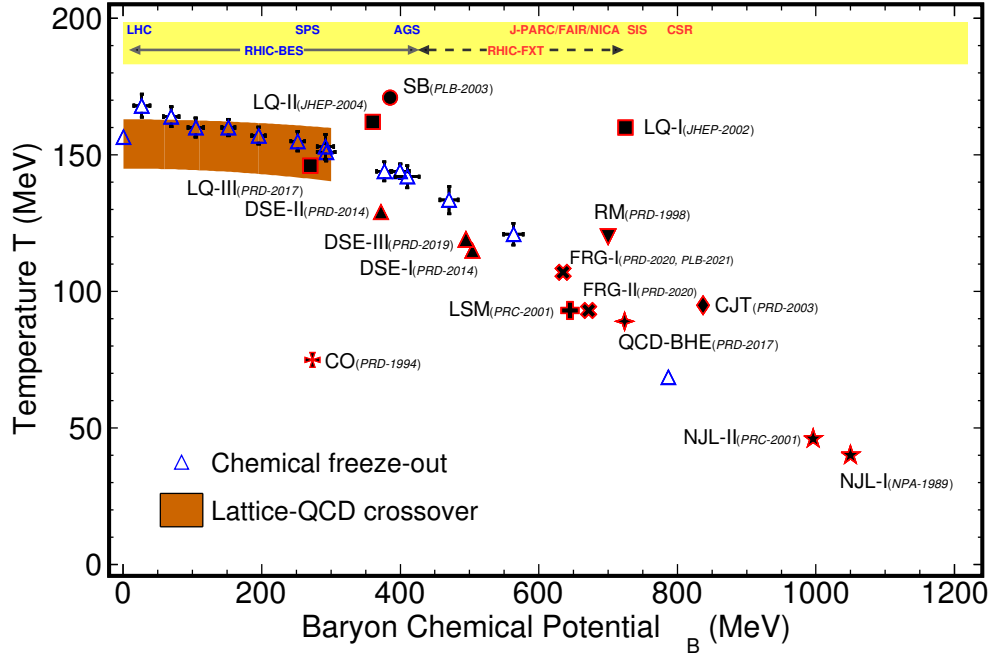


Figure 1.13: Theory predictions on the location of QCD critical point. The labels are abbreviated for various theoretical models and publications (LQ: Lattice-QCD, SB: Statistical Bootstrap Model, DSE: Dyson-Schwinger equations, FRG: Functional Renormalization Group, LSM: Linear Sigma Model, RM: Random Matrix Model, CO: Composite Operator formalism, QCD-BHE: QCD from Black Hole Engineering, and CJT: Cornwall-Jackiw-Tomboulis effective potential). Predictions are taken from Ref. [48–63]. The orange-colored band represents crossover from lattice-QCD calculations. The open triangle markers are locations of chemical freeze-out obtained from fitting of yields measured in various experiments (SPS, AGS, STAR, and ALICE) using a statistical thermal model. The μ_B range covered by various experimental facilities and programs is also shown on the top.

1.3.5 Critical Point

As we saw, LQCD predicts a smooth crossover between QGP and hadronic phase at high temperatures and vanishing baryonic density. We noted that at low temperatures and finite baryonic density, effective model calculations suggest a first-order phase transition. With these two pieces of information at hand, by thermodynamics arguments, there has to be a critical point at the end of the quark-hadron phase co-existence line where the first-order

phase transition changes to crossover. This critical point arising from the study of QCD phase transition is called the QCD critical point. Similar to the critical point in the liquid-gas phase transition in water, the QCD critical point is accompanied by the divergence of correlation length and long-range density fluctuations.

Due to the sign problem, the information on QCD critical point (the phase structure at large μ_B , in general) from first-principle lattice calculation is not highly robust. Some ways have been suggested to overcome this problem, such as (a) Reweighting of the partition function near the transition temperature and $\mu = 0$ [49], (b) Expansion of thermodynamic variables in μ/T about $\mu = 0$ using Taylor series [64], and (c) Choosing imaginary chemical potential to make the fermionic determinant positive [65]. Various effective models that are QCD-based are also used in the study of QCD critical point. But due to the many approximations involved in these approaches, the location and existence of the critical point directly from theory calculation still remain challenging. Predictions on the location of the QCD critical point from several theoretical calculations are shown in Fig. 1.13. The predictions vary over a wide region of $T = 40\text{--}180$ MeV and $\mu_B = 200\text{--}1100$ MeV [48–63]. Since, from the theoretical side, a concrete picture of the location of the critical point is missing at present, an experimental search for the critical point is crucial to validate it in the QCD phase diagram. The QCD critical point carries immense importance. It forms a landmark in the QCD phase diagram with the crossover to its left, first-order phase transition to its right, QGP at the top, and hadronic phase at its bottom. If proven to exist, it will be the second known point in the QCD phase diagram after the ground state of nuclear matter ($T \approx 0$ and $\mu_B \approx 925$ MeV).

1.3.6 Transition temperature

The transition temperature T_c is the temperature characterizing the transition between the hadronic phase and the QGP phase. The point of the sharpest change in the temperature dependence of the chiral susceptibility is used to estimate the QCD transition temperature in lattice calculations. Figure 1.14, shows a recent lattice QCD calculation on chiral susceptibility as a function of temperature for vanishing $\mu_{B,Q,S}$. A maximum in chiral susceptibility is seen at a temperature around $T_c \sim 156$ MeV. For accuracy of results, lattice calculations are extended to the continuum limit by allowing $N_\tau \rightarrow 0$. A resulting value of $T_c = 156.5 \pm 1.5 \text{ MeV}$ [66] at vanishing $\mu_{B,Q,S}$ was found.

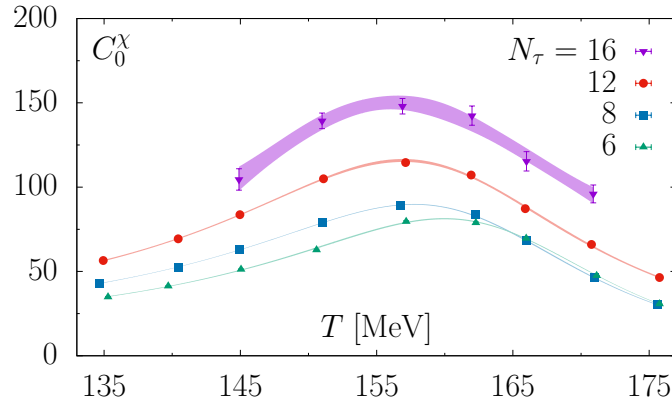


Figure 1.14: Chiral susceptibility from lattice as a function of temperature for vanishing $\mu_{B,Q,S}$. Calculations with different numbers of temporal extension N_τ are presented. The figure is adapted from Ref. [66].

The transition temperature is not a constant value as a function of μ_q (where $q = B, Q, S$), but rather shows a μ_q dependence. Using Taylor series expansion about vanishing μ_q , the following relation is obtained for the dependence of T_c on μ_q from lattice QCD calculation.

$$T_c(\mu_q) = T_c(0) \left[1 - \kappa_2^q \left(\frac{\mu_q}{T_c(0)} \right)^2 + \mathcal{O} \left(\left(\frac{\mu_q}{T_c(0)} \right)^4 \right) \right] \quad (1.3)$$

Here, κ_2^q is some constant that is extracted by studying the dependence of chiral condensate on μ_q .

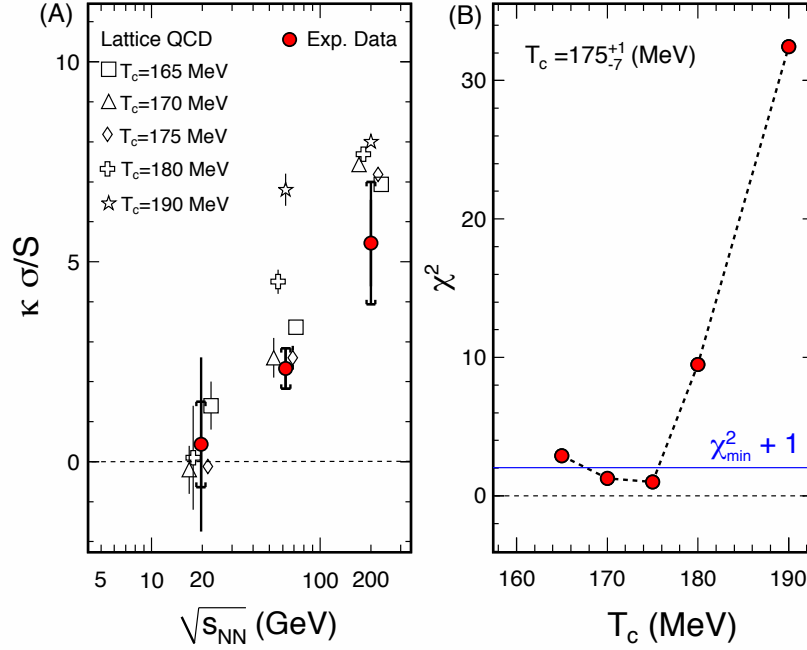


Figure 1.15: (A) Net-proton (proxy for net-baryon) cumulant ratio C_4/C_3 (red filled markers) along with lattice QCD calculation (open markers) with different T_c shown as a function of collision energy. (B) Chi-square values from the comparison of experimental data and lattice calculation with different values of T_c . The figure is adapted from Ref. [67].

Experimental study:

A data-driven approach to obtain T_c using LQCD was performed by authors of Ref. [67]. First, experimental measurements on net-proton (proxy for net-baryon) cumulant ratios up to fourth-order from STAR [68] were demonstrated to have good agreement with net-baryon cumulant ratios calculated from LQCD within uncertainties. It is worth mentioning here that LQCD requires T_c to calculate net-baryon cumulant ratios, which was taken to be $T_c = 175$ MeV for comparing with data. The next step was to invert the reasoning and calculate the net-baryon cumulant ratio from LQCD with different values of T_c to obtain the

best fit with experimental data. For this, the ratio of fourth-to-third order cumulant, C_4/C_3 , was considered in the fit (this choice of cumulant ratio was taken to have better control on uncertainties). Panel (A) of Fig. 1.15, shows a comparison of experimental data and LQCD calculations for C_4/C_3 (same as $\kappa\sigma/S$, where σ , S and κ are second, third and fourth moment, respectively) with different choices of T_c . Chi-square values from the comparison of data and lattice calculation with different T_c are shown in panel (B) of Fig. 1.15. The minimum chi-square corresponds to a value of $T_c = 175^{+1}_{-7}$ MeV. Though it is somewhat higher than the T_c corresponding to the chiral susceptibility peak in LQCD, one should keep in mind the large uncertainties in the data and the approximation and assumption involved in its evaluation (especially when comparing to low collision energies or higher μ_B).

1.4 Cumulants: probes of QCD phase structure

Event-by-event fluctuations of conserved quantities in strong interaction such as net-baryon, net-charge, and net-strangeness are predicted to be sensitive in the study of QCD phase structure [69–72]. By event, we mean here the collision of two nuclei. Fluctuations are sensitive to the correlation length (ξ) of a system [71]. Correlation length (ξ) is a measure of how variables co-vary across space and time. Since ξ diverges for an infinite system in the vicinity of a critical point, fluctuation measurements being related to ξ are used in the search for the QCD critical point. Fluctuations are measured in terms of cumulants. Cumulants quantify the subtleties of a distribution. They are also additive in nature, i.e., cumulant of a quantity which is an addition of random variates, can be obtained by the simple addition of cumulants of the constituent random variates. The cumulants of a

distribution up to the sixth order are defined as follows,

$$C_1 = \langle N \rangle \quad (1.4)$$

$$C_2 = \langle \delta N^2 \rangle \quad (1.5)$$

$$C_3 = \langle \delta N^3 \rangle \quad (1.6)$$

$$C_4 = \langle \delta N^4 \rangle - 3\langle \delta N^2 \rangle^2 \quad (1.7)$$

$$C_5 = \langle \delta N^5 \rangle - 5\langle \delta N^3 \rangle \langle \delta N^2 \rangle \quad (1.8)$$

$$C_6 = \langle \delta N^6 \rangle - 15\langle \delta N^4 \rangle \langle \delta N^2 \rangle - 10\langle \delta N^3 \rangle^2 + 30\langle \delta N^2 \rangle^3 \quad (1.9)$$

where N , for our case, is the net-particle number in a single event and $\langle N \rangle$ is the average of N across all the events and $\delta N = N - \langle N \rangle$. The first and second-order cumulants represent the mean ($M = \langle N \rangle$), and variance ($\sigma^2 = \langle \delta N^2 \rangle$) of the distribution, whereas the third and fourth-order cumulants reflect its skewness ($S = \frac{\langle \delta N^3 \rangle}{(\langle \delta N^2 \rangle)^{3/2}}$) and kurtosis ($\kappa = \frac{\langle \delta N^4 \rangle}{(\langle \delta N^2 \rangle)^2} - 3$), respectively. Skewness is the degree of asymmetry in a distribution, while kurtosis is a measure of the tailedness of a distribution. A normal distribution has zero skewness and zero kurtosis. A pictorial view of distributions with zero, positive and negative values for skewness and kurtosis is shown in Fig. 1.16. In this thesis, we will use the term *hyper-order* cumulant to refer to cumulant of order five or higher.

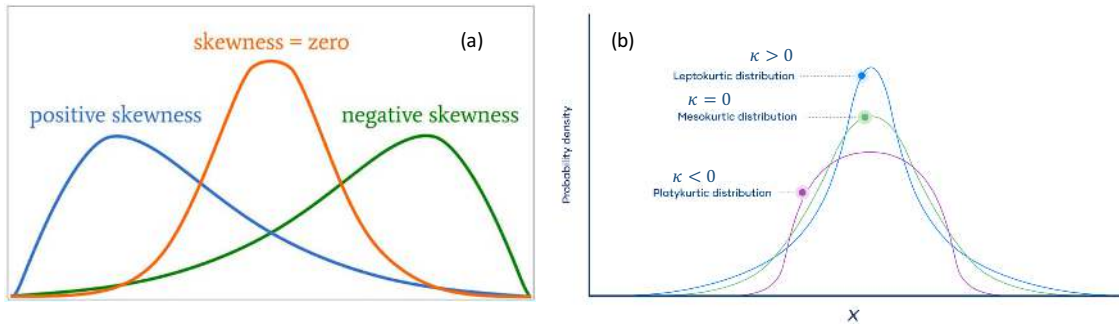


Figure 1.16: A pictorial view of distributions with zero, positive and negative values for skewness (panel a) and kurtosis (panel b) is shown. Figures are taken from Ref. [73, 74].

For a thermalized system, the ratio of cumulants can be directly related to conserved charge number susceptibilities calculated in a fixed volume, as done in LQCD and thermal models. In LQCD and thermal model calculations, using the grand canonical ensemble construct the n^{th} order number susceptibility (χ_n^q) associated with conserved charges, q ($q = B, Q, S$) can be obtained by taking derivative of dimensionless pressure (P/T^4) with respect to reduced chemical potential (μ_q/T) [33, 67, 75–77]. This is shown by the following equation,

$$\chi_n^q = \frac{\partial^n (P/T^4)}{\partial (\mu_q/T)^n}. \quad (1.10)$$

where T and P represent the system temperature and pressure, respectively. Pressure can be expressed in terms of the logarithm of the partition function (Z) as follows,

$$P/T^4 = \frac{1}{VT^3} \ln[Z(V, T, \mu_q)] \quad (1.11)$$

Using the above equations and statistical thermodynamics, it can be shown that cumulants and susceptibility are related by the following equation.

$$C_n^q = VT^3 \chi_n^q. \quad (1.12)$$

From equation 1.12, it is clear that by constructing the ratio of cumulants, the trivial system volume (V) dependence can be eliminated, and a direct comparison of cumulant ratio with susceptibility ratio can be made. While the cumulants can be measured experimentally, the susceptibility is calculated theoretically, like in LQCD, QCD-based models, and thermal models. The ratio of cumulants serves as a very important tool to test various theoretical predictions on QCD phase structure. However, there are a few caveats to be kept in mind when making such a comparison. The experimental measurements are made within a limited kinematic phase space allowed by the detector, and they probe the conserved charges

via forming proxies from the detected charged particles. On the other hand, theoretical calculations like those from the LQCD and QCD-based models deal with conserved charges and do not involve any kinematic constraints.

The cumulant ratios can also be expressed as the product of moments. Both, ratios of cumulants and the product of moments are often used in the existing literature to mean the same thing. The widely used products of moments are the σ^2/M , $S\sigma$, and $\kappa\sigma^2$, and their relation with cumulants are stated below.

$$\sigma^2/M = \frac{C_2}{C_1} \quad (1.13)$$

$$S\sigma = \frac{C_3}{C_2} \quad (1.14)$$

$$\kappa\sigma^2 = \frac{C_4}{C_2} \quad (1.15)$$

The n^{th} order cumulants measurement of a particle also contains correlations coming from lower order cumulants. To solely obtain a correlation of a particular order, factorial cumulants have been proposed by theorists [78]. Factorial cumulants are also called the irreducible correlation function. Their definition in terms of cumulants is as follows.

$$\kappa_1 = C_1 \quad (1.16)$$

$$\kappa_2 = -C_1 + C_2 \quad (1.17)$$

$$\kappa_3 = 2C_1 - 3C_2 + C_3 \quad (1.18)$$

$$\kappa_4 = -6C_1 + 11C_2 - 6C_3 + C_4 \quad (1.19)$$

$$\kappa_5 = 24C_1 - 50C_2 + 35C_3 - 10C_4 + C_5 \quad (1.20)$$

$$\kappa_6 = -120C_1 + 274C_2 - 225C_3 + 85C_4 - 15C_5 + C_6 \quad (1.21)$$

We now state various signals associated with fluctuation measurements for the study of QCD phase structure in a nutshell. These include, for critical point search – non

monotonic variation of C_4/C_2 with collision energy [71], for crossover search – negative C_6/C_2 [79], for first-order phase transition – large factorial cumulants which shows sign reversal with increasing order [80], for thermodynamics of QCD – ordering of cumulant ratios; $C_3/C_1 > C_4/C_2 > C_5/C_1 > C_6/C_2$ [79]. These theoretical predictions will be discussed in more detail in chapter 6 of this thesis.

1.5 Relativistic heavy-ion collisions

This section is a brief introduction to heavy-ion collisions and kinematic observables involved in the analysis of heavy-ion collisions. As we saw in the discussion of the QCD phase structure, the experimental study of the QCD phase diagram is carried out by performing heavy-ion collisions. As shown in Fig. 1.17, changing the collision energy of colliding ions results in the variation of both T and μ_B at chemical freeze-out. Note that these two quantities form the x and y axis of the QCD phase diagram. Hence experiments perform collisions of heavy ions over a wide range of collision energies which allows access to a wide region of the QCD phase diagram. By performing measurements of observables sensitive to the study of the phase structure of QCD across these collision energies, such as fluctuations, inferences about the QCD phase diagram are drawn.

1.5.1 Theoretical foundation and development

The theoretical foundation of performing high-energy heavy-ion or nuclear collision dates back as early as 1951. Fermi, in his paper, "High Energy Nuclear Events" [84], made use of a statistical model for explaining the pions yields and proposes the idea of applying thermodynamics to study particle production in high energy nuclear collisions. In 1953, Landau propounded that the system created in such nuclear collisions follows relativistic

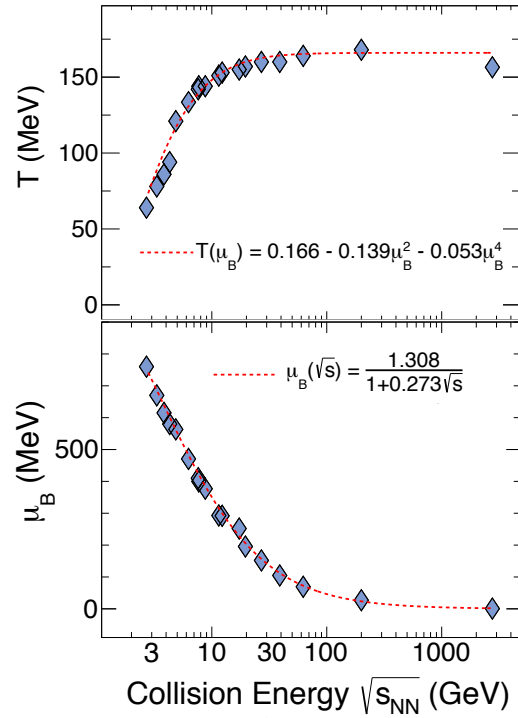


Figure 1.17: Chemical freeze-out parameters T and μ_B obtained by thermal model fits to experimental data on particle yields as a function of collision energies [81, 82]. Red lines represent parametrisations of T and μ_B on $\sqrt{s_{NN}}$ taken from Ref. [83].

hydrodynamical evolution, which implied that the system expands until the interaction cross-section of the particles produced is negligible and then freezes-out [85]. By 1970, the Statistical Bootstrap Model had been developed by Hagedorn to describe relativistic nuclear collisions, which gave the concept of "limiting temperature" or the Hagedorn temperature [86]. This is the temperature beyond which the hadronic matter ceases to exist. This hinted at the presence of a new phase of matter which we know today as the QGP. All these ideas are fundamental to the field of heavy-ion physics.

In the primordial universe, shortly (in time of the order of μs) after the Big Bang about 13.8 billion years ago, the QGP is believed to have existed. To recreate the phase transition from hadronic matter to QGP in laboratory, heavy-ion collisions are performed

at ultra-relativistic speed. The idea is to generate large energy density from collisions so that the QGP is produced and then study its properties and understand the quark-hadron phase transition by applying thermodynamics.

The earliest of the relativistic heavy ion collision experiments was started at the Bevalac at Lawrence Berkeley National Laboratory (LBNL) in the early 1970s. The Bevatron accelerator, which is credited for the discovery of antiproton and antineutron in 1955-1956, was combined with a linear accelerator called SuperHILAC, resulting in Bevalac. It operated at modestly relativistic conditions. However, a direct search to observe the phase transition of hadronic matter to QGP started with The Alternating Gradient Synchrotron (AGS) experiment at Brookhaven National Laboratory (BNL) in 1991 and the Super Proton Synchrotron (SPS) at CERN in 1994. Both of the experiments carried Fixed-Target (FXT) collisions. The heaviest ion accelerated at AGS was gold (Au^{79+}), and SPS was lead (Pb^{82+}). While AGS covered center-of-mass collision energy range $\sqrt{s_{NN}} = 2.6 - 4.85$ GeV, the SPS operated over the range $\sqrt{s_{NN}} = 6.4 - 17.3$ GeV. Though several interesting observations and foundations of the field were made from these experiments, many of the proposed signatures of the QGP could not be studied due to too low collision energies. New accelerators were needed at much higher collision energies. Thus began the new era of relativistic heavy ion collision experiments. The Relativistic Heavy Ion Collider (RHIC) at BNL came in the year 2000 which could carry collisions of gold nuclei in collider mode over a wide range of $\sqrt{s_{NN}} = 7.7 - 200$ GeV. The most recent addition is the Large Hadron Collider (LHC) at CERN in the year 2010, capable of colliding lead nuclei at TeV energy scales in collider mode.

1.5.2 Kinematics of heavy-ion collisions

This thesis reports results obtained from the analysis of data recorded at the Solenoidal Tracker at RHIC (STAR) experiment. To simplify the complexities in analysis of data recorded at STAR and relativistic heavy-ion collision experiments in general, it is helpful to define kinematic observables that are Lorentz invariant or undergo simple transformation under Lorentz boost from one frame of reference to another. This section outlines some of the kinematic observables that are frequently used in the analysis [87]. These kinematic variables are defined in light of the conventions followed in the experiments. As per the convention followed at the STAR experiment, the beam or the collision axis lies in the z-direction. Hence, before the collisions take place, there is no initial momentum in the x-y plane. The nominal interaction point (IP) is situated at (0,0,0). Though this point lies at the center of the STAR detector, all the collisions need not occur at this point. Instead, collisions are spread about this point. The point of collision for each event has to be reconstructed in the experiment and is called the primary vertex.

a) Center-of-mass energy

Center-of-mass energy is the square root of Mandelstam's variable 's'. Mandelstam's variable 's' is essentially the square of the sum of four momenta of two colliding particles. It is a Lorentz invariant quantity. Let's consider two particles, A and B; the variable 's' is defined as follows.

$$s = (p_A + p_B)^2 = (E_A + E_B)^2 - (\vec{p}_A + \vec{p}_B)^2. \quad (1.22)$$

Where p_A (p_B), E_A (E_B), and \vec{p}_A (\vec{p}_B) are the four momenta, energy, and momentum vector of particle A (B) respectively. In the center-of-mass frame, $\vec{p}_A + \vec{p}_B = 0$. If the two colliding particles are of the same mass, then $E_A = E_B = E$. Substituting these values in

equation 1.22, the resulting center-of-mass energy in such a scenario would be $\sqrt{s} = 2E$. In heavy-ion collisions, all the constituent nucleons of the ions are accelerated to collide; hence one often quotes the center-of-mass energy per nucleon $\sqrt{s_{NN}}$. For example, the highest center-of-mass collision energy achieved for Au+Au collisions at RHIC is $\sqrt{s_{NN}} = 200$ GeV. This means each of the 197 nucleons (mass number of Au) is accelerated at 100 GeV from opposite sides to collide with each other.

When heavy ions collide at ultra-relativistic energy, new particles are produced. Each of the charged particles follows a trajectory under the influence of the magnetic field of the detector before getting detected. The trajectory followed by the particle is called a track. Some of the important kinematic variables associated with these charged particles or tracks are as follows.

b) Transverse momentum

Since the beam axis (z-axis) and the transverse plane subtended by the x-y axis are perpendicular to each other, the momentum of a charged particle can be decomposed into two orthogonal components, one along the beam axis (p_z) and one along the transverse x-y plane (p_T). p_T is called the transverse momentum. It is a Lorentz invariant and is defined as follows.

$$p_T = \sqrt{p_x^2 + p_y^2}. \quad (1.23)$$

Here, p_x and p_y are the momenta along the x and y axis, respectively.

c) Azimuthal angle

The azimuthal angle ϕ is the angle between the momentum vector of charged particle projected to the x-y plane and the x-axis. In terms of momentum components p_x and p_y ,

ϕ can be defined as follows.

$$\phi = \tan^{-1}\left(\frac{p_y}{p_x}\right). \quad (1.24)$$

d) Rapidity

At the relativistic limit, the momentum and velocity are no longer additive quantities. Since heavy-ion collisions happen at relativistic velocity, the rapidity (y) of the charged particles serves as a more appropriate variable to use as it is additive in nature. It is also Lorentz invariant and is defined as follows.

$$y = \frac{1}{2} \ln\left(\frac{E + p_z}{E - p_z}\right). \quad (1.25)$$

Here, E is the energy of the charged particle.

e) Pseudo-rapidity

As seen from equation 1.25, the calculation of the rapidity of particles requires information on energy and momentum. In experiments, by studying the trajectory of charged track under a magnetic field, one measures the momentum. To obtain energy, one needs to perform particle identification techniques to get the mass of the charged particle (since energy calculation requires both mass and momentum). Often the measurement of mass could be challenging, and moreover, there are several analyses where the mass of the particle is not relevant to the physics being pursued. Hence, experimentalists introduced another variable called pseudo-rapidity (η). It is defined as

$$\eta = \frac{1}{2} \ln\left(\frac{p + p_z}{p - p_z}\right) = -\ln \tan \frac{\theta}{2}. \quad (1.26)$$

where a substitution $p_z = p \cos \theta$ is used, and θ is the polar angle made by the charged particle with respect to the beam axis. η is invariant under Lorentz transformation. As seen from equation 1.26, only θ is needed to calculate pseudo-rapidity.

f) Multiplicity

Multiplicity is defined as the number of particles produced in a collision of heavy-ion nuclei. By multiplicity, one generally means the charged particle multiplicity as in most of the experiments (including the STAR experiment), the tracking detector is only capable of measuring charged particles and neutral particles go undetected.

f) Invariant Yield

The Lorentz invariant differential yield of a particle is defined as $E \frac{d^3N}{dp^3}$. It can be expressed in terms of kinematic observables p_T and y through the following equation,

$$E \frac{d^3N}{dp^3} = \frac{d^2N}{2\pi p_T dp_T dy}. \quad (1.27)$$

where N represents the number of produced particles.

1.5.3 Natural unit

Physical Quantity	Natural unit	Conversion from SI unit
Mass	GeV	1 kg = 5.61×10^{26} GeV
Length	GeV ⁻¹	1 m = 5.07×10^{15} GeV ⁻¹
Time	GeV ⁻¹	1 s = 1.52×10^{24} GeV ⁻¹

Table 1.1: Mass, length, and time in natural units.

In heavy-ion physics, it is more convenient to express physical quantities in terms of a unit system such that the speed of light c and Planck's constant \hbar are equal to unity ($c = \hbar = 1$). Since this system of units is natural to elementary particle physics, it is called the natural unit. Due to these two constraints, of the three kinematic units (mass, length, and time), only one free choice remains. The kinematic unit of choice is taken to be energy. Thus, all the physical quantities in natural units are expressed in terms of energy. Table 1.1

summarizes natural units of mass, length, and time and the conversion factors from the SI unit.

1.6 Motivation for the thesis

The goal of the work reported in this thesis is to map the QCD phase diagram. The present understanding of the QCD phase diagram remains largely conjectured. The first-principle lattice QCD has established the quark-hadron phase transition to be a smooth crossover at vanishing μ_B . Such calculations to explore the QCD phase structure at finite μ_B (critical point and first-order phase transition) suffer from the sign problem. Hence, effective models are used at high μ_B . These model calculations are suggestive of a first-order phase transition that terminates at the QCD-critical point at finite μ_B . Due to the inapplicability of a rigorous first-principle calculation at finite μ_B , these conclusions are less robust than the crossover at vanishing μ_B . This deems experimental studies for QCD phase structure extremely important. Neither the presence of the QCD critical point nor the nature of the quark-hadron phase transition has been directly verified yet by experiments.

The thesis work carried out strives to experimentally address these questions by exploiting well-known features of fluctuations associated with phase transitions. Fluctuations are measured via the calculation of cumulants. Cumulants of conserved charges, especially of the higher order, are not only sensitive to the presence of QCD critical point but can also probe the nature of the phase transition of QCD matter from hadronic phase to QGP. The sign of hyper-order cumulants (order five or higher), in particular, is used to study the nature of phase transition. Though it is desired to measure cumulants of conserved charges, in many of the experiments, the neutrally charged particles (for example, neutron, which also carries conserved quantum number $B = 1$) are not detected by the detectors. Hence, proxies

are constructed from the detected charged particles. This thesis presents measurements of cumulants of event-by-event net-proton number (proxy for net-baryon, a conserved quantity) distribution in Au+Au collisions from the STAR experiment at RHIC. There are several theoretical works that suggest that the net-proton number fluctuations can effectively reflect the net-baryon number fluctuations in the study of QCD phase structure [88, 89].

Thesis outline:

Now we outline the contents of the thesis.

Chapter 1: This introductory chapter explains the phase transition in QCD, its phase diagram, and the rich QCD phase structure. It presents cumulants of conserved quantities as a tool to study the QCD phase structure. Discussions on relativistic heavy-ion collisions and how they facilitate the exploration of the QCD phase diagram is included in this chapter.

Chapter 2: This chapter reports a toy-model simulation study on statistics needed for the estimation of cumulants. Such a study is important because the experiment runs for a limited time to collect finite event statistics, and the higher-order cumulants are known to be statistic-hungry observables. The simulation study obtains the minimum event statistics required for a proper estimation of net-proton cumulants up to the seventh order.

Chapter 3: Chapter 3 describes the STAR experiment at RHIC. It explains how heavy-ion collisions take place at the RHIC facility, and data used for analysis are recorded by the STAR detectors and its subsystems. The detectors relevant to the analysis, particularly those responsible for tracking charged particles produced in collisions and their identification, are discussed in detail. The underlying mechanisms used for particle identification are explained towards the end.

Chapter 4: This chapter describes the experimental details and technicalities related to net-proton cumulant measurement. First, it lists the collision energies, the corresponding value of μ_B , and the event statistics available for cumulant measurement. Then discussions are made on the selection of good events and good tracks from heavy-ion collisions, determination of collision centrality, and selection of protons and antiprotons. Methods for correcting the measurements for finite detector efficiency and volume fluctuation effects are presented towards the end.

Chapter 5: This is a dedicated chapter on the estimation of statistical and systematic uncertainties on net-proton cumulant measurements. Higher-order cumulants of a distribution are sensitive to the details of the distribution, especially its tails. A minute change in the distribution could change the higher-order cumulants considerably. Hence a careful estimation of uncertainties on cumulants is important. The estimation of statistical uncertainties using three methods is discussed, and the suitability of these methods is verified. Estimation of systematic uncertainties on the measurements arising out of variation in different sources is described.

Chapter 6: This is the main chapter pertaining to the goal of the thesis. To facilitate the study of QCD phase structure, measurement of net-proton cumulants up to sixth-order are presented for Au+Au collisions across a wide range of collision energies $\sqrt{s_{NN}} = 7.7 - 200$ GeV from STAR experiment. This range consists of nine collision energies in total. The experimental results are relevant to the following topics: the test of QCD thermodynamics in heavy-ion collisions, probing the QCD critical point, probing the crossover, and probing the first-order phase transition. The theoretical prediction for each of these topics is presented first, followed by the experimental results. Comparison of the experimental

results is carried out with a variety of models to draw physics inferences.

Chapter 7: This is the concluding chapter of the whole thesis work presented. It outlines the progress made towards the realization of the goal of the thesis work, i.e., to experimentally study the QCD phase diagram.

Chapter 8: This chapter provides the future prospects and outlook for the analysis reported in this thesis.

Bibliography

- [1] D. Solnyskhov and G. Malpuech. “Love might be a second-order phase transition”. *Phys. Lett. A* 445 (2022), 128245. arXiv: [2203.13246](https://arxiv.org/abs/2203.13246) [cond-mat].
- [2] <https://ch302.cm.utexas.edu/physEQ/physical>.
- [3] P. Papon, Jacques Leblond, and P.H.E. Meijer. *The physics of phase transitions: Concepts and applications*. Jan. 2006, pp. 1–409.
- [4] David J. Gross and Frank Wilczek. “Ultraviolet Behavior of Nonabelian Gauge Theories”. *Phys. Rev. Lett.* 30 (1973). Ed. by J. C. Taylor, 1343–1346.
- [5] D. J. Gross and Frank Wilczek. “Asymptotically Free Gauge Theories - I”. *Phys. Rev. D* 8 (1973), 3633–3652.
- [6] H. David Politzer. “Reliable Perturbative Results for Strong Interactions?” *Phys. Rev. Lett.* 30 (1973). Ed. by J. C. Taylor, 1346–1349.
- [7] Siegfried Bethke. “Experimental tests of asymptotic freedom”. *Prog. Part. Nucl. Phys.* 58 (2007), 351–386. arXiv: [hep-ex/0606035](https://arxiv.org/abs/hep-ex/0606035).
- [8] N. Cabibbo and G. Parisi. “Exponential Hadronic Spectrum and Quark Liberation”. *Phys. Lett. B* 59 (1975), 67–69.
- [9] A. Pandav, D. Mallick, and B. Mohanty. “Search for the QCD critical point in high energy nuclear collisions”. *Prog. Part. Nucl. Phys.* 125 (2022), 103960. arXiv: [2203.07817](https://arxiv.org/abs/2203.07817) [nucl-ex].

- [10] Kenji Fukushima and Tetsuo Hatsuda. “The phase diagram of dense QCD”. *Rept. Prog. Phys.* 74 (2011), 014001. arXiv: [1005.4814 \[hep-ph\]](#).
- [11] Frithjof Karsch. “Lattice results on QCD thermodynamics”. *Nucl. Phys. A* 698 (2002). Ed. by T. J. Hallman, D. E. Kharzeev, J. T. Mitchell, et al., 199–208. arXiv: [hep-ph/0103314](#).
- [12] R. C. Hwa and X. N. Wang, eds. *Quark-gluon plasma 3*. Singapore: World Scientific, 2004.
- [13] Frithjof Karsch. “Lattice QCD at nonzero chemical potential and the resonance gas model”. *Prog. Theor. Phys. Suppl.* 153 (2004). Ed. by H. Suganuma, N. Ishii, M. Oka, et al., 106–117. arXiv: [hep-lat/0401031](#).
- [14] R. V. Gavai and Sourendu Gupta. “The Critical end point of QCD”. *Phys. Rev. D* 71 (2005), 114014. arXiv: [hep-lat/0412035](#).
- [15] F. Karsch, E. Laermann, and A. Peikert. “The Pressure in two flavor, (2+1)-flavor and three flavor QCD”. *Phys. Lett. B* 478 (2000), 447–455. arXiv: [hep-lat/0002003](#).
- [16] Heng-Tong Ding, Frithjof Karsch, and Swagato Mukherjee. “Thermodynamics of strong-interaction matter from Lattice QCD”. *Int. J. Mod. Phys. E* 24.10 (2015), 1530007. arXiv: [1504.05274 \[hep-lat\]](#).
- [17] John Adams et al. “Experimental and theoretical challenges in the search for the quark gluon plasma: The STAR Collaboration’s critical assessment of the evidence from RHIC collisions”. *Nucl. Phys. A* 757 (2005), 102–183. arXiv: [nucl-ex/0501009](#).
- [18] Zhe Xu, Carsten Greiner, and Horst Stocker. “PQCD calculations of elliptic flow and shear viscosity at RHIC”. *Phys. Rev. Lett.* 101 (2008), 082302. arXiv: [0711.0961 \[nucl-th\]](#).
- [19] G. Ferini, M. Colonna, M. Di Toro, et al. “Scalings of Elliptic Flow for a Fluid at Finite Shear Viscosity”. *Phys. Lett. B* 670 (2009), 325–329. arXiv: [0805.4814 \[nucl-th\]](#).
- [20] Salvatore Plumari, Armando Puglisi, Maria Colonna, et al. “Shear viscosity and chemical equilibration of the QGP”. *J. Phys. Conf. Ser.* 420 (2013). Ed. by Bao-An Li and Joseph Natowitz, 012029. arXiv: [1209.0601 \[hep-ph\]](#).

- [21] Edward Shuryak. “Why does the quark gluon plasma at RHIC behave as a nearly ideal fluid?” *Prog. Part. Nucl. Phys.* 53 (2004). Ed. by A. Faessler, 273–303. arXiv: [hep-ph/0312227](#).
- [22] S. Voloshin and Y. Zhang. “Flow study in relativistic nuclear collisions by Fourier expansion of Azimuthal particle distributions”. *Z. Phys. C* 70 (1996), 665–672. arXiv: [hep-ph/9407282](#).
- [23] M. Maseara, G. Ortona, M. G. Poghosyan, et al. “Anisotropic transverse flow introduction in Monte Carlo generators for heavy ion collisions”. *Phys. Rev. C* 79 (2009), 064909.
- [24] Miklos Gyulassy and Larry McLerran. “New forms of QCD matter discovered at RHIC”. *Nucl. Phys. A* 750 (2005). Ed. by D. Rischke and G. Levin, 30–63. arXiv: [nucl-th/0405013](#).
- [25] J. Adams et al. “Azimuthal anisotropy at RHIC: The First and fourth harmonics”. *Phys. Rev. Lett.* 92 (2004). [Erratum: *Phys.Rev.Lett.* 127, 069901 (2021)], 062301. arXiv: [nucl-ex/0310029](#).
- [26] John Adams et al. “Particle type dependence of azimuthal anisotropy and nuclear modification of particle production in Au + Au collisions at $s(\text{NN})^{1/2} = 200\text{-GeV}$ ”. *Phys. Rev. Lett.* 92 (2004), 052302. arXiv: [nucl-ex/0306007](#).
- [27] C. Adler et al. “Elliptic flow from two and four particle correlations in Au+Au collisions at $s(\text{NN})^{1/2} = 130\text{-GeV}$ ”. *Phys. Rev. C* 66 (2002), 034904. arXiv: [nucl-ex/0206001](#).
- [28] S. S. Adler et al. “Elliptic flow of identified hadrons in Au+Au collisions at $s(\text{NN})^{1/2} = 200\text{-GeV}$ ”. *Phys. Rev. Lett.* 91 (2003), 182301. arXiv: [nucl-ex/0305013](#).
- [29] P. Huovinen and P. V. Ruuskanen. “Hydrodynamic Models for Heavy Ion Collisions”. *Ann. Rev. Nucl. Part. Sci.* 56 (2006), 163–206. arXiv: [nucl-th/0605008](#).
- [30] Paul Sorensen. “Evidence from Identified Particles for Active Quark and Gluon Degrees of Freedom”. *J. Phys. G* 32 (2006), S135–S141. arXiv: [nucl-ex/0701048](#).
- [31] B. I. Abelev et al. “Energy and system size dependence of phi meson production in Cu+Cu and Au+Au collisions”. *Phys. Lett. B* 673 (2009), 183–191. arXiv: [0810.4979 \[nucl-ex\]](#).

- [32] A. Adare et al. “ J/ψ Production vs Centrality, Transverse Momentum, and Rapidity in Au+Au Collisions at $\sqrt{s_{NN}} = 200$ GeV”. *Phys. Rev. Lett.* 98 (2007), 232301. arXiv: [nucl-ex/0611020](#).
- [33] Sourendu Gupta, Debasish Mallick, Dipak Kumar Mishra, et al. “Limits of thermalization in relativistic heavy ion collisions”. *Phys. Lett. B* 829 (2022), 137021.
- [34] Raimond Snellings. “Elliptic Flow: A Brief Review”. *New J. Phys.* 13 (2011), 055008. arXiv: [1102.3010 \[nucl-ex\]](#).
- [35] P. Kovtun, Dan T. Son, and Andrei O. Starinets. “Viscosity in strongly interacting quantum field theories from black hole physics”. *Phys. Rev. Lett.* 94 (2005), 111601. arXiv: [hep-th/0405231](#).
- [36] Chungsik Song and Volker Koch. “Chemical relaxation time of pions in hot hadronic matter”. *Phys. Rev. C* 55 (1997), 3026–3037. arXiv: [nucl-th/9611034](#).
- [37] Ralf Rapp and Edward V. Shuryak. “Resolving the anti-baryon production puzzle in high-energy heavy ion collisions”. *Phys. Rev. Lett.* 86 (2001), 2980–2983. arXiv: [hep-ph/0008326](#).
- [38] Johann Rafelski, Jean Letessier, and Giorgio Torrieri. “Strange hadrons and their resonances: A Diagnostic tool of QGP freezeout dynamics”. *Phys. Rev. C* 64 (2001). [Erratum: *Phys.Rev.C* 65, 069902 (2002)], 054907. arXiv: [nucl-th/0104042](#).
- [39] Shreyasi Acharya et al. “Evidence of rescattering effect in Pb-Pb collisions at the LHC through production of $K^*(892)^0$ and $\phi(1020)$ mesons”. *Phys. Lett. B* 802 (2020), 135225. arXiv: [1910.14419 \[nucl-ex\]](#).
- [40] M. J. Matison, A. Barbaro-Galtieri, M. Alston-Garnjost, et al. “Study of $K^+\pi^-$ scattering in the reaction $K^+p \rightarrow K^+\pi^-\Delta^{++}$ at $12\frac{\text{GeV}}{c}$ ”. *Phys. Rev. D* 9 (7 1974), 1872–1893.
- [41] Y. Aoki, G. Endrodi, Z. Fodor, et al. “The Order of the quantum chromodynamics transition predicted by the standard model of particle physics”. *Nature* 443 (2006), 675–678. arXiv: [hep-lat/0611014](#).
- [42] Yoichiro Nambu and G. Jona-Lasinio. “Dynamical Model of Elementary Particles Based on an Analogy with Superconductivity. 1.” *Phys. Rev.* 122 (1961). Ed. by T. Eguchi, 345–358.

- [43] Peter N. Meisinger and Michael C. Ogilvie. “Chiral symmetry restoration and $Z(N)$ symmetry”. *Phys. Lett. B* 379 (1996), 163–168. arXiv: [hep-lat/9512011](#).
- [44] Murray Gell-Mann and M Levy. “The axial vector current in beta decay”. *Nuovo Cim.* 16 (1960), 705.
- [45] Shinji Ejiri. “Canonical partition function and finite density phase transition in lattice QCD”. *Phys. Rev. D* 78 (2008), 074507. arXiv: [0804.3227 \[hep-lat\]](#).
- [46] L. Adamczyk et al. “Beam-Energy Dependence of the Directed Flow of Protons, Antiprotons, and Pions in Au+Au Collisions”. *Phys. Rev. Lett.* 112.16 (2014), 162301. arXiv: [1401.3043 \[nucl-ex\]](#).
- [47] Horst Stoecker. “Collective flow signals the quark gluon plasma”. *Nucl. Phys. A* 750 (2005). Ed. by D. Rischke and G. Levin, 121–147. arXiv: [nucl-th/0406018](#).
- [48] Z. Fodor and S. D. Katz. “Lattice determination of the critical point of QCD at finite T and μ ”. *JHEP* 03 (2002), 014. arXiv: [hep-lat/0106002](#).
- [49] Z. Fodor and S. D. Katz. “Critical point of QCD at finite T and μ , lattice results for physical quark masses”. *JHEP* 04 (2004), 050. arXiv: [hep-lat/0402006](#).
- [50] Saumen Datta, Rajiv V. Gavai, and Sourendu Gupta. “Quark number susceptibilities and equation of state at finite chemical potential in staggered QCD with $N_t=8$ ”. *Phys. Rev. D* 95.5 (2017), 054512. arXiv: [1612.06673 \[hep-lat\]](#).
- [51] Christian S. Fischer, Jan Luecker, and Christian A. Welzbacher. “Phase structure of three and four flavor QCD”. *Phys. Rev. D* 90.3 (2014), 034022. arXiv: [1405.4762 \[hep-ph\]](#).
- [52] Xian-yin Xin, Si-xue Qin, and Yu-xin Liu. “Quark number fluctuations at finite temperature and finite chemical potential via the Dyson-Schwinger equation approach”. *Phys. Rev. D* 90.7 (2014), 076006. arXiv: [2109.09935 \[hep-ph\]](#).
- [53] M. Asakawa and K. Yazaki. “Chiral Restoration at Finite Density and Temperature”. *Nucl. Phys. A* 504 (1989), 668–684.
- [54] O. Scavenius, A. Mocsy, I. N. Mishustin, et al. “Chiral phase transition within effective models with constituent quarks”. *Phys. Rev. C* 64 (2001), 045202. arXiv: [nucl-th/0007030](#).

- [55] Yoshitaka Hatta and Takashi Ikeda. “Universality, the QCD critical / tricritical point and the quark number susceptibility”. *Phys. Rev. D* 67 (2003), 014028. arXiv: [hep-ph/0210284](#).
- [56] N. G. Antoniou and A. S. Kapoyannis. “Bootstrapping the QCD critical point”. *Phys. Lett. B* 563 (2003), 165–172. arXiv: [hep-ph/0211392](#).
- [57] Wei-jie Fu, Jan M. Pawłowski, and Fabian Rennecke. “QCD phase structure at finite temperature and density”. *Phys. Rev. D* 101.5 (2020), 054032. arXiv: [1909.02991 \[hep-ph\]](#).
- [58] Philipp Isserstedt, Michael Buballa, Christian S. Fischer, et al. “Baryon number fluctuations in the QCD phase diagram from Dyson-Schwinger equations”. *Phys. Rev. D* 100.7 (2019), 074011. arXiv: [1906.11644 \[hep-ph\]](#).
- [59] Adam Miklos Halasz, A. D. Jackson, R. E. Shrock, et al. “On the phase diagram of QCD”. *Phys. Rev. D* 58 (1998), 096007. arXiv: [hep-ph/9804290](#).
- [60] A. Barducci, R. Casalbuoni, Giulio Pettini, et al. “Chiral phases of QCD at finite density and temperature”. *Phys. Rev. D* 49 (1994), 426–436.
- [61] Fei Gao and Jan M. Pawłowski. “QCD phase structure from functional methods”. *Phys. Rev. D* 102.3 (2020), 034027. arXiv: [2002.07500 \[hep-ph\]](#).
- [62] Fei Gao and Jan M. Pawłowski. “Chiral phase structure and critical end point in QCD”. *Phys. Lett. B* 820 (2021), 136584. arXiv: [2010.13705 \[hep-ph\]](#).
- [63] Renato Critelli, Jorge Noronha, Jacquelyn Noronha-Hostler, et al. “Critical point in the phase diagram of primordial quark-gluon matter from black hole physics”. *Phys. Rev. D* 96.9 (2017), 096026. arXiv: [1706.00455 \[nucl-th\]](#).
- [64] Rajiv V. Gavai and Sourendu Gupta. “Pressure and nonlinear susceptibilities in QCD at finite chemical potentials”. *Phys. Rev. D* 68 (2003), 034506. arXiv: [hep-lat/0303013](#).
- [65] Owe Philipsen. “Towards the chiral critical surface of QCD”. *Nucl. Phys. A* 830 (2009). Ed. by Paul Stankus, David Silvermyr, Soren Sorensen, et al., 713C–716C. arXiv: [0907.4668 \[hep-ph\]](#).
- [66] A. Bazavov et al. “Chiral crossover in QCD at zero and non-zero chemical potentials”. *Phys. Lett. B* 795 (2019), 15–21. arXiv: [1812.08235 \[hep-lat\]](#).

- [67] Sourendu Gupta, Xiaofeng Luo, Bedangadas Mohanty, et al. “Scale for the Phase Diagram of Quantum Chromodynamics”. *Science* 332 (2011), 1525–1528. arXiv: [1105.3934 \[hep-ph\]](#).
- [68] M. M. Aggarwal et al. “Higher Moments of Net-proton Multiplicity Distributions at RHIC”. *Phys. Rev. Lett.* 105 (2010), 022302. arXiv: [1004.4959 \[nucl-ex\]](#).
- [69] Misha A. Stephanov, K. Rajagopal, and Edward V. Shuryak. “Event-by-event fluctuations in heavy ion collisions and the QCD critical point”. *Phys. Rev. D* 60 (1999), 114028. arXiv: [hep-ph/9903292](#).
- [70] Masayuki Asakawa, Shinji Ejiri, and Masakiyo Kitazawa. “Third moments of conserved charges as probes of QCD phase structure”. *Phys. Rev. Lett.* 103 (2009), 262301. arXiv: [0904.2089 \[nucl-th\]](#).
- [71] M. A. Stephanov. “On the sign of kurtosis near the QCD critical point”. *Phys. Rev. Lett.* 107 (2011), 052301. arXiv: [1104.1627 \[hep-ph\]](#).
- [72] Jiunn-Wei Chen, Jian Deng, Hiroaki Kohyama, et al. “Robust characteristics of nongaussian fluctuations from the NJL model”. *Phys. Rev. D* 93.3 (2016), 034037. arXiv: [1509.04968 \[hep-ph\]](#).
- [73] <https://www.allaboutcircuits.com/technical-articles/understanding-the-normal-distribution-parametric-tests-skewness-and-kurtosis>.
- [74] <https://www.scribbr.com/statistics/kurtosis>.
- [75] R. V. Gavai and Sourendu Gupta. “Lattice QCD predictions for shapes of event distributions along the freezeout curve in heavy-ion collisions”. *Phys. Lett. B* 696 (2011), 459–463. arXiv: [1001.3796 \[hep-lat\]](#).
- [76] Frithjof Karsch and Krzysztof Redlich. “Probing freeze-out conditions in heavy ion collisions with moments of charge fluctuations”. *Phys. Lett. B* 695 (2011), 136–142. arXiv: [1007.2581 \[hep-ph\]](#).
- [77] P. Garg, D. K. Mishra, P. K. Netrakanti, et al. “Conserved number fluctuations in a hadron resonance gas model”. *Phys. Lett. B* 726 (2013), 691–696. arXiv: [1304.7133 \[nucl-ex\]](#).

- [78] Adam Bzdak, Shinichi Esumi, Volker Koch, et al. “Mapping the Phases of Quantum Chromodynamics with Beam Energy Scan”. *Phys. Rept.* 853 (2020), 1–87. arXiv: [1906.00936 \[nucl-th\]](#).
- [79] A. Bazavov et al. “Skewness, kurtosis, and the fifth and sixth order cumulants of net baryon-number distributions from lattice QCD confront high-statistics STAR data”. *Phys. Rev. D* 101.7 (2020), 074502. arXiv: [2001.08530 \[hep-lat\]](#).
- [80] Adam Bzdak and Volker Koch. “Mapping the QCD phase diagram with statistics friendly distributions”. *Phys. Rev. C* 100.5 (2019), 051902. arXiv: [1811.04456 \[nucl-th\]](#).
- [81] Peter Braun-Munzinger and Johanna Stachel. “The quest for the quark-gluon plasma”. *Nature* 448 (2007), 302–309.
- [82] A. Andronic, P. Braun-Munzinger, and J. Stachel. “Hadron production in central nucleus-nucleus collisions at chemical freeze-out”. *Nucl. Phys. A* 772 (2006), 167–199. arXiv: [nucl-th/0511071](#).
- [83] J. Cleymans, H. Oeschler, K. Redlich, et al. “Comparison of chemical freeze-out criteria in heavy-ion collisions”. *Phys. Rev. C* 73 (2006), 034905. arXiv: [hep-ph/0511094](#).
- [84] Enrico Fermi. “High-energy nuclear events”. *Prog. Theor. Phys.* 5 (1950), 570–583.
- [85] L. D. Landau. “On the multiparticle production in high-energy collisions”. *Izv. Akad. Nauk Ser. Fiz.* 17 (1953), 51–64.
- [86] Rolf Hagedorn. “The Long Way to the Statistical Bootstrap Model: 1994”. *NATO Sci. Ser. B* 346 (1995). Ed. by Johann Rafelski, 13–46.
- [87] Ramona Vogt. *Ultrarelativistic heavy-ion collisions*. Amsterdam: Elsevier, 2007.
- [88] Y. Hatta and M. A. Stephanov. “Proton number fluctuation as a signal of the QCD critical endpoint”. *Phys. Rev. Lett.* 91 (2003). [Erratum: *Phys.Rev.Lett.* 91, 129901 (2003)], 102003. arXiv: [hep-ph/0302002](#).
- [89] Masakiyo Kitazawa and Masayuki Asakawa. “Relation between baryon number fluctuations and experimentally observed proton number fluctuations in relativistic heavy ion collisions”. *Phys. Rev. C* 86 (2012). [Erratum: *Phys.Rev.C* 86, 069902 (2012)], 024904. arXiv: [1205.3292 \[nucl-th\]](#).

Chapter 2

Statistics needed for cumulant estimation: a simulation study

Higher order cumulants of event-by-event net-proton number distribution in heavy ion collisions have been deemed to be important observables in the study of QCD phase diagram [1–4]. Their sign, especially, is sensitive to the nature of the quark-hadron phase transition. For example, the sixth-order cumulants are expected to show negative sign near a crossover occurring at small or vanishing baryonic potential μ_B [5–8].

It is well known that the measurement of higher-order cumulants is statistically demanding. Since the running of heavy-ion collision experiments is bound by time and cost factors, one has a sample with a limited number of event statistics available for cumulant calculations. Higher-order cumulants obtained from a small sample may not provide a good estimation of the cumulants of the population. So it is always good to have a prior estimate on how much event statistics is required to measure any observable of interest (cumulants for our case) with good precision so that a clear physics conclusion could be extracted. Statistically speaking, the sample size should be sufficient to make inferences

about the cumulant of the population. Furthermore, such a study helps give an estimate of number of events required, hence the duration of data taking while planning for the beam user request. This was the case when the phase II of Beam Energy Scan program was proposed at RHIC.

Using Monte-Carlo simulation, we studied the effect of limited statistics on estimating higher order cumulants of event-by-event net-proton distributions within two statistical models: (A) where protons and antiprotons follow independent Poisson distributions and (B) where they follow independent Binomial distributions. We call these two Poissonian and Binomial models, respectively. The difference of proton and antiproton distribution is then used to obtain the net-proton distribution.

2.1 Poissonian model

We simulated net-proton distribution assuming proton and antiproton are Poisson distributed and independent of each other. The resulting distribution from the difference of two Poisson variates is called a Skellam distribution. A Poisson distribution has only one parameter. Input parameters for simulated net-proton distribution in this model are the experimentally measured means of proton and antiproton distributions from STAR experiment [9]. There are two choices of input parameters considered for this study.

- Case 1: $\mu_1 = 5.66$, $\mu_2 = 4.11$ (efficiency corrected mean of proton and antiproton measured at mid-rapidity for top 5% Au+Au collision at $\sqrt{s_{NN}} = 200$ GeV at STAR [9]).
- Case 2: $\mu_1 = 7.25$, $\mu_2 = 3.13$ (efficiency corrected mean of proton and antiproton measured at mid-rapidity for top 5% Au+Au collision at $\sqrt{s_{NN}} = 62.4$ GeV at STAR [9]).

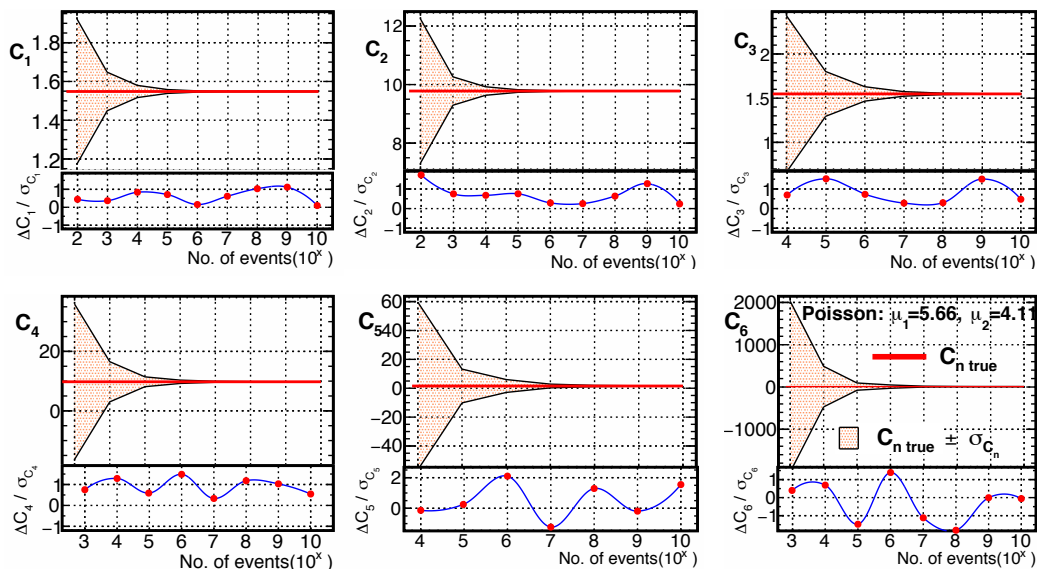


Figure 2.1: Cumulants of net-proton distribution up to sixth order presented as a function of event statistics [10]. The net-proton distribution is simulated as the difference of protons and antiprotons, which follow independent Poisson distributions. The experimental value of mean of proton ($\mu_1 = 5.66$) and antiproton ($\mu_2 = 4.11$) distributions in top 5% Au+Au collision at $\sqrt{s_{NN}} = 200$ GeV are taken as input parameters for the simulation. The orange band denotes the $\pm 1\sigma$ statistical uncertainties on cumulants. The solid red line is the true value of cumulants obtained analytically using the input parameters. The filled circle markers are the deviation of cumulants from their true value scaled by their statistical uncertainties.

Net-proton distribution following the Poissonian model was simulated with varying numbers of event statistics. The maximum size of the simulated sample is 10^{10} (10 billion events). The statistical uncertainties on the measurements were estimated using the Delta Theorem method (see chapter 5 for details of this method). With the information of input parameters at hand, the true cumulants or population's cumulants can be obtained analytically by applying the additive property of cumulants. A Poisson distribution has a special feature for cumulants: the cumulants of all order are exactly the same and equal to the mean. This makes the formulae for evaluating true cumulants of net-proton distribution

quite simple. They are given as follows;

$$C_{n_{odd}} = \mu_1 - \mu_2 \quad (2.1)$$

$$C_{n_{even}} = \mu_1 + \mu_2. \quad (2.2)$$

where $C_{n_{odd}}$ are odd orders cumulants (n_{odd} represents the orders: 1, 3, 5...), and $C_{n_{even}}$ are even-order cumulants (n_{even} represents the orders: 2, 4, 6...). Thus, for a Skellam distribution, the true value of all the odd-order cumulants are identical. The same also holds true for even-order cumulants.

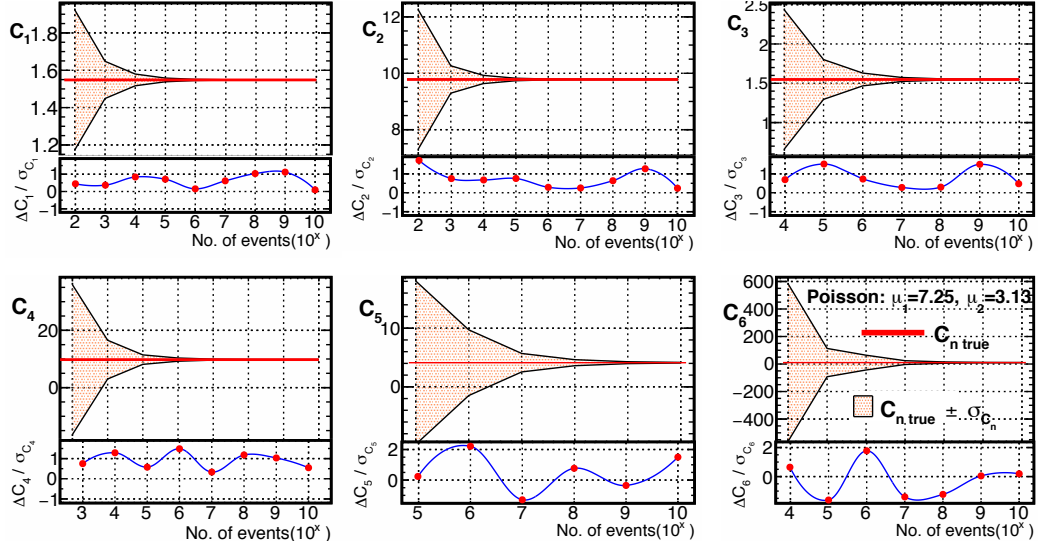


Figure 2.2: Cumulants of net-proton distribution up to sixth order presented as a function of event statistics [10]. The net-proton distribution is simulated as the difference of protons and antiprotons, which follow independent Poisson distributions. The experimental value of mean of proton ($\mu_1 = 7.25$) and antiproton ($\mu_2 = 3.13$) distributions in top 5% Au+Au collision at $\sqrt{s_{NN}} = 62.4$ GeV are taken as input parameters for the simulation. The orange band denotes the $\pm 1\sigma$ statistical uncertainties on cumulants. The solid red line is the true value of cumulants obtained analytically using input parameters. The filled circle markers are the deviation of cumulants from their true value scaled by their statistical uncertainties.

Cumulants of net-proton from the Poissonian model as a function of event statistics or sample size are presented for the two choices of input parameters: Fig. 2.1 for Case 1

and Fig. 2.2 for Case 2. For both cases, cumulants are seen to fluctuate randomly about the true value when the event statistics are small. With the increase in the number of events, the cumulants approach closer to the true values. The higher the order of cumulant, the more the statistics needed to converge towards the true value. Though theoretical calculations predict negative sign of C_5 and C_6 near a crossover quark-hadron transition, we find insufficient event statistics could also lead to their negative sign. But it is worth mentioning here that for the full range of sample size studied, the cumulants up to sixth order are mostly in agreement with their true value within $\sim 1\sigma$ statistical uncertainties.

2.2 Binomial model

In the Binomial model, net-proton distribution is simulated as the difference between proton and antiproton distributions where both proton and antiproton are assumed to be independent and Binomial distributed. A Binomial distribution has two parameters, the number of trials (n) and the probability of success (p). Input parameters required for simulating the net-proton distribution are the experimentally measured means and variance of proton and antiproton distributions from STAR experiment [9]. Like before, there are two choices of input parameters considered for Binomial model.

- Case 1: $\mu_{proton} = 5.66$, $\sigma_{proton}^2 = 5.58$, $\mu_{anti-proton} = 4.11$, $\sigma_{antiproton}^2 = 4.06$ (efficiency corrected mean and variance of proton distribution and antiproton, respectively, measured at mid-rapidity for top 5% Au+Au collision at $\sqrt{s_{NN}} = 200$ GeV at STAR [9]).
- Case 2: $\mu_{proton} = 7.26$, $\sigma_{proton}^2 = 7.06$, $\mu_{anti-proton} = 3.13$, $\sigma_{antiproton}^2 = 3.07$ (efficiency corrected mean and variance of proton distribution and antiproton, re-

spectively, measured at mid-rapidity for top 5% Au+Au collision at $\sqrt{s_{NN}} = 62.4$ GeV at STAR [9]).

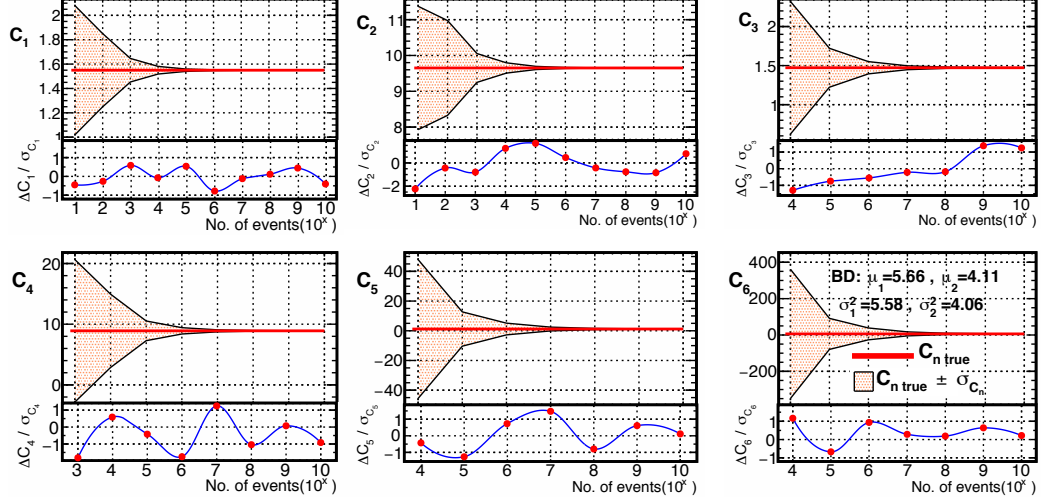


Figure 2.3: Cumulants of net-proton distribution up to sixth order presented as a function of event statistics [10]. The net-proton distribution is simulated as the difference of protons and antiprotons, which follow independent Binomial distributions. The experimental value of mean and variance of proton ($\mu_1 = 5.66$ and $\sigma_{proton}^2 = 5.58$) and antiproton ($\mu_2 = 4.11$ and $\sigma_{anti-proton}^2 = 4.06$) distributions in top 5% Au+Au collision at $\sqrt{s_{NN}} = 200$ GeV are taken as input parameters for the simulation. The orange band denotes the $\pm 1\sigma$ statistical uncertainties on cumulants. The solid red line is the true value of cumulants obtained analytically using input parameters. The filled circle markers are the deviation of cumulants from their true value scaled by their statistical uncertainties.

Net-proton distribution following the Binomial model was also simulated with different sample sizes. Like before, the maximum sample size studied is 10 billion events. Delta theorem method was used to estimate statistical uncertainties on the measurements. Since proton and antiproton are assumed to be independent, the true cumulants of net-proton distribution can be obtained analytically by applying the additive property of cumulants. An odd-order net-proton cumulant can be obtained as the difference of cumulants of proton and antiproton of the same order. An even-order net-proton cumulant is the sum of the cumulants of proton and antiproton of the same order. The following formulae show the

same.

$$C_{n_{odd}, net-proton} = C_{n_{odd}, proton} - C_{n_{odd}, antiproton} \quad (2.3)$$

$$C_{n_{odd}, net-proton} = C_{n_{odd}, proton} + C_{n_{odd}, antiproton} \quad (2.4)$$

Here, $C_{n_{odd}}$ and $C_{n_{even}}$ are odd and even order cumulants, respectively. For a Binomial distribution, cumulants up to the sixth order can be expressed using in terms of its parameters; the number of trials (n) and the probability of success (p) as follows:

$$\begin{aligned} C_1 &= np \\ C_2 &= np(1-p) \\ C_3 &= np(1-3p+2p^2) \\ C_4 &= np(1-7p+12p^2-6p^3) \\ C_5 &= np(1-15p+50p^2-60p^3+24p^4) \\ C_6 &= np(1-31p+180p^2-390p^3 \\ &\quad + 360p^4-120p^5). \end{aligned} \quad (2.5)$$

Fixing the first-order cumulant and second-order cumulant with the aforementioned input parameters from experimental data, n , and p are extracted. True values of higher-order net-proton cumulants can then be obtained using the equations 2.4 and 2.5.

Sample size dependence of cumulants of net-proton from the Binomial model is presented for the two choices of input parameters: Fig. 2.3 for Case 1 and Fig. 2.4 for Case 2. The observations are similar to what we made in the Poissonian model. Values of cumulants randomly fluctuate for smaller size of sample statistics, and the quality of agreement with true values improves by increasing the number of events in a sample. We find negative C_5 and C_6 for a few samples with low event statistics. However, in most of the cases, the cumulants agree with their true values within $\pm 1\sigma$ statistical uncertainties.

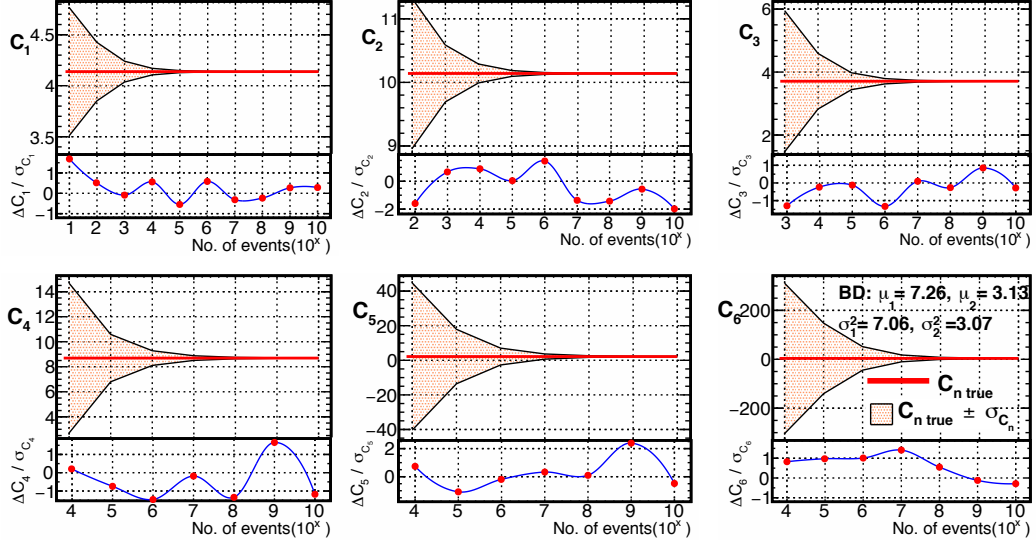


Figure 2.4: Cumulants of net-proton distribution up to sixth order presented as a function of event statistics [10]. The net-proton distribution is simulated as the difference of protons and antiprotons which follow independent Binomial distributions. The experimental value of mean and variance of proton ($\mu_{proton} = 7.26$ and $\sigma_{proton}^2 = 7.06$) and antiproton ($\mu_{anti-proton} = 3.13$ and $\sigma_{anti-proton}^2 = 3.07$) distributions in top 5% Au+Au collision at $\sqrt{s_{NN}} = 62.4$ GeV are taken as input parameters for the simulation. The orange band denotes the $\pm 1\sigma$ statistical uncertainties on cumulants. The solid red line is the true value of cumulants obtained analytically using input parameters. The filled circle markers are the deviation of cumulants from their true value scaled by their statistical uncertainties.

2.3 Limits on event statistics

As we noted in the previous section, increasing the event statistics in the simulated sample results in a better agreement of cumulants with their true values. We obtained the deviation of cumulants from their true value in terms of percentage. To do so, the absolute difference between the calculated cumulant and the true cumulant scaled by the true cumulant was evaluated first and then multiplied with 100. This was evaluated across the whole range of sample sizes studied. The sample size for which cumulants of various orders are within 5% agreement with their true values is presented in Fig. 2.5. The limits are presented for both the Poissonian model (panel A) and the Binomial model (panel B). They are the minimum

event statistics needed for the estimation of cumulants with a precision better than 5% of their true value. With increasing order of cumulants, the minimum event statistics needed also increases. There are some differences in the limiting events if the input parameters are varied, but they are of the same order in magnitude. Among various orders, we discuss here

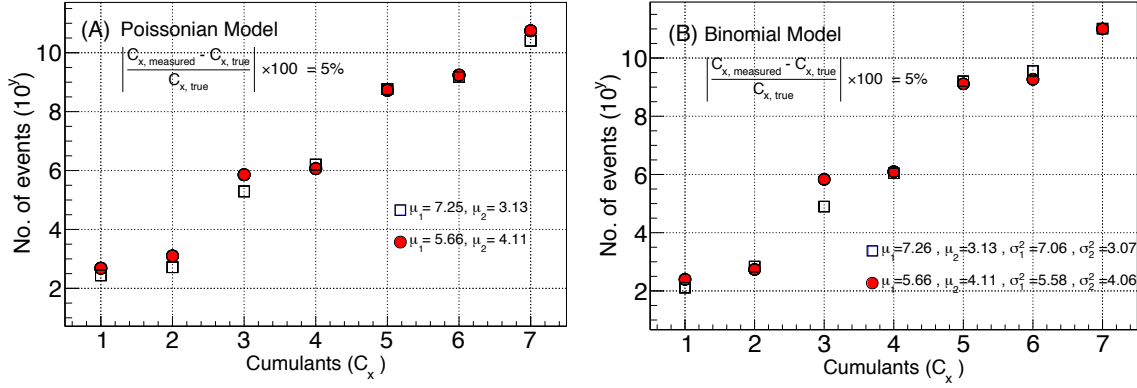


Figure 2.5: Minimum event statistics needed for estimation of net-proton cumulants from Poissonian model and Binomial model [10]. Net-proton distribution is simulated assuming both proton and antiprotons follow independent; (A): Poisson distributions and (B): Binomial distributions. There are two choices of input parameters considered for each of these models that are determined from experimental mean and/or variance of proton and antiproton distributions in top 5% Au+Au collisions at $\sqrt{s_{NN}} = 62.4$ GeV (open squares) and 200 GeV (filled circles).

the statistics needed for C_4 and C_6 measurements since they are very important observables in the study of QCD phase structure. Using the Poissonian model we find the estimation of C_4 (C_6) within a precision of 5% requires 1.2 million (1.5 billion) event statistics with input parameters taken from $\sqrt{s_{NN}} = 200$ GeV while they are found to be 1.6 million (1.5 billion) with input parameters from $\sqrt{s_{NN}} = 62.4$ GeV. From the Binomial model, we note that the measurement of C_4 (C_6) at a level of 5% precision demands 1.3 million (1.8 billion) events for the choice of input parameters from $\sqrt{s_{NN}} = 200$ GeV. Taking the inputs from $\sqrt{s_{NN}} = 62.4$ GeV also gives similar event statistic limits.

2.4 Effect of detection efficiency

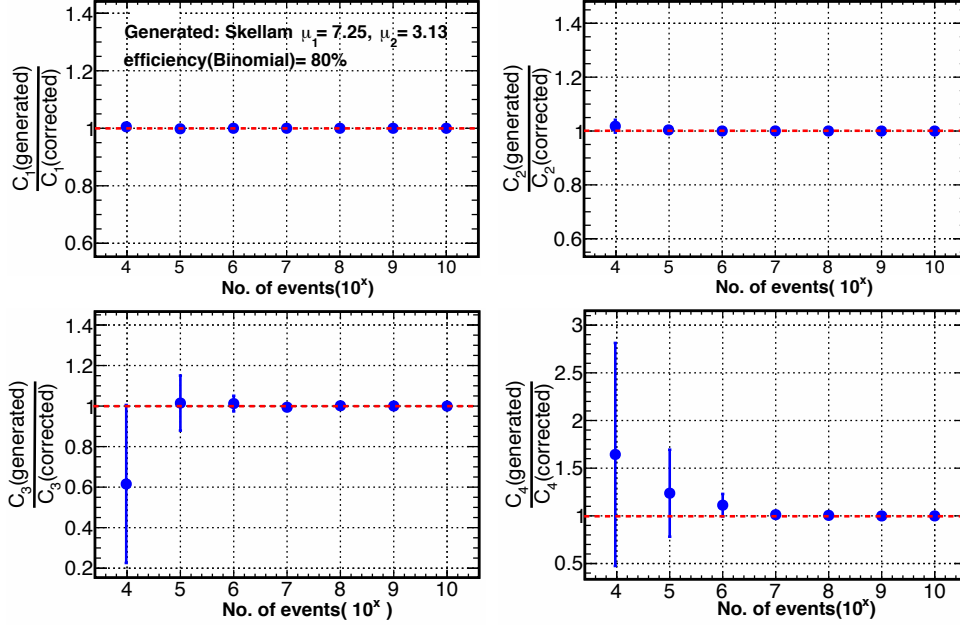


Figure 2.6: Ratio of cumulants of net-proton distribution at the generated level to those obtained after binomial efficiency correction is applied to the cumulants at the measured level (we call this corrected level) [10]. The study is performed with the Poissonian model for protons and antiprotons with mean $\mu_1 = 7.25$ and $\mu_2 = 3.13$, respectively.

The estimation of cumulants in experiments is also affected by detector efficiency. In this section, we show the results of studies on the effect of detector efficiency on the estimation of higher-order cumulants using a Monte Carlo toy model. We simulated net-proton distribution assuming proton and antiproton distributions are Poissonian with input parameters: $\mu_1 = 7.25$, $\mu_2 = 3.13$ (efficiency corrected mean of proton and antiproton distribution, respectively, measured at mid-rapidity for top 5% Au+Au collision at $\sqrt{s_{NN}} = 62.4$ GeV at STAR). We call the cumulants of the simulated distribution the cumulants at the generated level. To account for detection efficiency in real experiments, the generated Poisson distribution for proton and antiproton is then convoluted with a binomial distribution (with 80% efficiency). Taking the difference of proton and antiproton distribution, net-proton distri-

bution was constructed. We call this the net-proton distribution at the measured level. The cumulant of the net-proton distribution at the measured level is then corrected for efficiency effects using binomial efficiency correction method[11–13]. These are the cumulants at the corrected level. This procedure is performed for various event statistics up to a maximum of 10^{10} (10 billion). Cumulants of the net-proton distribution at the generated level and corrected level are compared for a range of event statistics in the Fig. 2.6. Their ratio for all orders presented agrees with unity within uncertainties, and the agreement improves with an increase in the event statistics. For a fixed value of event statistics, higher-order cumulants show a larger deviation from the generated level in comparison to lower-order cumulants. Although the efficiency effect further contributes to randomness in the estimation of cumulants, efficiency effects are negligible at the minimum event statistics limits presented in the previous section.

2.5 Summary

We now summarize the findings of the simulation study. The higher-order net-proton cumulants have been proposed as useful observables in the experimental study of the QCD phase diagram. For example, a negative sixth-order cumulant is expected near a crossover quark-hadron transition. Since the higher-order cumulants are statistic hungry and the experiments run only for a limited time, a prior estimate of the number of events needed for their proper measurement is important. This chapter reports a simulation study to obtain the minimum number of events needed for proper estimation of higher-order cumulants. Event-by-event net-proton distribution was simulated following two models: (A) Poissonian model; where protons and antiprotons followed independent Poisson distributions and (B) Binomial model; where protons and antiprotons followed independent

Binomial distributions. There are two choices of input parameters considered for each of these models that are determined from experimental mean and/or variance of proton and antiproton distributions in top 5% Au+Au collisions at $\sqrt{s_{NN}} = 62.4$ GeV and 200 GeV. With the information of the input parameters, the true value of the cumulants was obtained analytically. For both the models and choices of input parameters, cumulants are seen to fluctuate randomly about the true value when the event statistics are small. With the increase in the number of events, the cumulants approach closer to the true values. In our simulation, though there is no phase transition effect incorporated, C_4 , C_5 and C_6 were observed to be negative for a few event samples. The event statistics required for convergence towards the true value were also seen to increase with the order of cumulant. We then evaluated the deviation of calculated cumulants with respect to their true values to obtain the number of events needed for their proper estimation. With the assumption that any signal related to QCD phase structure is at a level of 5% above the statistical baseline, the minimum events statistics needed for accurate determination of cumulant of fourth (C_4) and sixth (C_6) order were found to be of the order 10^6 and 10^9 , respectively. A toy model study performed on the effects of finite detector efficiency suggests that these minimum statistics limits remain mostly unchanged. It is noteworthy to mention here that though the precision of agreement of cumulants with their true values is poorer with low event statistics and for a few low event samples, they showed negative values, the cumulants, irrespective of the sample sizes, are mostly consistent with their true values within 1σ of their respective statistical uncertainties. Hence a careful and proper estimation of statistical uncertainties on cumulants is very important.

Bibliography

- [1] Misha A. Stephanov, K. Rajagopal, and Edward V. Shuryak. “Event-by-event fluctuations in heavy ion collisions and the QCD critical point”. *Phys. Rev. D* 60 (1999), 114028. arXiv: [hep-ph/9903292](#).
- [2] Masayuki Asakawa, Shinji Ejiri, and Masakiyo Kitazawa. “Third moments of conserved charges as probes of QCD phase structure”. *Phys. Rev. Lett.* 103 (2009), 262301. arXiv: [0904.2089 \[nucl-th\]](#).
- [3] M. A. Stephanov. “On the sign of kurtosis near the QCD critical point”. *Phys. Rev. Lett.* 107 (2011), 052301. arXiv: [1104.1627 \[hep-ph\]](#).
- [4] Jiunn-Wei Chen, Jian Deng, Hiroaki Kohyama, et al. “Robust characteristics of nongaussian fluctuations from the NJL model”. *Phys. Rev. D* 93.3 (2016), 034037. arXiv: [1509.04968 \[hep-ph\]](#).
- [5] B. Friman, F. Karsch, K. Redlich, et al. “Fluctuations as probe of the QCD phase transition and freeze-out in heavy ion collisions at LHC and RHIC”. *Eur. Phys. J. C* 71 (2011), 1694. arXiv: [1103.3511 \[hep-ph\]](#).
- [6] Szabolcs Borsanyi, Zoltan Fodor, Jana N. Guenther, et al. “Higher order fluctuations and correlations of conserved charges from lattice QCD”. *JHEP* 10 (2018), 205. arXiv: [1805.04445 \[hep-lat\]](#).
- [7] A. Bazavov et al. “Skewness, kurtosis, and the fifth and sixth order cumulants of net baryon-number distributions from lattice QCD confront high-statistics STAR data”. *Phys. Rev. D* 101.7 (2020), 074502. arXiv: [2001.08530 \[hep-lat\]](#).
- [8] Wei-jie Fu, Xiaofeng Luo, Jan M. Pawłowski, et al. “Hyper-order baryon number fluctuations at finite temperature and density”. *Phys. Rev. D* 104.9 (2021), 094047. arXiv: [2101.06035 \[hep-ph\]](#).
- [9] L. Adamczyk et al. “Energy Dependence of Moments of Net-proton Multiplicity Distributions at RHIC”. *Phys. Rev. Lett.* 112 (2014), 032302. arXiv: [1309.5681 \[nucl-ex\]](#).
- [10] Ashish Pandav, Debasish Mallick, and Bedangadas Mohanty. “Effect of limited statistics on higher order cumulants measurement in heavy-ion collision experiments”. *Nucl. Phys. A* 991 (2019), 121608. arXiv: [1809.08892 \[nucl-ex\]](#).

- [11] Adam Bzdak and Volker Koch. “Acceptance corrections to net baryon and net charge cumulants”. *Phys. Rev. C* 86 (2012), 044904. arXiv: [1206.4286 \[nucl-th\]](#).
- [12] Xiaofeng Luo. “Unified description of efficiency correction and error estimation for moments of conserved quantities in heavy-ion collisions”. *Phys. Rev. C* 91.3 (2015). [Erratum: *Phys.Rev.C* 94, 059901 (2016)], 034907. arXiv: [1410.3914 \[physics.data-an\]](#).
- [13] Toshihiro Nonaka, Masakiyo Kitazawa, and ShinIchi Esumi. “More efficient formulas for efficiency correction of cumulants and effect of using averaged efficiency”. *Phys. Rev. C* 95.6 (2017). [Erratum: *Phys.Rev.C* 103, 029901 (2021)], 064912. arXiv: [1702.07106 \[physics.data-an\]](#).

Chapter 3

STAR experiment at RHIC

3.1 Introduction

To facilitate the experimental study of the QCD phase diagram, the STAR (Solenoidal Tracker at RHIC) experiment at the Relativistic Heavy-Ion Collider (RHIC) facility was designed at Brookhaven National Laboratory (BNL). It became operational in the year 2000, recording collisions of gold (Au^{79+}) nuclei at $\sqrt{s_{NN}} = 200$ GeV, which was the highest center-of-mass energy achieved by any experiment at that time. STAR is one of the four experiments situated at RHIC, the other three being the PHENIX [1], PHOBOS [2], and BRAHMS [3]. At present only STAR remains operational. PHENIX is undergoing a major upgrade to a new experiment called sPHENIX [4].

In this chapter, the RHIC collider facility, the STAR detector, and its sub-system (relevant to the analysis carried out in the thesis work) will be discussed. Since the analysis measures the fluctuation of net protons, clear particle identification in the experiment is an important step. The particle identification and tracking capabilities of the STAR detector will be discussed in particular.

3.2 The Relativistic Heavy-Ion Collider (RHIC) facility

The RHIC [5] is a versatile accelerator facility capable of accelerating a range of nuclei to ultra-relativistic speed. It belongs to the synchrotron type of particle accelerator, which accelerates the particles in a circular orbit by synchronized changing of electric and magnetic fields. The facility was initially designed to provide Au+Au collisions at $\sqrt{s_{NN}} = 200$ GeV and polarized p + p collisions at $\sqrt{s_{NN}} = 500$ GeV [6, 7]. Subsequently, accessing lower collision energy (down to $\sqrt{s_{NN}} = 7.7$ GeV in collider mode) also became possible, and Au+Au collisions were carried out over a range of center-of-mass energies in phase I of the BES program. The RHIC is the most versatile collider facility to date. It can accelerate ions of different species and provide collisions between asymmetric systems like p+A across a wide range of collision energies. It is the only facility to carry collision of polarized protons, which is relevant for studies related to proton spin [7]. RHIC ring has a circumference of approximately 3.8 km. An aerial view RHIC facility is shown in Fig.3.1.

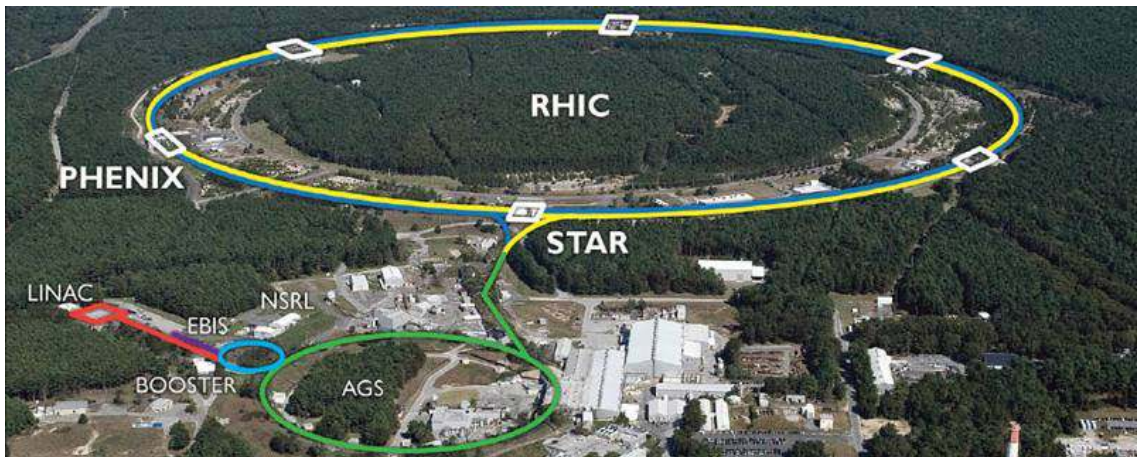


Figure 3.1: Aerial view of RHIC facility at Brookhaven National Laboratory. The figure is taken from Ref. [8].

Let's consider the case of the collision of gold nuclei. The acceleration of Au ions

happens in multiple steps at RHIC. A schematic diagram of the steps involved in the injection of the beam at RHIC is shown in Fig. 3.2. First, the ion source is needed. In the early days of RHIC, a cesium sputter ion source was used to produce negatively charged gold ions which were fed to a Tandem Van De Graaff [9]. By a two-stage acceleration of ions through a stripping foil in the Van De Graaff, a positively charged state of Au^{31+} with a kinetic energy of 1 MeV per nucleon is achieved. Since 2012, a more efficient ion source called the Electron-Beam Ion Source (EBIS) [10, 11] replaced the Tandem Van De Graaff. The EBIS provides the charged state of Au^{32+} by allowing electron beams to incident on the gas of gold and then accelerates the ions to a kinetic energy of 2 MeV per nucleon. The Au^{32+} ions are then transferred to Booster Synchrotron. In the Booster, the

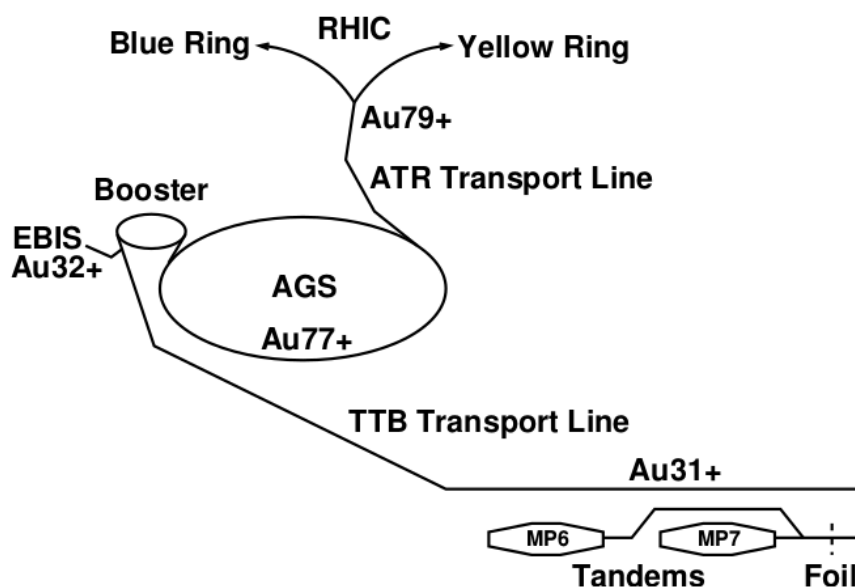


Figure 3.2: A schematic diagram of injection of ions to RHIC. The figure is taken from Ref. [8].

ions are accelerated to 95 MeV per nucleon and further stripped of electrons by passing through a stripping foil to a state of Au^{77+} before being fed to the Alternating Gradient Synchrotron (AGS). Ions from the Booster are filled in bunches to the AGS. From four

Booster cycles, twenty-four bunches are fed to the AGS, which are then debunched and rebunched to finally four bunches. Then they are accelerated to 8.86 GeV per nucleon. From AGS, en route to RHIC through the AGS-to-RHIC (ATR) transfer line, the bunches of ions are again passed through a stripping foil to remove the remaining two electrons to get to a state of Au^{79+} . At the end of this line, there is a point of diversion where a switching magnet sends the bunches to either left to follow a clockwise cycle in the RHIC ring or to the right for an anticlockwise cycle. The RHIC can act both as a storage ring as well as a particle accelerator. It consists of two independent storage/accelerator rings of superconducting magnets to accelerate and steer the ions: the blue ring, where ion bunches move in the clockwise direction, and the yellow ring, where it is anticlockwise. There are six interaction points along the RHIC ring where collisions of these bunches traveling in opposite directions can be performed. STAR is situated at one of the six interaction points. The RHIC can accelerate the ions to as high as 100 GeV per nucleon. Towards the lower energy, stable beams as low as 3.85 GeV per nucleon are possible. Collision of two gold beams from opposite ends, each with an energy of 100 GeV (3.85 GeV) per nucleon, would correspond to a center-of-mass energy of $\sqrt{s_{NN}} = 200$ GeV (7.7 GeV).

3.3 The STAR detector

The STAR [12] was designed to study the formation of the QGP and investigate its properties, thus aiding the understanding of the QCD phase diagram. The task meant that the aftermath of the collisions had to be meticulously recorded to be analyzed. As such, the measurements of hadron production over a wide acceptance, good tracking precision, and good particle identification were crucial. The STAR detector system convincingly accomplishes these requirements. The STAR detector consists of several sub-detector systems

which measure different quantities. A perspective view of the STAR detector system is shown in Fig 3.3. The detector is enclosed within a huge solenoidal magnet that generates

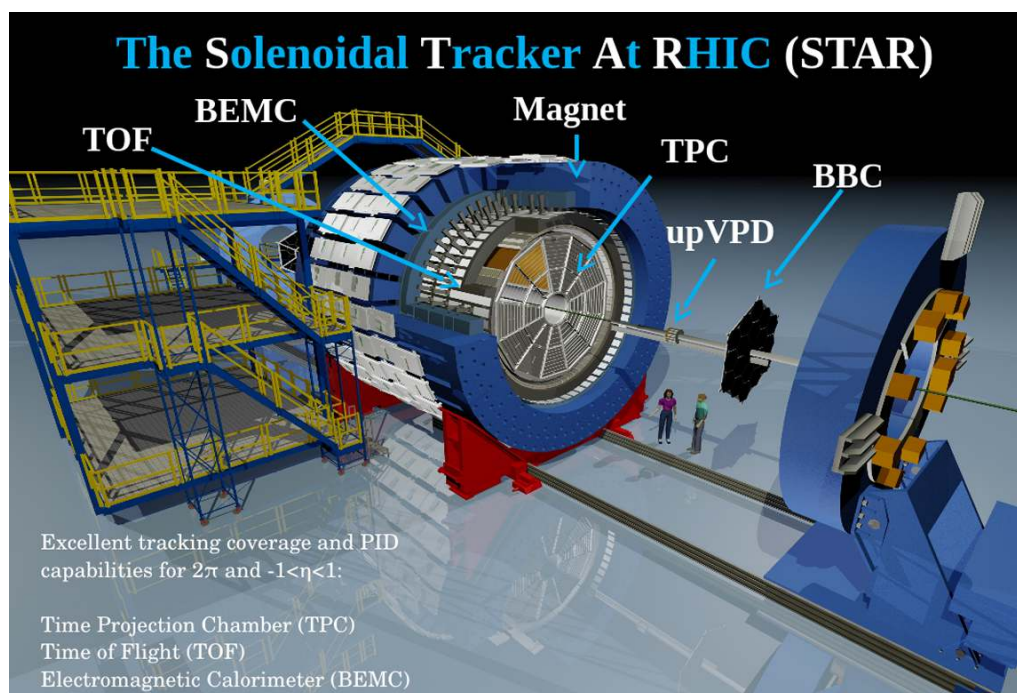


Figure 3.3: Perspective view of the STAR detector system. Figure adapted from Ref. [13].

a maximum magnetic field of 0.5 Tesla. The magnetic field is uniform and along the beam axis. The bending of charged particles under the influence of magnetic field is used to measure the momentum of the charged particle. Most of the sub-detectors have full azimuthal coverage. There are detectors like the Zero Degree Calorimeters (ZDCs), Beam-Beam Counter (BBCs), and Pseudo Vertex-position-detector (VPDs), which sit on opposite sides from the center of the detector and are used for triggering events. The trigger detectors are fast detectors that control the selection of events by triggering the slow detectors to record collision data. Two electromagnetic calorimeters are present, the Barrel Electromagnetic Calorimeter (BEMC) and the Endcap Electromagnetic Calorimeter (EEMC), to measure energy deposited by electrons and photons as they interact with matter. The heart

of the STAR detector is the Time-Projection-Chamber (TPC). TPC is used for tracking and particle identification. Particle identification is also provided by another detector called Time-Of-Flight (TOF). In this section, we will discuss the TPC and TOF detectors in more detail, explaining their role in particle identification.

3.3.1 The Time Projection Chamber: TPC

The TPC [14] is essentially a cylindrical volume of 4.2 m in length and 4 m diameter filled with P10 gas (90% Argon, 10% Methane). The argon is the primary source of ionization electrons, and being inert, it does not react with detector materials. Argon gas is extremely stable as well as relatively inexpensive, whereas Methane acts as a good absorber of energy. To prevent contamination from any potential leak, a pressure slightly above atmospheric pressure is maintained for the P10 gas. The TPC is the central element that surrounds the interaction vertex in addition to many other detectors. The TPC provides full azimuthal coverage around the beamline in the x-y plane. A central membrane divides it into two halves of drift chambers with a uniform electric field of strength 28 kV along the beam axis (z-axis). The central membrane acts as the cathode, and the end of the TPC connected to pad planes acts as the anode. Charged particles within ± 1.8 units of pseudo-rapidity (η) in the center-of-mass frame are tracked using the TPC. The 0.5 T magnetic field is also directed along the beam axis [15]. A schematic figure of the STAR TPC is shown as Fig 3.4. The P10 gas occupies the volume between two cylinders: inner and outer field cages. The radius of the inner field cage is 50 cm from the center of the STAR, and that of the outer field cage is about 200 cm. Each end of the TPC is divided into 12 sectors of trapezoidal shape. In each sector, there are multi-wire proportional chambers (MWPC), gating grids, and pad planes. The back of the pad planes is connected to readout electronics. The readout electronics for each of these sectors are facilitated by readout boards (RDOs)

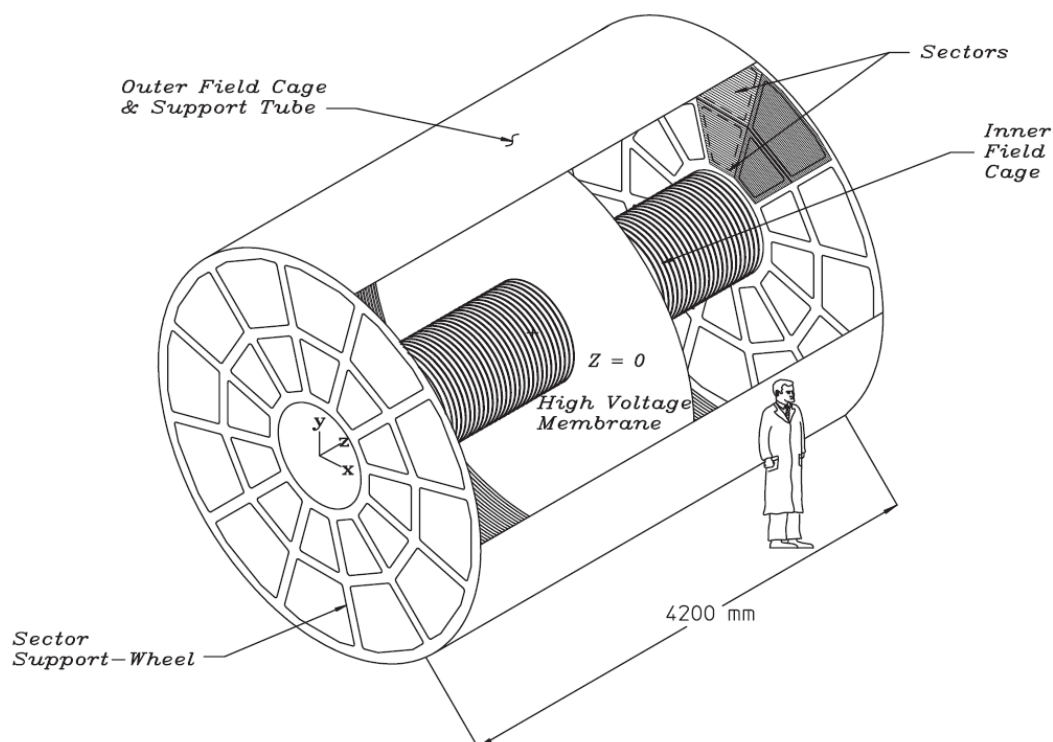


Figure 3.4: A schematic figure of the STAR TPC detector. Figure adapted from Ref. [14].

connected to Multi-Wire Proportional Chamber, which read from the front end electronic cards (FEEs). These FEE cards contain amplifiers, shapers, and digitizer circuits. The RDO boards multiplex the data to a single fiber that goes to the data acquisition (DAQ) system in the recording of an event.

The collision of ions leads to the production of charged particles. When these charged particles traverse through the TPC, they ionize the gas to electrons and positively charged ions. Under the influence of electric field, these clusters of ionized electrons drift toward the anode and get amplified due to the avalanche mechanism. The image charge formed at the anode pads is read out by the readout electronics. The pad plane of a sector of TPC is shown in Fig 3.5. Each sector is divided into inner sector and outer sector. While there are 13 pad rows in the inner sector, the outer sector has 32. This means each track could have

a maximum of 45 (13+32) hits along the pad rows.

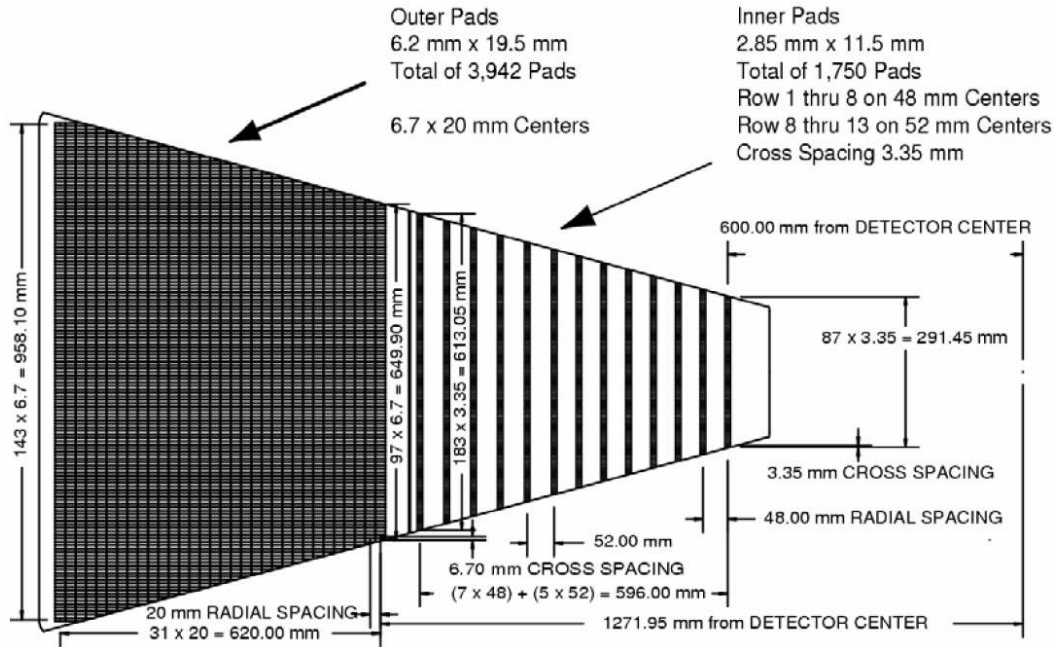


Figure 3.5: The layout of a TPC anode sector. The figure is taken from Ref. [14].

Due to the granular division of pad planes into pad rows, the x and y co-ordinate of ionization clusters are determined with good precision. Lasers are located at known positions around the TPC and are used to determine the TPC drift velocity. With the information of drift time of the ionization cluster to reach anode and drift velocity ($5.45 \text{ cm}/\mu\text{s}$), the z co-ordinate is obtained. After the co-ordinate of the ionization cluster is known, tracking software is used to reconstruct the track. The tracking clusters are fitted with helices to get information on momentum. The idea exploits the relation between the curvature of the trajectory followed by a charged particle under the influence of magnetic field and the strength of magnetic field. The direction of the bending of the charged particles allows the determination of the sign of the charged particle. Typical values for efficiency of reconstruction of proton (antiproton) tracks by the TPC within our analysis acceptance

ranged from 83% (81%) at $\sqrt{s_{NN}} = 7.7$ GeV to 62% (60%) at $\sqrt{s_{NN}} = 200$ GeV for top 5% Au+Au collisions.

Recently, the number of pad rows in each of the inner sectors of TPC were upgraded from 13 to 40 as part of inner-TPC or i-TPC upgrade for the phase II of Beam Energy Scan program. This upgrade extended the pseudo-rapidity coverage for measurements from $|\eta| < 1$ to $|\eta| < 1.6$. Considering 32 pad rows at the outer sector, a track now could have a maximum of 72 hits. Due to this significant increase in the number of hits available for reconstruction, especially from the inner sector, momentum resolution improved and lower momentum threshold was brought down from $p_T = 0.15$ GeV/c to 0.06 GeV/c.

3.3.2 The Time Of Flight Detector System

Though the TPC is used for particle identification at STAR, in the higher momentum region, this becomes a challenging task. For the higher momenta, the TOF system is used for the same. It consists of the Pseudo Vertex Position (VPD) [16] detectors and Time Of Flight (TOF) [17] detector. Together they measure the flight time of tracks.

Vertex Position Detector:VPD

Two VPD detectors sit outside the TPC, about 5.7m away on either side of the center of the TPC. They consist of very fast photomultipliers, which measure the forward photons from an event and determine the start time of the event. Their pseudo-rapidity coverage is $4.2 < \eta < 5.1$. In addition to determining the start time for each event, VPDs are also used to obtain the position of the event vertex along the beam axis.

Time of Flight:TOF

TOF detector has a cylindrical shell structure placed right outside of the TPC coaxial

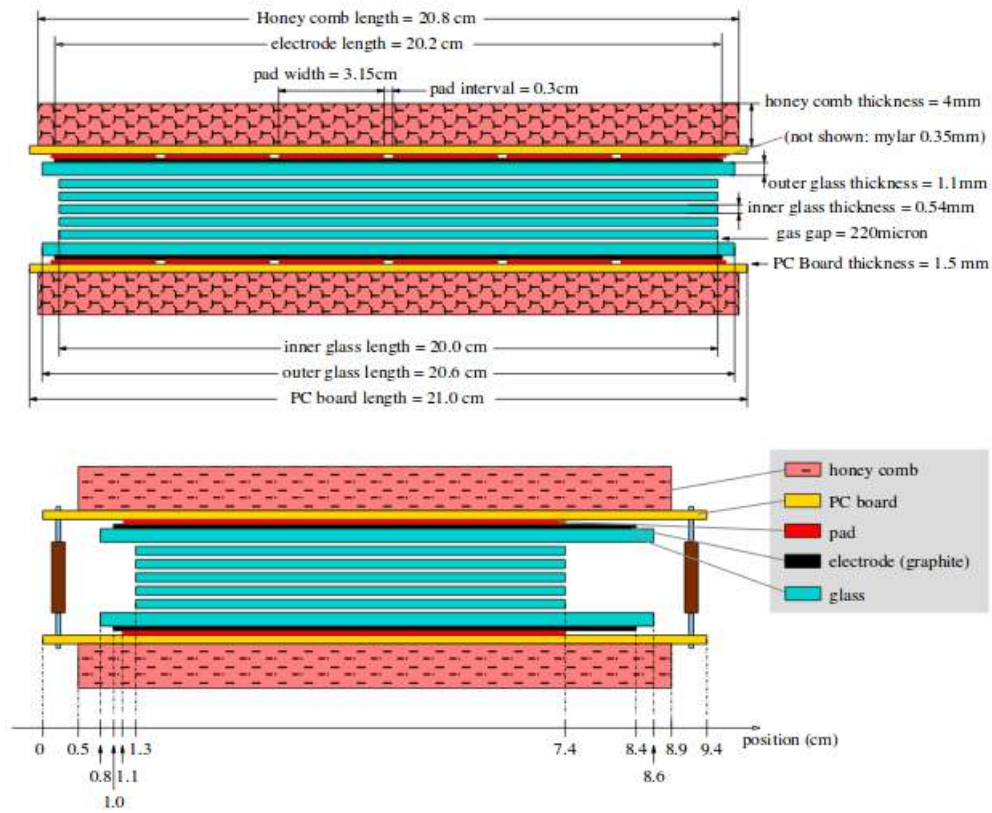


Figure 3.6: The internal layout of a TOF MRPC. Figure adapted from Ref. [18].

to it. The pseudo-rapidity coverage for the TOF is $|\eta| < 0.9$. TOF consists of 120 trays which together cover the full 2π azimuth. Each of these trays has 32 Multi-Gap Resistive Plate Chambers (MRPC) with readout pads. The internal layout of an MRPC is shown in Fig 3.6. These plates of MRPCs are placed between graphite electrodes. To generate a strong electric field, a high potential is applied across the electrodes. The gaps between the plates of MRPCs are filled with freon gas (mixture of 5% isobutane and 95% R-134a). Ionization of this gas takes place when a charged particle traverses the MRPCs. MRPCs obtain hits in the readout pads from the resulting electron avalanche. The readout pads have an area of $\approx 3.1 \times 6.1 \text{ cm}^2$. Each pad is separated from the other by a distance of 0.3 cm. This design of electronics and readout system delivers a timing resolution of

approximately 100 ps. The TOF essentially provides the "stop time" of the track. To match the hits recorded by TOF to the TPC hits, a matching algorithm is used. If a TPC track is associated with at least one hit in the TOF, it is called a TOF-matched track.

3.3.3 Particle identification (PID) using TPC and TOF

Since the energy loss of a charged particle is proportional to the electrons ionized by the charged particle, using proper calibration, the energy loss can be measured in TPC. The TPC uses the ionization energy loss mechanism of particles to identify them. The ionization energy loss is described by the Bethe-Bloch formula [19], given in equation 3.1.

$$\left\langle \frac{dE}{dx} \right\rangle = K z^2 \frac{Z}{A} \frac{1}{\beta^2} \left[\frac{1}{2} \log \frac{2m_e c^2 \beta^2 \gamma^2 T_{max}}{I^2} - \beta^2 - \frac{\delta(\beta\gamma)}{2} \right] \quad (3.1)$$

where

A = atomic mass of Absorber

Z = atomic number of Absorber

r_e = electron's radius

m_e = electron's mass

T_{max} = maximum energy transfer

I = mean excitation energy

$\delta(\beta\gamma)$ = Correction due to density effect

z = the atomic number of the incident particle.

The equation 3.1 shows that the deposition of kinetic energy by particles of different mass are different. Energy loss of charged particles in the P10 gas of the TPC was studied and found to be best described by the Bichsel curves [20]. Panel (a) of Fig 3.7 shows ionization energy loss $\langle dE/dx \rangle$ as a function of momentum over charge p/q measured by the TPC. The various bands in the $\langle dE/dx \rangle$ correspond to different particles, and they

are smeared around the theoretical expectation given by the Bichsel curves. A variable constructed from $\langle dE/dx \rangle$ information, called the $n\sigma$, is used to select identified particles. $n\sigma_X$ (where X corresponds to a particle) is defined as,

$$n\sigma_X = \frac{\log[(\langle dE/dx \rangle)_{measured}/(\langle dE/dx \rangle)_{theory}]}{\sigma_X}. \quad (3.2)$$

where $(\langle dE/dx \rangle)_{measured}$ is the measured ionization energy loss for the particle X and $(\langle dE/dx \rangle)_{theory}$ is the theory expectation from Bichsel formula for the particle. σ_X is the $\langle dE/dx \rangle$ resolution of the TPC. $n\sigma_X$ quantifies in terms of standard deviation, how much the measured values deviate from the theoretical predictions. With a $\langle dE/dx \rangle$ resolution of around 7 – 8%, TPC performs a good job in identifying charged particles in the low momentum region. However, in the high momentum region (around 1 GeV/c and above), the $\langle dE/dx \rangle$ bands begin to merge, and particles can no longer be identified solely with the TPC. Here, the TOF is used for PID.

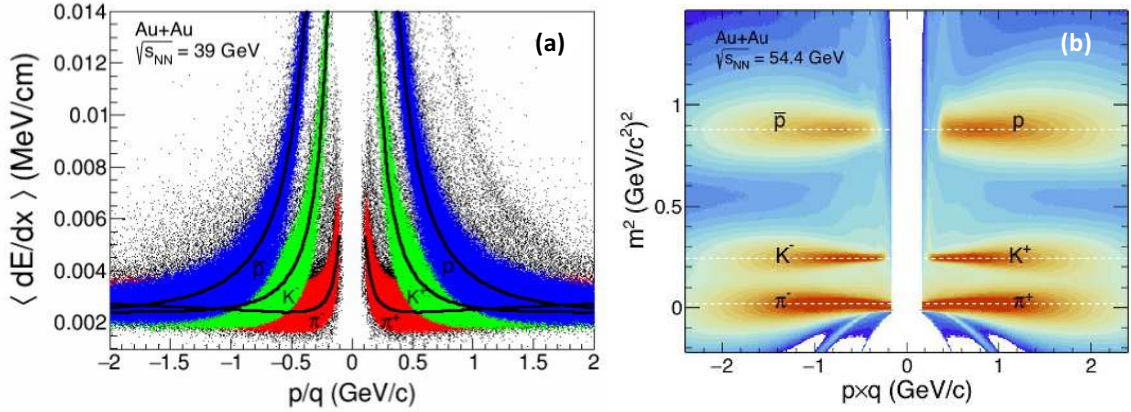


Figure 3.7: [Left panel (a)] $\langle dE/dx \rangle$ measured by TPC as a function of p/q in Au+Au collision at $\sqrt{s_{NN}} = 39$ GeV. The black lines are the Bichsel expectation for various charged particles. The figure is taken from Ref. [21]. [Right panel (b)] m^2 measured by TOF as a function of $p \times q$ for Au+Au collision at $\sqrt{s_{NN}} = 54.4$ GeV.

As we discussed earlier, the VPD detectors provide the start time. The TOF trays render the stop time of the tracks. The interval between these two times (Δt) is the flight time

of the track. Requiring the path length (L) from TPC, the velocity (β) of the track can be obtained as $\beta = \frac{L}{c\Delta t}$ (c is the speed of light). Taking the information on momentum p from TPC, mass-squared m^2 can be calculated using following relation.

$$\beta = \frac{p}{E} = \frac{p}{\sqrt{m^2 + p^2}} \quad (3.3)$$

$$m^2 = p^2 \left(\frac{(c\Delta t)^2}{L^2} - 1 \right) \quad (3.4)$$

As seen from the equation 3.4, for a fixed momentum and fixed path length, the heavier the particle, more is the time it takes to cover the path length. The measured mass-squared m^2 as a function of $p \times q$ is shown in panel (b) of Fig 3.7. As seen from the figure, the m^2 measurement show a clear separation of various charged particle even in the higher momentum region. The analysis reported in this thesis uses both TPC and TOF in the high momentum region ($0.8 < p_T < 2.0$ GeV/c) for selection of proton and antiproton tracks with better purity. Requirement of both the detectors in the higher momentum region introduces an addition efficiency related to matching of tracks between TPC and TOF detector (called the TOF matching efficiency). Typical values for TOF matching efficiency of proton (antiproton) tracks calculated within our analysis acceptance ranged from 72% (70%) at $\sqrt{s_{NN}} = 7.7$ GeV to 69% (68%) at $\sqrt{s_{NN}} = 200$ GeV for top 5% Au+Au collisions.

The purity of proton and antiproton sample considered for analysis is higher than 98% at all collision energies in the low momentum region ($0.4 < p_T < 8.0$ GeV/c) where only TPC was used for PID. With addition of TOF at the higher momentum region ($0.4 < p_T < 8.0$ GeV/c) purity above 97% is achieved.

Bibliography

- [1] K. Adcox et al. "PHENIX detector overview". *Nucl. Instrum. Meth. A* 499 (2003), 469–479.

- [2] M Adamczyk et al. “The BRAHMS experiment at RHIC”. *Nucl. Instrum. Meth. A* 499 (2003), 437–468.
- [3] B. B Back et al. “The PHOBOS detector at RHIC”. *Nucl. Instrum. Meth. A* 499 (2003), 603–623.
- [4] A. Adare et al. “An Upgrade Proposal from the PHENIX Collaboration” (Jan. 2015). arXiv: [1501.06197 \[nucl-ex\]](https://arxiv.org/abs/1501.06197).
- [5] M. Harrison, T. Ludlam, and S. Ozaki. “RHIC project overview”. *Nucl. Instrum. Meth. A* 499 (2003), 235–244.
- [6] L. C. Bland. “Spin physics at RHIC”. *AIP Conf. Proc.* 675.1 (2003). Ed. by Y. I. Makdisi, A. U. Luccio, and W. W. MacKay, 98–111. arXiv: [hep-ex/0212013](https://arxiv.org/abs/hep-ex/0212013).
- [7] M. Harrison, Stephen G. Peggs, and T. Roser. “The RHIC accelerator”. *Ann. Rev. Nucl. Part. Sci.* 52 (2002), 425–469.
- [8] <https://science.osti.gov/np/Facilities/User-Facilities/RHIC>.
- [9] D. B. Steski, J. Alessi, J. Benjamin, et al. “Operation of the Relativistic Heavy Ion Collider Au- ion source”. *Rev. Sci. Instrum.* 73 (2002). Ed. by Ka-Ngo Leung, 797–799.
- [10] James G. Alessi, E. N. Beebe, O. Gould, et al. “High Performance EBIS for RHIC”. *Conf. Proc. C* 070625 (2007). Ed. by C. Petit-Jean-Genaz, 3782.
- [11] Chris Gardner et al. “Operation of the RHIC Injector Chain with Ions from EBIS”. *6th International Particle Accelerator Conference*. 2015, THPF046.
- [12] K. H. Ackermann et al. “STAR detector overview”. *Nucl. Instrum. Meth. A* 499 (2003), 624–632.
- [13] *A. Schmah. Collaboration Communications.*
- [14] M. Anderson et al. “The Star time projection chamber: A Unique tool for studying high multiplicity events at RHIC”. *Nucl. Instrum. Meth. A* 499 (2003), 659–678. arXiv: [nucl-ex/0301015](https://arxiv.org/abs/nucl-ex/0301015).
- [15] F. Bergsma et al. “The STAR detector magnet subsystem”. *Nucl. Instrum. Meth. A* 499 (2003), 633–639.
- [16] W. J. Llope et al. “The TOFp/pVPD time-of-flight system for STAR”. *Nucl. Instrum. Meth. A* 522 (2004), 252–273. arXiv: [nucl-ex/0308022](https://arxiv.org/abs/nucl-ex/0308022).

- [17] B. Bonner, H. Chen, G. Eppley, et al. “A single Time-of-Flight tray based on multigap resistive plate chambers for the STAR experiment at RHIC”. *Nucl. Instrum. Meth. A* 508 (2003). Ed. by P. Fonte, M. Fraga, S. P. Ratti, et al., 181–184.
- [18] P Fachini et al. “Proposal for a Large Area Time of Flight System for STAR, STAR Note SN0621” (2004). <https://drupal.star.bnl.gov/STAR/files/tof-5-24-2004.pdf>.
- [19] C. Patrignani et al. “Review of Particle Physics”. *Chin. Phys. C* 40.10 (2016), 100001.
- [20] H. Bichsel. “A method to improve tracking and particle identification in TPCs and silicon detectors”. *Nucl. Instrum. Meth. A* 562 (2006), 154–197.
- [21] L. Adamczyk et al. “Bulk Properties of the Medium Produced in Relativistic Heavy-Ion Collisions from the Beam Energy Scan Program”. *Phys. Rev. C* 96.4 (2017), 044904. arXiv: [1701.07065 \[nucl-ex\]](https://arxiv.org/abs/1701.07065).

Chapter 4

Experimental analysis details and techniques

In this thesis work, the measurement of cumulants of event-by-event net-proton distributions up to sixth-order is performed with the goal to study the QCD phase structure. Au+Au collisions from a wide range of collision energies $\sqrt{s_{NN}} = 7.7 - 200$ GeV recorded by STAR detector at RHIC were analyzed. This chapter of the thesis describes the details and technicalities related to the analysis of recorded data. Figure 4.1 provides a flow chart briefing about the steps involved in the analysis. Item numbers 1, 2, and 3 of the flow chart will be covered in this chapter. Fourth item will be discussed in the Chapter 5. Chapter 6 and 7 will deal with fifth item of the flow chart.

4.1 Analysis details

This section briefs about the analysis-related details, such as the selection of good events and tracks for analysis, particle identification used for selecting protons and antiprotons, and the definition of collision centrality for geometry of collisions.

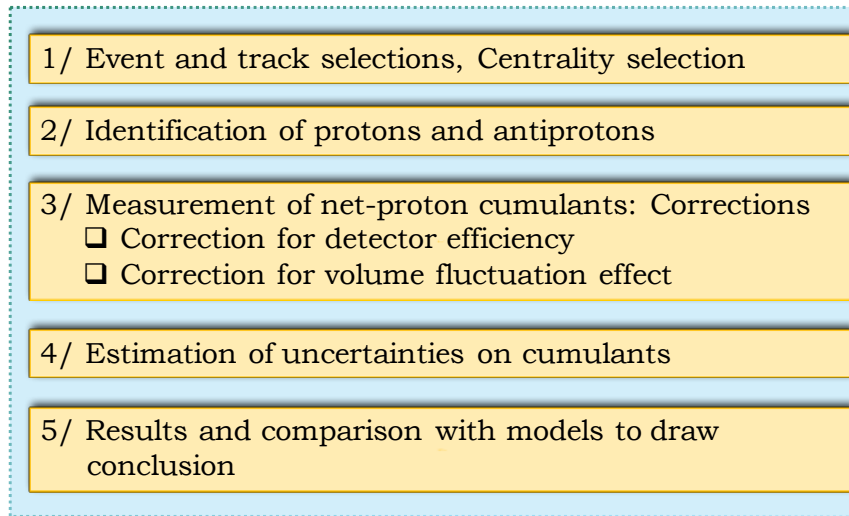


Figure 4.1: Analysis flow for net-proton fluctuation measurement.

4.1.1 Datasets

To measure net-proton fluctuations, Au+Au collisions at nine center-of-mass energies: $\sqrt{s_{NN}} = 7.7, 11.5, 14.5, 19, 27, 39, 54.4, 62.4,$ and 200 GeV recorded by the STAR experiment were analyzed. These nine collision energies constitute phase I of Beam Energy Scan (BES-I) at RHIC. The details of the data, such as the trigger Ids and production tag, event statistics are mentioned in the Table 4.1. The value of baryonic chemical potential (μ_B) at chemical freezeout obtained from Cleyman's parametrization [1] are also stated. The trigger Ids correspond to the minimum-bias condition. Minimum-bias events (as the name suggests, events with as little bias as possible) are those events where a coincidence of the signals from the zero-degree calorimeters (ZDCs), vertex position detectors (VPDs), and/or beam-beam counters (BBCs) situated at either side from the center of STAR detector is obtained [2–4]. The production tags are related to the software libraries used by STAR in the event reconstruction for various collision energies. As seen from the Table 4.1, these collision energies allow us to study the QCD phase diagram over a wide range of baryonic

Table 4.1: Center-of-mass collision energy, year, production tag, trigger Id used and μ_B at chemical freezeout from Cleymann's parametrization [1].

$\sqrt{s_{NN}}$ (GeV)	Year	Production Tag	Trigger Id	μ_B (MeV)
7.7	2010	P10ih	290001, 290004	420
11.5	2010	P10ih	310014	315
14.5	2014	P14ii	440005, 440015, 440006, 440016	264
19.6	2011	P11id	340001, 340011, 340021	206
27	2011	P11id	360001	156
39	2010	P10ih	280001	110
54.4	2017	P18ic	580001, 580021	83
62.4	2010	P10ik	270001, 270011, 270021	73
200	2010	P10ik	260001, 260011, 260021, 260031	24

chemical potential $\mu_B \sim 20 - 420$ MeV.

4.1.2 Event selection

Not all the recorded events (collision of nuclei) fulfill event quality criteria. The event selection criteria or cuts are imposed at all the collision energies to obtain good events, which are then analyzed in the realization of the physics goals. Here, we discuss the selection cuts employed in the analysis.

a) Run-by-run QA

The collection of events for a collision energy is done over several discrete time spans. Each of these time spans where the detector was continuously recording events is called a "run". We perform quality assurance (QA) checks for the selection of good runs. Each run consists of event and track information of the heavy-ion collisions recorded by the STAR detector. Averaged QA observables like $\langle Refmult \rangle$ (charged particle multiplicity at midrapidity measured by TPC), $\langle \phi \rangle$, $\langle p_T \rangle$, $\langle Tofmult \rangle$ (charged particle multiplicity at midrapidity measured by TOF), $\langle DCA \rangle$ (distance of closest approach of a track to

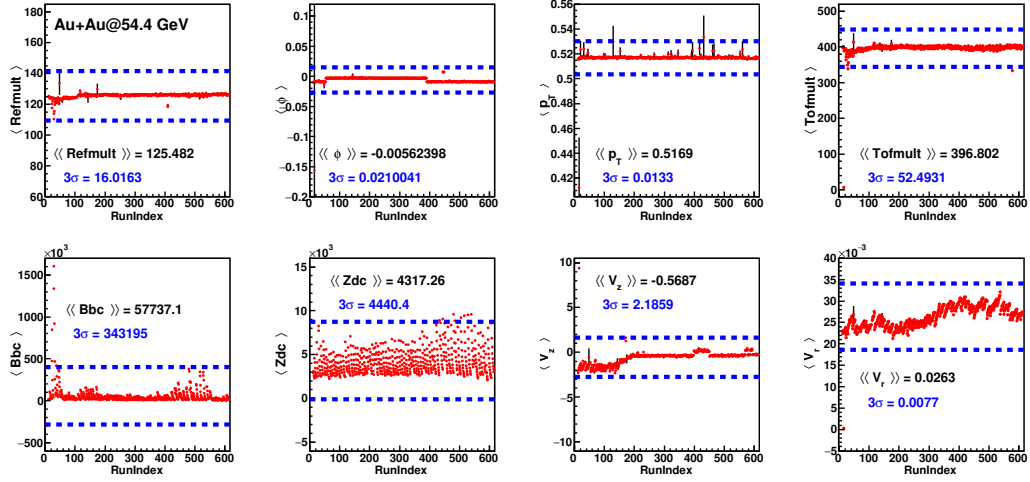


Figure 4.2: Bad run removal using 3σ outliers method on various QA observables for Au+Au collisions at $\sqrt{s_{NN}} = 54.4$ GeV. To avoid lengthy nomenclature of runs in the figure, each run shown in the x-axis is assigned an index (Run Index).

interaction point or primary vertex), $\langle V_z \rangle$ (z co-ordinate of the primary vertex), $\langle V_r \rangle$ ($V_r = \sqrt{V_x^2 + V_y^2}$, where V_x and V_y are the x and y co-ordinate of the primary vertex), $\langle BBC \rangle$ rates, $\langle ZDC \rangle$ rates, $\langle \eta \rangle$, etc., are calculated for each run. A plot with run-dependence of several QA observables is shown in Fig. 4.2. The averaged observable, say for e.g., $\langle p_T \rangle$, from all runs, forms a distribution defined by some global mean. The runs for which the averaged QA observables lie beyond $\pm 3\sigma$ away from their global means are identified as bad runs, and all the events from that run are removed from the analysis. This method is called the 3σ outliers method.

b) Signed DCA_{xy}

Even after performing the run-by-run QA to eliminate bad runs, it was found that there were a few runs that showed a strange variation of a quantity called the signed $\langle DCA_{xy} \rangle$ on an event-by-event basis. Here the average $\langle \rangle$ is over all tracks in an event. A plot on signed $\langle DCA_{xy} \rangle$ as a function of run time for one such run is shown in Fig. 4.3. It was

found that most of such runs were the runs taken just after the injection of the beam at RHIC, and mostly the early time of the run had unstable signed $\langle DCA_{xy} \rangle$. Signed DCA_{xy} is the projection of the three-dimensional DCA along the transverse plane where the sign is determined by its cross-product with momentum vector. This quantity was found to be particularly sensitive to the degradation of space charge calibration in the TPC. All the runs were scanned for this quantity, and runs or regions of a run, where it was unstable were removed from the analysis.

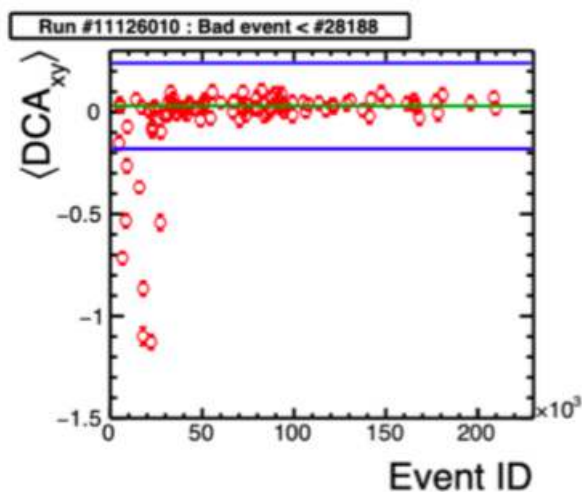


Figure 4.3: Signed $\langle DCA_{xy} \rangle$ as a function of run time (shown in x-axis as event id) for a run with unstable signed $\langle DCA_{xy} \rangle$ in its early phase. The green and blue lines represent the global mean and 5σ standard deviation, respectively.

c) Selection cuts on primary vertex

After the STAR TPC reconstructs the tracks produced in heavy-ion collisions, a vertexing algorithm is employed to extrapolate the reconstructed tracks to a common origin, known as the primary vertex. The x, y, and z co-ordinate of the primary vertex are labeled as (V_x, V_y, V_z) . For all of the collision energies reported in this analysis, the events are constrained to have V_z within ± 30 cm from the center of the TPC (except for $\sqrt{s_{NN}} = 7.7$

GeV, where it is ± 40 cm). This cut is optimized based on the competing needs of increasing

$\sqrt{s_{NN}}$ (GeV)	$ V_z $ (cm)	V_r (cm)	$ V_z - V_z(VPD) $ (cm)	Events (in millions)
7.7	< 40	< 2	–	2.2
11.5	< 30	< 2	–	6.8
14.5	< 30	< 1	–	14
19.6	< 30	< 2	–	14
27	< 30	< 2	–	31
39	< 30	< 2	< 3	92
54.4	< 30	< 2	< 3	550
62.4	< 30	< 2	< 3	43
200	< 30	< 2	< 3	230

Table 4.2: List of event cuts applied on primary vertex for each collision energy and the number of remaining good events. Note that at $\sqrt{s_{NN}} = 14.5$ GeV, $V_r < 1$ cm was applied since the beam pipe was narrower compared to other energies due to the installation of Heavy-Flavor tracker for that dataset [5].

event statistics and minimizing the change of detector acceptance and efficiency along the z-axis. The collection of events suffers immensely at low collision energies due to poor beam luminosity; hence $|V_z| < 40$ cm for $\sqrt{s_{NN}} = 7.7$ GeV was used to improve statistical precision. Further, the radial distance of vertex V_r from the z-axis ($V_r = \sqrt{V_x^2 + V_y^2}$) was required to be within 2 cm. This ensures collisions happening well within the beam pipe radius (which is 3 cm) are considered, and thus, any contamination from events originating from interaction with the beam pipe is avoided. Higher beam luminosity attained at high collision energies increases the chances of piling up of events. Pile-up happens if the measured multiplicity from an event has contributions from remnants of multiplicities from previous events. These undesired excesses of tracks in an event can misguide the track reconstruction, and subsequently, the vertex reconstruction algorithm followed by TPC to obtain the primary vertex. For collision energies $\sqrt{s_{NN}} \geq 39$ GeV, an additional constraint on z-vertex obtained using VPD detectors ($|V_z - V_z(VPD)| < 3$ cm) is used to suppress pile-up events. The applied vertex cuts for all collision energies and the number

of minimum bias events left after qualifying these selection cuts are listed in the table 4.2. Few representative plots for event selection using these cuts at $\sqrt{s_{NN}} = 54.4$ GeV are shown in the Figs. 4.4, 4.5, 4.6.

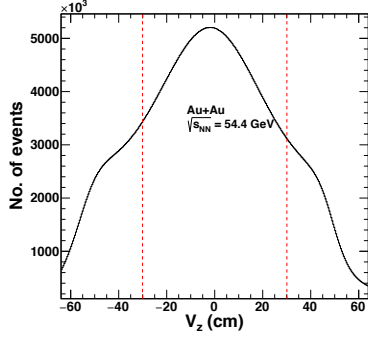


Figure 4.4: V_z distribution from Au+Au collisions at $\sqrt{s_{NN}} = 54.4$ GeV. Events enclosed by the red lines ($|V_z| < 30$ cm) are selected for analysis and the rest rejected.

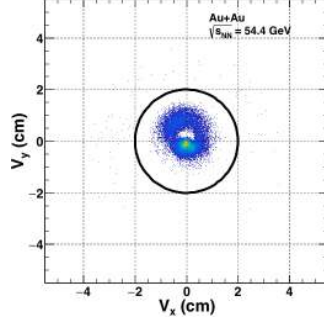


Figure 4.5: V_x vs. V_y from Au+Au collisions at $\sqrt{s_{NN}} = 54.4$ GeV. Events within the radius $\sqrt{V_x^2 + V_y^2} < 2$ cm shown by black circular line are selected for analysis.

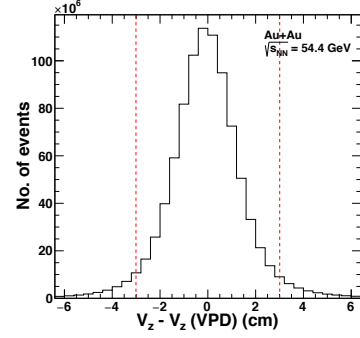


Figure 4.6: $V_z - V_z(VPD)$ distribution from Au+Au collisions at $\sqrt{s_{NN}} = 54.4$ GeV. Events enclosed by the red lines ($|V_z - V_z(VPD)| < 3$ cm) are selected for analysis.

d) Pile up event rejection

Due to the TPC drift time of $\sim 40\mu s$, it may be possible sometimes that all tracks from a single event are not collected by the TPC when the next event is triggered. Such events, which are actually two or more events reconstructed as a single event, are called pile-up events. This effect can artificially alter the real number of charged particles (including protons and antiprotons) in an event and thus affect the net-proton number fluctuation measurements. To remove pile up events, the correlation between the multiplicity registered at the TPC vs. the TOF detector is studied. The idea exploits the fact that TOF is a much faster detector than TPC. TOF with a timing resolution of ~ 100 ps sees much fewer track fragments from pile up compared to TPC. Figure 4.7 compares the number of charged

tracks measured by TPC with the number of TPC tracks that are matched to TOF detector (TOF matched tracks) in Au+Au collisions at $\sqrt{s_{NN}} = 54.4$ GeV. Pile-up events can be observed to fall off from an almost linear correlation band in the plot. By requiring that the TPC tracks and TOF-matched tracks follow a certain allowable correlation (for instance, $y > 0.46x - 10$, shown as the region above the red line in the figure), the pile-up events can be removed from the analysis. Such studies to remove pile-up events are carried out at all collision energies.

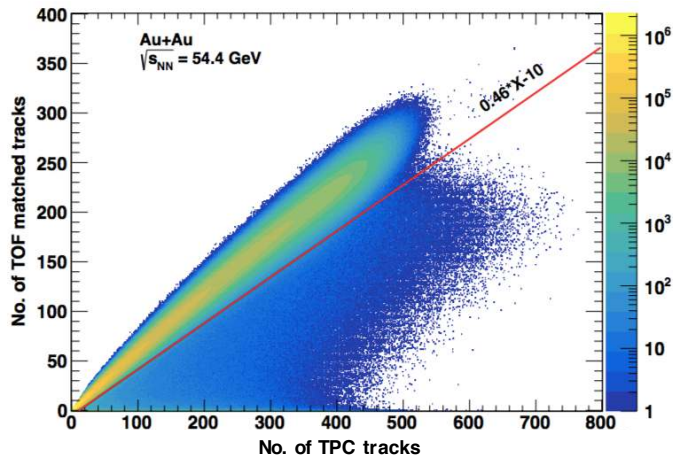


Figure 4.7: Number of TPC tracks vs. the number of TPC tracks matched to TOF in Au+Au collisions at $\sqrt{s_{NN}} = 54.4$ GeV. Events below the red line are identified as pile-up events and discarded from the analysis.

4.1.3 Track Selection

Selection criteria are also imposed on tracks to ensure good tracks for analysis. The selection cuts applied are as follows.

1. $DCA < 1$ cm
2. $nHitsFit > 20$

3. $n\text{HitsdEdx} > 5$

4. $n\text{HitsFit}/n\text{HitsPoss} > 0.52$

a) DCA (Distance of closest approach to primary vertex)

The DCA of a track is defined as its distance of closest approach to the primary vertex. The highly energetic particles produced in collisions (mostly pions) can interact with the detector apparatus, for e.g., the beam pipe made up of beryllium, and in the process, knock out some protons. These are called spallation protons. Since they are not produced from collisions, these proton tracks have large DCA with respect to the primary vertex. By requiring the DCA of tracks to be $\text{DCA} < 1$ cm, such protons are substantially suppressed. In addition, the applied DCA cut also helps in removing the tracks originating from the weak decays. With the $\text{DCA} < 1$ cm criterion in place, contamination from background protons are suppressed to less than 2-3% at $p_T \sim 0.4$ GeV/c and become negligible in the higher p_T region [6].

b) nHitsFit

In the reconstruction of tracks in the TPC, the hits points generated by the track as it traverses through the TPC gas are mapped along the TPC pad rows. These hit points are then fitted by the reconstruction algorithm, hence the name "nHitsFit points." Requiring a higher number of fit points improves the momentum resolution but, at the same time, also reduces the number of tracks. Tracks with more than 20 hit points, $n\text{HitsFit} > 20$, were chosen for analysis.

c) nHitsdEdx

Each hit on the TPC pads has an associated dE/dx measurement. The number of hit

points used in the calculation of the dE/dx of a track is called $nHitsdEdx$. As mentioned earlier, it is better to have more hits for dE/dx measurement, but not at the cost of losing too many tracks. There is a large fluctuation in ionization energy loss due to the short length over which energy loss is measured. This results in dE/dx being Landau distributed with a high-side tail. Hence, for the measurement of $\langle dE/dx \rangle$ in TPC, a truncated mean of dE/dx is used (30% of the ionization measurements are removed). For these reasons, a comparatively looser cut on $nHitsdEdx$, $nHitsdEdx > 5$, is used to select good tracks for analysis compared to $nHitsFit$.

d) $nHitsFit/nHitsPoss$

Sometimes in a reconstruction process, a real track could be reconstructed as two tracks due to improper association of hits in one region of the detector with those from another region. This effect is termed track splitting. Requiring the tracks to have a value of $nHitsFit$, such that $nHitsFit/nHitsPoss > 0.52$, such track splitting effects are suppressed. Here, $nHitsPoss$ is the possible number of hits a track could have based on its trajectory and is limited to a maximum value of 45 (this is the total number of pad rows available in the TPC for mapping hits).

4.1.4 Centrality determination

To study the system volume dependence of cumulants, events are classified into different centrality classes. Since the impact parameter (b) of collisions (defined as the distance between the geometrical centers of the colliding nuclei in the transverse plane) cannot be accessed directly, the centrality classification is based on the number of produced charged particle multiplicity in an event. Due to the strong correlation between the impact parameter and the number of produced charged particle multiplicity, the latter reflects

the initial geometry of colliding nuclei. A sketch diagram representing the geometry of

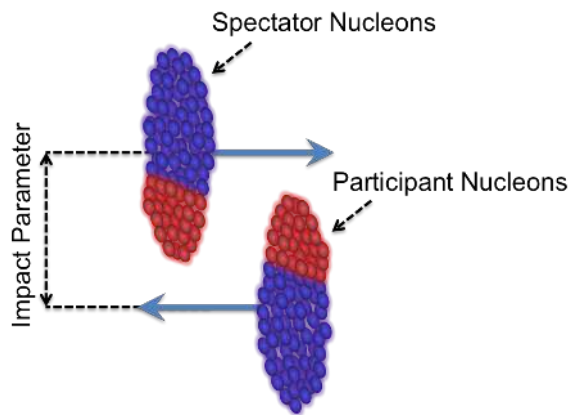


Figure 4.8: A sketch of the geometry of relativistic heavy-ion collision.

heavy-ion collisions is shown in Fig. 4.8. Only for head-on ($b = 0$) collisions, there is a complete overlap of the two nuclei, and all nucleons undergo collisions. But in most events, b has some nonzero value, and a partial overlap is possible. These overlapping nucleons participate in the collisions and are called participant nucleons. The rest are called spectator nucleons.

In the net-proton fluctuation analysis, a special kind of charged particle multiplicity, called Refmult3, is used to define centrality. Refmult3 distribution from all collision energies, $\sqrt{s_{NN}} = 7.7 - 200$ GeV, are shown in the Fig. 4.9. Refmult3 is essentially the number of charged particles in an event measured within η coverage of $|\eta| < 1$ excluding protons and antiprotons (proton and antiproton tracks are removed by requiring $n\sigma_{proton} < -3$, please refer to subsection 3.3.3 of chapter 3). Since the observable of interest is net-proton cumulants, the protons and antiprotons are excluded from the centrality definition to account for any self-correlation effect.

To obtain the geometrical quantities like the impact parameter, the number of participant nucleons (N_{part}), and the number of binary collisions (N_{coll}), the experimentally obtained

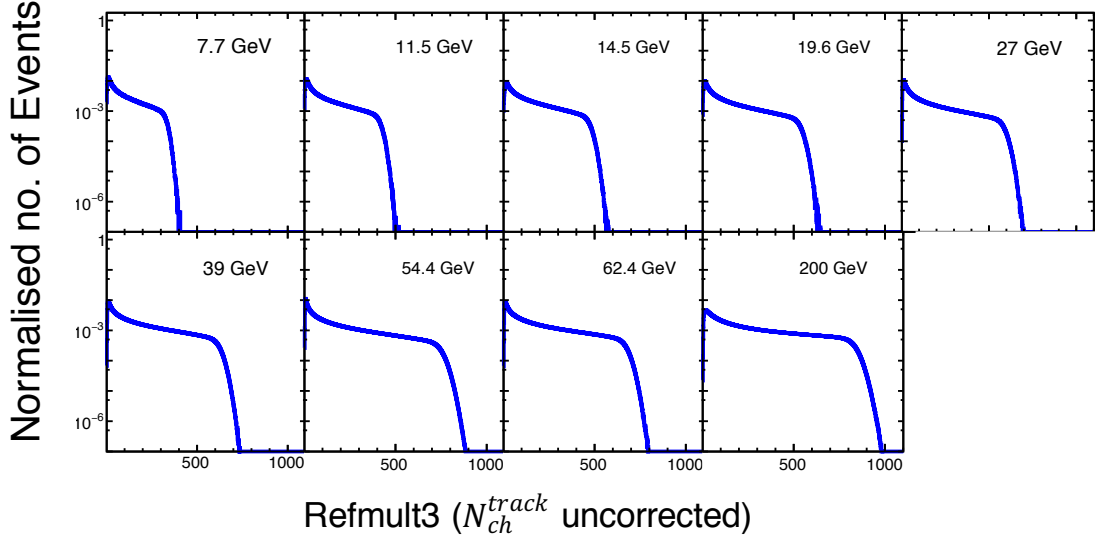


Figure 4.9: Normalized Refmult3 distributions from Au+Au collisions at $\sqrt{s_{NN}} = 7.7 - 200$ GeV.

charged particle multiplicity is mapped with Glauber Monte-Carlo (Glauber MC) model [7]. In the Glauber model, nucleons inside a nucleus are distributed following the Wood-Saxon probability density distribution [8]. They are then translated to collide by assigning a random impact parameter. The separation between the centers of nucleons is calculated. If this separation is less than $\sqrt{\sigma_{inel}^{NN}/\pi}$ (where σ_{inel}^{NN} is the inelastic nucleon-nucleon cross-section), the nucleons are said to undergo a binary collision. Nucleons that have undergone at least one binary collision are said to be participant nucleons. The value of σ_{inel}^{NN} for certain energy is obtained by fitting the pp total and inelastic cross-section obtained from PDG [9] (shown in Fig. 4.10) and then subtracting $\sigma_{elastic}^{pp}$ from σ_{total}^{pp} with the assumption that $\sigma_{inel}^{NN} = \sigma_{inel}^{pn} = \sigma_{inel}^{pn} = \sigma_{inel}^{pp}$.

Though the Glauber model can calculate the number of binary collisions (N_{coll}) and the number of participants (N_{part}), it requires a particle production model to be able to map with experimental data, i.e., Refmult3. Two Component Model is employed for particle

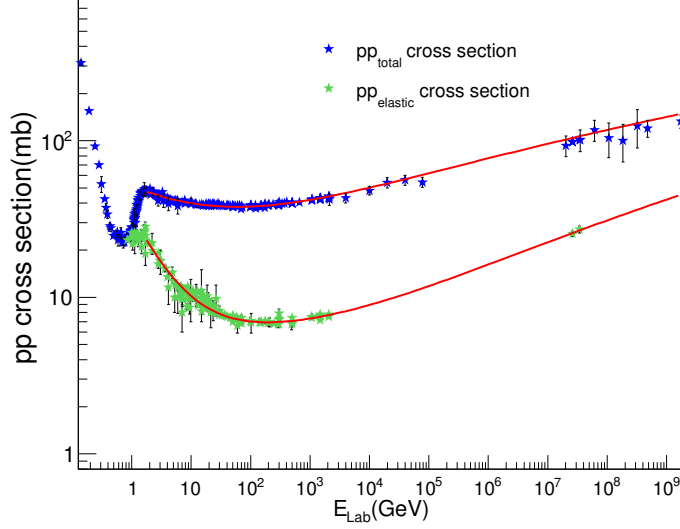


Figure 4.10: pp scattering cross section as a function of collision energy in the lab frame, E_{Lab} [9]. Red lines represent fit to data.

production [10]. Assuming that particle production is governed by contribution from soft component ($\propto N_{part}$) and hard component ($\propto N_{coll}$), it simulates the charged particle multiplicity ($\frac{dN_{ch}}{d\eta}$) distribution according to the following equation,

$$\frac{dN_{ch}}{d\eta} = n_{pp} \left((1-x) \frac{N_{part}}{2} + x N_{coll} \right) \quad (4.1)$$

where, x is the contribution arising from hard component, n_{pp} is the multiplicity from a pp collision of the same center-of-mass energy. UA5 collaboration had investigated the multiplicity distributions of pp collisions and found them to be well described by negative binomial distributions (NBD) [11]. Hence, n_{pp} in equation 4.1 is drawn randomly from an NBD distribution with parameters NBD ($n_{pp}; \langle n_{pp} \rangle, k$), where $\langle n_{pp} \rangle$ is the average multiplicity from pp collision and k is the width of the distribution. The simulated multiplicity distribution is then fitted with the experimentally obtained Refmult3. $\langle n_{pp} \rangle$, k , and x are kept as free parameters in the fitting. A Glauber MC fit to the Refmult3 distribution in Au+Au collisions in $\sqrt{s_{NN}} = 54.4$ GeV is shown in Fig. 4.11. Unlike

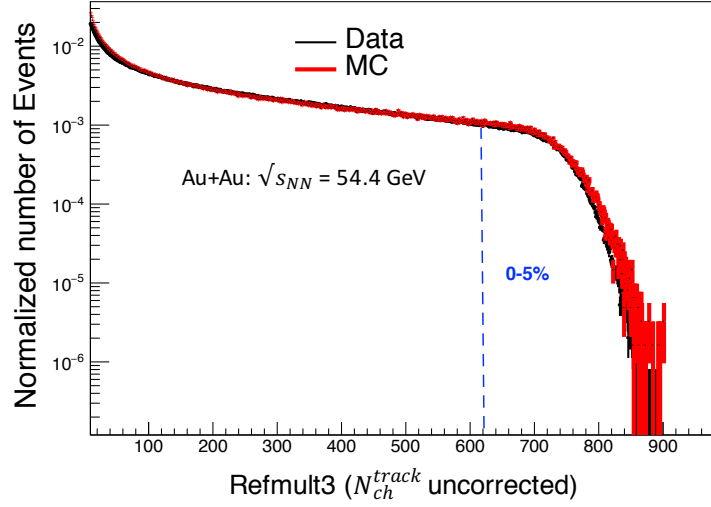


Figure 4.11: Refmult3 (black line) from Au+Au collisions at $\sqrt{s_{NN}} = 54.4$ GeV fitted with Glauber MC model (red line). Distributions are normalized. The blue dashed line represents the centrality cut for 0-5% collisions.

the measured Refmult3, the simulated Refmult3 does not suffer from trigger inefficiency due to very low number of produced charged particles (note from the Fig. 4.11 that the measured Refmult3 distribution at very small values is lower compared to the simulated distribution). Hence, the simulated multiplicity distribution is used to obtain cuts on the value of multiplicity which correspond to different centrality classes, for e.g., the top 5%, 5-10%, 10-20%, etc. of the distribution. Since each of the simulated Glauber events has information on geometric quantities, their averages, such as $\langle N_{part} \rangle$ and $\langle N_{coll} \rangle$ across a centrality class, can be readily obtained.

4.1.5 Proton acceptance and identification

Protons and antiprotons are identified using TPC [12] and TOF [13] detectors. They are selected at mid-rapidity ($|y| < 0.5$) within a momentum range $p_T = 0.4 - 2$ GeV/c. The choice of rapidity range ensures uniform acceptance and efficiency of the detector for the proton tracks. The lowest momentum threshold, $p_T = 0.4$ GeV/c, is selected in order to

suppress the contamination from spallation protons. The higher end of the p_T cut, $p_T = 2.0$ GeV/c, is considered such that the mean p_T of the protons is well within the p_T acceptance reach, also keeping in mind that the hard protons are avoided. Figure 4.12 represents the region of kinematic phase space where the protons and antiprotons are selected for analysis.

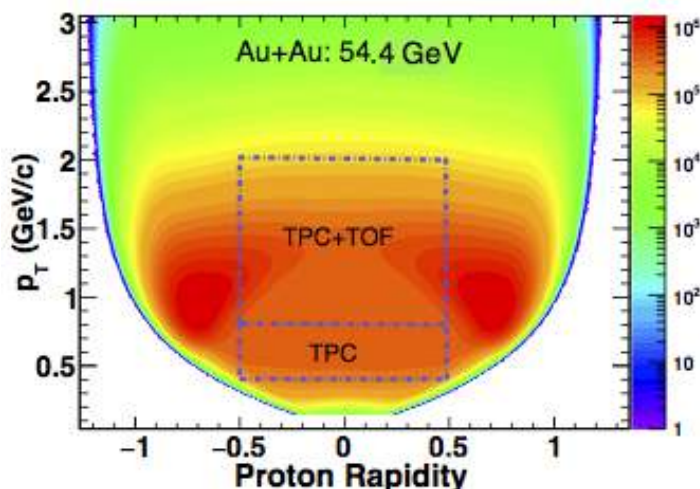


Figure 4.12: Proton phase-space acceptance shown in terms of transverse momentum (p_T) vs. rapidity (y) from Au+Au collisions at $\sqrt{s_{NN}} = 54.4$ GeV. The blue box is the region where protons and antiprotons are selected.

Identification in the momentum range $p_T = 0.4 - 0.8$ GeV/c is done with only the TPC. In the higher momentum range $p_T = 0.8 - 2$ GeV/c, both TPC and TOF are used for better purity. When using the TPC, protons are identified using the ionization energy loss ($\langle dE/dx \rangle$) measurements. As seen from Fig. 4.13, there is a separation of various charged particles based on their $\langle dE/dx \rangle$. Recall from the discussion in subsection 3.3.3 of chapter 3, we defined a quantity called $n\sigma_{proton}$, which evaluates the deviation of measured $\langle dE/dx \rangle$ from theoretical calculations in terms of the number of standard deviations. It

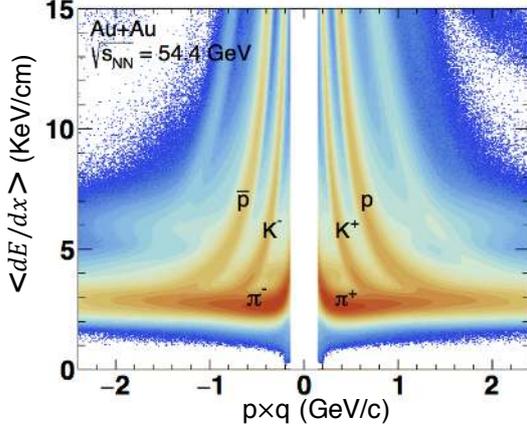


Figure 4.13: Ionization energy loss ($\langle dE/dx \rangle$) deposited by various charged particles in TPC for Au+Au collisions at $\sqrt{s_{NN}} = 54.4$ GeV vs. momentum.

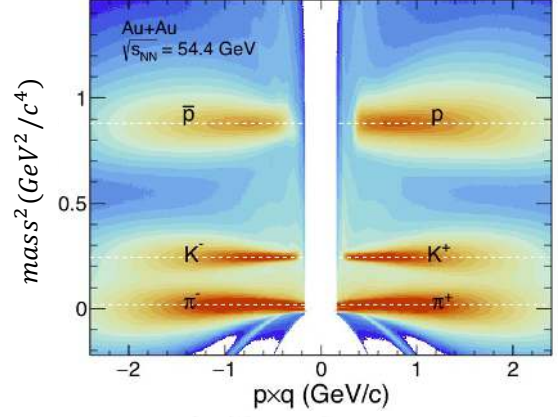


Figure 4.14: Mass-squared ($mass^2$) of various charged particles measured by TOF for Au+Au collisions at $\sqrt{s_{NN}} = 54.4$ GeV as a function of momentum.

was defined as follows,

$$n\sigma_{proton} = \frac{\log[(\langle dE/dx \rangle)_{measured}/(\langle dE/dx \rangle)_{theory}]}{\sigma_x}. \quad (4.2)$$

where, $(\langle dE/dx \rangle)_{measured}$ is the measured ionization energy loss for proton and $(\langle dE/dx \rangle)_{theory}$ is its theory expectation from Bichsel formula [14]. σ_x is the $\langle dE/dx \rangle$ resolution of TPC. A cut on this quantity, $|n\sigma_{proton}| < 2$, is used for identifying protons in the whole momentum range. From Fig. 4.13, the $\langle dE/dx \rangle$ band for proton can be seen to merge with those from kaons and pions at around ~ 1 GeV/c. From this point and onwards in the momentum axis, the measured dE/dx solely cannot be used to identify protons. Hence, mass squared measured from TOF is used to accomplish proton identification in the higher momentum range $p_T = 0.8 - 2$ GeV/c in addition to TPC. As discussed in section 3.3 of chapter 3, by measuring the flight time of charged tracks (Δt) and using the momentum (p) measurements from TPC, mass squared can be determined using the following equation,

$$mass^2 = p^2 \left(\frac{(c\Delta t)^2}{L^2} - 1 \right). \quad (4.3)$$

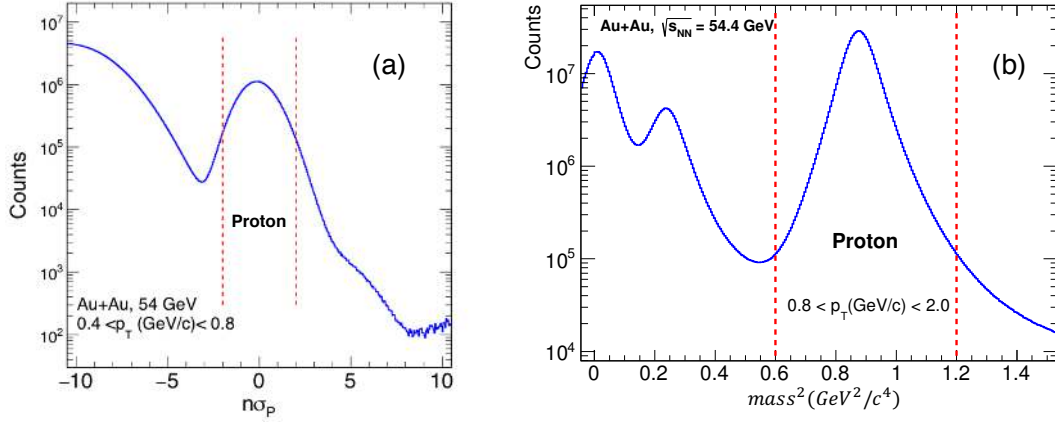


Figure 4.15: $n\sigma$ distribution for protons from TPC in the momentum range $0.4 < p_T < 0.8$ GeV/c (panel a) and $mass^2$ distribution for protons from TOF in the momentum range $0.8 < p_T < 2$ GeV/c (panel b) for Au+Au collisions at $\sqrt{s_{NN}} = 54.4$ GeV. The red dashed lines represent the cuts used for proton identification: $|n\sigma_{proton}| < 2$ and $0.6 < mass^2 < 1.2$ GeV²/c⁴. Other peaks in the distribution correspond to different particles.

where L is the path length of a track. Figure 4.2 shows the measured $mass^2$ at $\sqrt{s_{NN}} = 54.4$ GeV for various charged particles. Protons and other charged particles are seen to be clearly separated into different bands of $mass^2$ values. By requiring an additional detector to TPC, the proton number is reduced due to the efficiency effect, but this effect is accounted for when carrying out the measurement of net-proton cumulants. A representative plot for $n\sigma_{proton}$ and $mass^2$ from 54.4 GeV and the selection cuts used to identify protons are shown in panel (a) and (b) of Fig. 4.15, respectively. Multi-Gaussian fits are carried out on these distributions. By calculating the distribution area within the proton selection cuts and its overlap with distributions from other particles, contamination to the proton is evaluated. A purity of 98% and higher is found for protons in the lower momentum region when only TPC was used. With addition of TOF, proton purity of 97% and higher is achieved in the higher momentum region.

4.2 Analysis techniques

After selecting protons and antiprotons, the next step would be the calculation of net-proton cumulants. But before that, there are a few correction factors that need to be accounted for, such as the finite detector efficiency and the fluctuation of volume created in heavy-ion collisions. This section considers the correction of the cumulants for these effects.

4.2.1 Efficiency Correction

Not all the particles incident on the detectors get detected. Due to the finite efficiency of the detectors, the true multiplicity distribution gets convoluted along with the response of the detector. When saying finite efficiency, the detector's acceptance is also taken into account. The detection process of particles can be modeled as a Binomial sampling $B_{\epsilon,N}(n)$ where ϵ (probability of success) is the detection efficiency, and N (number of trials) is the true number of incident particles on the detector. The Binomial modeling of detector response has been found to be a reasonable assumption for the STAR detector [15–17]. Let's consider a simplistic case of particles getting detected with a probability ϵ , which is assumed to be independent for different particles. Let the measured multiplicity distribution be denoted as $\tilde{P}(n)$, where n is the number of detected particles. Then the true multiplicity distribution $\tilde{P}(N)$ is related to the measured multiplicity distribution as follows.

$$\tilde{P}(n) = \sum_{N=n}^{\infty} P(N) B_{\epsilon,N}(n). \quad (4.4)$$

When analyzing the detector response to true net-proton distribution, ($n = n_{net-p} = n_p - n_{\bar{p}}$), the bivariate case of the relation given by equation 4.4 need to be considered. Then, using the factorial cumulants generating function, the relation between cumulants of the true and

measured net-proton distribution can be obtained as follows [18].

$$C_1 = c_1/\epsilon, \quad (4.5)$$

$$C_2 = [c_2 - n_o(1 - \epsilon)]/\epsilon^2, \quad (4.6)$$

$$C_3 = [c_3 - c_1(1 - \epsilon^2) - 3(1 - \epsilon)(f_{20} - f_{02} - n_o c_1)]/\epsilon^3, \quad (4.7)$$

$$C_4 = [c_4 - n_o \epsilon^2(1 - \epsilon) - 3n_o^2(1 - \epsilon)^2 - 6\epsilon(1 - \epsilon)(f_{20} + f_{02}) + 12c_1(1 - \epsilon)(f_{20} - f_{02}) - (1 - \epsilon^2)(c_2 - 3c_1^2) - 6n_o(1 - \epsilon)(c_1^2 - c_2) - 6(1 - \epsilon)(f_{03} - f_{12} + f_{02} + f_{20} - f_{21} + f_{30})]/\epsilon^4.$$

Here, c_n and C_n are the cumulants of measured and true multiplicity distributions, respectively. $n_o = \langle n_p + n_{\bar{p}} \rangle$ and $f_{i,j}$ are the bivariate factorial cumulants of the measured multiplicity distributions. The formulae obtained are with the assumption that protons and antiprotons have the same efficiency ($\epsilon_p = \epsilon_{\bar{p}}$). But in the experiments, the efficiency for different particle species could be different. For our case, we have two charged particle species, protons and antiprotons, measured in two separate momentum windows using different combinations of TPC and TOF detectors. Hence multivariate joint probability distribution for net-proton distributions is considered to account for the difference in species and detectors used in different momentum ranges. The following relation between factorial cumulants of the measured and true multiplicity distribution is exploited to obtain the formulae for efficiency correction of cumulants [19].

$$F_{u,v,j,k}(N_{p_1}, N_{p_2}, N_{\bar{p}_1}, N_{\bar{p}_2}) = \frac{f_{u,v,j,k}(n_{p_1}, n_{p_2}, n_{\bar{p}_1}, n_{\bar{p}_2})}{(\epsilon_{p_1})^u (\epsilon_{p_2})^v (\epsilon_{\bar{p}_1})^j (\epsilon_{\bar{p}_2})^k}. \quad (4.8)$$

Here, the subscript p and \bar{p} denotes protons and antiprotons multiplicity, and index 1 and 2 denote the momentum range. N (e.g. N_{p_1}) represents true multiplicity, while n (e.g.

n_{p_1}) represents measured multiplicity. The $F_{u,v,j,k}$ and $f_{u,v,j,k}$ are the multivariate factorial cumulants of true and measured multiplicity distribution, respectively. The indices (u, v, j, k) stand for the order of factorial cumulants. The ϵ in the denominator are average efficiency values for protons and antiprotons for different momentum ranges. The methodology involved in deriving efficiency-corrected cumulants (see Ref. [19] for details) is quite rigorous and complex. Such complications can be reduced if cumulants and mixed cumulants are obtained for an observable $q_{(r,s)}$ defined as follows [20],

$$q_{(r,s)} = \sum_{i=1}^M (a_i^r / \epsilon_i^s) n_i \quad (4.9)$$

where, n_i represents the proton and antiproton multiplicity in i^{th} efficiency bin and a_i and ϵ_i are the quantum charge number and efficiency of particles in i^{th} bin, respectively. M is the total number of efficiency bins which, in our case is four. The correction of cumulants for efficiency, in terms of the cumulants and mixed cumulants of this observable, are presented in Ref. [20].

As we saw from the above discussion, the correction of net-proton cumulants requires two things; the uncorrected/measured multiplicity distribution and the average detection efficiency of protons and antiprotons. While for the former, the information is already at hand, for the latter, a Monte Carlo (MC) simulation called embedding is performed. In embedding simulation, input MC proton tracks (in numbers of a few percent of total tracks produced) are embedded into real events at a raw level. Then they are passed through a GEANT [21] program simulating the STAR TPC detector. This is followed by the reconstruction of tracks using the standard algorithm as used in real data. The track selection cuts applied to the reconstructed tracks in real data are also applied here. The ratio of the number of reconstructed tracks to that of input MC tracks is called the reconstruction efficiency. This methodology also accounts for acceptance effects. The

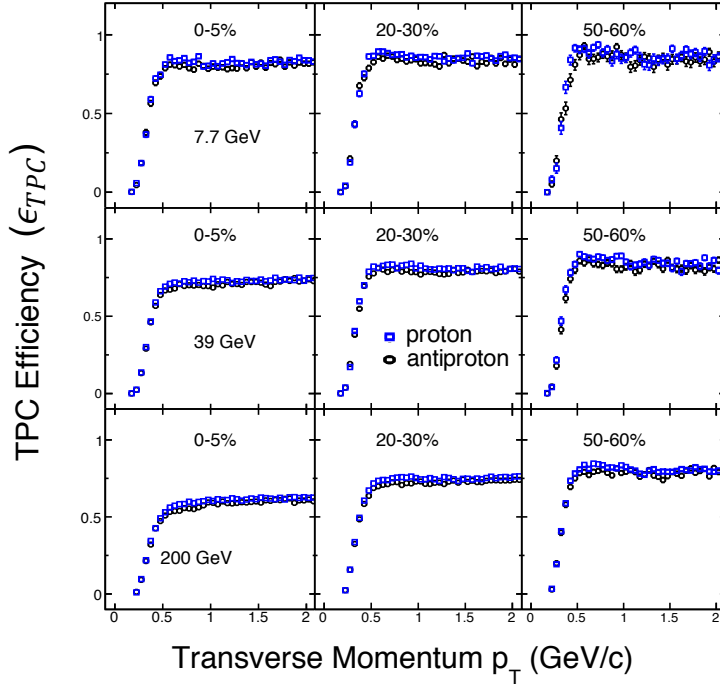


Figure 4.16: TPC efficiency of protons and antiprotons in Au+Au collisions at $\sqrt{s_{NN}} = 7.7, 39$ and 200 GeV for 0-5%, 20-30% and 70-80% centrality. Errors are only statistical.

proton and antiproton efficiencies thus obtained are shown in Fig. 4.16 as a function of transverse momentum (p_T). From these curves, average efficiency (ϵ_{av} , averaged with momentum as weight) is calculated using the following formula,

$$\epsilon_{av} = \frac{\int_a^b \epsilon(p_T) f(p_T) p_T dp_T}{\int_a^b f(p_T) p_T dp_T}, \quad (4.10)$$

where, $f(p_T)$ is p_T spectra of the particle and a and b denotes the momentum range over which p_T averaged efficiency is calculated. In the momentum range $p_T = 0.4 - 0.8$ GeV/c, where we use only the TPC, the above formula can be used to calculate average proton efficiency for a given centrality. But for higher momentum range $p_T = 0.8 - 2$ GeV/c, since we require m^2 measurement from the TOF detector along with the TPC, an additional efficiency factor related to matching between proton tracks incident on TPC to that of TOF detector also needs to be taken care. This is called the TOF matching efficiency (shown

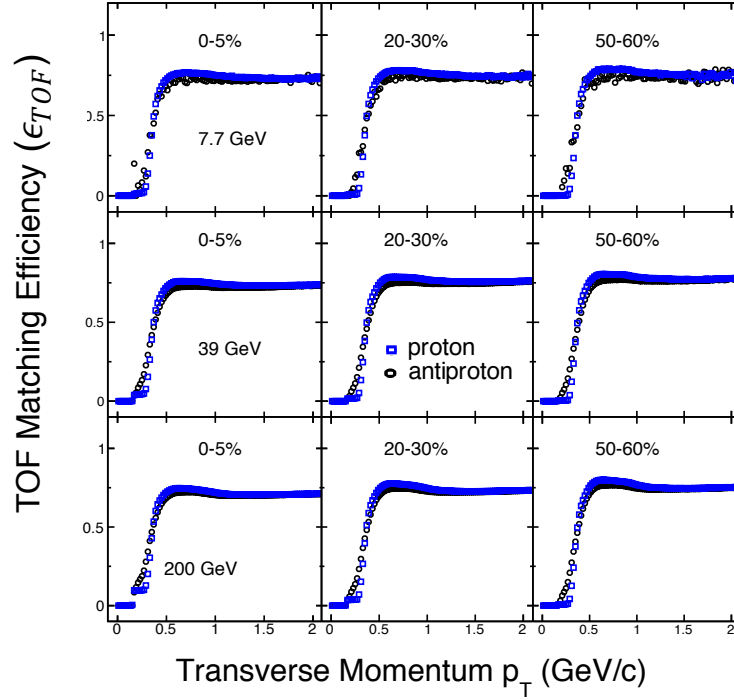


Figure 4.17: TOF matching efficiency of protons and antiprotons in Au+Au collisions at $\sqrt{s_{NN}} = 7.7, 39$ and 200 GeV for 0-5%, 20-30% and 70-80% centrality. Errors are only statistical.

in Fig. 4.17) and is defined as the ratio of the number of proton tracks measured by TPC that also have hit in the TOF detector to the total number of proton tracks measured with TPC. Thus, the total efficiency in the high momentum region is a multiplication of TPC efficiency and TOF matching efficiency, $\epsilon_{TPC} \times \epsilon_{TOF}$.

4.2.2 Centrality Bin Width Correction

Centrality in experiments is defined using the charged particle multiplicity (Refmult3, for our case). Any given centrality class, say 0–5% corresponds to a range of impact parameters and thus a range of charged particle multiplicity. The selection of narrow multiplicity bins helps to get rid of inherent fluctuations within each centrality class. The narrower the bin is, the more we suppress the geometrical fluctuation of the impact parameter. The

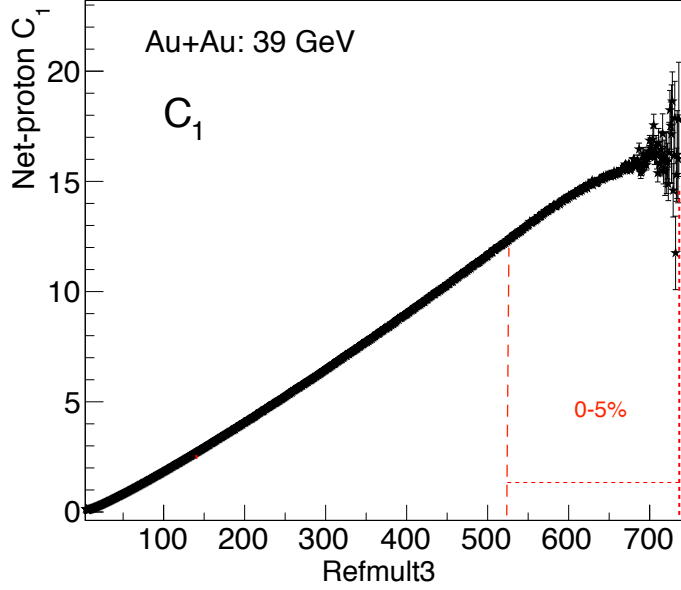


Figure 4.18: Refmult3 dependence of efficiency corrected net-proton C_1 (mean) for Au+Au collisions at $\sqrt{s_{NN}} = 39$ GeV. The area enclosed by the red region corresponds to 0-5% central events.

narrowest multiplicity bin that can be achieved is of unit width. The correction to net-proton cumulants accounting for the finite centrality bin width is called the centrality bin width correction [22] (CBWC). CBWC is an event-weighted averaging method aimed at suppressing the geometrical fluctuation of the collision volume. Mathematically, the following formula describes how CBWC is applied to n^{th} order cumulant,

$$C_n = \sum_r \omega_r C_{n,r} \quad (4.11)$$

$$\omega_r = \frac{n_r}{\sum_r n_r} = \frac{n_r}{N} \quad (4.12)$$

where n_r is the number of events in the r^{th} multiplicity bin, N is the total number of events in the centrality class where CBWC is applied, and \sum_r runs over all multiplicity bins in that centrality class. Using equation 4.12 and applying the standard error propagation formula, the statistical uncertainties on centrality bin width corrected cumulants can be calculated

as follows.

$$\sigma_{C_n} = \sqrt{\sum_r \omega_r^2 (\sigma_{C_{n,r}})^2}, \quad (4.13)$$

Here, $\sigma_{C_{n,r}}$ is the statistical error on n^{th} cumulant in r^{th} multiplicity bin.

Figure 4.18 demonstrates the need for such an averaging method. The efficiency corrected mean (C_1) of net-proton distribution is not flat as a function of Refmult3 but rather has a strong dependence on it for a given centrality class. Since all the higher-order cumulants include mean in their formula, this variation in mean in each multiplicity bin has to be accounted for when calculating higher-order cumulants for a centrality class. The CBWC correction accomplishes this job by obtaining properly averaged cumulants.

4.3 Summary

In this chapter, various details and methodologies related to net-proton cumulant analysis were discussed. In total, nine collision energies over the range $\sqrt{s_{NN}} = 7.7$ to 200 GeV were analyzed. The nine energies are $\sqrt{s_{NN}} = 7.7, 11.5, 14.5, 19.6, 27, 39, 54.4, 62.4,$ and 200 GeV. These energies allow coverage of a wide range of baryonic chemical potential, $\mu_B \sim 20 - 420$ MeV in the QCD phase diagram. By applying various event-level cuts, bad events were characterized and removed from the analysis. The total number of good events left for analysis ranged from ~ 2.2 million at $\sqrt{s_{NN}} = 7.7$ GeV to ~ 550 millions at $\sqrt{s_{NN}} = 54.4$ GeV. After selecting good events, various track-level cuts were applied to select good tracks for analysis. This was followed by the definition of collision centrality of events. A special definition of charged particle multiplicity distribution that excluded protons and antiprotons was used to define centrality. This definition was called Refmult3. The protons and antiprotons were excluded from the centrality definition to avoid any self-correlation with the observable of interest, i.e., the net-proton cumulants. Then protons and

antiprotons were identified using TPC and TOF detector at mid-rapidity $|y| < 0.5$ within momentum range $p_T = 0.4 - 2$ GeV/c. The ionization energy loss deposited by (anti-) proton tracks was used to identify them with the TPC detector. On the other hand, the flight time of proton tracks was used in their identification with the TOF. While only TPC was used over the momentum range, $p_T = 0.4 - 0.8$ GeV/c, at a higher momentum range $p_T = 0.8 - 2$ GeV/c, both TPC and TOF were used to remove contamination from other charged particles. A purity of 97% and above was obtained for the (anti-) proton sample with this combination of detectors for particle identification.

With proton and antiproton selected, the steps involved prior to obtaining the final results on net-proton cumulants were then discussed. These steps included corrections applied on the net-proton cumulant for artifacts related to measurements. The first one is to account for finite detection efficiency. To correct the cumulants for finite detection efficiency, analytical formulae connecting cumulants of true net-proton multiplicity distribution to the cumulants of measured net-proton multiplicity distribution and the detection efficiency were used. These formulae were obtained with the assumption of binomial detector response. While the measured net-proton distribution is already at hand, the proton and antiproton efficiencies were obtained using a Monte-Carlo (MC) simulation called embedding. Input MC proton tracks were embedded into real events and passed through a GEANT simulation of the STAR detector. The track reconstruction algorithm was run to obtain the number of reconstructed tracks after satisfying the same selection cuts as imposed in real data. Its ratio with respect to the number of input MC tracks gave the efficiency of proton. In addition to correction for finite efficiency, cumulant measurement also needed to be corrected for volume fluctuation effects. To correct for geometrical fluctuation of collision volume, cumulants were calculated in the narrowest possible Refmult3 multiplicity bin, i.e., bin of unity-width. Then a proper weighted averaging over the cumulants from each multiplicity

bin was performed across a centrality class (e.g., 0-5%) with events from those bins as weights. This event-weighted averaging procedure is referred to as the centrality bin width correction (CBWC). The CBWC is required because the net-proton mean, a quantity that manifests in all higher-order cumulants, itself varies within a centrality class. The CBWC is applied while obtaining final results at all collision energies.

Bibliography

- [1] J. Cleymans, H. Oeschler, K. Redlich, et al. “Comparison of chemical freeze-out criteria in heavy-ion collisions”. *Phys. Rev. C* 73 (2006), 034905. arXiv: [hep-ph/0511094](https://arxiv.org/abs/hep-ph/0511094).
- [2] W. J. Llope et al. “The TOFP/pVPD time-of-flight system for STAR”. *Nucl. Instrum. Meth. A* 522 (2004), 252–273. arXiv: [nuc1-ex/0308022](https://arxiv.org/abs/nuc1-ex/0308022).
- [3] *STAR note: sn0448*. <https://drupal.star.bnl.gov/STAR/starnotes/public/sn0448>.
- [4] C. A. Whitten. “The beam-beam counter: A local polarimeter at STAR”. *AIP Conf. Proc.* 980.1 (2008). Ed. by Ahovi Kponou, Yousef Makdisi, and Anatoli Zelenski, 390–396.
- [5] K. Schweda. “A Heavy-flavor tracker for STAR”. *Nucl. Phys. A* 774 (2006). Ed. by T. Csorgo, P. Levai, G. David, et al., 907–910. arXiv: [nuc1-ex/0510003](https://arxiv.org/abs/nuc1-ex/0510003).
- [6] L. Adamczyk et al. “Bulk Properties of the Medium Produced in Relativistic Heavy-Ion Collisions from the Beam Energy Scan Program”. *Phys. Rev. C* 96.4 (2017), 044904. arXiv: [1701.07065 \[nuc1-ex\]](https://arxiv.org/abs/1701.07065).
- [7] Michael L. Miller, Klaus Reygers, Stephen J. Sanders, et al. “Glauber modeling in high energy nuclear collisions”. *Ann. Rev. Nucl. Part. Sci.* 57 (2007), 205–243. arXiv: [nuc1-ex/0701025](https://arxiv.org/abs/nuc1-ex/0701025).
- [8] Roger D. Woods and David S. Saxon. “Diffuse Surface Optical Model for Nucleon-Nuclei Scattering”. *Phys. Rev.* 95 (1954), 577–578.
- [9] Donald E. Groom et al. “Review of particle physics. Particle Data Group”. *Eur. Phys. J. C* 15 (2000), 1–878.

- [10] Dmitri Kharzeev and Marzia Nardi. “Hadron production in nuclear collisions at RHIC and high density QCD”. *Phys. Lett. B* 507 (2001), 121–128. arXiv: [nucl-th/0012025](#).
- [11] M. Bleicher et al. “Relativistic hadron hadron collisions in the ultrarelativistic quantum molecular dynamics model”. *J. Phys. G* 25 (1999), 1859–1896. arXiv: [hep-ph/9909407](#).
- [12] M. Anderson et al. “The Star time projection chamber: A Unique tool for studying high multiplicity events at RHIC”. *Nucl. Instrum. Meth. A* 499 (2003), 659–678. arXiv: [nucl-ex/0301015](#).
- [13] B. Bonner, H. Chen, G. Eppley, et al. “A single Time-of-Flight tray based on multigap resistive plate chambers for the STAR experiment at RHIC”. *Nucl. Instrum. Meth. A* 508 (2003). Ed. by P. Fonte, M. Fraga, S. P. Ratti, et al., 181–184.
- [14] H. Bichsel. “A method to improve tracking and particle identification in TPCs and silicon detectors”. *Nucl. Instrum. Meth. A* 562 (2006), 154–197.
- [15] L. Adamczyk et al. “Collision Energy Dependence of Moments of Net-Kaon Multiplicity Distributions at RHIC”. *Phys. Lett. B* 785 (2018), 551–560. arXiv: [1709.00773 \[nucl-ex\]](#).
- [16] Mohamed Abdallah et al. “Cumulants and correlation functions of net-proton, proton, and antiproton multiplicity distributions in Au+Au collisions at energies available at the BNL Relativistic Heavy Ion Collider”. *Phys. Rev. C* 104.2 (2021), 024902. arXiv: [2101.12413 \[nucl-ex\]](#).
- [17] Mohamed Abdallah et al. “Measurement of the Sixth-Order Cumulant of Net-Proton Multiplicity Distributions in Au+Au Collisions at $\sqrt{s_{NN}} = 27, 54.4,$ and 200 GeV at RHIC”. *Phys. Rev. Lett.* 127.26 (2021), 262301. arXiv: [2105.14698 \[nucl-ex\]](#).
- [18] Adam Bzdak and Volker Koch. “Acceptance corrections to net baryon and net charge cumulants”. *Phys. Rev. C* 86 (2012), 044904. arXiv: [1206.4286 \[nucl-th\]](#).
- [19] Xiaofeng Luo. “Unified description of efficiency correction and error estimation for moments of conserved quantities in heavy-ion collisions”. *Phys. Rev. C* 91.3 (2015). [Erratum: *Phys.Rev.C* 94, 059901 (2016)], 034907. arXiv: [1410.3914 \[physics.data-an\]](#).

- [20] Toshihiro Nonaka, Masakiyo Kitazawa, and ShinIchi Esumi. “More efficient formulas for efficiency correction of cumulants and effect of using averaged efficiency”. *Phys. Rev. C* 95.6 (2017). [Erratum: *Phys.Rev.C* 103, 029901 (2021)], 064912. arXiv: [1702.07106 \[physics.data-an\]](#).
- [21] S. Agostinelli et al. “GEANT4—a simulation toolkit”. *Nucl. Instrum. Meth. A* 506 (2003), 250–303.
- [22] Xiaofeng Luo, Ji Xu, Bedangadas Mohanty, et al. “Volume fluctuation and auto-correlation effects in the moment analysis of net-proton multiplicity distributions in heavy-ion collisions”. *J. Phys. G* 40 (2013), 105104. arXiv: [1302.2332 \[nucl-ex\]](#).

Chapter 5

Estimating uncertainties on cumulant measurements

Higher-order cumulants of distribution are sensitive to its subtleties, especially tails. A minor change in the distribution shape may alter the higher-order cumulants considerably. Hence a careful estimation of uncertainties on cumulant measurements is important. The uncertainties on the net-proton cumulants reported in the thesis are of two types: statistical and systematic.

5.1 Statistical uncertainty

Since we intend to measure cumulants of event-by-event net-proton distribution, it is always good to have as many events as possible. The definition of an event in our context is the collision of two heavy-ion nuclei. The collection of events in heavy-ion collision experiments is limited by the time and cost factors of running the detectors. Hence a sample with limited events is available to carry out the measurement of net-proton cumulants. The uncertainty in the measurements associated with finite event statistics is called statistical

uncertainty.

5.1.1 Methods

We will outline three methods of uncertainty estimation and discuss them.

a) Delta theorem method

Delta theorem method is an analytical method of obtaining statistical uncertainties using standard error propagation. The method exploits the central limit theorem (CLT), an important theorem on the convergence of probability. The statement from CLT is as follows:

Central Limit Theorem: Let's suppose y_1, y_2, \dots, y_n is a collection of n random variates that are identically distributed and independent such that $E[y_i] = \mu$ and $\text{Var}[y_i] = \sigma^2$, then in the limit n tends to infinity, the variate $\sqrt{n}(M_n - \mu)$ should converge to a normal distribution $N(0, \sigma^2)$, where $M_n = (y_1 + y_2 + \dots + y_n)/n$. In other words, M_n approximately follows a normal distribution $N(\mu, \sigma^2/n)$ for a large value of n . This implies that several important random variables and estimators are asymptotically normal.

The Delta theorem method deals with functions of random variates. It prescribes approximation of the asymptotic behavior of functions of a random variate if the random variate itself is asymptotically normal [1]. To state it mathematically:

Delta theorem: Let Y_n be a sequence of random statistics such that

$$Y_n \xrightarrow{d} N(\theta, \sigma^2(\theta)/n), \quad \sigma(\theta) > 0. \quad (5.1)$$

Let $g(\theta)$ be a real differentiable function such that $g'(\theta) \neq 0$. Then,

$$g(Y_n) \xrightarrow{d} N(g(\theta), [g'(\theta)]^2 \sigma^2(\theta)/n). \quad (5.2)$$

Here, the \xrightarrow{d} symbol represents convergence over distribution. The theorem can be easily extended to the multivariate case. The convergence statement is then modified to the following;

$$\mathbf{g}(\mathbf{Y}) \xrightarrow{d} N(\mathbf{g}(\boldsymbol{\theta}), \mathbf{D}\boldsymbol{\Sigma}\mathbf{D}'/n) \quad (5.3)$$

where, $\mathbf{Y} = \{Y_n\}$ is a sequence of random vectors that are normally distributed, i.e., $\mathbf{Y} \xrightarrow{d} N(\boldsymbol{\theta}, \boldsymbol{\Sigma}/n)$, $\boldsymbol{\theta}$ is a constant vector, called the mean vector, $\boldsymbol{\Sigma}$ is the covariance matrix, and \mathbf{D} is the Jacobian of \mathbf{g} .

Before prescribing the formula to obtain error on cumulants, we will state another theorem used to study the convergence of a sequence of sample moments. The theorem is actually a corollary of the multivariate central limit theorem.

If central moments $\mu_{2k} = E[(Y - \mu)^{2k}]$ are finite, then the random vector

$$(\hat{\mu}_2 - \mu_2, \dots, \hat{\mu}_k - \mu_k) \xrightarrow{d} N((0, 0, 0, \dots, 0), \boldsymbol{\Sigma}/n), \quad (5.4)$$

where, $\boldsymbol{\Sigma}$ is a $(k - 1) \times (k - 1)$ covariance matrix, with elements,

$$\Sigma_{i,j} = \mu_{i+j} - \mu_i\mu_j - i\mu_{i-1}\mu_{j+1} - j\mu_{i+1}\mu_{j-1} + ij\mu_{i-1}\mu_{j-1}\mu_2. \quad (5.5)$$

Note that the standard deviation (square root of variance) of the asymptotically normal distribution in equation 5.4 is the statistical uncertainty on central moments. Recall that the first-order cumulant is the mean, whose convergence is discussed in the CLT theorem itself (the variate S_n). The second and third-order cumulants are the central moments μ_2 and μ_3 , respectively. Setting $i = j = m$ ($m \geq 2$) in the equation. 5.5 yields the variances of central moments μ_2 and μ_3 . Using the CLT and the theorem stated above, statistical

uncertainties/errors on cumulants up to the third order can be obtained as follows [2–5]:

$$\begin{aligned} \text{Var}(C_1) &= \mu_2/n \\ \text{Var}(C_2) &= (\mu_4 - \mu_2^2)/n \\ \text{Var}(C_3) &= (\mu_6 - \mu_3^2 + 9\mu_2^3 - 6\mu_2\mu_4)/n. \end{aligned} \quad (5.6)$$

Expressions for variances of the cumulants are presented in Eqn. 5.6 to avoid the use of the square root symbol repetitively (statistical uncertainty is simply the square roots of the variance). To calculate the error on the fourth-order cumulant, we will make use of the Delta theorem stated in equation.5.3.

The fourth-order cumulant in terms of the central moment is given as; $C_4 = \mu_4 - 3\mu_2$. Taking $g(\mu_2, \mu_4) = C_4 = \mu_4 - 3\mu_2$,

$$\mathbf{D}\Sigma\mathbf{D}' = \begin{pmatrix} \partial g/\partial \mu_2 & \partial g/\partial \mu_4 \end{pmatrix} \begin{pmatrix} \Sigma_{11} & \Sigma_{12} \\ \Sigma_{21} & \Sigma_{22} \end{pmatrix} \begin{pmatrix} \partial g/\partial \mu_2 \\ \partial g/\partial \mu_4 \end{pmatrix}. \quad (5.7)$$

Since the transformation involves central moments μ_2 and μ_4 , the covariance matrix elements are $\Sigma_{11} = \text{Var}(\mu_2)$, $\Sigma_{22} = \text{Var}(\mu_4)$, and $\Sigma_{12} = \Sigma_{21} = \text{Cov}(\mu_2, \mu_4)$. The variances and covariances of μ_2 and μ_4 can be calculated using equation. 5.5. Substituting the values,

$$\mathbf{D}\Sigma\mathbf{D}' = \begin{pmatrix} -6\mu_2 & 1 \end{pmatrix} \begin{pmatrix} \mu_4 - \mu_2^2 & \mu_6 - 4\mu_3^2 - \mu_4\mu_2 \\ \mu_6 - 4\mu_3^2 - \mu_4\mu_2 & \mu_8 - \mu_4^2 - 8\mu_3\mu_5 + 16\mu_2\mu_3^2 \end{pmatrix} \begin{pmatrix} -6\mu_2 \\ 1 \end{pmatrix}. \quad (5.8)$$

Using the above equation, the variance on C_4 [4, 5] is obtained to be as follows:

$$\text{Var}(C_4) = \mathbf{D}\Sigma\mathbf{D}'/n = (\mu_8 - 12\mu_6\mu_2 - 8\mu_5\mu_3 - \mu_4^2 + 48\mu_4\mu_2^2 + 64\mu_3^2\mu_2 - 36\mu_2^4)/n. \quad (5.9)$$

Extending the same approach, statistical uncertainties on fifth and sixth-order cumulants

are also obtained to be as follows [4]:

$$\begin{aligned} Var(C_5) = & (\mu_{10} - \mu_5^2 - 10\mu_4\mu_6 + 900\mu_2^5 - 20\mu_3\mu_7 - 20\mu_8\mu_2 + 125\mu_2\mu_4^2) \\ & + (200\mu_4\mu_3^2 - 1000\mu_3^2\mu_2^2 + 160\mu_6\mu_2^2 - 900\mu_4\mu_2^3 + 240\mu_2\mu_3\mu_5)/n. \end{aligned} \quad (5.10)$$

$$\begin{aligned} Var(C_6) = & (-30\mu_4\mu_8 + 510\mu_4\mu_2\mu_6 + 1020\mu_4\mu_3\mu_5 + 405\mu_8\mu_2^2 - 2880\mu_6\mu_2^3) \\ & - (9720\mu_3\mu_5\mu_2^2 - 30\mu_2\mu_{10} + 840\mu_2\mu_3\mu_7 + 216\mu_2\mu_5^2 - 40\mu_3\mu_9 \\ & + 440\mu_6\mu_3^2 - 3600\mu_2^2\mu_4^2 - 9600\mu_2\mu_4\mu_3^2 + 13500\mu_4\mu_2^4 + 39600\mu_2^3\mu_3^2 + \mu_{12} \\ & - \mu_6^2 - 12\mu_5\mu_7 + 225\mu_4^3 - 8100\mu_2^6 - 400\mu_3^4)/n. \end{aligned} \quad (5.11)$$

It can be seen that with increasing order of cumulant, the formula for uncertainties on the cumulant becomes more lengthy and tedious. Note that the central moments appearing on the right-hand side of the formulae are that of the population, which are estimated using the sample itself when obtaining statistical uncertainties. As an alternative to this analytical approach, one often uses resampling methods for statistical uncertainty estimation. Two such methods: Bootstrap and Sub-sampling, are studied in this thesis.

b) Bootstrap method

The Bootstrap method is a resampling method for estimating statistical uncertainties [4–7]. Let's suppose we have a sample of events over which we want to perform measurement of a certain statistic of interest " t ". We call this the parent sample. In a resampling method, new samples are generated from the parent sample using Monte-Carlo simulation. Particularly in the Bootstrap method, several new samples of the same size (same number of events) as that of the parent sample are generated by a random draw of elements of the parent sample with replacement. We call these Bootstrap samples. An illustrative diagram demonstrating the creation of Bootstrap samples is shown in Fig. 5.1. The statistic t is calculated for each

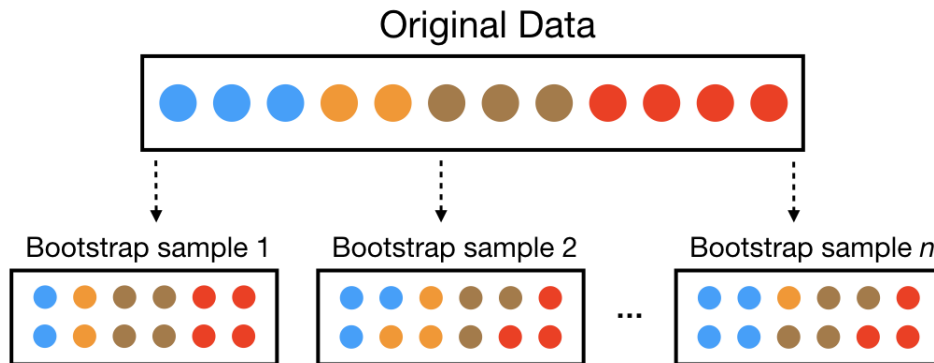


Figure 5.1: An illustrative diagram of Bootstrap sample generation by random draw of elements from the parent sample ("Original data" in the diagram), with replacement allowed. The size of Bootstrap samples is same as the parent sample. The sketch is adapted from Ref. [8].

of these bootstrap samples. The sampling variance of the statistic over these bootstrap samples is the statistical uncertainties on it. To summarize the steps involved;

- Given a parent sample (P) consisting of n number of events, we randomly draw n events from it with replacement and generate a new sample (S_1).
- The statistic of interest t is calculated for the newly generated bootstrap sample (S_1).
- In the same way, more Bootstrap samples (S_2, S_3, S_4, \dots) are generated, and statistic t is calculated for each of them.
- The average of statistic t given by \bar{t} is evaluated considering B number total generated sample.

If there are B number of Bootstrap samples generated and \bar{t} is the average of statistic t over the Bootstrap samples, then the variance of t is given as:

$$\sigma_{Bootstrap, t}^2 = \frac{\sum_i^B (t_i - \bar{t})^2}{B - 1} \quad (5.12)$$

where the index i in \sum_i runs over the number of Bootstrap samples.

The $\sigma_{Bootstrap, t}$ in equation 5.12 is the statistical uncertainty on the statistic t measured with parent sample P . Choosing the statistic of interest t to be cumulants, statistical uncertainty on cumulant of any order can be evaluated using the Bootstrap formalism described above. The number of Bootstrap samples needed for proper evaluation of statistical uncertainties varies from case to case depending upon the sample size of the parent. Nonetheless, the larger the value of B , the better the uncertainty estimation.

c) Subgroup method

Subgroup is also a resampling method of statistical uncertainty estimation [4]. In this method, the parent sample is divided into several sub-groups/sub-samples of equal size. Each sub-sample reflects a random sub-set of events from the parent sample. The statistic of interest t is calculated from the sub-samples. The sampling variance of the statistic t over these sub-samples scaled by the total number of sub-samples gives the statistical uncertainty on the statistic t . The steps involved are summarized below.

- Given a parent sample (P) consisting of n number of events, we divide it to create S number of sub-samples, each with n/S number of events.
- The statistic of interest t is calculated for each of the sub-samples.

Denoting \bar{t} as the average of t over the sub-samples, the variance of t is given as:

$$\sigma_{Subgroup, t}^2 = \frac{\sum_i^S (t_i - \bar{t})^2}{S(S-1)} \quad (5.13)$$

The $\sigma_{Subgroup, t}$ in the equation 5.13 is the statistical uncertainty on the statistic t using the Subgroup method.

5.1.2 Method comparisons and application in experiments

After defining various methods for estimating statistical uncertainty on cumulants, we compare them by employing a Gaussian verification procedure [4]. Statistical uncertainty is also known as the standard error in the theory of statistics. The standard error/statistical uncertainty on a statistic t for a given sample size n implies that there is an underlying parent distribution (population), and if we randomly create many samples of size n from this parent distribution, then $\sim 68.3\%$ of all such samples will have the values of statistic t between $\pm\sigma_t$, i.e., within the statistical uncertainties. This is a consequence of the asymptotically normal/Gaussian behavior of estimators, as per the central limit theorem. To verify this Gaussian nature of statistical uncertainty, we performed a simulation study. A Skellam sample of size 100 million with input parameters determined from STAR experimental data [4] was considered for the study. The cumulants of this sample were evaluated. Uncertainties on cumulants were then estimated with three methods: Delta theorem, Bootstrap, and Subgroup method. From this Skellam sample, 10000 random samples, each of the same size, i.e., 100 million, were generated by performing random draw of entries with replacement, and cumulants for each of these generated samples were obtained. We focus on the fourth (C_4), sixth (C_6), and eighth-order (C_8) cumulant in our study. As seen from Fig. 5.2, the uncertainties estimated by Bootstrap and Delta theorem method are in good agreement with the width obtained from Gaussian fit to the distribution of cumulants. The Subgroup method was observed to underestimate the value of uncertainties. Considering uncertainties estimated using the Delta theorem and Bootstrap method, we find $\sim 68\%$ of the generated samples had C_4 , C_6 , and C_8 within their respective uncertainties, satisfying the Gaussian test. With the Subgroup method, however, the fraction drops quite below 68% (as low as 58.6% for C_6).

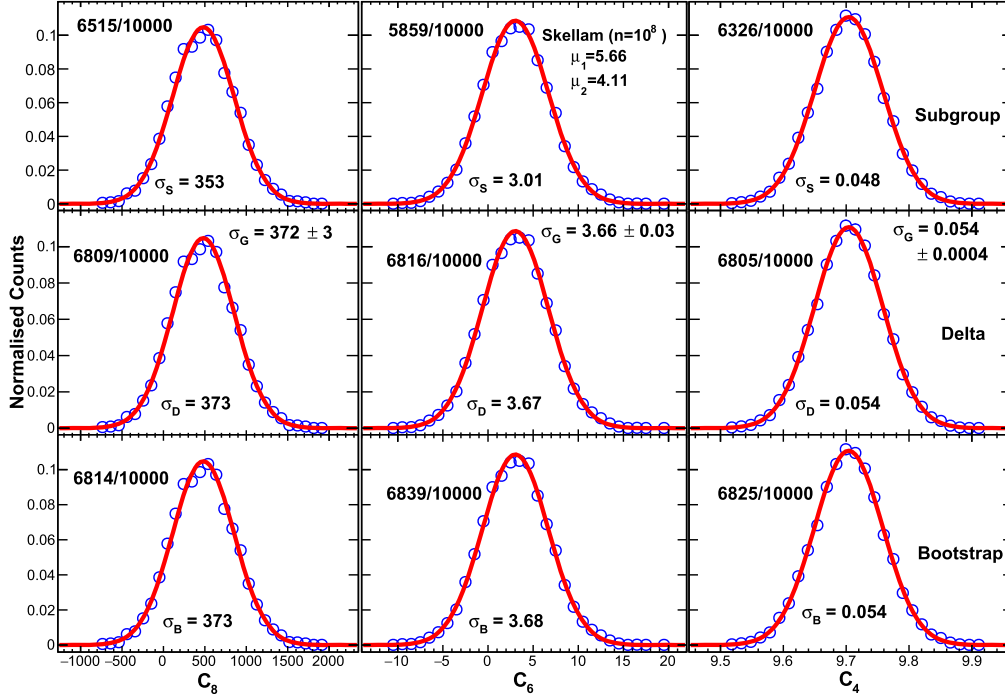


Figure 5.2: Verification of Gaussian nature of statistical uncertainties obtained with different methods for a Skellam sample of size 10^8 . The Skellam sample is characterized by its parameters $\mu_1 = 5.66$, $\mu_2 = 4.11$ (efficiency corrected mean of proton and antiproton measured at mid-rapidity for top 5% Au+Au collision at $\sqrt{s_{NN}} = 200$ GeV at STAR [9]). The distributions presented in each panel are values of fourth (C_4), sixth (C_6), and eighth-order (C_8) cumulants from 10000 samples generated from the parent Skellam sample using Bootstrap sampling. σ_G is the width of distributions obtained by fitting with a Gaussian function. The top, middle, and bottom rows correspond to Subgroup (σ_S), Delta theorem (σ_D), and Bootstrap method (σ_B), respectively. The number of random samples out of 10000 that have values of cumulants within $\pm 1\sigma$ statistical uncertainties estimated with various methods are also shown [4].

As noted from our study, Subgroup is an inefficient method to calculate statistical uncertainties on cumulants. Hence Bootstrap and Delta theorem methods were used to estimate statistical uncertainties on the experimentally measured net-proton cumulants. From Fig. 5.3, a good agreement between the statistical uncertainty on cumulants of net-proton distribution in Au+Au collisions at $\sqrt{s_{NN}} = 19.6$ GeV, using Bootstrap and Delta theorem methods is observed. The table 5.1 lists the percentage relative statistical

uncertainties on measured net-proton cumulant ratio C_4/C_2 and C_6/C_2 at $\sqrt{s_{NN}} = 7.7, 39$ and 200 GeV [10–12](the uncertainty values are quoted for cumulant ratios since they are the main observable of our study; recall that the theoretical predictions are for cumulant ratios rather than just cumulants).

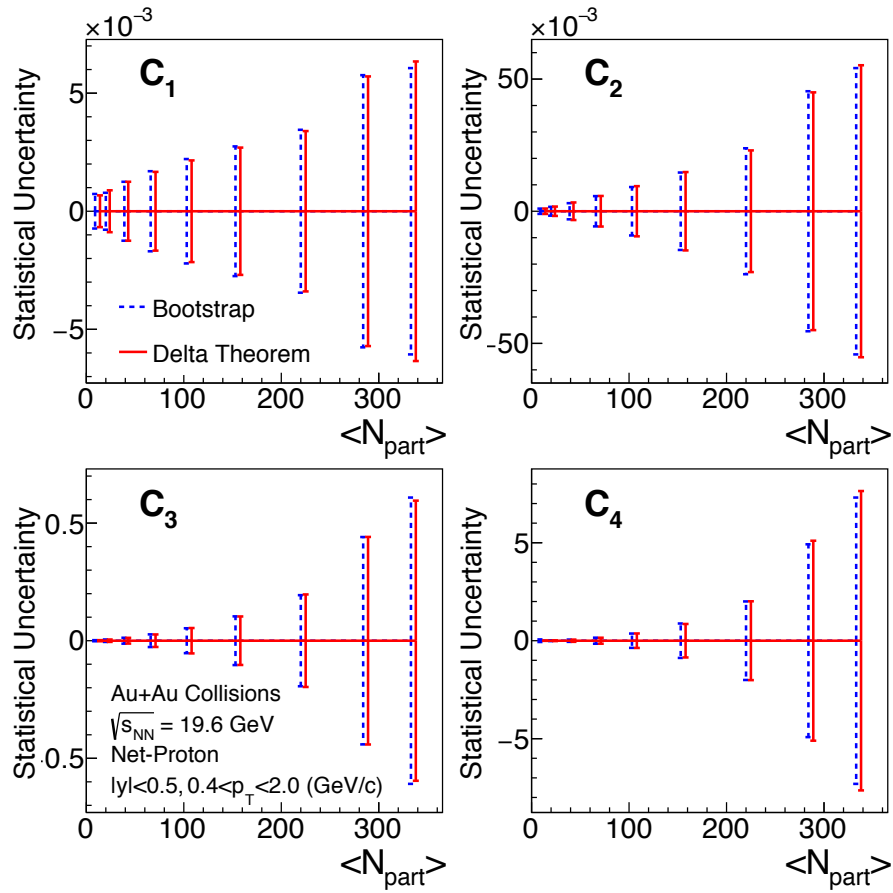


Figure 5.3: Comparison of statistical uncertainty on net-proton cumulants up to fourth-order in Au+Au collisions at $\sqrt{s_{NN}} = 19.6$ GeV, estimated using Bootstrap and Delta theorem method [10]. The uncertainties are presented as a function of average number of participant nucleons ($\langle N_{part} \rangle$). The red and dashed blue lines represent uncertainties from the Delta theorem and Bootstrap methods, respectively.

It is worth mentioning that while estimating statistical uncertainty on cumulants experimentally, detection efficiency also comes to play [3]. Using the formula provided for error

Table 5.1: Percentage relative statistical uncertainties (σ_Y/Y , Y is an observable) for net-proton cumulant ratios C_4/C_2 (0-5% centrality) and C_6/C_2 (0-40% centrality) in Au+Au collisions at $\sqrt{s_{NN}} = 7.7, 39, \text{ and } 200$ GeV. 0-40% centrality is chosen for C_6/C_2 to reduce the statistical uncertainties.

$\sqrt{s_{NN}}$ (GeV)	7.7	39	200
C_4/C_2 (0-5%)	65%	20%	23%
C_6/C_2 (0-40%)	32%	49%	72%

on cumulants using the Delta theorem, it can be seen that statistical uncertainty on m^{th} order cumulant of distribution is related to the width (σ) of the distribution and number of events n , as follows:

$$\text{stat. uncert. } (C_m) \propto \frac{\sigma^m}{\sqrt{n}}. \quad (5.14)$$

Hence larger width leads to larger statistical uncertainties. This is the reason for the increasing magnitude of statistical uncertainties towards more central collisions, as seen from Fig. 5.3. In addition to increased particle production, efficiency correction also increases the width of the distribution (the measured net-proton distribution width is smaller than the true/corrected width due to finite detector efficiency). The smaller the efficiency, the larger the change of the width of measured distribution and thus larger statistical uncertainties on the efficiency corrected cumulant compared to the uncorrected case.

5.2 Systematic uncertainty

While the statistical uncertainties are associated with limited event statistics, the systematic uncertainties are associated with the limitation of the "system." Systematic uncertainties are the uncertainties arising from the protocols followed in the measurement. In this section, we will discuss the systematic uncertainty estimation on cumulant measurements.

5.2.1 Sources

Recall from our discussion on analysis details (see chapter 4), we made several selection cuts aimed at ensuring good quality of data and removal of backgrounds to our measurements. We vary those selection cuts in the study of systematic uncertainties. The variations undertaken are listed in Tab. 5.2 along with the default selection cuts.

Source	Default cut	Variation	Number of variations (n_{var})
nHitsFit	> 20	> 15 > 18 > 22 > 25	4
DCA (cm)	< 1.0	< 0.8 < 0.9 < 1.1 < 1.2	4
$n\sigma_{proton}$	$ n\sigma_{proton} < 2.0$	< 1.6 < 1.8 < 2.2 < 2.5	4
Proton $mass^2$ (GeV^2/c^4)	(0.6, 1.2)	(0.5, 1.1) (0.55, 1.15) (0.65, 1.25) (0.7, 1.3)	4
Efficiency	default obtained from MC simulation	+5% of the default -5% of the default	2

Table 5.2: Table of selection cut variations from different sources considered for estimating systematic uncertainties on net-proton cumulants along with the default selection criteria.

Hence, there are five sources of systematics considered to obtain systematic uncertainties on net-proton cumulants. The selection cuts were made such that mean of (anti-)proton is permitted to change within certain allowable limits (of the order of a few percent). Note that the listed sources do not change the number of events since that would introduce statistical fluctuation on cumulants. Each of the sources: nHitsFit, DCA, $n\sigma_{proton}$, $mass^2$,

efficiency, has several variations. First, the average contribution from each source is calculated. Supposing n_{var} as the number of variations of a source, the average contribution of that source to the systematic uncertainty on an observable on interest (cumulants/ratio of cumulant) is evaluated using the following formula;

$$\sigma_{source} = \sqrt{\frac{1}{n_{var}} \sum_{i=1}^{n_{var}} (Y_i - Y_{def.})^2}. \quad (5.15)$$

where Y_i is the observable calculated from i^{th} variation, $Y_{def.}$ is its value with default selection cut, and the \sum_i sums the difference between the two in quadrature over all variations made for the source. It is worth mentioning here that in calculating Y_i for each i^{th} variation (except efficiency variation), the detector efficiency is re-estimated. This is done by applying exactly the same selection cuts in the Monte Carlo embedding simulation during the reconstruction process. Barring the case of efficiency, where two variations ($n_{var} = 2$) are considered, for all the remaining sources, there are four systematic variations ($n_{var} = 4$). Before adding contributions from individual sources, we subject the sources to Barlow check.

5.2.2 Barlow check

Barlow check is a method to examine that the uncertainties on an observable (Y) associated with variation of a source are indeed due to systematic variation and not mere statistical fluctuations [13]. In Barlow check, first a quantity $\Delta Y/\sigma_B$ where $\Delta Y = Y_{def} - Y_{sys}$ and $\sigma_B = \sqrt{\sigma_{def}^2 - \sigma_{sys}^2}$ (σ_{def} and σ_{sys} are the statistical uncertainties on Y with default cut selection and a systematic cut variation, respectively) is evaluated for each source. If the distribution of Δ/σ_B obtained from the variation of a source follows a Normal distribution $N(0, 1)$, then the difference in variable due to the systematic variation can be attributed to statistical effects. We calculated this quantity for net-proton C_4/C_2 . Since there are only

nine centralities where we measured C_4/C_2 for a source, there are fewer entries constituting the $\Delta Y/\sigma_B$ distribution. We relaxed the Barlow criteria from strictly Gaussian or Normal distribution to the following constraints.

- Mean < 0.3
- Standard deviation < 1.3
- 55 – 68% entries within 1σ of the $\Delta Y/\sigma_B$ distribution
- 80 – 95% entries within 2σ of the $\Delta Y/\sigma_B$ distribution

If three of the four conditions are satisfied for a source, then the Barlow criteria is passed, indicating that the difference in observable Y arising from that source is within statistical fluctuations and does not reflect the real systematics. Thus, if the Barlow test failed for a source, then that source should be considered in the estimation of systematic uncertainties. We subjected the five different sources (nHitsFit, DCA, $n\sigma_{proton}$, $mass^2$ and efficiency) that we considered for estimating systematic uncertainties to the Barlow test and found all of them failed the test. A representative plot on $\Delta Y/\sigma_B$ for net-proton C_4/C_2 from different variations of DCA in 0-5% central Au+Au collisions at $\sqrt{s_{NN}} = 54.4$ GeV is shown in Fig. 5.4.

The contribution from each of these sources of systematic variation is then added in quadrature to render the total systematic uncertainty. The following equation demonstrates the same.

$$\sigma_{sys} = \sqrt{\sigma_{nHitsFit}^2 + \sigma_{DCA}^2 + \sigma_{n\sigma_{proton}}^2 + \sigma_{mass^2}^2 + \sigma_{eff}^2} \quad (5.16)$$

Contribution of each source to the total systematic uncertainties on net-proton cumulant ratio C_4/C_2 in 0-5% central Au+Au collisions at $\sqrt{s_{NN}} = 54.4$ GeV is shown in Fig. 5.5.

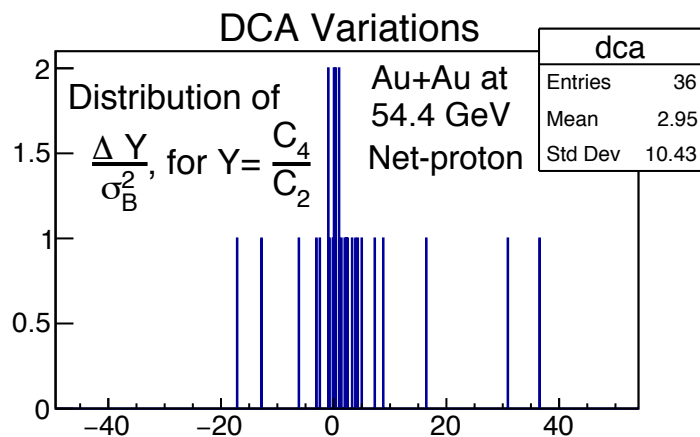


Figure 5.4: $\Delta Y/\sigma_B$ obtained from DCA variations for net-proton cumulant ratio C_4/C_2 in 0-5% central Au+Au collisions at $\sqrt{s_{NN}} = 54.4$ GeV.

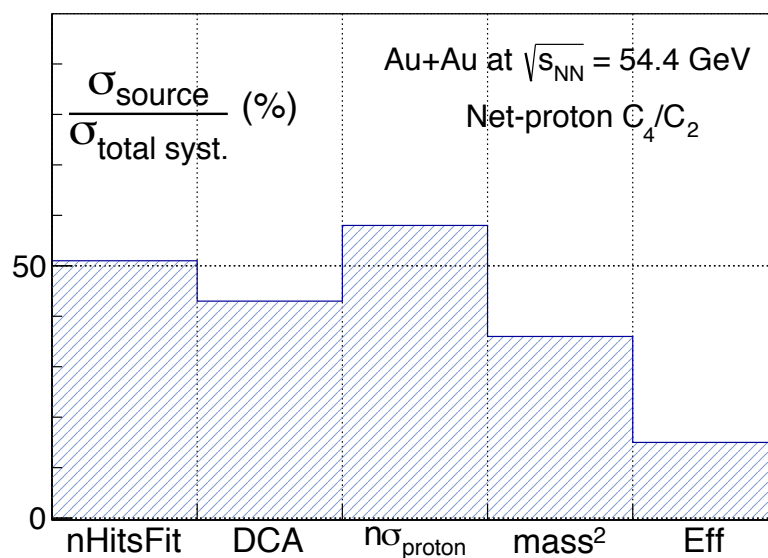


Figure 5.5: Contribution from each source relative to total systematic uncertainties (in percentage) for net-proton cumulant ratio C_4/C_2 in 0-5% central Au+Au collisions at $\sqrt{s_{NN}} = 54.4$ GeV.

The table 5.3, lists the percentage relative systematic uncertainties on net-proton cumulant ratio C_4/C_2 and C_6/C_2 at $\sqrt{s_{NN}} = 7.7, 39$ and 200 GeV [10–12]. In general, the systematic uncertainties are seen to increase with collision centrality. Figure 5.6 shows collision

Table 5.3: Percentage relative systematic uncertainties (σ_Y/Y) for net-proton cumulant ratios C_4/C_2 (0-5% centrality) and C_6/C_2 (0-40% centrality) in Au+Au collisions at $\sqrt{s_{NN}} = 7.7, 39, \text{ and } 200$ GeV.

$\sqrt{s_{NN}}$ (GeV)	7.7	39	200
C_4/C_2 (0-5%)	23%	18%	15%
C_6/C_2 (0-40%)	50%	67%	81%

centrality dependence of net-proton cumulants up to fourth-order for Au+Au collisions at $\sqrt{s_{NN}} = 54.4$ GeV. It is noted that the larger the magnitude of the observable, the larger the systematic uncertainties on it.

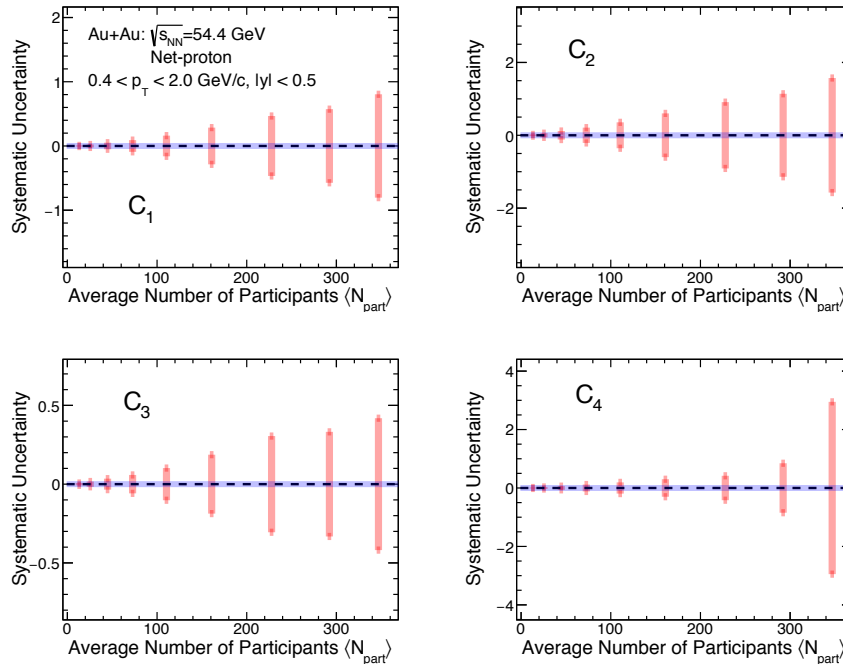


Figure 5.6: Systematic uncertainties on net-proton cumulants up to fourth-order as a function of collision centrality (average number of participant nucleons, $\langle N_{part} \rangle$) in Au+Au collisions at $\sqrt{s_{NN}} = 54.4$ GeV. The systematic uncertainties are shown as $\pm\sigma_{sys}$ on the horizontal line at $y = 0$.

5.3 Summary

The higher-order cumulants of a distribution are sensitive to its shape. Their values are driven by the distribution's tail. Hence a careful estimation of uncertainties on higher-order cumulants is necessary. This chapter dealt with the estimation of uncertainties on the cumulant of net-proton distribution measured in the STAR experiment.

First, statistical uncertainty was discussed. Three methods of estimating statistical uncertainties: Delta theorem, Bootstrap, and Subgroup method were presented. While the Delta theorem is an analytical method that exploits the Central Limit Theorem, the latter two are resampling methods. Resampling methods, though computer-intensive, can be used as an alternative to avoid the lengthy and complicated formulae prescribed by the Delta theorem method. In the Bootstrap method, new samples are generated by performing random draw of events from the parent sample with replacement allowed. Cumulants are calculated for these generated samples, and the width of the resulting sampling distribution provided the statistical uncertainty. On the other hand, the Subgroup method accounts for this randomness by dividing the parent sample into several sub-samples with lesser event statistics. The width of the sampling distribution of cumulants over the sub-samples scaled with the number of sub-samples gave the statistical uncertainty using the Subgroup method. The validity of the three methods was verified by subjecting them to a test to satisfy the Gaussian nature of statistical uncertainties. The verification involved generating random samples from a parent and testing if $\sim 68\%$ of the random samples had cumulants lying within $\pm 1\sigma$ statistical uncertainties evaluated by these three methods. While the Bootstrap and Delta theorem methods satisfied the Gaussian nature of uncertainties, the Subgroup method failed. The Subgroup method was inefficient in estimating statistical uncertainties primarily because of decrease in statistics due to the splitting of the parent sample into

sub-samples. For these reasons, Bootstrap and Delta theorem methods were used to obtain the statistical uncertainties on experimentally measured cumulant. Both methods gave consistent values of statistical uncertainties. The statistical uncertainties were found to increase with increasing collision centrality. This is primarily because of the increasing width of net-proton distribution towards central collisions. The relative percentage value of statistical uncertainties on net-proton cumulant ratios C_4/C_2 for 0-5% centrality (C_6/C_2 for 0-40% centrality) in Au+Au collisions at $\sqrt{s_{NN}} = 7.7, 39, \text{ and } 200 \text{ GeV}$ was found to be 65% (32%), 20% (49%) and 23% (72%), respectively.

Next, we discussed the estimation of systematic uncertainties on net-proton cumulant measurements. Several selection cuts aimed at ensuring good quality of data and removal of backgrounds to our measurements were varied. In total, five sources of systematics were considered: nHitsFit, DCA, $n\sigma_{proton}$, $mass^2$, and efficiency. For each of the sources, four variations of the selection cuts (except for reconstruction efficiency, which had two variations) were considered. After modifying the selection cuts in data, the efficiency was also recalculated, and net-proton cumulants were computed again. Their difference with respect to cumulants with default selection cut is considered over all variations to render the average contribution from a source. These five sources were subjected to Barlow check to examine if their contribution to systematic uncertainty could be just due to statistical fluctuations. All the considered sources failed the test, indicating that they should be considered in the estimation of systematic uncertainties. Contributions from all sources are then added in quadrature to obtain the final systematic uncertainty. The systematic uncertainties on net-proton cumulants were observed to increase with increasing collision centrality. Their relative percentage values for net-proton C_4/C_2 for 0-5% centrality (C_6/C_2 for 0-40% centrality) in Au+Au collisions at $\sqrt{s_{NN}} = 7.7, 39, \text{ and } 200 \text{ GeV}$ were found to be 23% (50%), 18% (67%) and 15% (81%), respectively.

Bibliography

- [1] Anirban DasGupta. *Asymptotic Theory of Statistics and Probability*.
- [2] Xiaofeng Luo. “Error Estimation for Moments Analysis in Heavy Ion Collision Experiment”. *J. Phys. G* 39 (2012), 025008. arXiv: [1109.0593 \[physics.data-an\]](#).
- [3] Xiaofeng Luo. “Unified description of efficiency correction and error estimation for moments of conserved quantities in heavy-ion collisions”. *Phys. Rev. C* 91.3 (2015). [Erratum: *Phys.Rev.C* 94, 059901 (2016)], 034907. arXiv: [1410.3914 \[physics.data-an\]](#).
- [4] Ashish Pandav, Debasish Mallick, and Bedangadas Mohanty. “Effect of limited statistics on higher order cumulants measurement in heavy-ion collision experiments”. *Nucl. Phys. A* 991 (2019), 121608. arXiv: [1809.08892 \[nucl-ex\]](#).
- [5] A. Pandav, D. Mallick, and B. Mohanty. “Search for the QCD critical point in high energy nuclear collisions”. *Prog. Part. Nucl. Phys.* 125 (2022), 103960. arXiv: [2203.07817 \[nucl-ex\]](#).
- [6] B. Efron. “Bootstrap Methods: Another Look at the Jackknife”. *Annals Statist.* 7.1 (1979), 1–26.
- [7] Bradley Efron. “Computers and the Theory of Statistics: Thinking the Unthinkable”. *SIAM Review* 21.4 (1979), 460–480.
- [8] <https://bradleyboehmke.github.io/HOML/process.html>.
- [9] L. Adamczyk et al. “Energy Dependence of Moments of Net-proton Multiplicity Distributions at RHIC”. *Phys. Rev. Lett.* 112 (2014), 032302. arXiv: [1309.5681 \[nucl-ex\]](#).
- [10] Mohamed Abdallah et al. “Cumulants and correlation functions of net-proton, proton, and antiproton multiplicity distributions in Au+Au collisions at energies available at the BNL Relativistic Heavy Ion Collider”. *Phys. Rev. C* 104.2 (2021), 024902. arXiv: [2101.12413 \[nucl-ex\]](#).
- [11] J. Adam et al. “Nonmonotonic Energy Dependence of Net-Proton Number Fluctuations”. *Phys. Rev. Lett.* 126.9 (2021), 092301. arXiv: [2001.02852 \[nucl-ex\]](#).
- [12] “Beam Energy Dependence of Fifth and Sixth-Order Net-proton Number Fluctuations in Au+Au Collisions at RHIC” (July 2022). arXiv: [2207.09837 \[nucl-ex\]](#).

- [13] Roger Barlow. “Systematic errors: Facts and fictions”. *Conference on Advanced Statistical Techniques in Particle Physics*. July 2002, 134–144. arXiv: [hep-ex/0207026](https://arxiv.org/abs/hep-ex/0207026).

Chapter 6

Experimental results on net-proton cumulants

This is the main chapter pertaining to the goal of the thesis work, i.e., to experimentally probe the QCD phase diagram via cumulants of net-proton number distributions. The prior three chapters focused on the STAR detector, analysis details and techniques employed in the experimental measurement of net-proton cumulants, and estimation of uncertainties. This chapter reports the final results from the analysis of the experimental data.

6.1 Net-proton cumulant measurements

Recall from our discussions in chapter 4; we analyzed Au+Au collisions at nine center-of-mass collision energies: $\sqrt{s_{NN}} = 7.7, 11.5, 14.5, 19.6, 27, 39, 54.4, 62.4,$ and 200 GeV. Collision data from these energies were recorded by the STAR detector during the years 2010 to 2017 as part of the phase-I of the Beam Energy Scan program (BES-I) at RHIC [1, 2]. They allow access to a wide range of baryon chemical potential from $\mu_B \approx 20$ to 420 MeV in the QCD phase diagram. Measurement of net-proton fluctuations

via cumulants of event-by-event net-proton distributions is carried out at all energies. Protons and antiprotons were selected at midrapidity ($|y| < 0.5$) within momentum range $p_T = 0.4 - 2.0$ GeV/c, using STAR's Time-Projection-Chamber (TPC) and Time-of-Flight (TOF) detectors. A special definition of charged particle multiplicity distribution (called Refmult3, see chapter 4 for details) that excluded protons and antiprotons was used to define centrality to avoid self-correlations arising out of overlapping acceptance used for centrality and fluctuation observables. The effect of decay induced self-correlations on fluctuation observables due to choice of centrality were also found to be negligible from a model-based study (we checked for net-proton C_4/C_2 , see appendix 6.8.1 for more discussions). After constructing net-proton distributions from detected (anti-) protons for different centralities, their cumulants are then obtained applying corrections to account for finite detector efficiency and finite centrality width. A careful estimation of statistical and systematic uncertainties on cumulants was then carried out.

Before presenting the cumulants, first, we show event-by-event raw net-proton distribution from all energies.

6.1.1 Event-by-event net-proton number distribution

Figure 6.1 shows raw net-proton distributions constructed using identified protons and antiprotons for top 5% Au+Au collisions from $\sqrt{s_{NN}} = 7.7 - 200$ GeV. By "raw", we mean the distributions are not corrected for detector efficiency and finite centrality width. The distributions are normalized with respect to events. The mean of the distributions shows an increasing trend with decreasing energy. Such a trend is understood to be due to increased baryon stopping and a decrease in antiproton production at low collision energies. The width of the net-proton distribution is largest at $\sqrt{s_{NN}} = 7.7$ GeV among all energies. Wider width coupled with the low number of events (2.2 million) at $\sqrt{s_{NN}} = 7.7$ GeV, results in

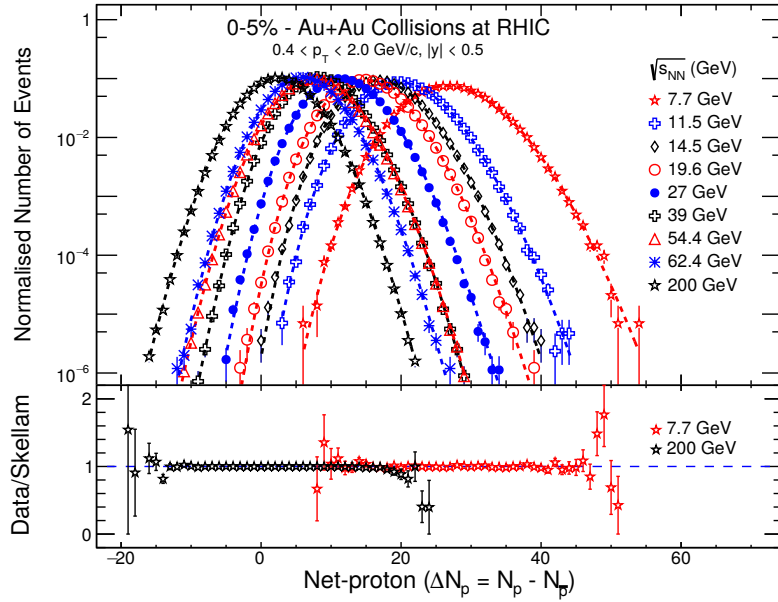


Figure 6.1: Event-by-event net-proton number distributions in central (0-5%) Au+Au collisions from $\sqrt{s_{NN}} = 7.7$ to 200 GeV [3–5]. The distributions are not corrected for detector efficiency and finite centrality width. The dashed lines represent fit with the Skellam function. The lower panel shows the ratio of data to Skellam expectations at $\sqrt{s_{NN}} = 7.7$ and 200 GeV.

statistical uncertainties on net-proton cumulants being largest at this energy compared to others. The Skellam function (difference of two Poisson functions) fit to the distributions is able to describe the mean and width of the distribution, but deviations are seen towards the tail. The differences can be more clearly observed by ratio of Skellam fit to data shown in the lower panel of Fig. 6.1. Since higher-order cumulants are sensitive to the tails, they are expected to deviate from a baseline that assumes a Skellam net-proton distribution. The net-proton distributions from peripheral collisions (70-80% centrality class) are shown in Fig. 6.2. The smaller variation of the distribution's mean and width is observed compared to 0-5% central collisions. The ratio of Skellam fit to data also shows lesser differences towards the tail compared to that for 0-5% centrality. Nonetheless, in neither of the two centrality classes discussed: 0-5% and 70-80%, do we see the net-proton distributions fully

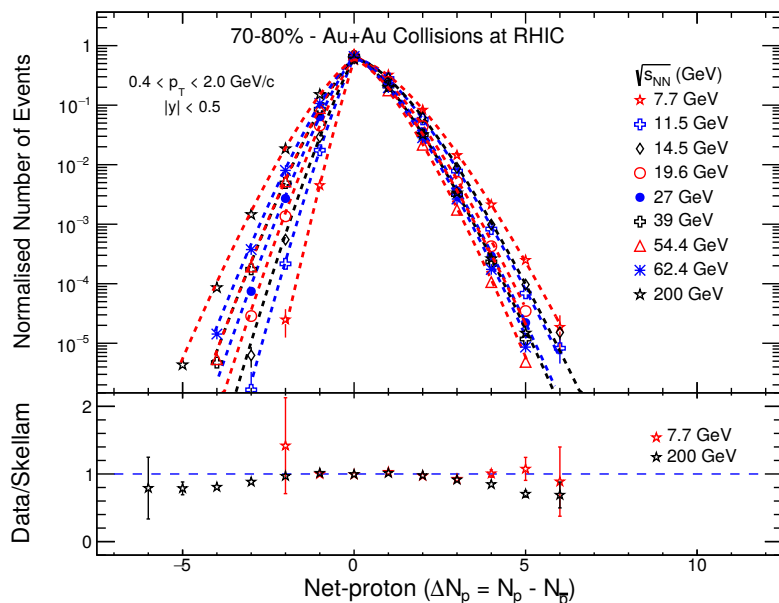


Figure 6.2: Event-by-event net-proton number distributions in peripheral (70-80%) peripheral Au+Au collisions from $\sqrt{s_{NN}} = 7.7$ to 200 GeV [3–5]. The distributions are not corrected for detector efficiency and finite centrality width. The dashed lines represent fit with the Skellam function. The lower panel shows the ratio of data to Skellam expectations for $\sqrt{s_{NN}} = 7.7$ and 200 GeV.

explained by the Skellam function.

6.1.2 Centrality dependence

From the measured raw event-by-event net-proton distributions, cumulants can be calculated. But they need to be corrected for experimental artifacts. To account for finite detection efficiency, an analytical formalism derived with the assumption of a Binomial detector response was employed. The Binomial nature of distribution for detector response has been demonstrated to be a good working assumption for the STAR detector [4, 6]. To correct for volume fluctuations arising from finite centrality width, the event-weighted averaging method: CBWC was used (please refer to Chapter 4 for more details on CBWC and efficiency correction). The cumulant results reported from here onwards are efficiency

and CBWC corrected. The cumulants of net-proton number distribution up to fourth-order ($C_n, n \leq 4$) [3, 4] as a function of collision centrality (presented in terms of the average number of participant nucleons in a centrality) are shown in Fig. 6.3. Up to third-order cumulants,

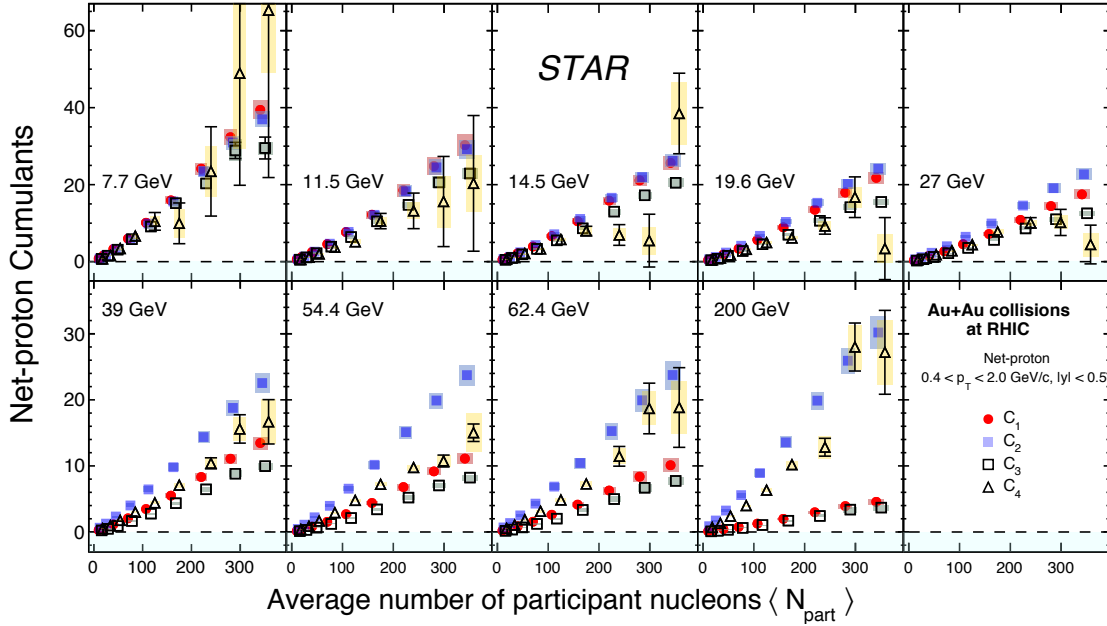


Figure 6.3: Cumulants of net-proton number distribution up to fourth-order in Au+Au collisions from $\sqrt{s_{NN}} = 7.7$ to 200 GeV presented as a function of centrality [3, 4]. Measurements are done with rapidity coverage of $|y| < 0.5$ and momentum coverage of $p_T = 0.4 - 2.0$ GeV/c. The bars and the shaded bands on the data points represent statistical and systematic uncertainties, respectively.

a progressively increasing trend of measurements is observed with increasing collision centrality (increasing $\langle N_{part} \rangle$) at all energies. The trend in net-proton C_1 (mean) can be visualized due to an increase in particle production (favoring matter over anti-matter) from peripheral to central collisions. The C_2 (variance) also increases due to the same reason. Since proton and antiproton production increases with centrality, so does the variance of proton and antiproton distribution. The resulting variance of the net-proton distribution is a constructive combination of the variance of its constituents (for example, a Skellam

distribution's variance is a simple addition of the variance of its constituents). The third-order and fourth-order cumulant, in general, also increases with $\langle N_{part} \rangle$, but at 19.6 and 27 GeV, a dip in C_4 is seen for the 0-5% central collisions. Note that with increasing order of cumulants, the statistical uncertainties on them also increase. An increase in collision centrality also leads to larger uncertainties on cumulants due to increasing variance/width of the net-proton distribution. The data at $\sqrt{s_{NN}} = 7.7$ GeV has the largest statistical uncertainty among all the energies reported.

6.1.3 Energy dependence

From Fig. 6.3, we select cumulants $C_1 - C_4$ from three centralities: 0-5%, 30-40%, and 70-80%, and present them as a function of collision energy in Fig 6.4. The odd-order cumulants C_1 and C_3 monotonically decreases with increasing collision energies for 0-5% centrality. The even-order cumulants C_2 and C_4 show a non-monotonic collision energy dependence for the same centrality, which is particularly sharper for C_4 . Such energy-dependence trends become weaker for 30-40% centrality and almost negligible for 70-80% centrality. The peripheral 70-80% data is close to zero. The dependence of C_1 and C_2 on collision energy is consistent with the observation made from the net-proton distributions shown in Fig. 6.1.

6.1.4 Hyper-order fluctuations

Measurement of net-proton cumulants was also extended to the fifth and sixth order (also called hyper-orders) [6, 7]. As we noted earlier, the higher the order of cumulants, the larger the uncertainties on them. Hence hyper-order fluctuation of net-proton distribution is often presented as ratio of cumulants than the individual cumulants to have better control over uncertainties. The ratio of sixth-to-second order net-proton cumulant (C_6/C_2) from

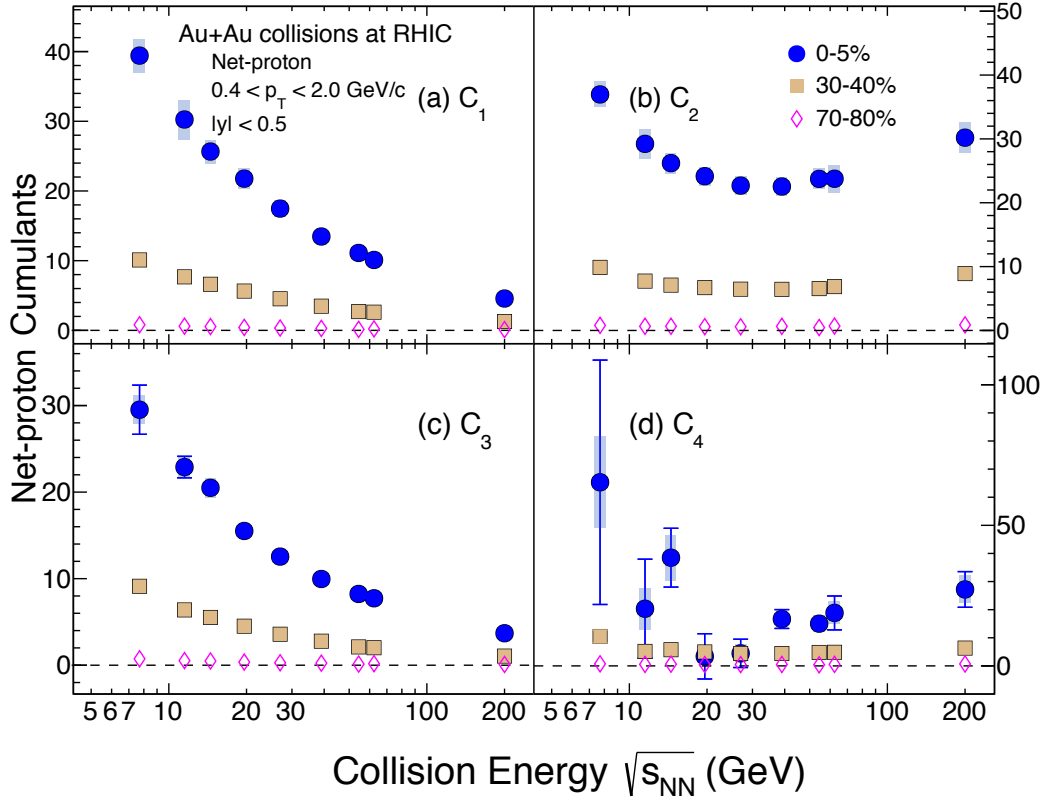


Figure 6.4: Cumulants of net-proton number distribution up to fourth-order for 0-5% (filled circles), 30-40% (filled squares) and 70-80% (open diamond) collision centrality in Au+Au collisions from $\sqrt{s_{NN}} = 7.7$ to 200 GeV [3, 4]. Measurements are done with rapidity coverage of $|y| < 0.5$ and momentum coverage of $p_T = 0.4 - 2.0$ GeV/c. The bars and the shaded bands on the data points represent statistical and systematic uncertainties, respectively.

Au+Au collisions at center-of-mass energies $\sqrt{s_{NN}} = 27, 54.4$ and 200 GeV are shown in Fig. 6.5. The 27 GeV results were obtained using data recorded in the year 2018 of RHIC operation that collected around ~ 300 million minimum bias events. The 200 GeV results were obtained by utilizing data recorded in the year 2010 and 2011 (collectively accounting for ~ 900 million minimum bias events) to increase statistical precision.

The C_6/C_2 measurements for 200 GeV show a progressively decreasing trend from peripheral to central collisions. The data points for $\sqrt{s_{NN}} = 27$ GeV also follow a similar

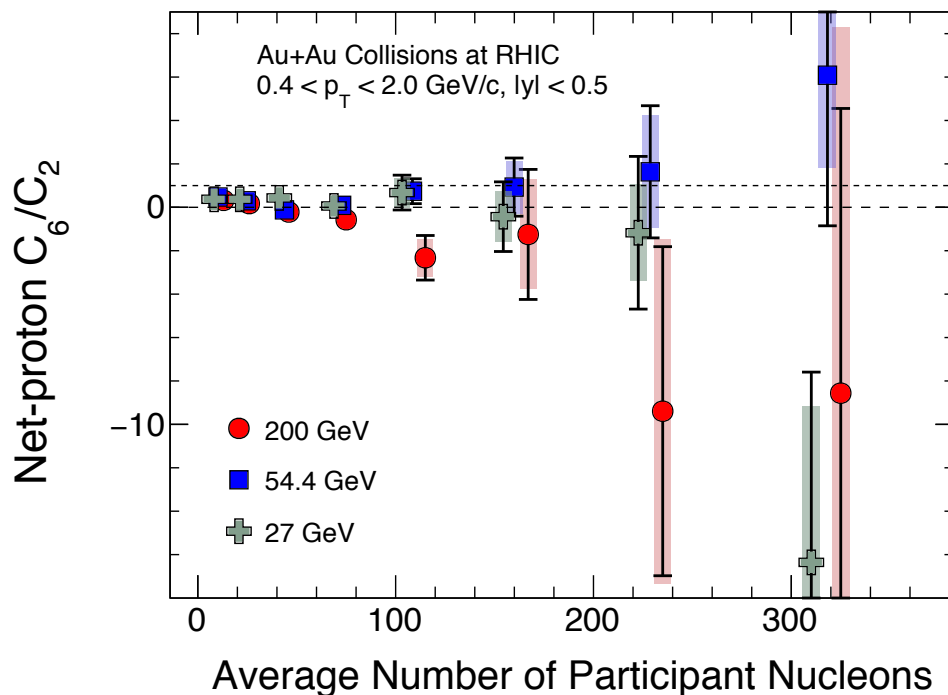


Figure 6.5: Ratio of sixth-to-second order cumulant (C_6/C_2) of net-proton distributions as a function of centrality from Au+Au collisions at $\sqrt{s_{NN}} = 27$ (green crosses), 54.4 (blue squares) and 200 GeV (red circles) [6]. Results from eight centralities: (0-10%, 10-20%, 20-30%, 30-40%, 40-50%, 50-60%, 60-70%, and 70-80%) are presented. Measurements are done with rapidity coverage of $|y| < 0.5$ and momentum coverage of $p_T = 0.4 - 2.0$ GeV/c. The bars and the shaded bands on the data points represent statistical and systematic uncertainties, respectively.

trend from mid-central to central collisions. The measurements at 54.4 GeV show a flat collision centrality dependence and are consistent with zero within uncertainties for central collisions. The measurements at all three energies are closer to unity in peripheral collisions. The large statistical uncertainties observed at 200 GeV is due to the large width of net-proton distribution at this energy compared to the remaining two.

Measurement on the collision energy dependence of ratio of fifth-to-first (C_5/C_1) and sixth-to-second (C_6/C_2) order net-proton cumulants were also carried out. Figure 6.6 shows the net-proton C_5/C_1 and C_6/C_2 as a function of collision energy for 0-40% and 70-80%

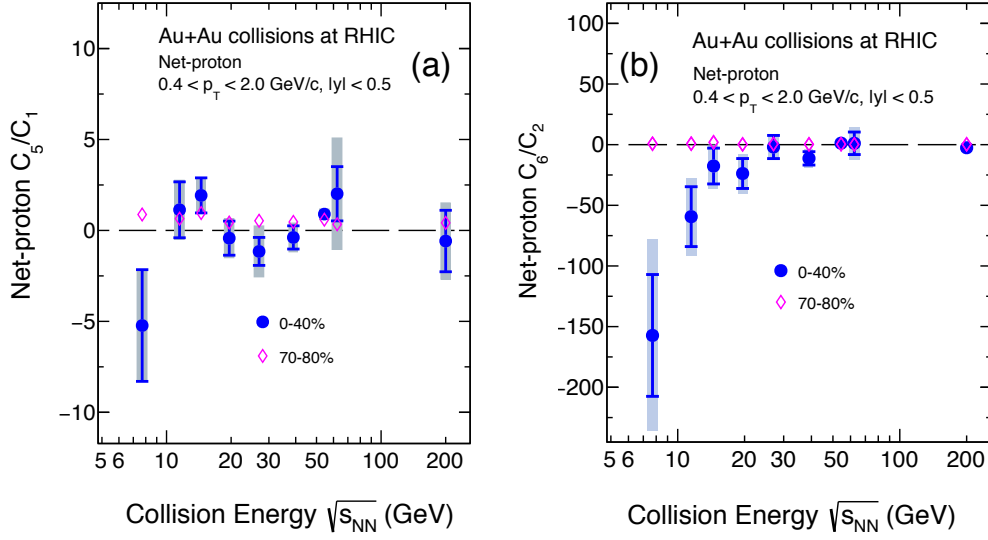


Figure 6.6: Ratio of fifth-to-first order cumulant (C_5/C_1 , panel (a)) and sixth-to-second order cumulant (C_6/C_2 , panel (b)) of net-proton distributions in Au+Au collisions as a function of collision energy from $\sqrt{s_{NN}} = 7.7 - 200$ GeV [7]. Results are presented for 0-40% and 70-80% centrality. Measurements are done with rapidity coverage of $|y| < 0.5$ and momentum coverage of $p_T = 0.4 - 2.0$ GeV/c. The bars and the shaded bands on the data points represent statistical and systematic uncertainties, respectively.

centrality. A wider 0-40% centrality was chosen to improve the statistical significance of the measurements. The C_5/C_1 data points fluctuate around zero and show a weak collision energy dependence for 0-40% centrality. On the other hand, the C_6/C_2 within uncertainties exhibits a decreasing trend with the decrease in collision energy. The peripheral 70-80% data points for both the cumulant ratios are found to be close to zero and show a flat energy dependence.

6.2 Baselines with no QCD criticality and phase transition

Our goal is to use the experimentally measured cumulant to study the QCD phase structure, especially the critical point and QCD phase transition. In this study, the comparison of experimental data to model calculations that do not include any critical point and

phase transition effects is very important to draw clear physics conclusions. The model calculations are used as baselines for the measured net-proton number fluctuations. In this context, we discuss three such models in this section and compare the trends observed in experimental measurements with expectations from the models.

6.2.1 Models

The models employed in comparison with experimental data can be categorized as a purely statistical model, a thermal model, and a transport model. None of these models include either the QCD critical point or the QCD phase transition. They are briefly discussed as follows.

a) Statistical Baseline: Skellam

The statistical baseline is the expectation under the assumption that the fluctuations occur purely due to statistical reasons. One of the widely employed statistical baselines is that of a Skellam baseline [5]. The distribution of difference of two variates that follow independent Poisson distribution is Skellam by nature. In the Skellam model (also often called the Poisson model) considered for net-proton fluctuation, protons and antiprotons are assumed to be Poisson distributed and independent of each other. The cumulants of net-proton distribution under the Skellam model can be obtained analytically by exploiting the following properties: (1) cumulants of two independent variates are additive in nature, and (2) Poisson distribution has a characteristic feature of having identical values for all the order of cumulants, which is equal to its mean. To mathematically show the additive property of cumulants, consider two independent variates X and Y and another variate Z , constructed by their combination ($Z = X \pm Y$). The n^{th} -order cumulant of Z can be obtained by addition of n^{th} -order cumulants of X and Y , i.e., $C_n^Z = C_n^X + (-1)^n C_n^Y$. Using

the additivity formula and invoking the property (2), it can be easily realized that all the odd-order cumulants of a Skellam distribution are identical and equal to the difference in the mean of constituent variates, while all the even-order cumulants are also identical but equal to the sum of the mean of constituent variates. Thus, the ratio of cumulants involving either only odd orders (e.g., C_3/C_1 and C_5/C_1) or only even orders (C_4/C_2 and C_6/C_2) is equal to unity as per the Skellam baseline.

Since a Poisson distribution is characterized by a single parameter, i.e., its mean, the Skellam baseline for net-proton cumulants requires two input parameters: means of proton and antiproton distributions. Taking the experimentally measured mean of proton and antiproton distribution as input parameters, Skellam expectations for all orders of net-proton cumulants/ratio of cumulants are obtained for comparison with experimental data.

b) Thermal model: HRG

The ideal hadron resonance gas (HRG) model consists of a gas of point-like non-interacting hadrons and resonances in thermal equilibrium. The logarithm of the partition function (Z^{ideal}) for such a system in the grand canonical ensemble (GCE) can be expressed in terms of the partition function of its constituents (Z_i^{ideal}) as follows.

$$\ln Z^{ideal} = \sum \ln Z_i^{ideal} \quad (6.1)$$

where the summation over index i runs over all hadrons and resonances. The Z_i^{ideal} is given by the following equation

$$\ln Z_i^{ideal} = \pm \frac{V g_i}{2\pi^2} \int d^3 p [\ln 1 \pm \exp(\mu_i - E)/T]. \quad (6.2)$$

where, V is the system volume, g_i is the degeneracy factor, $\mu_i = B_i \mu_B + S_i \mu_S + Q_i \mu_Q$ is the chemical potential associated with conserved quantum numbers (B , Q , S) of i^{th}

particle, E is the energy, and T is the temperature. The \pm sign is for baryons and mesons, respectively. With the information on the partition function of hadron resonance gas, the pressure and, subsequently, the thermodynamic susceptibility can be obtained (Refer to section 1.4 of chapter 1). Since ratios of cumulants are directly linked to the ratios of susceptibility for a thermalized system, the HRG model provides the thermal baseline for experimentally measured cumulant ratios. There are various extensions to the HRG model where interactions are introduced among hadrons. For example, in excluded-volume HRG (HRG EV), one introduces Van-der-Waal-type repulsive interactions by considering the geometrical size of hadrons as opposed to the point-like size assumed in ideal HRG. Both attractive and repulsive Van-der-Waals interactions can also be incorporated into the HRG model (HRG VDW). Varieties of the HRG models calculation on thermodynamic susceptibilities have been carried out in existing literature [8–14]. Majority of these calculations employ GCE framework where quantum numbers are conserved on an average. But the canonical ensemble (CE) can also be considered in the HRG model calculations, which allow for exact quantum number conservation [15]. Since net-baryon is a conserved quantity over the full phase space, the experimental measurement of net-proton fluctuations is constrained by the requirement of exact baryon number conservation. This effect on net-proton fluctuations is expected to be larger at low center-of-mass collision energies where bulk to the total phase space lies within the analysis acceptance.

c) Transport model: UrQMD

Transport theory aims to map the time evolution of heavy-ion collision from its initial stages till freezeout. The Ultra-relativistic Quantum Molecular Dynamics (UrQMD) model is a hadronic transport model that treats the full space-time evolution of hadrons by employing the transport theory [16]. It is an event generator simulating the transportation of hadrons

event by event. The model does not rely on an equilibrium assumption. The particle production in this model happens via the fragmentation of strings that are made of valence quarks of the original colliding hadrons, decays, and resonance excitations. Effects like rescattering, baryon stopping at lower energies, and baryon number conservation are also included, making it a suitable model to provide baselines for measurements in collision energies at RHIC.

6.2.2 Cumulant ratios and comparison with models

We now present a comparison of the experimental measurements with the expectations from the aforementioned models. Since various models (including lattice QCD and QCD-based models) actually calculate thermodynamic susceptibilities instead of cumulants, it is convenient to use the ratios of experimentally measured cumulants to facilitate a direct comparison with model expectations (Refer to section 4 of chapter 1 for details). From the measured net-proton cumulants reported in the earlier section, ratios of cumulants are constructed. The net-proton cumulant ratio C_2/C_1 , C_3/C_2 , C_4/C_2 , C_5/C_1 and C_6/C_2 are shown in Fig. 6.7 as a function of collision energy [3, 4, 6, 7]. The calculation from the ideal HRG model in GCE, Skellam/Poisson baseline, and UrQMD model are also presented for comparison. With the impression that number of produced particles in peripheral collisions are quite small to constitute a thermodynamic system, often measurements from peripheral collisions are used to serve as experimental baselines to those from central collisions.

The cumulant ratio C_2/C_1 smoothly increases with collision energy, while C_3/C_2 decreases. The observed trend is reproduced by UrQMD, HRG, and Skellam baselines. Nonetheless, there are quantitative differences with respect to data, more so for higher-order cumulant ratios. For C_4/C_2 , the experimental measurements from 0-5% central collisions decrease with decreasing collision energy till 19.6 GeV; then a rise is seen within

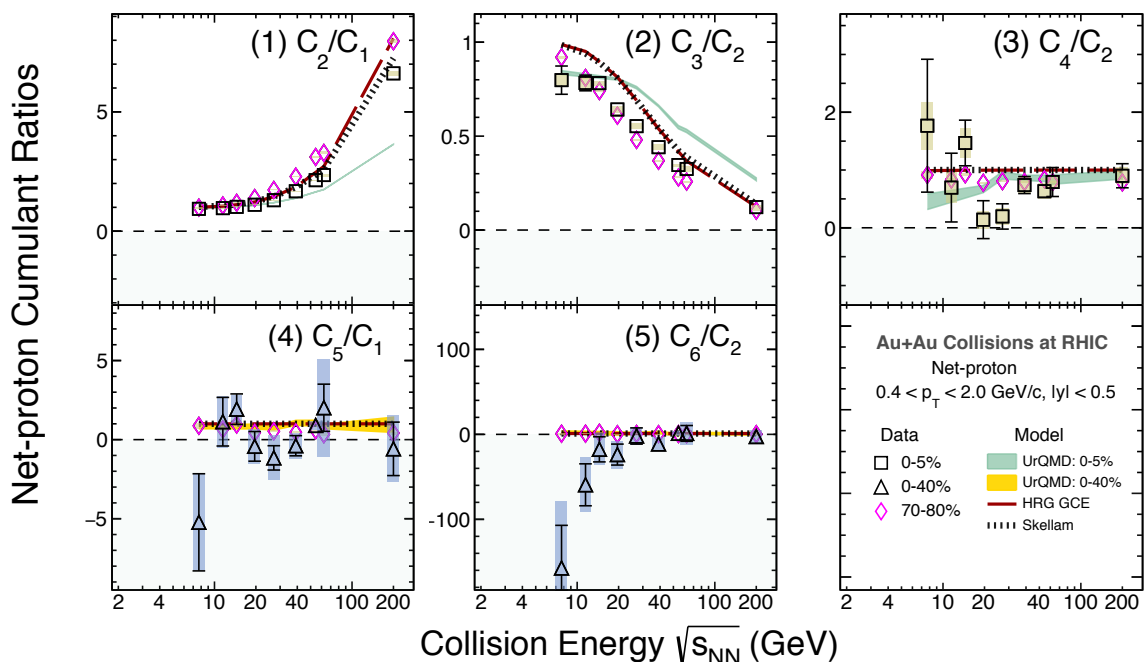


Figure 6.7: Ratio of cumulants up to sixth-order of net-proton distributions in Au+Au collisions as a function of collision energy from $\sqrt{s_{NN}} = 7.7 - 200$ GeV. Results are presented for 0-5% (for cumulant ratio up to fourth-order), 0-40% (for hyper-order cumulant ratios), and 70-80% centrality. For hyper-order cumulant ratios, a wider 0-40% centrality range is considered to improve the statistical precision of measurement. The bars and the shaded bands on the data points represent statistical and systematic uncertainties, respectively. The expectation from the UrQMD model, ideal HRG (GCE) model, and Skellam baseline are also presented [3, 4, 6, 7].

uncertainties when energy is lowered further. None of the model expectations presented show such a pattern in energy dependence. The HRG and Skellam baselines for C_4/C_2 always remain at unity, and the UrQMD calculation only shows decreasing trend with a lowering of energy. The peripheral (70-80%) C_4/C_2 data points show a flat energy dependence but remain below unity. The C_5/C_1 measurements for 0-40% centrality oscillate around zero, while the C_6/C_2 decreases with the lowering of collision energy for the same centrality. Expectations from all three models and peripheral (70-80%) data show a weak energy dependence for both of these hyper-order cumulant ratios. Particularly, the calcu-

lations from HRG and Skellam baseline are at unity across all collision energies. There is a good overall agreement between the Skellam baselines and HRG calculations presented for all cumulant ratios.

In addition to the centrality and energy dependence of cumulant ratios, phase-space acceptance dependence has also been studied. With decreasing acceptance, the cumulant ratios approach their Skellam limit (see appendix 6.8.2 for more details).

6.3 Test of QCD thermodynamics

6.3.1 Proposed theoretical prediction

In the experimental exploration of the QCD phase diagram using fluctuation measurements, it is important to test whether the matter created in heavy-ion collisions is governed by QCD thermodynamics. In this regard, the predictions made by first-principle calculations, such as lattice QCD (LQCD) are of immense help. Ratio of thermodynamic susceptibilities associated with conserved charges (equivalent to the ratio of their cumulants) can be calculated from LQCD. These calculations have been extended to finite baryon chemical potential, $\mu_B \leq 110$ MeV (which corresponds to the collision energy range of $\sqrt{s_{NN}} \geq 39$ GeV) using Taylor Series expansion about vanishing μ_B . The LQCD predicts a specific ordering of net-baryon cumulant ratios for a system obeying QCD thermodynamics [17]. The predicted ordering of cumulant ratios for thermalized QCD matter is as follows.

$$\boxed{C_3/C_1 > C_4/C_2 > C_5/C_1 > C_6/C_2.} \quad (6.3)$$

Note that the ordering given by equation 6.3 is in contrast with the calculation from the HRG model with an ideal gas equation of state in a grand canonical ensemble, where all four cumulant ratios are identical to unity.

6.3.2 Experimental results and model comparison

To test the LQCD prediction using experimental data, we employ the measurements on the cumulant ratio of net-proton (taken as proxy for net-baryon) distribution in Au+Au collisions. The four cumulant ratios: C_3/C_1 , C_4/C_2 , C_5/C_1 , and C_6/C_2 , at nine center-of-mass collision energies from $\sqrt{s_{NN}} = 7.7$ to 200 GeV for 0-40% collision centrality are presented in Fig. 6.8 [7]. Calculations from the UrQMD model, LQCD, and a QCD-based model called the functional renormalization group (FRG) [18] are also shown.

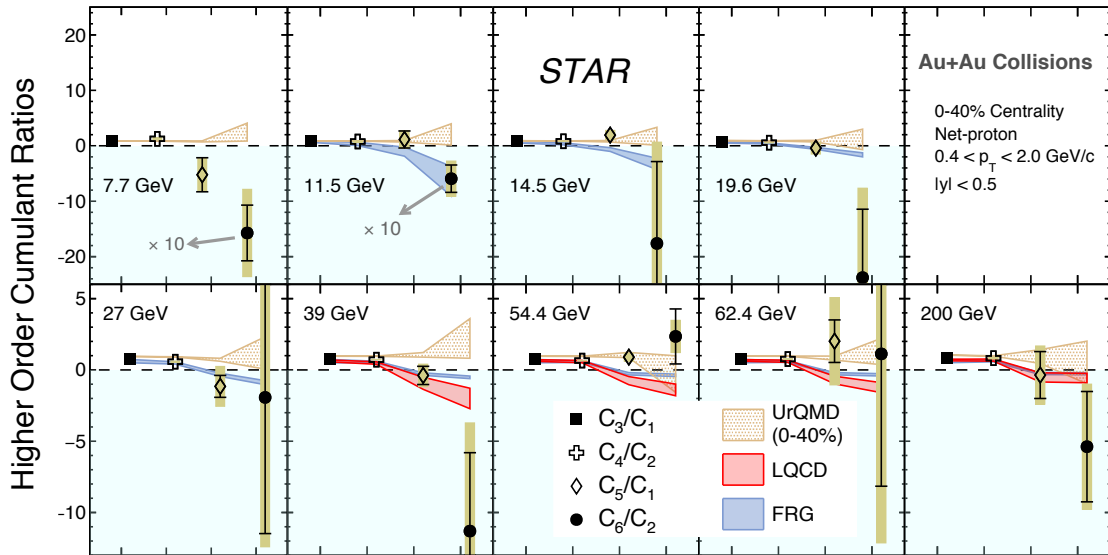


Figure 6.8: Cumulant ratios of net-proton distributions: C_3/C_1 (filled square), C_4/C_2 (open cross), C_5/C_1 (open diamond) and C_6/C_2 (filled circle), in 0-40% Au+Au collisions from 7.7 GeV to 200 GeV [7]. The bars and the shaded bands on the data points represent statistical and systematic uncertainties, respectively. The red, blue, and brown bands represent LQCD (39 – 200 GeV) [17], FRG (7.7 – 200 GeV) [18] and UrQMD calculations (0-40% centrality), respectively. The C_6/C_2 data at 7.7 and 11.5 GeV are scaled down by a factor of 10 for clarity of presentation.

Within uncertainties, an overall consistency is seen between the LQCD predicted ordering and the ordering exhibited by the measured cumulant ratios from 0-40% centrality over the whole collision energy range reported. Note that although at 54.4 and 62.4 GeV,

the hierarchy is not as clear as at other energies within large uncertainties. However, these two energies lie within a wide range of collision energies $\sqrt{s_{NN}} = 7.7$ to 200 GeV where the QCD predicted ordering is observed. While the calculations from the QCD-based FRG model are in agreement with the predicted hierarchy, calculations from the hadronic transport model UrQMD do not show any clear ordering within uncertainties.

6.4 Probing the QCD critical point

6.4.1 Proposed theoretical prediction

Higher order cumulants of conserved charges are sensitive to the QCD critical point (CP) due to their relation with the correlation length (ξ) of the medium formed in heavy-ion collision experiments. The correlation length diverges for a static and infinite system as it approaches criticality. The sudden growth of correlation length at criticality results in the divergence of thermodynamic response functions, such as susceptibility. However, in heavy-ion collisions, such a divergence of correlation length is limited by the femto-scopic size of the medium created and its short-lived and dynamically evolving nature [19]. Fortunately, model calculations suggest that the higher the order of cumulants higher its sensitivity to ξ [20]. For example, while variance(σ^2) varies as $\sigma^2 \sim \xi^2$, the kurtosis (κ) depends as $\kappa \sim \xi^7$. Thus, enhanced critical signals are expected with higher-order cumulants. The exponent of ξ on which a certain order cumulant depends upon is universal. In view of the static critical phenomena, the QCD critical point falls into the Ising universality class. The linear sigma model qualitatively predicts the universal behavior of the kurtosis of the order parameter fluctuations, *i.e.*, of the σ field near the CP. By introducing coupling of the σ -field with particles, fluctuation of σ -field can be converted to those of particle number. As shown in Fig. 6.9, upon approaching the CP from the crossover side, the

kurtosis of the order parameter is universally negative. Receding past the CP towards the region of the first-order phase transition, it becomes positive. In terms of particle number fluctuation, such a sign change would imply that there is a baseline/background fluctuation, and kurtosis shows deviation below the baseline when approaching CP from the crossover side and rises above the baseline after passing the CP. As the system moves far away from the basin of attraction, kurtosis falls back to the baseline. Such a dependence of scaled

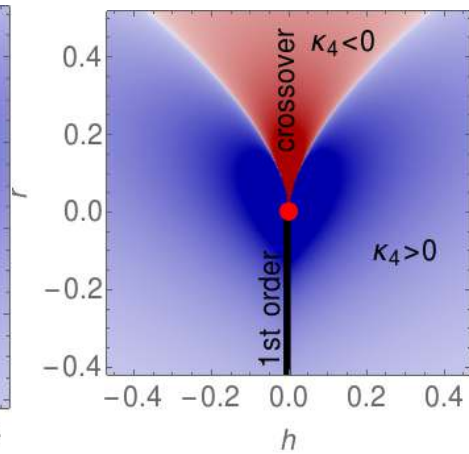


Figure 6.9: Quartic cumulant κ_4 of the Ising model magnetization near the critical point (shown as red point) [20]. The y axis is the reduced temperature, and the x axis reflects the external ordering field.

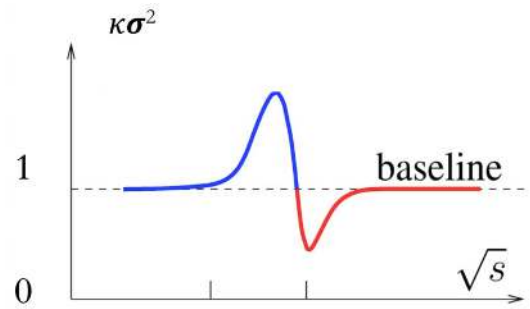


Figure 6.10: A sketch depicting the behavior of net-proton kurtosis as a function of collision energy $\sqrt{s_{NN}}$ in the presence of QCD critical point from linear sigma model calculations [20].

kurtosis $\kappa\sigma^2$ (scaled by variance) of net-proton number is shown as a sketch diagram in Fig. 6.10. Thus, the QCD critical point-induced correlations results in the non-monotonic collision energy dependence of net-proton $\kappa\sigma^2$ as per the linear sigma model. Such energy dependence trend in the presence of a critical point is also predicted by several other QCD-based models like the Polyakov loop extended Quark Meson Model (PQM) [21] and Nambu–Jona-Lasinio (NJL) model [22].

6.4.2 Experimental results and model comparison

To search for critical point induced signal, experimental measurements of net-proton C_4/C_2 (same as $\kappa\sigma^2$) were carried out in Au+Au collisions across a wide range of collision energies from $\sqrt{s_{NN}} = 7.7 - 200$ GeV [3, 4]. The collision energy dependence of measurements, along with various non-critical baselines, are presented in Fig. 6.11.

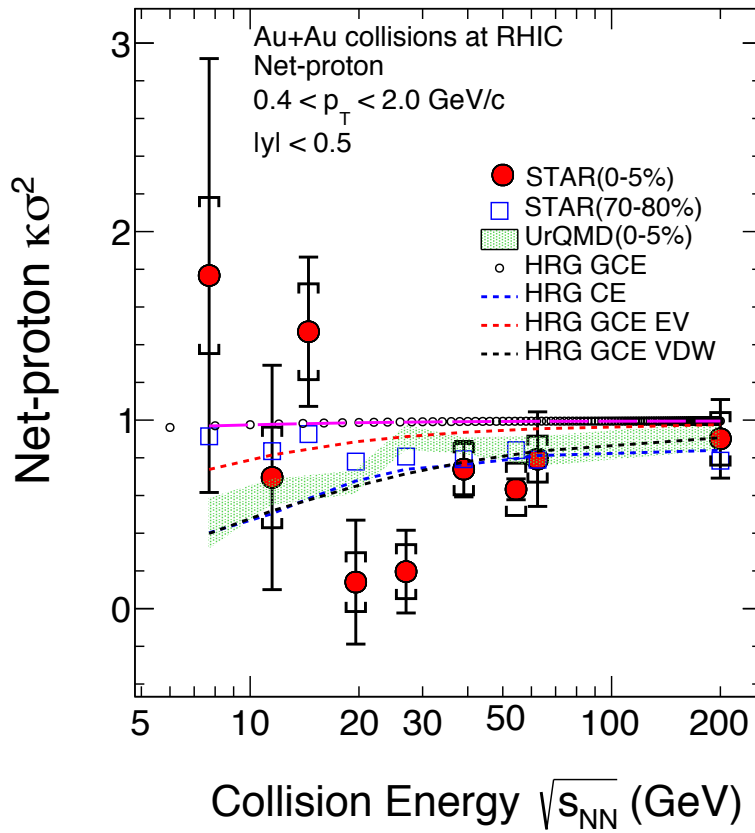


Figure 6.11: The ratio of fourth to second-order cumulant, C_4/C_2 (same as $\kappa\sigma^2$) of net-proton distributions in Au+Au collisions as a function of collision energies over the range $\sqrt{s_{NN}} = 7.7 - 200$ GeV [3–5]. The results are shown for 0-5% and 0-80% collision centrality. The bars and brackets on the data points represent the statistical and systematic uncertainties, respectively. Also presented are expectations from various variants of the HRG model and the UrQMD model [5]. The Skellam baseline for C_4/C_2 is at unity.

The measurements from the most central 0-5% collisions exhibit a non-monotonic

variation with collision energy. The non-monotonic trend is driven by low collision energies and is neither reproduced by the hadronic transport model UrQMD nor by various variants of the HRG model. Such a trend is also not seen in peripheral 70-80% collision data which instead show a weak collision energy dependence and remain smaller than the Skellam baseline at unity. The expectation from ideal-HRG (HRG GCE in the figure) is consistent with the Skellam baseline. The HRG model calculations in grand canonical ensemble considering: (A) Van-der-Waals type attractive and repulsive interactions (HRG GCE VDW) and (B) only repulsive interactions (HRG GCE EV) remain consistently below unity and grow increasingly smaller with the decrease in collision energy. HRG canonical ensemble (HRG CE) and UrQMD model, both of which incorporate exact baryon number conservation, show progressively increased suppression of C_4/C_2 with decreasing energy. Thus, in contrast to the non-monotonic trend of the 0-5% centrality measurements, all the presented models and 70-80% centrality data show a monotonic variation with collision energy. The observed non-monotonic collision energy dependence of C_4/C_2 for 0-5% centrality is qualitatively consistent with expectation from the linear sigma model calculation that includes a QCD critical point.

The deviation of $\kappa\sigma^2$ measurements in 0-5% centrality from various non-critical baselines considered in Fig. 6.11 is quantified in terms of the number of standard deviation (σ) and shown in Fig. 6.12 as a function of collision energy. Also presented is the case where the peripheral 70-80% data serves as a baseline to the 0-5% central measurements. Irrespective of the choice of baseline, the 0-5% $\kappa\sigma^2$ measurements always show positive as well as negative deviation from the baseline at a level of $\lesssim 3\sigma_{tot}$ (σ_{tot} is the total uncertainties) across the whole collision energy range. The deviations above and below the baselines are largest at low collision energies, $\sqrt{s_{NN}} \leq 27$ GeV. These results are indicative of the robustness of non-monotonic collision energy dependence of 0-5% $\kappa\sigma^2$ measurements

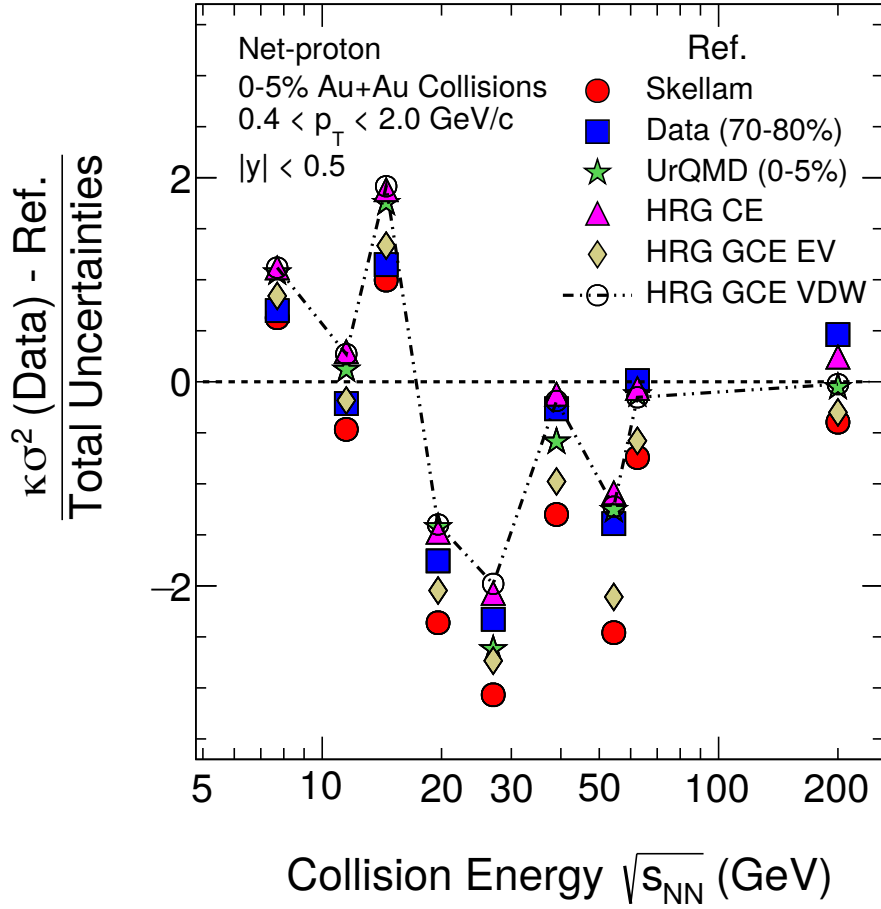


Figure 6.12: Difference of measured $\kappa\sigma^2$ of net-proton distribution in 0-5% Au+Au collisions from calculations from UrQMD, various variants of HRG, Skellam baseline, and measured 70-80% peripheral data [3–5]. The obtained differences are scaled with total uncertainties and presented as a function of collision energy over the range $\sqrt{s_{NN}} = 7.7 - 200$ GeV. The total uncertainties are evaluated by adding the statistical uncertainties and systematic uncertainties in quadrature (uncertainties in model calculations, if any, are also included in the evaluation of total uncertainties by adding in quadrature).

with respect to various baselines.

To corroborate our findings on the differences between the measurements and model calculations, a χ^2 test was performed between data and model expectations for the collision energy range $\sqrt{s_{NN}} = 7.7 - 27$ GeV and corresponding right-tailed p -value was calculated [3,

4]. The right-tailed p -value is defined using the following formula.

$$p - \text{value} = 1 - \text{cdf}_{\chi^2, d}(\chi_c^2). \quad (6.4)$$

where, $\text{cdf}_{\chi^2, d}$ represents the cumulative distribution function of the χ^2 with d degrees of freedom and χ_c^2 denotes the calculated value of χ^2 . Given the number of degrees of freedom and calculated χ^2 score, the right-tailed p -value is obtained using the table of the probability distribution of χ^2 [23]. A standard criterion on right-tailed p -value used to ascertain a significant deviation between the data and model calculation is $p < 0.05$. The p -values from the χ^2 test between data and calculations from the UrQMD model and various variants of the HRG model are summarized in table 6.1. The small p -values ($p < 0.05$) derived from the χ^2 test demonstrate that the 0-5% $\kappa\sigma^2$ measurements significantly differ from model expectations.

Table 6.1: The right tail p -value obtained from χ^2 test between experimentally measured net-proton C_4/C_2 in 0-5% centrality and expectations from UrQMD model and various variants of HRG models using Grand canonical ensemble: ideal HRG (HRG GCE), HRG with excluded volume (HRG GCE EV) and using canonical ensemble (HRG CE) calculated over the collision energy range of $\sqrt{s_{NN}} = 7.7 - 27$ GeV.

Model	UrQMD	HRG GCE	HRG EV	HRG CE
Right tailed p -value	0.0221	0.0053	0.045	0.0145

Significance calculation

A mathematical way to validate the non-monotonic energy dependence of net-proton $\kappa\sigma^2$ in 0-5% centrality is to fit the measurements with a function that best describes the energy dependence trend, evaluate the function's derivative, and then look for a change in sign of the derivatives as a function of collision energy. The ratio of $\kappa\sigma^2$ measurements relative to baselines from Skellam, HRG CE, and UrQMD model along with their respective polynomial fits are shown in Fig. 6.13 as a function of collision energy from $\sqrt{s_{NN}} = 7.7$ to

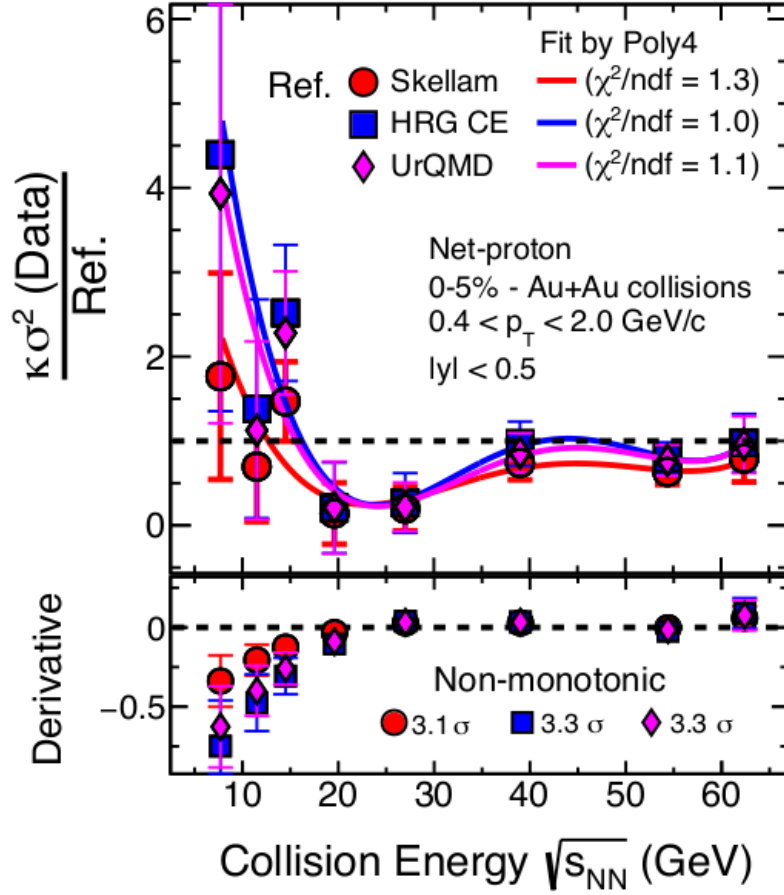


Figure 6.13: The ratio of measured net-proton $\kappa\sigma^2$ from 0-5% central Au+Au collisions with expectations from Skellam baseline, HRG model with canonical ensemble (HRG CE), and UrQMD over the collision energy range $\sqrt{s_{NN}} = 7.7 - 62.4$ GeV [3–5]. The bars on the ratios represent total uncertainties obtained by adding statistical and systematic uncertainties in quadrature (uncertainties in model calculations, if any, are also included in the evaluation of total uncertainties by adding in quadrature). The polynomial fits to the obtained ratios with respect to Skellam, HRG CE, and UrQMD calculations are shown as red, magenta, and blue lines, respectively. The chi-square values per degree of freedom from these fits are also mentioned. Derivatives of the polynomial fit functions from the three cases are shown in the lower panel for each energy. The bars on derivatives are the total uncertainties obtained by the quadrature sum of statistical and systematic uncertainties.

62.4 GeV. The values of $\chi^2/n.d.f.$ close to unity indicate that the polynomial fits describe the data reasonably well. The derivative of the fitted polynomial functions (shown in

lower panels of Fig. 6.13) changes sign as a function of collision energy, demonstrating the non-monotonic energy dependence of the measurements. The statistical and systematic uncertainties on derivatives are found using the sampling distribution of derivatives obtained by randomly varying the data points at each energy within their respective statistical and systematic uncertainties and then re-fitting them with the polynomial function. They are then added in quadrature to obtain total uncertainties on derivatives. Since the data point at $\sqrt{s_{NN}} = 200$ GeV is far away in the collision energy axis, it was excluded to have a better description of the energy trend using polynomial fits. Moreover, the theoretical predictions on the location of critical point have much larger values of μ_B than that corresponding to $\sqrt{s_{NN}} = 200$ GeV.

The significance of the observed non-monotonicity of measurements over the collision energy $\sqrt{s_{NN}} = 7.7 - 62.4$ GeV compared to various baselines has been quantified using a statistical procedure to be at the level of $3.1 - 3.3\sigma$ [3, 4]. The procedure undertaken is described as follows. Let's consider the case of the Skellam baseline shown in Fig. 6.13. We note that the energy dependence of measurements is fitted with a fourth-order polynomial function yielding a $\chi^2/n.d.f \sim 1.3$. The polynomial function of fourth-order among all orders gives the best fit to data. The measurements at each energy were randomly varied within their total Gaussian uncertainties (obtained by quadrature sum of statistical and systematic uncertainties) simultaneously. The newly obtained energy dependence of measurements was re-fitted with a fourth-order polynomial function, and derivatives were calculated. This process was repeated a million (1000000) times (we call these trials). Of these million trials, there are 1143 such trials where derivatives at all the energies had the same sign, indicating that the function was monotonic. Thus, the probability of trials that had at least one energy with the sign of derivative different than the rest is

$1 - 1143/1000000 = 0.99886$. This probability corresponds to a 3.1σ effect. Using this procedure, the observed non-monotonicity of $\kappa\sigma^2$ with respect to HRG CE and UrQMD baselines was found to be of 3.3σ significance.

We also repeated the statistical study with lower order cumulant ratios, C_2/C_1 and C_3/C_2 and found that while C_3/C_2 was non-monotonic at a level of 1σ , C_2/C_1 had a monotonic collision energy dependence with 3.4σ significance over the range $\sqrt{s_{NN}} = 7.7 - 62.4$ GeV (see appendix 6.8.3 for more details). Hence with the increase in the order of cumulants, the energy dependence changes from monotonic to non-monotonic, suggesting their increased level of sensitivity.

6.5 Probing the crossover

6.5.1 Proposed theoretical prediction

The QCD critical point marks the end of the first-order phase transition and the beginning of the crossover in the QCD phase diagram. If both the crossover and first-order phase transition can be experimentally established, applying basic thermodynamic arguments, the existence of a QCD critical point is guaranteed.

The theoretical guidance to search for crossover comes from first-principle lattice QCD (LQCD) computations. LQCD and as well as QCD-based FRG model incorporate a crossover quark-hadron transition in their calculations. Up to the fourth order of net-proton/net-baryon cumulant ratios, the sign of experimental measurements, as well as various model calculations, are positive. These model calculation includes LQCD and QCD-based model FRG and also those without any phase transition effects like the UrQMD and HRG model. It is only after extending the order of cumulant ratios to five and six (also collectively called hyper-orders) do the model calculations show a distinct difference in

sign based on the absence or presence of QCD phase transition.

LQCD calculations that include a crossover quark-hadron phase transition predict negative signs of fifth and sixth-order net-baryon cumulant ratios in the vicinity of the transition temperature. Using the Taylor series expansion technique about vanishing μ_B , calculations have been extended to $\mu_B \leq 110 \text{ MeV}$ [17, 24]. As seen from panel (a) of Fig 6.14, the fifth and sixth-order net-baryon cumulant ratios from LQCD grow more negative with decreasing $\sqrt{s_{NN}}$ (alternately, increasing μ_B). The QCD-based model FRG also predicts the same sign and trend for both of these observables [18] over a wide μ_B range 20 – 420 MeV corresponding to central Au+Au collisions at $\sqrt{s_{NN}} = 200 - 7.7 \text{ GeV}$. Panel (b) of Fig 6.14 shows net-baryon C_6/C_2 from the FRG model as a function of collision energy. In contrast, the ideal HRG model predicts a positive value (equal to unity) of the hyper-order cumulant ratios.

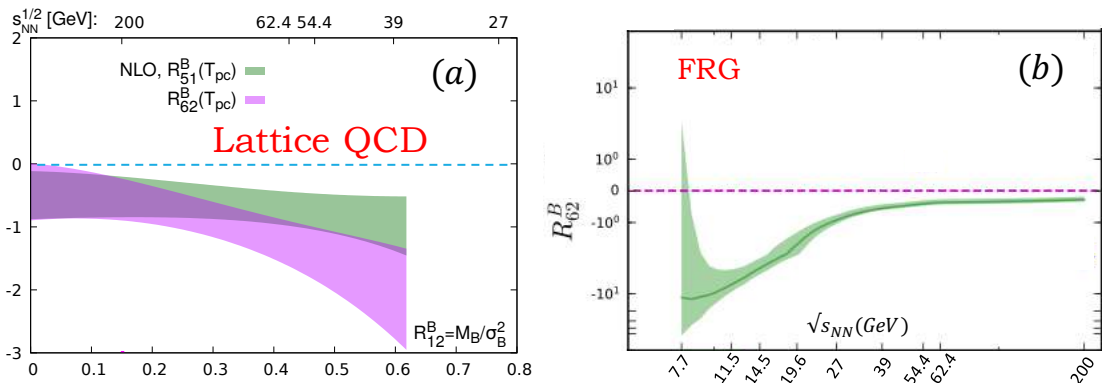


Figure 6.14: Panel (a): Ratio of fifth-to-first (R_{51}^B) and sixth-to-second (R_{62}^B) order net-baryon number susceptibility (equivalently cumulant ratios C_5/C_1 and C_6/C_2) as a function of collision energy from LQCD [17]. Panel (b): R_{62}^B from FRG model as a function of collision energy [18].

Thus, the signal for crossover search constitutes a negative sign of net-baryon hyper-order cumulant ratios that increase in magnitude with decreasing collision energy.

6.5.2 Experimental results and model comparison

Hyper-order cumulants of net-proton (as proxy for net-baryon) number distribution is measured in Au+Au collisions from center-of-mass energy $\sqrt{s_{NN}} = 7.7$ to 200 GeV [6, 7]. Since, we are now extending cumulants to even higher-order than earlier, a wider 0-40% collision centrality was chosen to increase the statistical precision of measurements. The

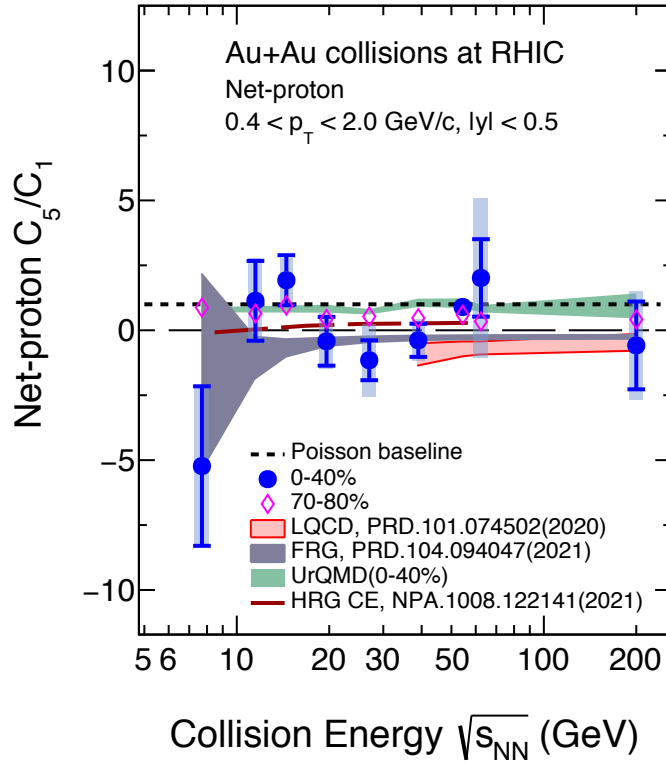


Figure 6.15: Cumulant ratio C_5/C_1 of net-proton distribution in Au+Au collision as a function of collision energy from $\sqrt{s_{NN}} = 7.7$ to 200 GeV [7]. Measurements are presented for 0-40% (filled circles) and 70-80% centralities (open diamonds). The bars and the shaded bands on the data points represent statistical and systematic uncertainties, respectively. Calculations from LQCD [17] (red band), FRG [18] (grey band), HRG CE [15] (dashed brown line), Poisson baseline (dotted black line), and UrQMD (green band) models are also presented.

net-proton C_5/C_1 and C_6/C_2 as a function of collision energy are presented in Fig. 6.15 and Fig. 6.16, respectively. Results from peripheral 70-80% collisions and theoretical

calculations from LQCD, FRG, HRG CE, Poisson baseline, and UrQMD model are also presented along with the 0-40% measurements.

The net-proton C_5/C_1 from 0-40% centrality shows weak dependence on collision energy. While LQCD and FRG predicted a negative sign of C_5/C_1 , the experimental measurements fluctuate about zero at a level of $\lesssim 2.2\sigma_{\text{tot}}$ significance (σ_{tot} is the total uncertainties obtain by quadrature sum of statistical and systematic uncertainties). The peripheral 70-80% data, Poisson baseline, and UrQMD calculation remain consistently positive at all collision energies. The HRG CE expectations are also positive, except at the lowest collision energy.

While C_5/C_1 does not provide any clear trend within current uncertainties, the more sensitive observable for crossover search, i.e. the C_6/C_2 shows interesting features. Within uncertainties, the C_6/C_2 from 0-40% centrality are found to be increasingly negative with decreasing collision energy. The deviations of measurements from zero are within $1.7\sigma_{\text{tot}}$ at all the energies. Both the aspects: the negative sign of measurements and their trend of being progressively negative with lowering of energy are consistent with the sign and trend predicted by LQCD calculations (for $\mu_B \leq 110$ MeV) with a crossover quark-hadron transition. The QCD-based FRG model also predicted the same sign and trend. In contrast, the peripheral 70-80% data, calculations from the UrQMD model, and the Poisson baseline have a flat collision energy dependence and are either positive or consistent with zero within uncertainties. The HRG CE calculations are also positive for most of the collision energies ($\sqrt{s_{NN}} > 19.6$ GeV) and become negative only at lower energies.

The C_6/C_2 (0-40%) at 7.7 GeV has the largest uncertainty. Since this is the energy with the lowest event statistics (1.2 million events in 0-40% centrality) among all, within the current statistical limitations, the robustness of the negative sign of C_6/C_2 observed at 7.7 GeV was verified by performing additional studies that include: (a) measurement of

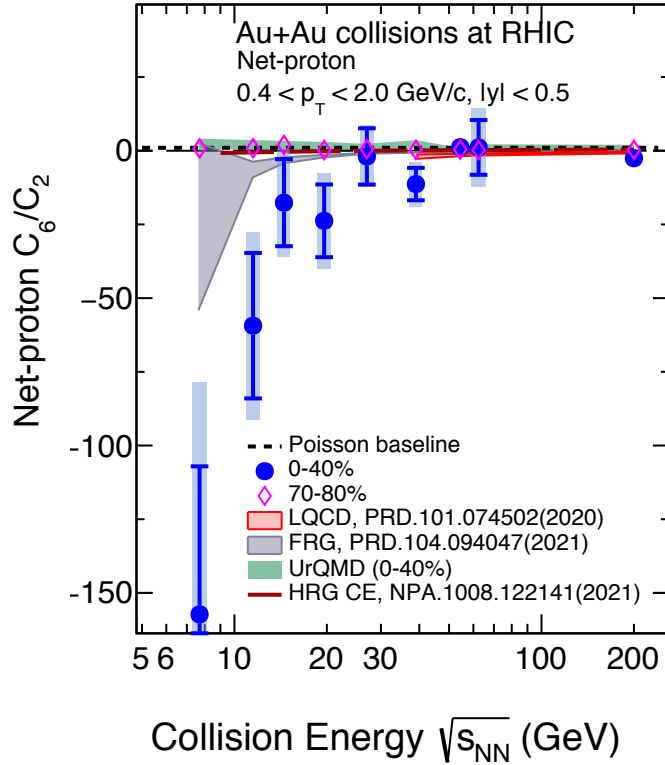


Figure 6.16: Cumulant ratio C_6/C_2 of net-proton distribution in Au+Au collision as a function of collision energy from $\sqrt{s_{NN}} = 7.7$ to 200 GeV [7]. Measurements are presented for 0-40% (filled circles) and 70-80% centralities (open diamonds). The bars and the shaded bands on the data points represent statistical and systematic uncertainties, respectively. Calculations from LQCD [17] (red band), FRG [18] (grey band), HRG CE [15] (dashed brown line), Poisson baseline (dotted black line at unity), and UrQMD (green band) model are also presented.

K-statistics [25] which are known to be unbiased estimators of a population's cumulants and (b) examining the sample size dependence of C_6/C_2 which involved the creation of random samples with varying number of event statistics from the data at $\sqrt{s_{NN}} = 7.7$ GeV. These checks can be found in the appendix 6.8.4 and 6.8.5.

Significance calculation

We noted that the C_6/C_2 (0-40%) exhibited increasing negative values with decreasing

energy. The overall significance of observing negative C_6/C_2 values in more than half of all collision energies reported is obtained to be 1.7σ using a statistical procedure. The steps considered are discussed as follows. The C_6/C_2 data points are randomly varied simultaneously at all the nine collision energies from $\sqrt{s_{NN}} = 7.7$ to 200 GeV within their respective total Gaussian uncertainties (obtained by quadrature sum of statistical and systematic uncertainties) a million times. Of these million times, the number of times at least five or more collision energies had negative C_6/C_2 are counted. This probability (95.3522%) converted to significance corresponds to a 1.7σ effect.

6.6 Probing the first-order phase transition

6.6.1 Proposed theoretical prediction

The theoretical attempts to study the first-order phase transition and QCD phase structure at large μ_B , in general, are quite challenging due to the issue of sign problem encountered by first-principle calculations, such as from LQCD. Hence experimental evidence of first-order phase transition is very crucial.

Various model studies have been done to aid in the search for first-order phase transition. One such study exploits the two-component/bimodal nature of proton multiplicity distribution near a first-order phase transition. A first-order phase transition is characterized by the presence of a mixed phase. The multiplicity distribution of charged particles, such as protons, could develop a two-component/bimodal structure due to contributions from the two distinct phases constituting the mixed phase. An example of a two-component distribution is shown in Fig 6.17. Mathematically a two-component distribution ($P(N)$) can be expressed as follows;

$$P(N) = (1 - \alpha)P_A(N) + \alpha P_B(N), \quad (6.5)$$

where $P_A(N)$ and $P_B(N)$ are the probability distribution of the two constituents, and the parameter α (such that $\alpha \leq 1$) specifies their relative contribution.

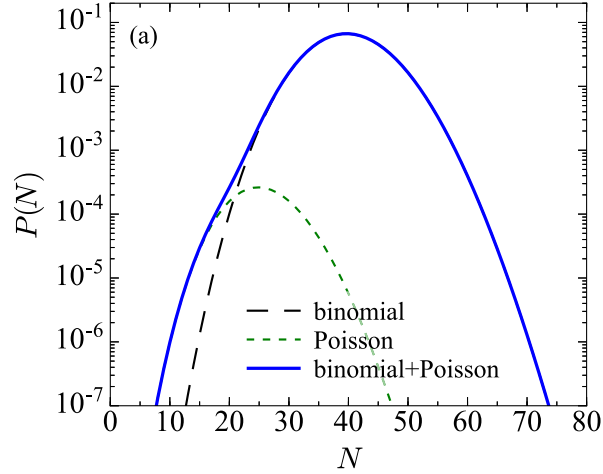


Figure 6.17: A pictorial representation of a two-component/bimodal distribution with Poissonian and Binomial distribution as its constituents. Figure adapted from Ref. [26].

The two-component structure could lead to an interesting behavior of factorial cumulants. Constructing a two-component distribution comprising of a Binomial and Poissonian by taking inputs from experimental data on proton factorial cumulants up to fourth-order, the authors of Ref. [26] found that the resulting distribution is characterized by a large value of higher-order factorial cumulants. Not only were they large, but with increasing order, the factorial cumulants rapidly rose in magnitude and alternated their signs [26]. These features of factorial cumulants are utilized in the experimental search for first-order phase transition.

6.6.2 Experimental results and model comparison

To search for a possible two-component structure of proton multiplicity distribution induced from a first-order phase transition, higher-order factorial cumulants (κ_n) of proton multiplicity distribution were measured from Au+Au collisions over the wide collision en-

energy range $\sqrt{s_{NN}} = 7.7 - 200$ GeV [7]. The factorial cumulants κ_n can be easily extracted from the regular cumulants C_n analytically (see section 1.4 of chapter 1). The results were presented for central (0-40%) and peripheral (50-60%) collisions. A wider 0-40% centrality was chosen to have better precision on measurements. The measurements are shown in Fig. 6.18, along with calculations from the UrQMD model and a Two-component model. The Two-component model (with Binomial and Poisson distributions as constituent components) considered for our study required κ_n up to the fourth order as inputs in determining its parameters and then predicted values of κ_5 and κ_6 (see appendix 6.8.6 for more details).

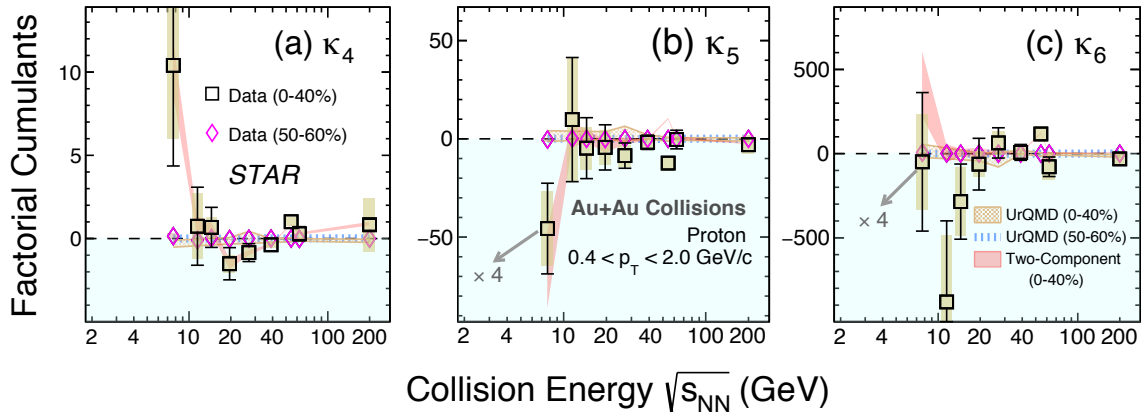


Figure 6.18: Factorial cumulants κ_4 (a), κ_5 (b), κ_6 (c) of proton multiplicity distribution from Au+Au collisions at collision energies from $\sqrt{s_{NN}} = 7.7 -$ to 200 GeV. The measurements are presented for 0-40% (square markers) and 50-60% (diamond markers) centralities. The bars and the shaded bands on the data points represent statistical and systematic uncertainties, respectively. Also shown are the calculations from Two-Component Model (for 0-40%) and the UrQMD model (for 0-40% and 50-60%) as red, brown bands, and blue dashed lines, respectively. The Two-Component Model (with Binomial and Poisson distributions as constituent components) considers factorial cumulants up to the fourth order as inputs in its construction to predict κ_5 and κ_6 . Uncertainties on the model calculations are purely statistical. The Poisson baseline for κ_n presented is at zero. For clarity of presentation, the κ_5 and κ_6 measurements at 7.7 GeV for 0-40% centrality are scaled down by a factor of 4 [7].

Large positive values for κ_4 and negative values for κ_5 are observed for measurements from 0-40% centrality at 7.7 GeV, albeit with large uncertainties. While the two-component model calculations are able to reproduce these trends at 7.7 GeV, calculations from the UrQMD model and peripheral (50-60%) data fail to do so and remain close to the Poisson baseline at zero. Except for 7 GeV, at all the remaining collision energies, small deviations from zero and UrQMD expectations are seen for factorial cumulants of all the orders presented within uncertainties. The overall energy dependence trend observed for the κ_5 and κ_6 measurements is largely reproduced by Two-Component Model calculation. Vanishing factorial cumulants from Two-component Model implies that only the Poissonian component survives. The observation of small deviation of the κ_n measurements from the Poisson baseline at zero and the lack of a sign change with the increasing order within uncertainties for collision energies above 7.7 GeV suggest the absence of a two-component structure in proton multiplicity distributions at those energies. Note that at 54.4 GeV, a sign change at a level of $2.5 - 3 \sigma_{\text{tot}}$ (σ_{tot} is the quadrature sum of statistical and systematic uncertainties) is observed for the three factorial cumulants with increasing order. However, such a trend is not seen in the Two-Component Model calculations. The UrQMD calculations and peripheral data from 50-60% centrality are found to be small in magnitude and mostly consistent with zero within uncertainties at all energies.

6.7 Summary

This chapter is the main chapter pertaining to the goal of the thesis. Net-proton number fluctuations measured in the Au+Au collisions over a wide range of collision energy from $\sqrt{s_{NN}} = 7.7 - 200$ GeV in the STAR experiment were presented and discussed in regards to the study of QCD phase structure. These collision energies provided access to a μ_B coverage

of $\sim 20-420$ MeV. Before reporting the net-proton cumulants, we presented raw (efficiency uncorrected) event-by-event net-proton number distributions for most central (0-5%) and peripheral (70-80%) collisions as a function of collision energy. A smooth increase in mean was observed from the distribution with decreasing collision energy which was attributed to the baryon-stopping effect. Deviation of the tails of the measured distribution with respect to a Skellam functional fit suggested that the experimentally measured distribution (and thus all its cumulants) as a whole cannot be explained by invoking statistical description, such as a Skellam distribution. Since higher-order cumulants are sensitive to the tails of a distribution, any departure from the statistical baseline will be obvious from their measurements. The observations made from the net-proton distributions were confirmed by measuring their cumulants and applying all necessary corrections, such as due to finite efficiency and finite centrality width. Both collision centrality and energy dependence of cumulants were studied. The cumulants up to third-order, in general, showed a smooth increasing trend with collision centrality. While the first (C_1) and third (C_3) order cumulant showed a decreasing trend with increasing energy, non-monotonic variations with respect to energy were observed for the second (C_2) and fourth (C_4) order cumulant. Subsequently, we extended the order of cumulant to even higher orders, i.e., to fifth and sixth order (also known as hyper-orders). Since with increasing order, the statistical uncertainty on cumulant increases, to have better control on uncertainties, the hyper-order fluctuations were reported in terms of cumulant ratios C_5/C_1 and C_6/C_2 and for a wider 0-40% centrality class. The C_6/C_2 , in particular, showed a decreasing trend towards lower energies.

When exploiting the measurements to draw physics conclusions, often comparisons with respect to various baselines are needed. Various models which do not incorporate any QCD critical point or phase transition effects are utilized to provide baselines in our study. We discussed the purely statistical Skellam baseline, the thermal model HRG and

the hadronic transport model UrQMD in this context. The UrQMD and HRG calculations requiring canonical ensemble incorporate baryon number conservation and are deemed as effective baselines, especially at low collision energies. Ratios of cumulants constructed from the measured cumulant values were compared with calculations from these models. None of the models provide a quantitative description of experimental data over the full range of collision energy reported. Only qualitative agreements are seen for the trends observed in cumulant ratios up to the third order.

We then invoked the measured cumulant ratios in the experimental study of the QCD phase structure.

First, we tested for observation of QCD thermodynamics in Au+Au collisions by employing net-proton (proxy for net-baryon) cumulant ratios up to sixth-order. An ordering of the cumulant ratios ($C_3/C_1 > C_4/C_2 > C_5/C_1 > C_6/C_2$) as predicted by lattice QCD for thermalized QCD matter was observed in general for the experimental measurements for 0-40% centrality. Such an ordering is not reproduced by the models like UrQMD, ideal HRG GCE, and Skellam baseline, which show an absence of any hierarchy within uncertainties.

Next, C_4/C_2 measurements were presented in regard to the QCD critical point search. A non-monotonic collision energy dependence of net-proton C_4/C_2 was observed for 0-5% collision centrality. Such a trend is consistent with model predictions that include a QCD critical point. In contrast, the peripheral 70-80% data and calculations from various variants of thermal model HRG, transport model UrQMD and Skellam baseline show monotonic collision energy dependence. The deviations of 0-5% C_4/C_2 measurements above and below the non-critical baselines at all energies are found to be $\lesssim 3\sigma_{tot}$ (where σ_{tot} is the quadrature sum of statistical and systematic uncertainties). The observed non-monotonic trend was established analytically by fitting the data with a polynomial function

(a fourth-order polynomial best describes the measurements) and then demonstrating that the derivative of the polynomial function changes sign with energy. Using a statistical procedure the non-monotonic energy dependence within the range $\sqrt{s_{NN}} = 7.7 - 62.4$ GeV was quantified to be of 3.1σ significance.

Since QCD critical point is marked by the end of the first-order phase transition and the beginning of crossover, the experimental study of the nature of the quark-hadron phase transition is also important.

Lattice QCD calculations ($\mu_B \leq 110$ MeV) on net-baryon hyper-order cumulant ratios C_5/C_1 and C_6/C_2 suggest a negative sign of these quantities for a crossover quark-hadron transition which grows in magnitude with increasing μ_B (decreasing $\sqrt{s_{NN}}$). Motivated by the lattice QCD prediction, hyper-order net-proton (as proxy for net-baryon) cumulant ratios C_5/C_1 and C_6/C_2 were measured at all collision energies. The measured C_5/C_1 for 0-40% centrality does not show a clear sign and fluctuates about zero as a function of collision energy at a level of $\lesssim 2\sigma_{tot}$. Interestingly the more sensitive observable, C_6/C_2 for the same centrality within uncertainties, is found to be increasingly negative with decreasing collision energy. Both the features: the negative sign and the observed energy dependence trend, are consistent with predictions from lattice QCD and also a QCD-based FRG model that includes a crossover quark-hadron transition. The deviation of measurements from zero was found to be within $1.7\sigma_{tot}$. The overall significance of observing negative C_6/C_2 in half of the collision energies from $\sqrt{s_{NN}} = 7.7$ to 200 GeV was also quantified to be 1.7σ . In contrast, the peripheral (70-80%) data and calculations from the UrQMD model and Skellam baseline are either consistent with zero or positive. The HRG (canonical ensemble) model calculations remain positive for collision energy higher than 19.6 GeV and become negative only at lower energies.

Features of a two-component distribution for proton multiplicity expected near a first-

order phase transition due to the presence of mixed-phase were exploited in the search for first-order phase transition. Large values of higher order factorial cumulants (κ_n) are expected in the presence of a two-component structure, which progressively increases in magnitude and alternates in sign with increasing order. Large positive κ_4 and negative κ_5 were measured at 7.7 GeV for 0-40% centrality, albeit with large uncertainties. The observed trend at 7.7 GeV is reproduced by calculation from the Two-Component model, which requires measured κ_n up to fourth-order as input. However, small deviations from zero and absence of sign-change in higher-order factorial cumulants for $\sqrt{s_{NN}} \geq 11.5$ GeV do not support the two-component structure of proton multiplicity distribution expected from a first-order phase transition at those energies. The peripheral (50-60%) data and UrQMD calculations at all energies are close to zero within uncertainties.

6.8 Appendices

6.8.1 Appendix A: Study on decay induced self-correlation

Self-correlation between centrality definition and net-proton fluctuation measurements could also arise due to resonance decays where one daughter particle from the decay falls within analysis acceptance used for net-proton selection, and the other daughter is selected for centrality definition (which is done using charged particle multiplicity). Weak decay of hyperons, such as Λ , Ξ , Ω and decays from Delta baryons Δ^0 and Δ^{++} produces protons and other charged particles like kaons and pions. There is a possibility that protons from these decays are considered in net-proton fluctuation measurements while pions and/or kaons from the same decay are taken in defining centrality. Although the experimental requirement of DCA cut ($DCA < 1$ cm) on tracks largely suppresses the background contributions from decays, it may not be fully eliminated.

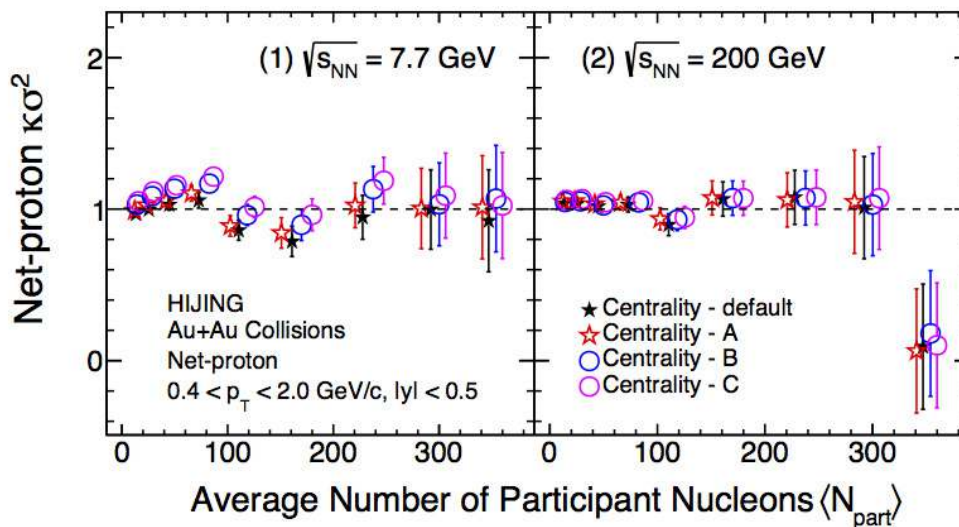


Figure 6.19: Collision centrality dependence of net-proton cumulant ratio C_4/C_2 in Au+Au collision at center-of-mass energy $\sqrt{s_{NN}} = 7.7$ (panel 1) and 200 GeV (panel 2) from HIJING model [5]. Results are obtained from different choices of centrality definitions labeled as (a) Centrality - default: the centrality definition as used in the experimental data, (b) Centrality - A: same as (a) except pions and kaons from weak decays are removed provided the daughter protons for such decay are considered in net-proton fluctuation measurement, (c) Centrality - B: same as (b) except we removed pions from Δ decays instead of weak decay, (d) Centrality - C: its a combination of (b) and (c), i.e., pions and kaons from weak decays as well as Δ decays are removed.

Hence, we performed a HIJING model [27] based simulation on studying the effect of decay-induced self-correlation on net-proton C_4/C_2 considering weak decays and decays of Delta baryons. Various choices of centrality definitions were made that aimed at excluding the pions and/or kaons from these decays if the daughter protons are selected for net-proton fluctuation studies. The results are shown in panels (a) and (b) of Fig. 6.19 for Au+Au collisions at $\sqrt{s_{NN}} = 7.7$ and 200 GeV, respectively. We find that the C_4/C_2 results from all the newly considered centrality definitions aimed at removing decay-induced self-correlation and from the standard/default centrality definition as used in the experiment are quite consistent with each other within uncertainties [5]. This suggests that decay-induced self-correlation effects, if any, are negligible.

6.8.2 Appendix B: Acceptance dependence of cumulant ratios

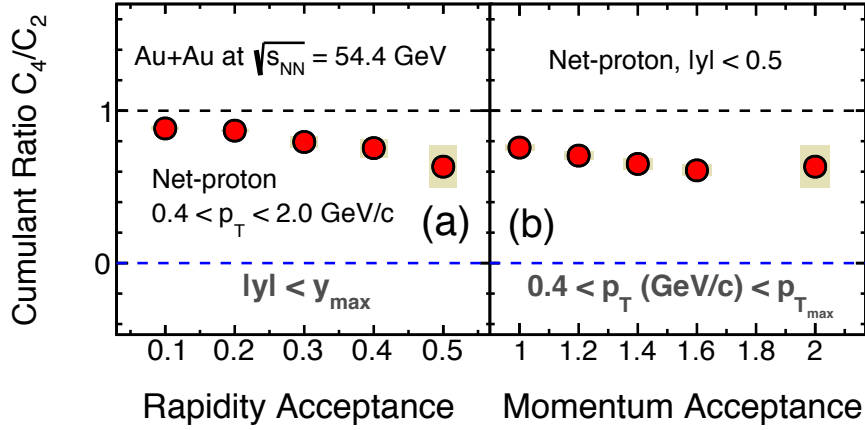


Figure 6.20: Net-proton C_4/C_2 from 0-5% central collisions as a function of rapidity coverage (a) and momentum coverage (b) in Au+Au collisions at $\sqrt{s_{NN}} = 54.4$ GeV [3, 4]. The bars and the shaded bands on the data points represent the statistical and systematic uncertainties, respectively.

The phase space acceptance dependence of measurements is studied by varying the phase space variables, rapidity (y), and momentum (p_T) within the limitations of finite detector acceptance. Figure 6.20 presents the net-proton C_4/C_2 measurements from 0-5% central collisions at $\sqrt{s_{NN}} = 54.4$ GeV as a function of increasing rapidity acceptance (panel a) and momentum acceptance (panel b) [3, 4]. The maximum rapidity coverage used for measurements is $|y| < 0.5$, and the maximum momentum coverage is $0.4 < p_T < 2.0$ GeV/c. As the y and p_T acceptance is increased, the C_4/C_2 measurements show a decreasing trend. The measurements approach the Skellam baseline at unity when the acceptance is small due to the low number of protons and antiprotons. With wider acceptance, increased suppression with respect to the Skellam baseline is observed. This could be attributed to the increasing level of correlations among (anti-) protons, especially due to the baryon number conservation effect.

6.8.3 Appendix C: Significance of energy dependence of C_2/C_1 and C_3/C_2

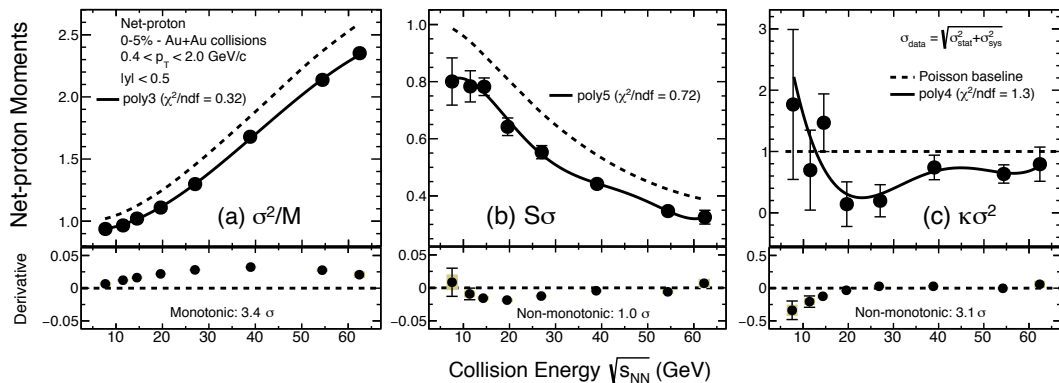


Figure 6.21: Energy dependence of net-proton cumulant ratios C_2/C_1 (same as σ^2/M) (a), C_3/C_2 (same as $S\sigma$) (b) and C_4/C_2 (same as $\kappa\sigma^2$) (c) from 0-5% central Au+Au collisions over the range $\sqrt{s_{NN}} = 7.7 - 62.4$ GeV [3, 4]. The bars on the data points represent total uncertainties obtained by adding statistical and systematic uncertainties in quadrature. Polynomial fits to data points along with χ^2/ndf value are shown. The lower panels show the derivative of the fitted polynomials as a function of energy.

The significance calculation for C_4/C_2 shown in panel (c) of Fig. 6.21 was discussed in section 3 of this chapter. By employing a similar statistical procedure, significance was evaluated for the energy dependence of C_2/C_1 and C_3/C_2 [3, 4]. Polynomial of third and fifth order (of all order polynomials) gave the best description (in terms χ^2/ndf closest to unity) of C_2/C_1 and C_3/C_2 measurements over the collision energy 7.7 to 62.4 GeV, respectively. As seen from Fig. 6.21, the derivative of the fitted polynomial does not change sign with respect to collision energy for C_2/C_1 indicating its monotonic energy dependence. For C_3/C_2 , a change in the sign of derivative is observed, suggesting the non-monotonic energy dependence, although the magnitude of sign change is quite weak.

Similar to the statistical study done for C_4/C_2 , the significance of energy dependence for C_2/C_1 and C_3/C_2 was obtained by randomly varying the data points within total uncer-

tainties a million times and then refitting them with the third and fifth order polynomial, respectively, to obtain derivatives at each energy. From these million times, the probability of observing the same sign of derivatives at all energies (0.999663 for C_2/C_1) and of observing at least one energy with the sign of derivative different than the rest (0.84136 for C_3/C_2) was calculated. These probability numbers converted to significance yielded a 3.4σ level of monotonic variation of C_2/C_1 and 1σ level of non-monotonic variation for C_3/C_2 .

6.8.4 Appendix D: Cumulants and K-statistics

In the majority of statistical analyses, the sample is used to make inferences about the population. The information on population is never known a priori. However, the sample being a subset of the population is expected to reflect the features of the population. For a sufficiently large sample, the cumulants measured from the sample itself serve as reasonable estimates for cumulants of the population. Often a quantity called K -statistics is measured from samples, which are known to be unbiased estimators of cumulants of the population [25]. If the sample size is sufficiently large, both K -statistics and cumulant measured from the sample should be consistent. Hence a comparison between the two quantities helps to assess the adequacy of a sample size. K -statistics (KS_n) up to sixth-order can be derived from the central moments (μ_n) of the sample using the following

formulae [25].

$$KS_1 = C_1 \quad (6.6)$$

$$KS_2 = \frac{n}{n-1} \mu_2 \quad (6.7)$$

$$KS_3 = \frac{n^2}{(n-1)(n-2)} \mu_3 \quad (6.8)$$

$$KS_4 = \frac{n^2}{(n-1)(n-2)(n-3)} [(n+1)\mu_4 - 3(n-1)\mu_2^2] \quad (6.9)$$

$$KS_5 = \frac{n^3}{(n-1)(n-2)(n-3)(n-4)} [(n+5)\mu_5 - 10(n-1)\mu_2\mu_3] \quad (6.10)$$

$$KS_6 = \frac{n^2}{(n-1)(n-2)(n-3)(n-4)(n-5)} [(n+1)(n^2 + 15n - 4)\mu_6 - 15(n-1)^2(n+4)\mu_2\mu_4 - 10(n-1)(n^2 - n + 4)\mu_3^2] \quad (6.11)$$

$$+ 30n(n-1)(n-2)\mu_2^3] \quad (6.12)$$

Just for completeness, the expressions for cumulants (C_n) in terms of central moments are provided as follows.

$$C_1 = m_1 \quad (6.13)$$

$$C_2 = \mu_2 \quad (6.14)$$

$$C_3 = \mu_3 \quad (6.15)$$

$$C_4 = \mu_4 - 3\mu_2^2 \quad (6.16)$$

$$C_5 = \mu_5 - 10\mu_3\mu_2 \quad (6.17)$$

$$C_6 = \mu_6 - 15\mu_4\mu_2 - 10\mu_3^2 + 30\mu_2^3 \quad (6.18)$$

where m_1 is the first raw moment or the mean.

Using the above formulae, it can be easily realized that for large sample size (n) such that $n \sim (n-1)$, the cumulants and K -statistics are essentially the same.

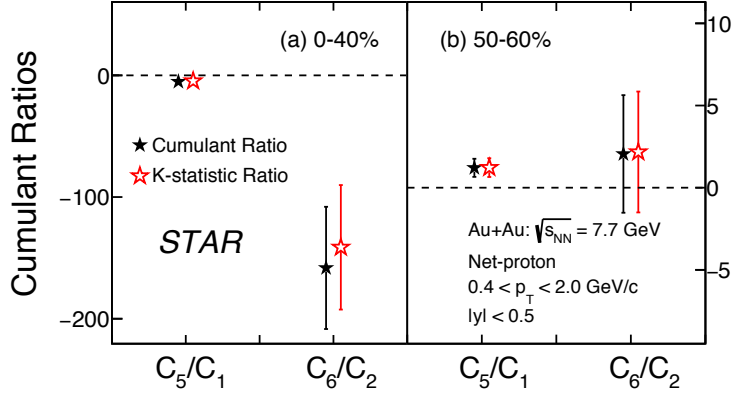


Figure 6.22: The cumulant ratio C_5/C_1 and C_6/C_2 of net-proton distribution in Au+Au collisions at $\sqrt{s_{NN}}=7.7$ GeV and their corresponding K -statistics ratios. Results are presented for 0-40% (a) and 50-60% (b) collision centrality class. Only statistical uncertainties on data points are presented [7].

The context of our discussion in regards to K -statistics and cumulants is the experimental measurement of C_6/C_2 from Au+Au collisions at $\sqrt{s_{NN}} = 7.7$ GeV where the number of events (or sample size) is least among all collision energies. Thus, we measured fifth-to-first and sixth-to-second order K -statistics ratios and compared them with corresponding cumulant ratios C_5/C_1 and C_6/C_2 at 7.7 GeV for 0-40% and 50-60% centrality classes [7]. From Fig. 6.22, a good consistency is observed between the two estimators for both the centrality classes. This demonstrates that event statistics at 7.7 GeV are sufficient to attain an agreement between the fifth- and sixth-order K -statistics and cumulants.

6.8.5 Appendix E: Statistics dependence of C_6/C_2

Sample size dependence of sixth-order net-proton cumulant and K -statistics was studied by performing random sampling from STAR data [7]. Recall from our studies on crossover search; we observed increasingly negative values of C_6/C_2 from 0-40% centrality with decreasing collision energy. Since at $\sqrt{s_{NN}}=7.7$ GeV, the event statistics available for measurements were lowest among all energies, we conducted the sample size dependence

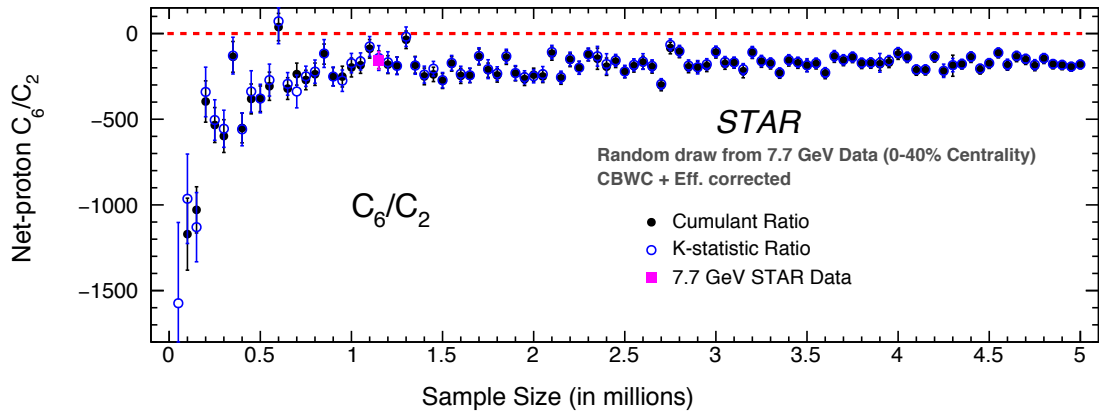


Figure 6.23: Sample size dependence of C_6/C_2 (filled circles) and the corresponding K -statistics ratio (open circles). Samples of varying sizes are constructed by random draw of events from the recorded events in 0-40% central Au+Au collision by STAR at $\sqrt{s_{NN}} = 7.7$ GeV. Measurements are corrected for finite detection efficiency and finite centrality width (by applying CBWC). The observed STAR C_6/C_2 data for 0-40% centrality (filled square in magenta color) is also shown. Only statistical uncertainties are presented [7].

study at this energy to examine the effect of changing event statistics on the sign of C_6/C_2 . Sub-samples of varying sizes were constructed by randomly drawing events from observed events at $\sqrt{s_{NN}} = 7.7$ GeV (0-40% centrality) with replacement allowed. Each sub-sample is independent of the other. While the total number of events recorded by STAR at 7.7 GeV for 0-40% centrality is ~ 1.2 million, the simulated subsamples have events ranging from 0.05 – 5 million in steps of 0.05 million. The net-proton C_6/C_2 from these subsamples, along with their corresponding K -statistics ratio, are shown in Fig. 6.23 as a function of subsample size. All the needed corrections, as done with STAR data, are carried out when obtaining C_6/C_2 from each subsample. In the full range of subsample sizes studied, the C_6/C_2 is always found to be negative (with the exception of a very few subsample sizes where it is consistent with zero within statistical uncertainties). The value is more negative for the small size of the subsample, and as the subsample size increases, a saturation of C_6/C_2 is seen close to the observed value in the true data sample at $\sqrt{s_{NN}} = 7.7$ GeV. There

were no cases where the subsample had a positive C_6/C_2 . The corresponding K -statistics ratio also shows a similar trend and sign and is found to be consistent with C_6/C_2 within uncertainties. Note that this study has a caveat that the random draw of events from the real data is constrained by the total available events recorded by STAR.

6.8.6 Appendix F: Two-component Model calculation

In a two-component/bimodal distribution, the total probability distribution $P(N)$ can be written as a combination of the probability distribution of its two constituting components $P_A(N)$ and $P_B(N)$, such that

$$P(N) = (1 - \alpha)P_A(N) + \alpha P_B(N), \quad (6.19)$$

where the α -parameter ($\alpha \leq 1$) represents the relative contribution of the constituents. The factorial cumulants (κ_n) up to the sixth order for such a two-component distribution can be expressed in terms of individual factorial cumulants of its components (κ_{nA} and κ_{nB}) as

follows [28].

$$\kappa_1 = \kappa_{1A} - \alpha \Delta \kappa_1 \quad (6.20)$$

$$\kappa_2 = \kappa_{2A} - \alpha [\Delta \kappa_2 - (1 - \alpha) \Delta \kappa_1^2] \quad (6.21)$$

$$\kappa_3 = \kappa_{3A} - \alpha [\Delta \kappa_3 (1 - \alpha) ((1 - 2\alpha) \Delta \kappa_1^3 - 3 \Delta \kappa_1 \Delta \kappa_2)] \quad (6.22)$$

$$\begin{aligned} \kappa_4 = \kappa_{4A} - \alpha [\Delta \kappa_4 - (1 - \alpha) ((1 - 6\alpha + 6\alpha^2) \Delta \kappa_1^4 - 6(1 - 2\alpha) \Delta \kappa_1^2 \Delta \kappa_2 \\ + 4 \Delta \kappa_1 \Delta \kappa_3 + 3 \Delta \kappa_2^2)] \end{aligned} \quad (6.23)$$

$$\begin{aligned} \kappa_5 = \kappa_{5A} - \alpha [\Delta \kappa_5 + (1 - \alpha) ((1 - 2\alpha)(1 - 12\alpha + 12\alpha^2) \Delta \kappa_1^5 \\ - 10(1 - 6\alpha + 6\alpha^2) \Delta \kappa_1^3 \Delta \kappa_2 + 10(1 - 2\alpha) \Delta \kappa_1^2 \Delta \kappa_3 \\ + 15(1 - 2\alpha) \Delta \kappa_1 \Delta \kappa_2^2 - 5 \Delta \kappa_1 \Delta \kappa_4 - 10 \Delta \kappa_2 \Delta \kappa_3)] \end{aligned} \quad (6.24)$$

$$\begin{aligned} \kappa_6 = \kappa_{6A} - \alpha [\Delta \kappa_6 - (1 - \alpha) ((1 - 30\alpha(1 - \alpha)(1 - 2\alpha)^2) \Delta \kappa_1^6 \\ - 15(1 - 2\alpha)(1 - 12\alpha + 12\alpha^2) \Delta \kappa_1^4 \Delta \kappa_2 + 20(1 - 6\alpha + 6\alpha^2) \Delta \kappa_1^3 \Delta \kappa_3 \\ - 15 \Delta \kappa_1^2 (\Delta \kappa_4 (1 - 2\alpha) - 3 \Delta \kappa_2^2 (1 - 6\alpha + 6\alpha^2)) \\ + 6 \Delta \kappa_1 (\Delta \kappa_5 - 10 \Delta \kappa_2 \Delta \kappa_3 (1 - 2\alpha)) \\ - 15(1 - 2\alpha) \Delta \kappa_2^3 + 10 \Delta \kappa_3^2 + 15 \Delta \kappa_2 \Delta \kappa_4)] \end{aligned} \quad (6.25)$$

where $\Delta \kappa_n = (\kappa_{nA} - \kappa_{nB})$ for $n = 1 - 6$.

To obtain the Two-Component Model expectations for fifth and sixth-order proton factorial cumulants reported in the study of first-order phase transition, we follow the procedure as suggested in Refs. [26, 28]. The constituent distributions of this Two-Component Model are considered to be Binomial ($P_A(N)$) and Poissonian ($P_B(N)$) distributions; this choice of combination is made keeping baryon number conservation effect in mind [28]. Such a combination for Two-Component Model requires four parameters as inputs: α (the relative contribution), the probability of success (p) and the number of trials (B) for the Binomial component, and mean (λ) for the Poissonian component. Based on the recommendation

Table 6.2: The parameters of the Two-Component Model calculations at all collision energies [7].

$\sqrt{s_{NN}}$ (GeV)	3	7.7	11.5	14.5	19.6	27	39	54.4	62.4	200
p	0.04035	0.0601	0.0483	0.0411	0.0429	0.03088	0.0284	0.0647	0.0285	0.0313
α	0.306096	0.00745336	0.0642206	0.0221282	0.793785	0.562374	0.587115	0.999963	0.0226576	0.0135979
λ	16.98	15.16	18.32	16.46	12.78	12.39	11.22	10.17	11.73	8.3

from Ref. [28], the parameter B (number of trials in Binomial) is fixed to $B = 350$, and the remaining parameters are extracted by solving the equation for factorial cumulants of first, third, and fourth-order given in equations 6.25 for their experimentally measured values at all energies (except at 7.7 GeV, where the equations for first, second, and fourth-order factorial cumulants were used instead as the former choice provided an unphysical value of α , i.e., $\alpha > 1$, though there is no change in physics conclusion obtained with both set of parameters). The parameters extracted at all energies are listed in Table 6.2 [7]. With information on all four parameters at hand, Two-Component Model predictions for the fifth and sixth-order factorial cumulants were obtained. The statistical uncertainties on the predictions were evaluated using the resampling method suggested in Ref. [26, 28].

Bibliography

- [1] L. Adamczyk et al. “Bulk Properties of the Medium Produced in Relativistic Heavy-Ion Collisions from the Beam Energy Scan Program”. *Phys. Rev. C* 96.4 (2017), 044904. arXiv: [1701.07065 \[nucl-ex\]](#).
- [2] B. I. Abelev et al. “Identified particle production, azimuthal anisotropy, and interferometry measurements in Au+Au collisions at $\sqrt{s_{NN}} = 9.2$ GeV”. *Phys. Rev. C* 81 (2010), 024911. arXiv: [0909.4131 \[nucl-ex\]](#).
- [3] J. Adam et al. “Nonmonotonic Energy Dependence of Net-Proton Number Fluctuations”. *Phys. Rev. Lett.* 126.9 (2021), 092301. arXiv: [2001.02852 \[nucl-ex\]](#).
- [4] Mohamed Abdallah et al. “Cumulants and correlation functions of net-proton, proton, and antiproton multiplicity distributions in Au+Au collisions at energies avail-

- able at the BNL Relativistic Heavy Ion Collider”. *Phys. Rev. C* 104.2 (2021), 024902. arXiv: [2101.12413 \[nucl-ex\]](#).
- [5] A. Pandav, D. Mallick, and B. Mohanty. “Search for the QCD critical point in high energy nuclear collisions”. *Prog. Part. Nucl. Phys.* 125 (2022), 103960. arXiv: [2203.07817 \[nucl-ex\]](#).
- [6] Mohamed Abdallah et al. “Measurement of the Sixth-Order Cumulant of Net-Proton Multiplicity Distributions in Au+Au Collisions at $\sqrt{s_{NN}} = 27, 54.4, \text{ and } 200 \text{ GeV}$ at RHIC”. *Phys. Rev. Lett.* 127.26 (2021), 262301. arXiv: [2105.14698 \[nucl-ex\]](#).
- [7] “Beam Energy Dependence of Fifth and Sixth-Order Net-proton Number Fluctuations in Au+Au Collisions at RHIC” (July 2022). arXiv: [2207.09837 \[nucl-ex\]](#).
- [8] Frithjof Karsch and Krzysztof Redlich. “Probing freeze-out conditions in heavy ion collisions with moments of charge fluctuations”. *Phys. Lett. B* 695 (2011), 136–142. arXiv: [1007.2581 \[hep-ph\]](#).
- [9] P. Garg, D. K. Mishra, P. K. Netrakanti, et al. “Conserved number fluctuations in a hadron resonance gas model”. *Phys. Lett. B* 726 (2013), 691–696. arXiv: [1304.7133 \[nucl-ex\]](#).
- [10] Jinghua Fu. “Higher moments of net-proton multiplicity distributions in heavy ion collisions at chemical freeze-out”. *Phys. Lett. B* 722 (2013), 144–150.
- [11] Abhijit Bhattacharyya, Supriya Das, Sanjay K. Ghosh, et al. “Fluctuations and correlations of conserved charges in an excluded volume hadron resonance gas model”. *Phys. Rev. C* 90.3 (2014), 034909. arXiv: [1310.2793 \[hep-ph\]](#).
- [12] Abhijit Bhattacharyya, Rajarshi Ray, Subhasis Samanta, et al. “Thermodynamics and fluctuations of conserved charges in a hadron resonance gas model in a finite volume”. *Phys. Rev. C* 91.4 (2015), 041901. arXiv: [1502.00889 \[hep-ph\]](#).
- [13] Volodymyr Vovchenko, Attila Pasztor, Zoltan Fodor, et al. “Repulsive baryonic interactions and lattice QCD observables at imaginary chemical potential”. *Phys. Lett. B* 775 (2017), 71–78. arXiv: [1708.02852 \[hep-ph\]](#).
- [14] Subhasis Samanta and Bedangadas Mohanty. “Estimation of attractive and repulsive interactions from the fluctuation observables at RHIC using van der Waals hadron resonance gas Model” (May 2019). arXiv: [1905.09311 \[hep-ph\]](#).

- [15] P. Braun-Munzinger, B. Friman, K. Redlich, et al. “Relativistic nuclear collisions: Establishing a non-critical baseline for fluctuation measurements”. *Nucl. Phys. A* 1008 (2021), 122141. arXiv: [2007.02463 \[nucl-th\]](#).
- [16] M. Bleicher et al. “Relativistic hadron hadron collisions in the ultrarelativistic quantum molecular dynamics model”. *J. Phys. G* 25 (1999), 1859–1896. arXiv: [hep-ph/9909407](#).
- [17] A. Bazavov et al. “Skewness, kurtosis, and the fifth and sixth order cumulants of net baryon-number distributions from lattice QCD confront high-statistics STAR data”. *Phys. Rev. D* 101.7 (2020), 074502. arXiv: [2001.08530 \[hep-lat\]](#).
- [18] Wei-jie Fu, Xiaofeng Luo, Jan M. Pawłowski, et al. “Hyper-order baryon number fluctuations at finite temperature and density”. *Phys. Rev. D* 104.9 (2021), 094047. arXiv: [2101.06035 \[hep-ph\]](#).
- [19] Boris Berdnikov and Krishna Rajagopal. “Slowing out-of-equilibrium near the QCD critical point”. *Phys. Rev. D* 61 (2000), 105017. arXiv: [hep-ph/9912274](#).
- [20] M. A. Stephanov. “On the sign of kurtosis near the QCD critical point”. *Phys. Rev. Lett.* 107 (2011), 052301. arXiv: [1104.1627 \[hep-ph\]](#).
- [21] Bengt Friman. “Probing the QCD phase diagram with fluctuations”. *Nucl. Phys. A* 928 (2014). Ed. by James M. Lattimer, Edward Shuryak, and Avraham Gal, 198–208. arXiv: [1404.7471 \[nucl-th\]](#).
- [22] Jiunn-Wei Chen, Jian Deng, Hiroaki Kohyama, et al. “Robust characteristics of nongaussian fluctuations from the NJL model”. *Phys. Rev. D* 93.3 (2016), 034037. arXiv: [1509.04968 \[hep-ph\]](#).
- [23] H. Toutenburg. “Fisher, R. A., and F. Yates: Statistical Tables for Biological, Agricultural and Medical Research. 6th Ed. Oliver & Boyd, Edinburgh and London 1963. X, 146 P. Preis 42 s net”. *Biometrische Zeitschrift* 13.4 (1971), 285–285. eprint: <https://onlinelibrary.wiley.com/doi/pdf/10.1002/bimj.19710130413>.
- [24] Szabolcs Borsanyi, Zoltan Fodor, Jana N. Guenther, et al. “Higher order fluctuations and correlations of conserved charges from lattice QCD”. *JHEP* 10 (2018), 205. arXiv: [1805.04445 \[hep-lat\]](#).

- [25] R. A. Fisher. “Moments and Product Moments of Sampling Distributions”. *Proceedings of the London Mathematical Society* s2-30.1 (1930), 199–238. eprint: <https://londmathsoc.onlinelibrary.wiley.com/doi/pdf/10.1112/plms/s2-30.1.199>.
- [26] Adam Bzdak and Volker Koch. “Mapping the QCD phase diagram with statistics friendly distributions”. *Phys. Rev. C* 100.5 (2019), 051902. arXiv: [1811.04456 \[nucl-th\]](https://arxiv.org/abs/1811.04456).
- [27] Xin-Nian Wang and Miklos Gyulassy. “HIJING: A Monte Carlo model for multiple jet production in p p, p A and A A collisions”. *Phys. Rev. D* 44 (1991), 3501–3516.
- [28] Adam Bzdak, Volker Koch, Dmytro Oliinychenko, et al. “Large proton cumulants from the superposition of ordinary multiplicity distributions”. *Phys. Rev. C* 98.5 (2018), 054901. arXiv: [1804.04463 \[nucl-th\]](https://arxiv.org/abs/1804.04463).

Chapter 7

Conclusion

As stated in the introductory chapter, the current understanding of the QCD phase diagram is largely conjectured. Discovery of QCD critical point and/or confirmation of a crossover quark-hadron phase transition at small μ_B and a first-order phase transition at large μ_B are necessary to transform the phase diagram from theoretical speculations to text-book knowledge. This deems the experimental study of QCD phase structure extremely important. Experimental exploration of the QCD phase structure is carried out by collisions of heavy ions at ultra-relativistic velocity, which results in the transition of QCD matter from the hadronic phase to the QGP phase. Performing collisions over a wide range of center-of-mass energies facilitate an in-depth study of this phase transition by allowing access to a broad region of the QCD phase diagram.

Event-by-event fluctuations of conserved quantities have been suggested as sensitive observables in the study of QCD phase structure. This thesis presented experimental measurements on event-by-event net-proton (as proxy for net-baryon, a conserved quantity) number fluctuations from Au+Au collisions recorded by the STAR detector at RHIC. Fluctuations were measured via cumulants (C_n) up to the sixth order. The experimental

search for the QCD critical point and nature of the quark-hadron phase transition was the prime focus of the thesis. The center-of-mass collision energies analyzed ranged from $\sqrt{s_{NN}} = 7.7$ to 200 GeV. These energies constituted phase I of the BES program at RHIC and allowed an extensive coverage of baryonic chemical potential from $\mu_B = 20$ to 420 MeV in the QCD phase diagram. The total number of good events considered for analysis varied from a few million at low collision energies to several hundred million at higher collision energies. A simulation study with the assumption that any signal related to QCD phase structure is at a level of 5% above the statistical baseline was performed, which suggested the required number of events for accurate determination of C_4 (C_6) of net-proton distribution to be of the order of 10^6 (10^9). Most importantly, the study found that even with a much lower number of events, the cumulants generally do not deviate from their true values beyond $\pm 1\sigma$ statistical uncertainty.

Collisions of gold (Au) ions were categorized in terms of their centrality using charged particle multiplicity that excluded protons and antiprotons in its definition to avoid self-correlation between centrality and net-proton cumulants. Using STAR's TPC and TOF detectors, proton and antiproton tracks were selected at mid-rapidity ($|y| < 0.5$) within the momentum acceptance of $0.4 < p_T < 2.0$ GeV/c to construct the event-by-event net-proton distribution. Cumulants of the net-proton distributions were measured by applying corrections accounting for finite detection efficiency and volume fluctuation effects. A careful estimation of uncertainties on cumulants was carried out. Three methods of estimating statistical uncertainty: Delta theorem, Bootstrap, and Sub-group, were studied for their suitability. The Sub-group method was found to be inefficient in estimating statistical uncertainties on higher-order cumulants. Hence Delta theorem and Bootstrap methods were used. The systematic uncertainties were estimated by variation of different sources after subjecting them to Barlow check. These sources included track selection, particle

identification criteria, background estimates, and track reconstruction efficiency.

To facilitate a comparison of experimental measurements with theoretical calculations made in reference to QCD phase structure, ratio of cumulants were constructed from the measured cumulants. The cumulant ratios were also compared to various model calculations (the thermal model HRG, the hadronic transport model UrQMD, and the statistical Skellam baseline), which do not incorporate a QCD critical point or any QCD phase transition effects. The observations made from the measurements in regard to various aspects of the QCD phase diagram studied in this thesis are summarized as follows.

Test of QCD thermodynamics

To check whether matter produced in Au+Au collisions obeys QCD thermodynamics, inspiration was taken from lattice QCD calculation on a specific ordering of cumulant ratios $C_3/C_1 > C_4/C_2 > C_5/C_1 > C_6/C_2$ for thermalized QCD matter. Within uncertainties, the experimental measurements, in general, were found to satisfy this hierarchy expected from QCD thermodynamics over the energy range of 7.7 to 200 GeV. In contrast, the calculations from the ideal HRG, UrQMD, and Skellam baseline, which do not incorporate any QCD effects, showed the absence of any hierarchy.

Probing the QCD critical point

The experimental search for QCD critical point is motivated by theoretical calculations from the linear sigma model that predict a non-monotonic collision energy dependence of net-proton C_4/C_2 with respect to baseline fluctuations in the presence of a QCD critical point. The experimentally measured C_4/C_2 from 0-5% centrality exhibited a non-monotonic collision energy dependence at a significance level of $3.1 - 3.3\sigma$ with respect to various non-critical baselines provided by the HRG model, UrQMD model, and Skellam

baseline. These non-critical baselines and the peripheral 70-80% data, on the other hand, showed monotonic variations as a function of energy.

Probing the crossover

The search for crossover is inspired by lattice QCD calculations ($\mu_B \leq 110$ MeV) on hyper-order net-baryon cumulant ratios predicting their negative values for a crossover quark-hadron transition that increases in magnitude with μ_B . The experimentally measured net-proton (as proxy for net-baryon) cumulant ratio C_6/C_2 is found to be progressively negative with decreasing collision energy (increasing μ_B) within uncertainties. The observed negative sign and trend are consistent with the lattice QCD prediction. The overall significance of observing a negative C_6/C_2 in half of the collision energies from $\sqrt{s_{NN}} = 7.7$ to 200 GeV was quantified to be 1.7σ . In contrast, the peripheral 70-80% data and calculation from ideal HRG, UrQMD, and Poisson baseline are non-negative at all energies.

Probing the first-order phase transition

The two-component nature of proton multiplicity distribution expected near a first-order phase transition was exploited in the experimental search for first-order phase transition. Large factorial cumulants (κ_n) that alternated signs with increasing order were expected. The experimental measurements showed small deviations from zero and a lack of sign-change within uncertainties for $\sqrt{s_{NN}} \geq 11.5$ GeV suggesting the absence of a two-component structure in proton multiplicity distribution at those energies. At 7.7 GeV, there are indications of large factorial cumulants with the possibility of a sign change, although the uncertainties are large.

While many important and exciting features were observed from the net-proton fluc-

tuation studies up to the sixth order, drawing solid and clear conclusions would require reducing the uncertainties considerably. Various signals exhibited by the measurements in the study of QCD phase structure were limited to a significance of $\lesssim 3\sigma$ due to large uncertainties. For example, the energy dependence trends of C_4/C_2 and C_6/C_2 , which were studied in relevance to critical point search and crossover search, respectively, were driven by low collision energies where the uncertainties on measurements were large. For confirmation of these signals observed in phase I of BES, a second phase of the BES program (BES-II) was recently carried out at RHIC. With the aim of improving the statistical precision of measurements and enhancing the quality of the signal, BES-II collected a large number of events and made several important detector upgrades. New measurements from BES-II await us in the experimental quest to map the QCD phase diagram in the near future.

Chapter 8

Future direction: Phase II of Beam

Energy Scan

8.1 Prospects

Improved event statistics

Several interesting observations were made in regard to the QCD phase structure from BES-I net-proton fluctuation measurements. Nonetheless, the measurements lacked the rigor to claim a discovery due to large uncertainties on them, especially at low collision energies. To confirm the observed trends, BES-II collected enormous Au+Au collision events (about 10 – 20 times than that of BES-I) over the collision energy range $\sqrt{s_{NN}} = 7.7 - 19.6$ GeV in collider mode [1]. Additionally, two new center-of-mass collision energies at $\sqrt{s_{NN}} = 9.2$ and 17.3 GeV are included. The location of these two energies is strategically important in reference to the non-monotonic energy dependence of C_4/C_2 observed at BES-I. The events statistics collected for all these energies are listed in table 8.1, along with the corresponding μ_B at chemical freeze-out.

Table 8.1: Event statistics collected for Au+Au collisions from BES-II at various center-of-mass energies from 7.7 GeV to 19.6 GeV in collider mode and their corresponding μ_B values [2].

$\sqrt{s_{NN}}$ (GeV)	Events (millions)	μ_B (MeV)
7.7	100	420
9.2	160	370
11.5	230	315
14.5	300	264
17.3	250	230
19.6	400	206

Exploration of the high μ_B region is important to observe the return of critical point-induced fluctuations to the baseline. The turn-off of the QGP signatures is also expected at large μ_B . To extend the fluctuation measurements to an even higher μ_B region than at 7.7 GeV, a fixed (FXT) target program was also added to BES-II [1]. Collecting events by decreasing the center-of-mass energy below $\sqrt{s_{NN}} = 7.7$ GeV in collider mode is technically and economically quite challenging. Hence the fixed target mode was chosen. The FXT program collected a large number of Au+Au collision events and extended the accessible center-of-mass energy down to $\sqrt{s_{NN}} = 3$ GeV. The events statistics collected for all energies as part of the FXT program are listed in table 8.1 along with the corresponding μ_B at chemical freeze-out. The $\sqrt{s_{NN}} = 7.7$ GeV is common between collider mode and FXT mode and allows for checking consistency of results obtained with these two modes of detector operation.

Detector upgrades in BES-II

In addition to the availability of huge event statistics and access to a large μ_B region, BES-II also aims to improve the quality of signals predicted in regard to the study of QCD phase structure. For this, several detector upgrades were carried out for the STAR detector [1, 3, 4]. The upgrades included the installation of inner chambers of the TPC

Table 8.2: Event statistics collected for Au+Au collisions from BES-II at various center-of-mass energies from 3 GeV to 7.7 GeV in fixed target mode and their corresponding μ_B values [2].

$\sqrt{s_{NN}}$ (GeV)	Events (millions)	μ_B (MeV)
7.7	160	420
6.2	120	486
5.2	100	541
4.5	100	587
3.9	120	633
3.5	120	669
3.2	200	698
3.0	260	720
3.0	2000	720

(i-TPC), the addition of an end-cap time of flight (e-TOF) detector, and a new event plane detector (EPD). They are briefly described as follows.

a) Inner-TPC (i-TPC)

The i-TPC upgrade was done to enhance the segmentation of inner pad planes. The number of pad rows were increased from 13 to 40 and size of pad planes was also enlarged. This was carried out for all the 24 sectors of the TPC. The upgrade increased the pseudo-rapidity coverage from $|\eta| < 1$ to $|\eta| < 1.6$. Furthermore, it also provided better momentum resolution and a 25% improvement in dE/dx resolution. The improved segmentation of pad planes helped to bring down the lower momentum threshold from its previous value of $p_T = 0.15$ GeV/c to 0.06 GeV/c.

b) End-cap Time Of Flight (e-TOF)

The e-TOF upgrade installed TOF modules along the pseudo-rapidity coverage from $1.1 < \eta < 1.6$, thus extending particle identification to forward rapidity. A total of 36 TOF modules were added to 12 sectors with 3 Multi-gap Resistive Plate Counters

(MRPCs) in each module. This upgrade is particularly helpful for FXT datasets where detector acceptance is assymmetric about mid-rapidity.

c) Event Plane Detector (EPD)

The EPD detector is a new addition to the STAR detector set-up that allows for precise event plane determination. The detector covers the pseudo-rapidity range of $2.1 < \eta | < 5.1$. Its design constitutes scintillator tiles with 24 azimuthal segments and 16 radial segments. With timing resolution of ~ 1 ns, the EPD serves as a good trigger detector for low collision energies. By collecting ionization signals, the EPD also provides collision centrality independent of the TPC. This is imporant to avoid any self-correlation effects between observables of interest which are usually measured with the TPC and the centrality definition.

These upgrades will bring new scopes to the fluctuation measurements, such as enlarged rapidity acceptance (due to i-TPC), extended particle identification (due to e-TOF) and centrality definition at forward rapidity (due to EPD).

Author's contribution

The author of the thesis contributed to i-TPC upgrade. Increasing the segmentation of inner sectors of TPC meant that the electronics involved in obtaining signals from the hits generated by charged tracks also needed upgradation. The STAR detector uses the multi-wire proportional chambers (MWPCs) detectors in tracking the trajectory of a charged particle. The readout system accompanied with the MWPCs comprising of read out boards (RDOs) and front end electronics (FEE) were updated to handle increased number of pad rows and larger size of pad planes. Due to high probability of obtaining multiple hits on a single TPC pad, each pad is read out with a waveform digitizer. Amplifiers are also

needed to improve the signal strength. The FEE cards are employed for this. The FEE cards consists of digitizer and amplifier circuits. These cards are read out by the RDOs. The RDO boards multiplex the data from different FEE cards to a single fibre that goes to the Data Acquisition (DAQ) electronics in the recording of an event.

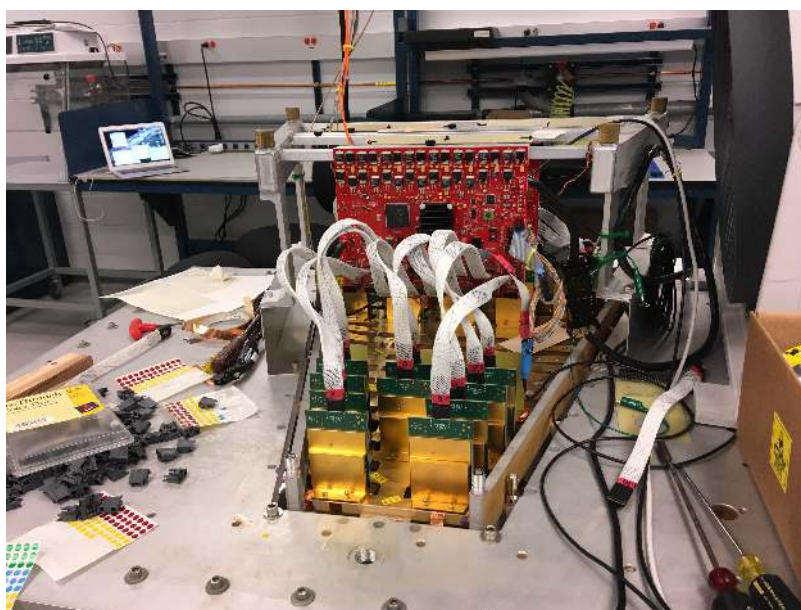


Figure 8.1: A photo of testing of FEE cards (green colored circuit boards with a golden structure attached to it). The FEE cards are assembled with sink (the golden structure) and mounted on a single sector of TPC. The output from all FEE cards are fed to a RDO board (red colored circuit board).

Under the supervision of senior scientists and engineers at the Brookhaven Lab, the author was involved in testing of the FEE cards and its installation at the STAR detector site. The FEE cards were assembled with their sinks and tested for their proper working conditions by mounting them on a sector of TPC available at the lab. Figure 8.1 shows a visual taken by the author on the testing of FEE cards. There were more than 900 FEE cards that were assembled and verified. After confirming their proper working condition, they were installed on the STAR detector along with the RDOs.

Study of the QCD phase diagram with BES-II

With BES-II, a precise study of QCD phase structure at high μ_B would be possible. Recently, the first results from Au+Au collisions at $\sqrt{s_{NN}} = 3$ GeV from the FXT program were reported. The proton C_4/C_2 measurements at 3 GeV along with net-proton C_4/C_2 from BES-I energies are shown in Fig. 8.2 [5–7]. Proton fluctuations were reported for 3 GeV instead of net protons because of the negligible number of antiprotons at this energy (less by six orders of magnitude compared to the number of protons). A suppression of measurement is seen at 3 GeV compared to higher energies. Such suppression is explained by the UrQMD baseline, which includes baryon number conservation and baryon stopping effects in its calculation. These results indicate that the QCD critical point, if accessible to heavy-ion collisions, could only exist above 3 GeV. The remaining energy from the BES-II program will shed more light on the critical point search.

Acceptance dependence studies of C_4/C_2 measurements with the extended rapidity coverage offered by i-TPC coverage will complement the critical point search by energy scan. This would also require proton and antiproton identification provided by e-TOF at higher rapidity. The initial state fluctuations, such as those induced from a QCD critical point, are long-range in nature and grow with acceptance. A power law behavior of fluctuation measurements as a function of rapidity window [10] is expected in the presence of a critical point, which can be tested with wide rapidity acceptance at BES-II. If hints of criticality are seen between two energies, then a rapidity scan of measurements can help to pinpoint the location of the critical point. This is possible because of the non-trivial dependence of μ_B on rapidity [11].

We had noted that net-proton C_6/C_2 measurements from BES-I energies had exhibited a progressively negative trend with decreasing energy. Results on proton C_6/C_2 were also reported for 3 GeV [12]. While the negative sign for C_6/C_2 is predicted for a crossover

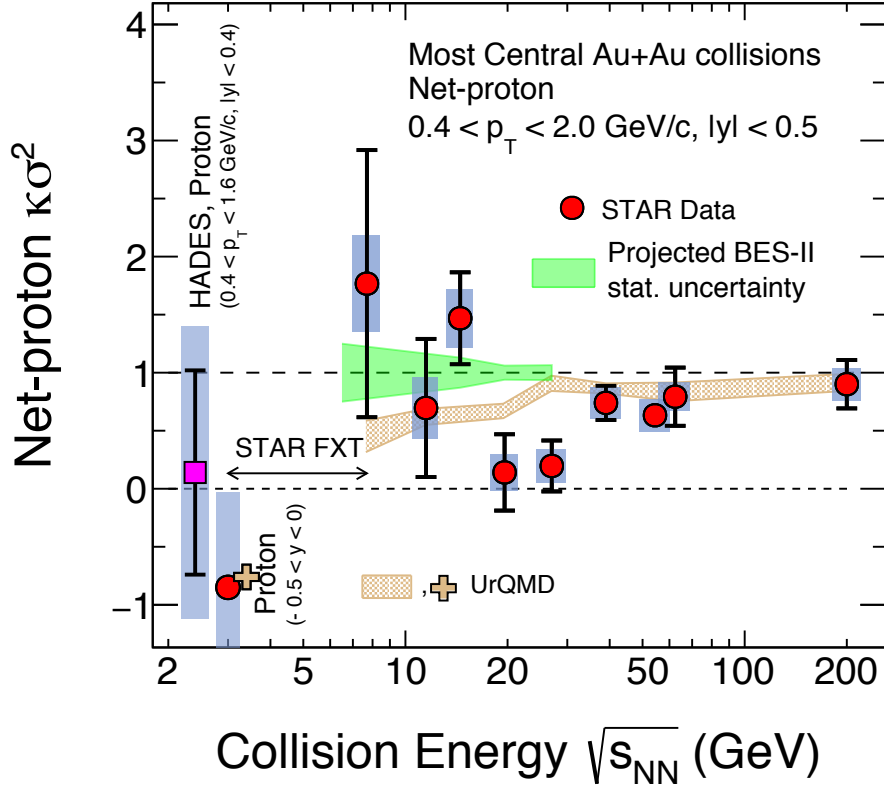


Figure 8.2: Net-proton/proton C_4/C_2 in 0-5% Au+Au collisions from $\sqrt{s_{NN}} = 3.0$ to 200 GeV [5–8]. The 3 GeV results were measured with half rapidity coverage ($-0.5 < y < 0$). Also shown are results from HADES for 0-10% centrality [9]. The bars and shaded bands on the data points represent the statistical and systematic uncertainties, respectively. The brown marker (only at 3 GeV) and the band are UrQMD model calculations. The current projection of statistical uncertainty from BES-II at collider energies is shown as a green band. The double-headed arrow demarcates the energy range covered by the FXT program [1].

transition by lattice QCD [13], measurements (0-40%) at 3 GeV are found to be positive (shown in Fig. 8.3). The observed sign at 3 GeV is reproduced by UrQMD model calculation which does not include any phase transition effects. Furthermore, the cumulant ratios at 3 GeV were found to violate the ordering expected from QCD thermodynamics [13] with 3.8σ significance by exhibiting an exact reverse ordering [12]. Such reverse ordering was also reproduced by the UrQMD model. The good agreement of 3 GeV results with UrQMD

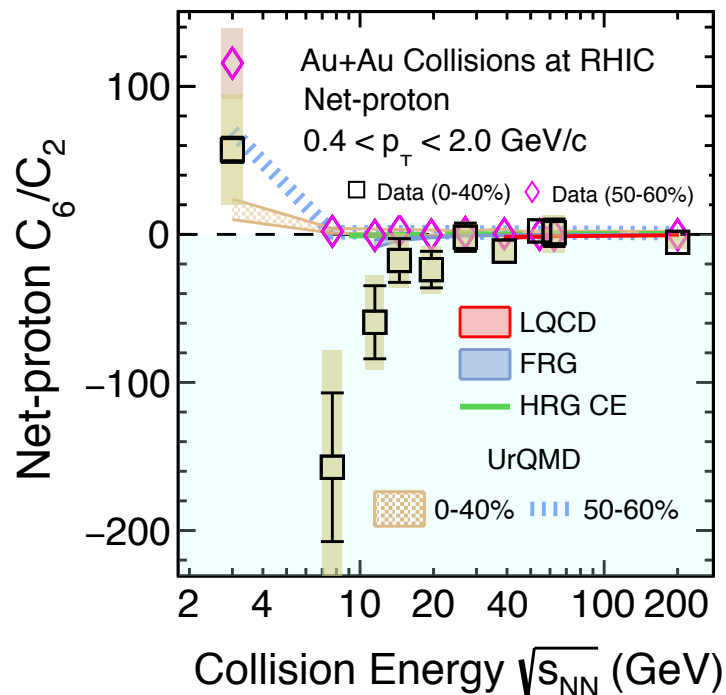


Figure 8.3: Net-proton/proton C_6/C_2 in 0-40% and 50-60% Au+Au collisions from $\sqrt{s_{NN}} = 3.0$ to 200 GeV [12]. The 3 GeV results were measured with half rapidity coverage ($-0.5 < y < 0$). The bars and the shaded bands on the data points represent statistical and systematic uncertainties, respectively. Calculations from LQCD (red band), FRG (blue band), HRG CE (green line), and UrQMD (brown band and dashed lines) models are also presented.

suggests the QCD matter produced in such low collision energies is dominantly hadronic.

The new results at 3 GeV and their contrast with measurement from BES-I energies indicate that the QCD phase structure at high $\mu_B \sim 720$ MeV ($\sqrt{s_{NN}} = 3$ GeV) is starkly different than those at low $\mu_B \sim 24$ MeV ($\sqrt{s_{NN}} = 200$ GeV). The 3 GeV results were obtained with ~ 150 million good events. BES-II also collected 2 billion events at 3 GeV in a later run of RHIC, which included the detector upgrades. The trends of higher-order fluctuations, their signs, and ordering from all BES-II energies will be important in the precise determination of the QCD phase structure. In this regard, precision measurements in the collision energy range of 3 – 7.7 GeV from the FXT mode and 7.7 – 19.6 GeV from

the collider mode are highly awaited.

8.2 Challenges

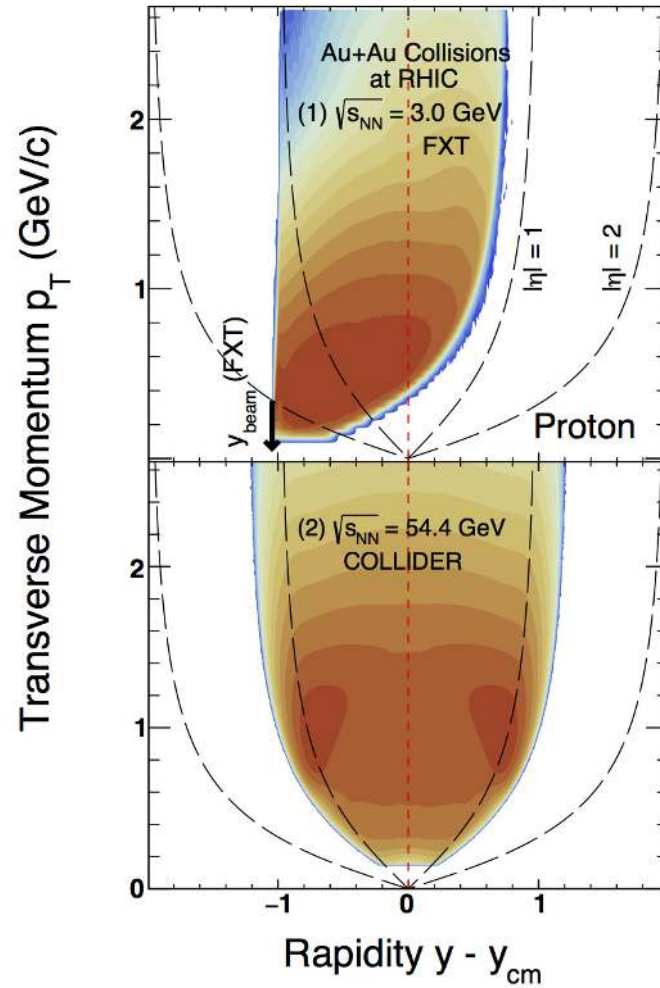


Figure 8.4: Proton phase space acceptance in terms of rapidity ($y - y_{cm}$ where y_{cm} is the rapidity in center-of-mass frame) vs. momentum (p_T) coverage from Au+Au collisions [8]. The top panel is for collision at $\sqrt{s_{NN}} = 3$ GeV collected in FXT mode, while the bottom panel is for collision at $\sqrt{s_{NN}} = 54.4$ GeV collected in collider mode.

Acceptance: Collider vs. FXT

In addition to collision energy, the mode of collision (FXT or collider) also determines

the phase space acceptance for the charged particles. For example, as shown in Fig. 8.4, the protons acceptance is asymmetric in FXT mode (top panel) while it is symmetric in the collider mode (bottom panel). The degree of asymmetry and the location of mid-rapidity varies with collision energies in FXT mode. In contrast, for collider mode, the mid-rapidity is situated at zero because the y_{cm} (rapidity in the center of mass frame) is always zero. With changing phase space acceptance and changing y_{cm} , the selection of mid-rapidity (anti-) protons for fluctuation measurements at FXT energies could pose a challenge, given the limited coverage of detectors. For $\sqrt{s_{NN}} = 3$ GeV accessing mid-rapidity with TPC is possible. However, for higher FXT energies, i-TPC (inner - TPC) and e-TOF (extended - TOF) detectors will be needed to provide phase-space coverage around the mid-rapidity, though it may not be possible for all FXT energies.

Volume fluctuation

The data-driven CBWC method [14] was employed in the measurement of cumulants at BES-I energies to account for the volume fluctuation effect. For the CBWC method to effectively suppress the volume fluctuations, the resolution of the centrality estimator should be sufficiently high. While this is the case for BES-I energies, the FXT energies in BES-II suffer from poor centrality resolution due to a very small number of produced charged particles [7, 15]. As a consequence volume fluctuation effects become significant. To demonstrate the same, correlation between charged particle multiplicity from the UrQMD model obtained within the same acceptance as used for centrality definition at STAR and the number of participant nucleons (N_{part}) are presented in Fig. 8.5 [15]. A thick correlation band is seen due to the low number of charged particle multiplicity, indicating that the events selected with centrality definition using N_{part} and charged particle multiplicity are not the same. In fact, the poor centrality resolution mixes the events belonging to different

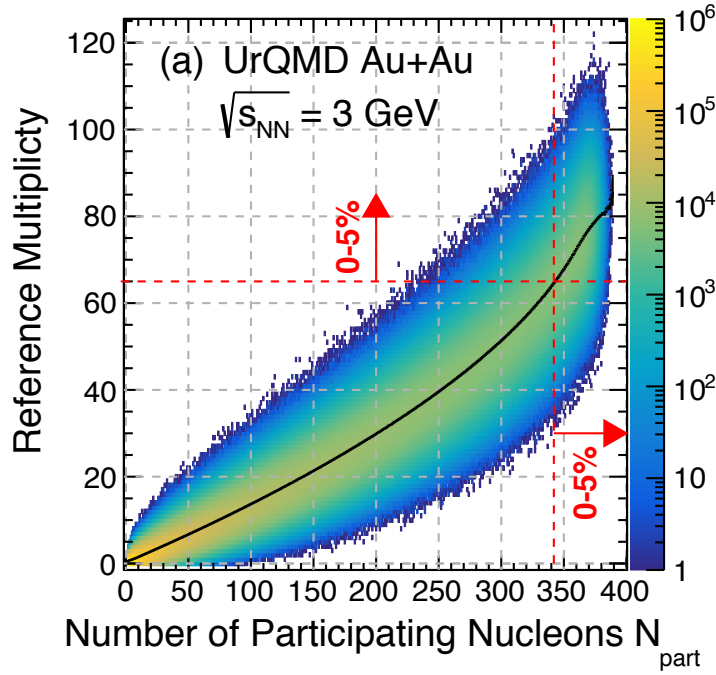


Figure 8.5: A correlation plot of charged particle multiplicity from UrQMD model selected within same acceptance as used for centrality definition in $\sqrt{s_{NN}} = 3$ GeV at STAR vs. the number of participant nucleons (N_{part}) [15]. The red horizontal and vertical lines represent the centrality cuts obtained using charged particle multiplicity and N_{part} , respectively, for selecting 0-5% central Au+Au collision events. The figure taken from Ref. [15].

centrality classes together.

Due to poor centrality resolution at FXT energies, the CBWC may not be fully effective. Another method called Volume fluctuation Correction (VFC) [16, 17], which requires information of N_{part} as input from models, shows severe model dependencies. UrQMD model studies at 3 GeV indicate the volume fluctuation effects on fluctuation measurements are not fully suppressed by employing either of the CBWC and VFC methods [15]. Hence more effective methods are needed to address this issue.

A complete study of fluctuation measurements from BES-II (FXT program to be particular) will be accompanied by these challenges. While the i-TPC and e-TOF detector would

be able to compensate for the asymmetric phase space acceptance at FXT energies to a good extent, fully suppressing the volume fluctuations effects at FXT energies will require additional studies. All things considered, the BES-II program, with significantly increased event statistics, wide μ_B coverage, and important detector upgrades, carries immense potential to map the QCD phase diagram with remarkable precision and help establish it as part of textbook curriculum.

Bibliography

- [1] *BES-II whitepaper, STAR note: SN0598*. <https://drupal.star.bnl.gov/STAR/starnotes/public/sn0598>.
- [2] J. Cleymans, H. Oeschler, K. Redlich, et al. “Comparison of chemical freeze-out criteria in heavy-ion collisions”. *Phys. Rev. C* 73 (2006), 034905. arXiv: [hep-ph/0511094](https://arxiv.org/abs/hep-ph/0511094).
- [3] David Tlusty. “The RHIC Beam Energy Scan Phase II: Physics and Upgrades”. *13th Conference on the Intersections of Particle and Nuclear Physics*. Oct. 2018. arXiv: [1810.04767](https://arxiv.org/abs/1810.04767) [[nucl-ex](#)].
- [4] C. Yang and Q. Yang. “The STAR Detector Upgrades for the BES-II and at Forward Rapidity”. *JINST* 15.07 (2020), C07040.
- [5] J. Adam et al. “Nonmonotonic Energy Dependence of Net-Proton Number Fluctuations”. *Phys. Rev. Lett.* 126.9 (2021), 092301. arXiv: [2001.02852](https://arxiv.org/abs/2001.02852) [[nucl-ex](#)].
- [6] Mohamed Abdallah et al. “Cumulants and correlation functions of net-proton, proton, and antiproton multiplicity distributions in Au+Au collisions at energies available at the BNL Relativistic Heavy Ion Collider”. *Phys. Rev. C* 104.2 (2021), 024902. arXiv: [2101.12413](https://arxiv.org/abs/2101.12413) [[nucl-ex](#)].
- [7] M. S. Abdallah et al. “Measurements of Proton High Order Cumulants in $\sqrt{s_{NN}} = 3$ GeV Au+Au Collisions and Implications for the QCD Critical Point”. *Phys. Rev. Lett.* 128.20 (2022), 202303. arXiv: [2112.00240](https://arxiv.org/abs/2112.00240) [[nucl-ex](#)].

- [8] A. Pandav, D. Mallick, and B. Mohanty. “Search for the QCD critical point in high energy nuclear collisions”. *Prog. Part. Nucl. Phys.* 125 (2022), 103960. arXiv: [2203.07817 \[nucl-ex\]](#).
- [9] J. Adamczewski-Musch et al. “Proton-number fluctuations in $\sqrt{s_{NN}} = 2.4$ GeV Au + Au collisions studied with the High-Acceptance DiElectron Spectrometer (HADES)”. *Phys. Rev. C* 102.2 (2020), 024914. arXiv: [2002.08701 \[nucl-ex\]](#).
- [10] Bo Ling and Mikhail A. Stephanov. “Acceptance dependence of fluctuation measures near the QCD critical point”. *Phys. Rev. C* 93.3 (2016), 034915. arXiv: [1512.09125 \[nucl-th\]](#).
- [11] Jasmine Brewer, Swagato Mukherjee, Krishna Rajagopal, et al. “Searching for the QCD critical point via the rapidity dependence of cumulants”. *Phys. Rev. C* 98.6 (2018), 061901. arXiv: [1804.10215 \[hep-ph\]](#).
- [12] “Beam Energy Dependence of Fifth and Sixth-Order Net-proton Number Fluctuations in Au+Au Collisions at RHIC” (July 2022). arXiv: [2207.09837 \[nucl-ex\]](#).
- [13] A. Bazavov et al. “Skewness, kurtosis, and the fifth and sixth order cumulants of net baryon-number distributions from lattice QCD confront high-statistics STAR data”. *Phys. Rev. D* 101.7 (2020), 074502. arXiv: [2001.08530 \[hep-lat\]](#).
- [14] Xiaofeng Luo, Ji Xu, Bedangadas Mohanty, et al. “Volume fluctuation and auto-correlation effects in the moment analysis of net-proton multiplicity distributions in heavy-ion collisions”. *J. Phys. G* 40 (2013), 105104. arXiv: [1302.2332 \[nucl-ex\]](#).
- [15] “Higher-Order Cumulants and Correlation Functions of Proton Multiplicity Distributions in $\sqrt{s_{NN}} = 3$ GeV Au+Au Collisions at the STAR Experiment” (Sept. 2022). arXiv: [2209.11940 \[nucl-ex\]](#).
- [16] V. Skokov, B. Friman, and K. Redlich. “Volume Fluctuations and Higher Order Cumulants of the Net Baryon Number”. *Phys. Rev. C* 88 (2013), 034911. arXiv: [1205.4756 \[hep-ph\]](#).
- [17] P. Braun-Munzinger, A. Rustamov, and J. Stachel. “Bridging the gap between event-by-event fluctuation measurements and theory predictions in relativistic nuclear collisions”. *Nucl. Phys. A* 960 (2017), 114–130. arXiv: [1612.00702 \[nucl-th\]](#).